Implications of Intense Magnetic Fields on Neutron-Star Physics

Jeremy Samuel Heyl

Board of Studies in Astronomy and Astrophysics
University of California at Santa Cruz

A thesis submitted to the University of California
in partial fulfillment of the requirements
for the degree of Doctor of Philosophy

March 1998

Contents

List of Figures

List of Tables

Abstract

Astrophysics and fundamental physics converge in the study of neutron stars. In this thesis, I will examine how intense magnetic fields influence physical processes in the vicinity of and inside neutron stars.

Even with the absence of matter, an intense magnetic field can have dramatic effects on the propagation of electromagnetic radiation and the structure of a dipole field. To understand these effects, we first derive a compact analytic form for the effective Lagrangian of quantum electrodynamics (QED) with an external field. An intense field modifies the propagators of the virtual electron-positron pairs formed as a photon travels. We first treat the effects of QED as an effective magnetic permeability and electric permittivity. Using the macroscopic Maxwell equations it is straightforward to derive compact expressions for the index of refraction of a low-frequency photon traveling through an electric or magnetic field. Also in the same manner we examine the one-loop corrections to a macroscopic magnetic dipole and find that the non-linear paramagnetic properties of the vacuum result in dipole, hexapole, $2n$-pole moments which are a function of distance from the dipole.

The speed of light in a magnetized vacuum is slightly less than c and is a function of the strength of the fields. We propose an experiment using the existing LIGO testbed interferometer which can measure this effect with a signal-to-noise ratio of fifteen within a week to several months depending on the size and strength of the magnet used. If successful, this would be the first direct measurement of the photon-photon coupling with a uniform external field, one of the original predictions of QED. Also, since the speed of light is a function of the strength of the local field, we expect an intense magnetic field to affect the propagation of an electromagnetic wave. We treat the electromagnetic field as a relativistic fluid and derive the equations for the characteristics. The characteristics of the wave begin to cross after a number of wavelengths which depends on the strength of the wave and of the external field. A shock forms. The energy of the wave dissipates into electron-positron pairs shortly thereafter.

We next discuss how an intense magnetic field affects atomic structure. First using a simple, yet accurate model for a hydrogen atom in an intense magnetic field, we find that the bound electron shields the nucleus quite effectively and that the cross section for nuclear fusion reactions is dramatically increased. We then revisit the study of atomic structure and develop both an analytic and a convenient numerical technique to accurately study the properties of simple atoms and molecules in an intense magnetic field.

Again we increase the scale from atomic physics to solid-state physics to understand how an intense magnetic field affects the transmission of heat through the envelope of a cooling neutron star. We develop a plane-parallel analytic treatment of the neutron star envelope in a sufficient intense magnetic field and find that the surface emission in this limit is proportional to the square of the cosine of the angle between the radial direction and the magnetic field, the $\cos^2\psi$ rule. This observation with the assumption that the neutron star surface radiates as a blackbody allows us to calculate the observed spectra from a neutron star including the effects of the deflection of null geodesics by the intense gravitational field of the neutron star.

We reexamine the problem of heat flow for weaker fields by numerically integrating the thermal structure of the envelope, again in the plane-parallel approximation. We derive the relationship between core temperature and transmitted flux over a wide range of field strengths and geometries. We find that in weaker fields especially for warmer neutron stars the $\cos^2\psi$ rule is less accurate and a dipolar magnetic field introduces only a negligible perturbation on the moment of inertia of the neutron star.

Combining the results of this study of neutron star envelopes with a model for the cooling of a neutron star, we explore how an intense magnetic field affects the observed flux from neutron stars with both iron and light-element envelopes. We find that although a magnetic field strongly affects the thermal evolution of the neutron star, the effect of altering the composition of the envelope is more dramatic. We propose that the emission from anomalous X-ray pulsars is simply the surface thermal emission from isolated neutron stars.

Preface

The text of this dissertation includes reprints of the following previously published material:

- Chapter 2: Heyl, J. S. & Hernquist, L. 1997, *Phys. Rev. D,* **55**, 2449.
- Chapter 3: Heyl, J. S. & Hernquist, L. 1997, *Jour. Phys. A,* **30**, 6485.
- Chapter 4: Heyl, J. S. & Hernquist, L. 1997, *Jour. Phys. A,* **30**, 6475.
- Chapter 6: Heyl, J. S. & Hernquist, L. 1997, *Electromagnetic Shocks in Strong Magnetic Fields*, submitted to *Phys. Rev D.*
- Chapter 7: Heyl, J. S. & Hernquist, L. 1996, *Phys Rev C,* **54**, 2751.
- Chapter 8: Heyl, J. S. & Hernquist, L. 1997, *Hydrogen and Helium Atoms and Molecules in an Intense Magnetic Field*, submitted to *Phys Rev A.*
- Chapter 9: Heyl, J. S. & Hernquist, L. 1997, *Almost Analtyic Models of Ultramagnetized Neutron Star Envelopes*, submitted to *MNRAS.*
- Chapter 11: Heyl, J. S. & Hernquist, L. 1997, *ApJL,* **491**, 95.
- Chapter 12: Heyl, J. S. & Hernquist, L. 1997, *ApJL,* **489**, 67.
- Chapter 13: Heyl, J. S. & Hernquist, L. 1997, *What is the Nature of RXJ-0720?*, accepted for publication in *MNRAS.*

The co-author listed in these publications directed and supervised the research which forms the basis for the dissertation.

For Jenny.

Chapter 1

Introduction

1.1 Physical Overview

Neutron stars are among the most extreme objects studied by physicists. They are the remnants of one of the most energetic phenomena in the universe, a supernova. A supernova's violent explosion results from the even more violent implosion of a massive star's core to nuclear densities. After the implosion, the stellar core has a radius of ten kilometers yet comprises the mass of one and a half suns. It is now a neutron star.

The supernova has merged the astronomical with the commonplace. Not only is the size of a neutron star extremely small by astronomical standards and usual by laboratory standards, in many respects they are described by theories more familiar to the condensed matter and plasma physicist than to the astrophysicist. The central region of the neutron star is likely to consist of neutron and proton superfluids with sufficient electrons present to maintain charge neutrality. The outermost kilometer consists of nuclei and free electrons, a metal, and the final quarter kilometer insulates the core of the neutron star from space. Here, the flow of heat is impeded as electrons scatter off of nuclei and phonons, and the temperature declines from several tens or hundreds of million of degrees to a million degrees or so. The properties of this outermost 250 meters determine the luminosity of the cooling neutron star and how it will appear to X-ray telescopes orbiting the Earth.

During the collapse, not only is matter compressed, but the magnetic field of the progenitor star is compressed and may be amplified up to $\sim 10^{13}$ G and beyond. Although Baade and Zwicky proposed in 1934 that neutron stars may be formed in supernova explosions, it was not until

1967 that the first neutron star was discovered (Hewish et al. 1968). The rotation of its intense magnetic field generates a pulsating radio signal, and the object was identified as a pulsar. Since then nearly one-thousand radio pulsars have been discovered (Taylor, Manchester & Lyne 1993), and many types of objects have been associated with intensely magnetized neutron stars.

This thesis focuses on how an intense magnetic field affects the physical processes in and near neutron stars. Even laboratory magnetic fields can have a dramatic effect on matter. The weak magnetic field of the Earth of about one gauss is sufficient to magnetize ferromagnetic materials and align them along the direction of the field. Some aquatic bacteria carry nodules of magnetite to orient themselves along the Earth's inclined magnetic field and swim toward the mud (Balkemore & Frankel 1981). Magnetic fields ten thousand times stronger than the Earth's (10^4 G) are routinely used in magnetic resonance imaging (MRI) and in particle accelerators. Magnetic fields much stronger than this tend to crush the apparatus which generates them; consequently, the strongest magnetic fields produced on Earth are about a megagauss.

Magnetic fields yet a thousand times larger crush not only bulk material but the atoms that make matter. Fields stronger than 10^9 G dominate the electrostatic forces that determine the structure of ordinary matter. Magnetic fields stronger than this effectively confine electrons to move in one dimension along the direction of the magnetic field. Furthermore, the fact that the motion of the electrons perpendicular to the field is quantized (*e.g.* Landau & Lifshitz 1989) becomes crucial in understanding the properties of the material. Atoms become cylindrical, and heat flows efficiently only along the magnetic field lines. Throughout this thesis we will designate magnetic fields sufficiently strong to dominate atomic structure, as intense magnetic fields (IMFs). The most weakly magnetized neutron stars which have been detected as pulsars, the millisecond pulsars have $B \sim 10^8$ G.

Increasing the strength of the magnetic field one hundred thousand times further to $\sim 10^{13}$ G uncovers new phenomena. At this field strength, the energy spacing between the cyclotron levels of an electron is comparable to its rest mass energy. A comparably strong electric field will short itself out even in vacuo by producing electron-positron pairs (see Chapter 2); this is the Klein paradox of relativistic quantum mechanics (*e.g.* Bjorken & Drell 1964). A magnetic field is not unstable in this way, and several pulsars have been observed which have field strengths approaching the so called quantum critical field of 4.4×10^{13} G (Taylor, Manchester & Lyne 1993). In this ultramagnetized regime, the magnetic field magnetizes the vacuum itself.

The magnetization and polarization of the vacuum have dramatic effects on the electromagnetic fields near a neutron star. The vacuum acts as a nonlinear dielectric. Photons traveling through an intense magnetic field may split into two or coalesce. Even a static magnetic field is altered by the induced magnetization of the surrounding vacuum. The nonlinearity of the electromagnetic field may explain features of the emission from the surface of neutron stars as well as the mechanism that generates the pulsating radio emission that belied the existence of the first discovered neutron stars.

The next milestone along the path of ever increasing magnetic field strengths lies at 1.2×10^{18} G. At this field strength, the characteristic cyclotron energy of the W particle is comparable to its rest-mass energy, and the unification of electromagnetism into the electroweak theory is crucial. Above this field strength, the nonabelian character of the electroweak theory may dramatically complicate the dynamics.

1.2 Thesis Outline

This thesis is organized into four independent parts. Each part may be considered separately from the others.

The first part discusses how an ultrastrong magnetic field affects the structure of the vacuum within the framework of quantum electrodynamics (QED). Chapter 2 presents a simple analytic form for the effective Lagrangian of QED and applies this result to pair production in an intense electric field and the splitting of photons at low energies. Chapter 3 and Chapter 4 explore the paramagnetic and dielectric properties of an intense field. Both Chapter 4 and Chapter 6 focus on the nonlinear properties of the electromagnetic field. The first chapter examines how the static field on a magnetic dipole is altered by the nonlinear paramagnetic vacuum surrounding it. The latter chapter discusses the propagation of electromagnetic waves through an intense magnetic field and argues that the nonlinearity of the vacuum can lead to the formation of electromagnetic shocks. The final chapter (Chapter 5) of the first part proposes an experiment to measure the nonlinear properties of the vacuum in QED.

The second part focuses on the effects of an intense magnetic field on the structure of atoms. An intense magnetic field compresses an atom both along and transverse to the field lines. Since the electron cloud surrounding the nucleus is much more compact than without a magnetic field, we consider the possibility that bound electrons can effectively screen the nuclei from each other, allowing nuclear reactions to proceed (Chapter 7). The second chapter (Chapter 8) examines the structure hydrogen and helium, atoms and molecules in an intense magnetic field more precisely, delving into magnetic chemistry.

The core of a neutron star is insulated from the surrounding vacuum by a thin envelope. This envelope determines the rate of thermal emission from the surface of an isolated neutron. Chapter 9 presents an analytic treatment to study the envelopes of ultramagnetized neutron stars ($B \geq 10^{14}$ G), while Chapter 9 treats the same problem numerically focusing on weaker fields (10^{12} G $\geq B \geq 10^{14}$ G).

The final part translates the results of the third part into the observable realm. It examines the properties of cooling neutron stars in three regimes. Chapter 11 focuses on neutron stars with $B \geq 10^{14}$ G and envelopes which consists of iron. Chapter 12 contrasts the early cooling (1000 yr $< t <$ 10^6 yr) of neutron stars with iron and light element envelopes. The final chapter (Chapter 13) discusses the cooling of neutron stars with a range of field strengths and compositions during the epoch where photon and neutrino cooling compete ($t \sim 10^6$ yr).

Part I

Magnetic Fields and the Vacuum

Chapter 2

An Analytic Form for the Eective Lagrangian of QED and its Application to Pair Production and Photon Splitting

SUMMARY

We derive an analytic form for the Heisenberg-Euler Lagrangian in the limit where the component of the electric field parallel to the magnetic field is small. We expand these analytic functions to all orders in the field strength ($F_{\mu\nu} F^{\mu\nu}$) in the limits of weak and strong fields, and use these functions to estimate the pair-production rate in arbitrarily strong electric fields and the photon-splitting rate in arbitrarily strong magnetic fields.

2.1 Introduction: The One-Loop Effective Lagrangian of QED

When one-loop corrections are included in the Lagrangian of the electromagnetic field one obtains a non-linear correction term:

$$\mathcal{L} = \mathcal{L}_0 + \mathcal{L}_1 . \tag{2.1}$$

Both terms of the Lagrangian can be written in terms of the Lorentz invariants,

$$I = F_{\mu\nu}F^{\mu\nu} = 2\left(|\mathbf{B}|^2 - |\mathbf{E}|^2\right) \tag{2.2}$$

and

$$K = \{\epsilon^{\lambda\rho\mu\nu}F_{\lambda\rho}F_{\mu\nu}\}^2 = -(4\mathbf{E}\cdot\mathbf{B})^2, \tag{2.3}$$

following Heisenberg & Euler (1936). We do not expect terms which are odd powers of $\epsilon^{\lambda\rho\mu\nu}F_{\lambda\rho}F_{\mu\nu}$ to appear in the effective Lagrangian as these terms would yield a Lagrangian which would violate the C and P symmetries of the tree-level Lagrangian.

Heisenberg & Euler (1936) and Weisskopf (1936) independently derived the effective Lagrangian of the electromagnetic field using electron-hole theory. Schwinger (1951) later rederived the same result using quantum electrodynamics. In rationalized electromagnetic units, the Lagrangian is given by

$$\begin{aligned}
\mathcal{L}_0 &= -\frac{1}{4}I && (2.4)\\
\mathcal{L}_1 &= \frac{e^2}{hc}\int_0^\infty e^{-\zeta}\frac{d\zeta}{\zeta^3}\Bigg\{i\zeta^2\frac{\sqrt{-K}}{4}\times \\
&\quad \frac{\cos\left(\frac{\zeta}{B_k}\sqrt{-\frac{I}{2}+i\frac{\sqrt{-K}}{2}}\right)+\cos\left(\frac{\zeta}{B_k}\sqrt{-\frac{I}{2}-i\frac{\sqrt{-K}}{2}}\right)}{\cos\left(\frac{\zeta}{B_k}\sqrt{-\frac{I}{2}+i\frac{\sqrt{-K}}{2}}\right)-\cos\left(\frac{\zeta}{B_k}\sqrt{-\frac{I}{2}-i\frac{\sqrt{-K}}{2}}\right)} && (2.5)\\
&\quad +|B_k|^2+\frac{\zeta^2}{6}I\Bigg\}. && (2.6)
\end{aligned}$$

where $B_k = E_k = \frac{m^2c^3}{e\hbar} \approx 2.2\times10^{15}\,\mathrm{V\,cm^{-1}} \approx 4.4\times10^{13}\,\mathrm{G}$. Both Heisenberg & Euler (1936), and Mielniczuk (1982) present alternative expressions for these integrals in terms of infinite series.

2.2 The Analytic Expansion

For many interesting problems, one needs an expansion of this Lagrangian in the limit where the component of the electric field in the direction of the magnetic field is small (small K)

$$\mathcal{L}_1 = \mathcal{L}_1(I,0) + K\left.\frac{\partial\mathcal{L}_1}{\partial K}\right|_{K=0} + \frac{K^2}{2}\left.\frac{\partial^2\mathcal{L}_1}{\partial K^2}\right|_{K=0} + \cdots \tag{2.7}$$

where the terms are given by the following integrals

$$\begin{aligned}
\mathcal{L}_1(I,0) &= \frac{e^2}{hc}\frac{I}{2}X_0\left(\frac{1}{\xi}\right) \\
&= \frac{e^2}{hc}\frac{I}{2}\int_0^\infty e^{-u/\xi}\frac{\mathrm{d}u}{u^3}\left(-u\coth u+1+\frac{u^2}{3}\right) \qquad (2.8)\\
\left.\frac{\partial\mathcal{L}_1}{\partial K}\right|_{K=0} &= \frac{e^2}{hc}\frac{1}{16I}X_1\left(\frac{1}{\xi}\right) \\
&= \frac{e^2}{hc}\frac{1}{16I}\int_0^\infty e^{-u/\xi}\frac{\mathrm{d}u}{u^2}\Big(\coth u \\
&\qquad -\frac{2}{3}u^2\coth u-u\,\mathrm{csch}^2\,u\Big) \qquad (2.9)\\
\left.\frac{\partial^2\mathcal{L}_1}{\partial K^2}\right|_{K=0} &= \frac{e^2}{hc}\frac{1}{384I^3}X_2\left(\frac{1}{\xi}\right) \\
&= \frac{e^2}{hc}\frac{1}{384I^3}\int_0^\infty e^{-u/\xi}\frac{\mathrm{d}u}{u^2}\Big(-9u\,\mathrm{csch}^2\,u-4u^3\,\mathrm{csch}^2\,u \\
&\qquad +2u^2\coth u+15\coth u \\
&\qquad +\frac{8}{15}u^4\coth u-6u^2\coth^3 u\Big) \qquad (2.10)
\end{aligned}$$

and we have defined

$$\xi=\frac{1}{B_k}\sqrt{\frac{I}{2}}\ \text{and}\ u=\frac{\zeta}{B_k}\sqrt{\frac{I}{2}}. \qquad (2.11)$$

Note that ξ is a dimensionless measure of the strength of the field.

The auxiliary functions X_i may be calculated analyically:

$$\begin{aligned}
X_0(x) &= 4\int_0^{x/2-1}\ln(\Gamma(v+1))\mathrm{d}v+\frac{1}{3}\ln\left(\frac{1}{x}\right)+2\ln 4\pi-4\ln A-\frac{5}{3}\ln 2 \\
&\quad -\left[\ln 4\pi+1+\ln\left(\frac{1}{x}\right)\right]x+\left[\frac{3}{4}+\frac{1}{2}\ln\left(\frac{2}{x}\right)\right]x^2 \qquad (2.12)\\
X_1(x) &= -2X_0(x)+xX_0^{(1)}(x)+\frac{2}{3}X_0^{(2)}(x)-\frac{2}{9}\frac{1}{x^2} \qquad (2.13)\\
X_2(x) &= -24X_0(x)+9xX_0^{(1)}(x)+(8+3x^2)X_0^{(2)}(x)+4xX_0^{(3)}(x) \\
&\quad -\frac{8}{15}X_0^{(4)}(x)+\frac{8}{15}\frac{1}{x^2}+\frac{16}{15}\frac{1}{x^4} \qquad (2.14)
\end{aligned}$$

where

$$X_0^{(n)}(x)=\frac{\mathrm{d}^n X_0(x)}{\mathrm{d}x^n} \qquad (2.15)$$

Because of the near symmetry between I and K in Equation 2.6, higher derivatives with respect to K may be calculated in principle, and represented by a sum of derivatives of $\mathcal{L}(I,0)$ with respect to I. The constant A is defined as

$$\ln A = \lim_{n\to\infty}\left(\sum_{i=1}^{n} i\ln i\right) - \left[\left(\frac{n^2}{2}+\frac{n}{2}+\frac{1}{12}\right)\ln n - \frac{n^2}{4}\right] \quad (2.16)$$

$$= \frac{1}{12} - \zeta^{(1)}(-1) = 0.248754477, \quad (2.17)$$

in analogy to the Euler-Mascheroni constant (Barnes 1900). Here $\zeta^{(1)}(x)$ denotes the first derivative of the Riemann Zeta function.

Barnes (1900) evaluates the definite integral of $\ln\Gamma(x)$ in terms of the G-function

$$\int_0^{x/2-1} \ln(\Gamma(v+1))\mathrm{d}v = \left(\frac{x}{2}-1\right)\ln\Gamma\left(\frac{x}{2}\right) - \ln G\left(\frac{x}{2}\right) - \frac{x^2}{8} + \frac{x}{4}\left(1+\ln 2\pi\right) - \frac{1}{2}\ln 2\pi. \quad (2.18)$$

where

$$G(z) = (2\pi)^{\frac{z-1}{2}} e^{-\frac{z(z-1)}{2}} e^{-\gamma\frac{(z-1)^2}{2}} \prod_{k=1}^{\infty}\left[\left(1+\frac{z-1}{k}\right)^k e^{1-z+\frac{(z-1)^2}{2k}}\right]. \quad (2.19)$$

The integral of $\ln\Gamma(x)$ may also be expressed in terms of the generalized Riemann Zeta function (Dittrich, Tsai & Zimmermann 1979)

$$\int_0^{x/2-1} \ln(\Gamma(v+1))\mathrm{d}v = \zeta^{(1)}\left(-1,\frac{x}{2}-1\right) - \zeta^{(1)}(-1) + \frac{\ln 2\pi}{2}\left(\frac{x}{2}-1\right) - \frac{x}{4}\left(\frac{x}{2}-1\right) + \left(\frac{x}{2}-1\right)\ln\left(\frac{x}{2}-1\right) \quad (2.20)$$

Our expression for X_0 was also found by Dittrich, Tsai & Zimmermann (1979). Ivanov (1992) derived a similar expression as well, but his result differs from ours and that of Dittrich *et al.* in the constant term. Unlike Ivanov's expression, ours approaches zero as ξ goes to 0 which from examination of Equation 2.8 is the correct limiting behavior. In addition, the above form for X_0 reproduces the asymptotic strong-field limit given by Heisenberg & Euler (1936).

These functions can be expanded in both the weak-field and strong-field limits. In the weak-field limit ($\xi < 0.5$) we obtain

$$X_0\left(\frac{1}{\xi}\right) = -\sum_{j=1}^{\infty}\frac{2^{2j}B_{2(j+1)}}{j(j+1)(2j+1)}\xi^{2j} \quad (2.21)$$

$$X_1\left(\frac{1}{\xi}\right) = -\frac{14}{45}\xi^2 + \frac{1}{3}\sum_{j=2}^{\infty}\frac{2^{2j}\left(6B_{2(j+1)} - (2j+1)B_{2j}\right)}{j(2j+1)}\xi^{2j} \quad (2.22)$$

$$X_2\left(\frac{1}{\xi}\right) = \frac{1}{15}\sum_{j=3}^{\infty}\frac{2^{2j}}{j}\left[2j(2j-1)B_{2(j-1)} + 60(j-1)B_{2j} - 180\frac{j-2}{2j+1}B_{2(j+1)}\right]\xi^{2j} \quad (2.23)$$

where B_j denotes the jth Bernoulli number. In the strong-field limit ($\xi > 0.5$), we obtain

$$\begin{aligned} X_0\left(\frac{1}{\xi}\right) &= \left(\frac{1}{3}\ln 2 - 4\ln A + \frac{1}{3}\ln\xi\right) + (1 - \ln\pi + \ln\xi)\,\xi^{-1} \\ &+ \left(\frac{1}{2}(\ln 2 - \gamma) + \frac{3}{4} + \frac{1}{2}\ln\xi\right)\xi^{-2} \\ &+ \sum_{j=3}^{\infty}\frac{(-1)^{j-1}}{2^{j-2}}\frac{1}{j}\frac{1}{j-1}\zeta(j-1)\xi^{-j} \end{aligned} \quad (2.24)$$

$$\begin{aligned} X_1\left(\frac{1}{\xi}\right) &= -\frac{2}{3}\xi + \left(8\ln A - \frac{1}{3} - \frac{2}{3}\gamma\right) \\ &+ \left(\ln\pi + \frac{1}{18}\pi^2 - 2 - \ln\xi\right)\xi^{-1} + \left(-\frac{1}{2} - \frac{1}{6}\zeta(3)\right)\xi^{-2} \\ &+ \sum_{j=3}^{\infty}\frac{(-1)^{j-1}}{2^{j-2}}\left[\frac{j-2}{j(j-1)}\zeta(j-1) + \frac{1}{6}\zeta(j+1)\right]\xi^{-j} \end{aligned} \quad (2.25)$$

$$\begin{aligned} X_2\left(\frac{1}{\xi}\right) &= \frac{16}{15}\xi^3 - 4\xi + \left(-6 - 8\gamma + \frac{4}{15}\zeta(3) + 96\ln A\right) \\ &+ \left(-27 + \pi^2 - 15\ln\pi - \frac{1}{225}\pi^4 - 15\ln\xi\right)\xi^{-1} \\ &+ \left(\frac{2}{5}\zeta(5) - 9 - 4\zeta(3)\right)\xi^{-2} \\ &+ \sum_{j=3}^{\infty}\frac{(-1)^{j-1}}{2^{j-2}}\left[\frac{3(j+4)(j-2)}{j(j-1)}\zeta(j-1) \right. \\ &\left. + (j+2)\left(\zeta(j+1) - \frac{j+1}{30}\zeta(j+3)\right)\right]\xi^{-j}. \end{aligned} \quad (2.26)$$

The Lagrangian may also be expanded in terms of the invariants themselves or the electric and magnetic fields. In the weak-field limit we obtain

$$\mathcal{L}_1(I,0) = \frac{1}{180}\frac{e^2}{hc}B_k^2\left(\frac{I^2}{B_k^4}-\frac{2}{7}\frac{I^3}{B_k^6}+\frac{2}{7}\frac{I^4}{B_k^8}+\cdots\right) \tag{2.27}$$

$$\left.\frac{\partial\mathcal{L}_1}{\partial K}\right|_{K=0} = -\frac{7}{720}\frac{e^2}{hc}\frac{1}{B_k^2}\left(1-\frac{13}{49}\frac{I}{B_k^2}+\frac{44}{147}\frac{I^2}{B_k^4}+\cdots\right) \tag{2.28}$$

$$\left.\frac{\partial^2\mathcal{L}_1}{\partial K^2}\right|_{K=0} = \frac{19}{15120}\frac{e^2}{hc}\frac{1}{B_k^6}\left(1-\frac{889}{209}\frac{I}{B_k^2}+\frac{66324}{2717}\frac{I^2}{B_k^4}+\cdots\right) \tag{2.29}$$

This weak-field expansion agrees with the Heisenberg & Euler (1936) result.

In the strong-field limit, for direct comparison with Heisenberg & Euler (1936) we define $a = E/E_k$ and $b = B/B_k$ and take the limit $b \gg 1$ and $a \ll 1$. We take, $\xi^2 = b^2 - a^2$, $\xi \approx b - \frac{a^2}{2b}$ and $K = -16B_k^4(ab)^2$. We obtain

$$\begin{aligned}\mathcal{L}_1(a,b) = 4\frac{e^2}{hc}B_k^2\Bigg[& b^2\left(\frac{\ln b}{12}-\ln A+\frac{\ln 2}{12}\right)+\frac{b}{4}\left(\ln b+1-\ln\pi\right)\\ & +\frac{\ln b}{8}+\frac{3}{16}+\frac{\ln 2-\gamma}{8}\\ & -\frac{a^2}{12}\left(\ln b+\ln 2-\gamma\right)\\ & +b\left(\frac{a^2}{12}+\frac{a^4}{90}+\cdots\right)+\cdots\Bigg]\end{aligned} \tag{2.30}$$

which agrees numerically with the corresponding expansion in Heisenberg & Euler (1936).

2.3 Pair Production in an Arbitrarily Strong Electric Field

In a strong electric field with no magnetic field, the value of the first invariant is negative, $I = -2|\mathbf{E}|^2$ and $K = 0$. The analytic expressions for the Lagrangian are valid for values of ξ throughout the complex plane, with a branch cut along the negative real axis. Using an imaginary value of

$$\xi = i\left(\frac{E}{E_k}\right) = iy,\ y > 0 \tag{2.31}$$

and taking $w = 2(4\pi\hbar)^{-1}\,\mathrm{Im}\,\mathcal{L}$ gives the pair production rate per unit volume (Berestetskii, Lifshitz & Pitaevskii 1982). From examination of Equation 2.21, for $\xi < 0.5$ the pair-production rate is apparently zero.

However, since Equation 2.21 is a power series in $\xi/2$, the imaginary part of X_0 may be exponentially small. Berestetskii, Lifshitz & Pitaevskii (1982) derive for a weak field,

$$w = 2(4\pi\hbar)^{-1}\,\mathrm{Im}\,\mathcal{L} \sim \frac{1}{4\pi^3}\left(\frac{\hbar}{mc}\right)^{-3}\left(\frac{\hbar}{mc^2}\right)^{-1} y^2 \exp\left(-\frac{\pi}{y}\right) \tag{2.32}$$

To simplify the numerics we use an alternate definition of $X_0(x)$ obtained by means of a change of variables

$$\begin{aligned} X_0(x) &= 4\left(\frac{x}{2}-1\right)\int_0^1 \ln\left(\Gamma\left(u\left(\frac{x}{2}-1\right)+1\right)\right)\mathrm{d}u + \frac{1}{3}\ln\left(\frac{1}{x}\right) \\ &\quad + 2\ln 4\pi - (4\ln A + \frac{5}{3}\ln 2) - \left[\ln 4\pi + 1 + \ln\left(\frac{1}{x}\right)\right]x \\ &\quad + \left[\frac{3}{4} + \frac{1}{2}\ln\left(\frac{2}{x}\right)\right]x^2. \end{aligned} \tag{2.33}$$

With this definition and the property of the Gamma function, $\ln\Gamma(\bar{x}) = \overline{\ln\Gamma(x)}$, we see that $X_0(\bar{x}) = \overline{X_0(x)}$, so

$$\begin{aligned} w &= 2(4\pi\hbar)^{-1}\,\mathrm{Im}\,\mathcal{L}|_{I=-2y^2E_k^2, K=0} \\ &= i\frac{e^2}{8\pi^2\hbar^2 c}E_k^2 y^2\left(X_0\left(-\frac{i}{y}\right) - X_0\left(\frac{i}{y}\right)\right) \\ &= \frac{1}{8\pi^2}\left(\frac{\hbar}{mc}\right)^{-3}\left(\frac{\hbar}{mc^2}\right)^{-1}\left[-\frac{1}{3}\pi y^2 - 8y^2\,\mathrm{Im}\,Q(y)\right. \\ &\qquad \left. - 2y(\ln y + \ln 4\pi + 1) + 4y\,\mathrm{Re}\,Q(y) + \frac{1}{2}\pi\right] \end{aligned} \tag{2.34}$$

where

$$Q(y) = \int_0^1 \ln\left(\Gamma\left(u\left(\frac{i}{2y}-1\right)+1\right)\right)\mathrm{d}u \tag{2.35}$$

and the scaling constant

$$\frac{1}{8\pi^2}\left(\frac{\hbar}{mc}\right)^{-3}\left(\frac{\hbar}{mc^2}\right)^{-1} = 1.7\times 10^{51}\mathrm{cm}^{-3}\mathrm{s}^{-1}. \tag{2.36}$$

This expression for w, the pair-production rate, agrees numerically with the results of Itzykson & Zuber (1980) for an arbitrarily strong electric field.

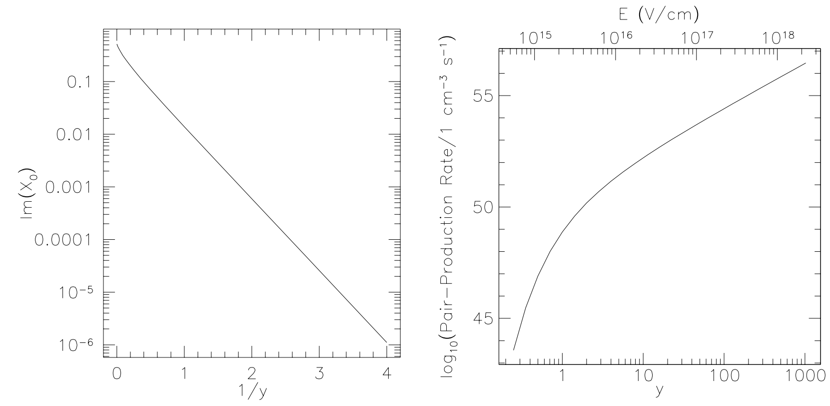

Figure 2.1: The left panel depicts the imaginary part of X_0 as a function of $1/y$. For weak fields the imaginary component is approximately $\pi^{-1}\exp(-\pi/y)$. The right panel depicts the pair-production rate for near and super-critical fields.

In the strong-field limit we use Equation 2.24 and take the imaginary part

$$\begin{aligned} w &= \frac{1}{8\pi^2}\left(\frac{\hbar}{mc}\right)^{-3}\left(\frac{\hbar}{mc^2}\right)^{-1}\Bigg[-\frac{\pi}{3}y^2+2(1-\ln\pi+\ln y)y \\ &\quad +\frac{\pi}{2}+\sum_{k=1}^{\infty}\frac{(-1)^{3k}\zeta(2k)}{2^{2k-1}k(2k+1)}y^{-(2k-1)} \end{aligned} \tag{2.37}$$

Figure 2.1 depicts the imaginary component of X_0 for $I=-2y^2E_k^2$ and the pair-production rate per unit volume. From the left panel, we verify that the imaginary component of X_0 is approximately $\pi^{-1}\exp(-\pi/y)$ for weak fields. The right panel shows the pair-production rate which increases as y^2 for strong fields and is damped exponentially in weak fields.

2.4 Auxiliary Functions for Photon Splitting

To calculate the photon splitting rates we follow the technique by Adler (1971) for the low-frequency limit. In this limit, Adler expresses the opacity for photon spliting by means of auxiliary functions which are simply derivatives of the Lagrangian and therefore of the functions X_i above

$$\begin{aligned}
\kappa\,[\| \to \| + \|] &= \frac{\alpha^6}{2\pi^2}\frac{\hbar^{13}}{m^{16}c^{24}}B^6\sin^6\theta\frac{\omega^5}{30}C_1(\xi)^2 && (2.38)\\
&= \frac{\alpha^3}{2\pi^2}\left(\frac{B\sin\theta}{B_k}\right)^6\left(\frac{\hbar\omega}{mc^2}\right)^5\frac{C_1(\xi)^2}{30}\left(\frac{mc}{\hbar}\right) && (2.39)\\
&= 17.0\,\mathrm{cm}^{-1}\left(\frac{B\sin\theta}{B_k}\right)^6\left(\frac{\hbar\omega}{mc^2}\right)^5 C_1(\xi)^2 && (2.40)\\
\kappa\,[\| \to\perp + \perp] &= \frac{\alpha^6}{2\pi^2}\frac{\hbar^{13}}{m^{16}c^{24}}B^6\sin^6\theta\frac{\omega^5}{30}C_2(\xi)^2 && (2.41)\\
\kappa\,[\perp\to \| + \perp] &= 2\frac{\alpha^6}{2\pi^2}\frac{\hbar^{13}}{m^{16}c^{24}}B^6\sin^6\theta\frac{\omega^5}{30}C_2(\xi)^2, && (2.42)
\end{aligned}$$

The conversion of $\perp$ to $\| + \perp$ proceeds through two channels hence the two-fold increase in the opacity for this process. C_1 and C_2 are defined by

$$\begin{aligned}
\left.\frac{\partial^3\mathcal{L}_{\rm Adler}}{\partial\mathcal{F}^3}\right|_{\mathcal{G}=0,\mathcal{F}=\frac{1}{2}B^2} &= \frac{64}{4\pi}\left.\frac{\partial^3\mathcal{L}_1}{\partial I^3}\right|_{K=0,I=2B^2} && (2.43)\\
&= -\frac{\alpha^3\hbar^6}{2\pi^2m^8c^{10}}C_1(\xi) = -\frac{\alpha}{2\pi^2B_k^4}C_1(\xi) && (2.44)\\
\left.\frac{\partial^3\mathcal{L}_{\rm Adler}}{\partial\mathcal{F}\partial\mathcal{G}^2}\right|_{\mathcal{G}=0,\mathcal{F}=\frac{1}{2}B^2} &= -\frac{128}{4\pi}\left.\frac{\partial^2\mathcal{L}_1}{\partial I\partial K}\right|_{K=0,I=2B^2} && (2.45)\\
&= -\frac{\alpha}{2\pi^2B_k^4}C_2(\xi) && (2.46)
\end{aligned}$$

and θ is the angle between the direction of propagation of the photon and the external magnetic field. The factors of 128 and 64 result from the definitions of Adler's $\mathcal{F}$ and $\mathcal{G}$ in terms of I and K,

$$\begin{aligned}
\mathcal{F} &= \frac{1}{2}\left(|\mathbf{B}|^2 - |\mathbf{E}|^2\right) = \frac{I}{4} && (2.47)\\
\mathcal{G} &= \mathbf{B}\cdot\mathbf{E} = \frac{1}{4}\sqrt{-K} && (2.48)
\end{aligned}$$

An additional factor of 4π appears because we are using rationalized Gaussian units while Adler employs unrationalized units.

Given the analytic forms for X_0 and X_1 we obtain

$$\begin{aligned}
C_1(\xi) &= \frac{1}{4\xi^7}\left(X_0^{(3)}\left(\frac{1}{\xi}\right) + 3X_0^{(2)}\left(\frac{1}{\xi}\right)\xi - 3X_0^{(1)}\left(\frac{1}{\xi}\right)\xi^2\right) && (2.49)\\
C_2(\xi) &= -\frac{1}{4\xi^5}\left(X_1^{(1)}\left(\frac{1}{\xi}\right) + 2X_1\left(\frac{1}{\xi}\right)\xi\right) && (2.50)
\end{aligned}$$

The functions, C_1 and C_2, have the appropriate limits as $\xi \rightarrow 0$ which correspond to the lowest order hexagon diagrams for the splitting process,

$$C_1(I) = 16 \sum_{j=2}^{\infty} \frac{2^{j-1}(j-1)B_{2(j+1)}}{2j+1} \left(\frac{I}{B_k^2}\right)^{j-2} \tag{2.51}$$

$$= 6 \cdot \frac{8}{315} - \frac{64}{105}\frac{I}{B_k^2} + \frac{320}{99}\left(\frac{I}{B_k^2}\right)^2 \cdots \tag{2.52}$$

$$C_2(I) = \frac{1}{3} \sum_{j=2}^{\infty} \frac{2^{j+1}(j-1)\left(6B_{2(j+1)} - (2j+1)B_{2j}\right)}{j(2j+1)} \left(\frac{I}{B_k^2}\right)^{j-2} \tag{2.53}$$

$$= 6 \cdot \frac{13}{945} - \frac{176}{945}\frac{I}{B_k^2} + \frac{332}{495}\left(\frac{I}{B_k^2}\right)^2 \cdots \tag{2.54}$$

In the strong field limit we obtain

$$C_1(\xi) = \frac{1}{3}\xi^{-4} - \frac{3}{4}\xi^{-5}\left(\ln\xi - \ln\pi + \frac{2}{3}\right) - \xi^{-6} - \sum_{j=3}^{\infty} \frac{(-1)^j}{2^j}\frac{j^2-4}{j-1}\zeta(j-1)\xi^{-j-4} \tag{2.55}$$

$$C_2(\xi) = \frac{1}{6}\xi^{-3} + \xi^{-4}\left(\frac{1}{6} + \frac{1}{3}\gamma - 4\ln A\right) + \frac{3}{4}\xi^{-5}\left(\ln\xi - \ln\pi + \frac{5}{3} - \frac{1}{18}\pi^2\right) + \frac{1}{2}\xi^{-6}\left(1 + \frac{1}{3}\zeta(3)\right) + \sum_{j=3}^{\infty} \frac{(-1)^j(j^2-2)}{2^j}\left(\frac{\zeta(j-1)}{j(j-1)} + \frac{\zeta(j+1)}{6(j-2)}\right)\xi^{-j-4} \tag{2.56}$$

These expressions for the photon-splitting rate are only valid in the low-frequency limit since the Heisenberg-Euler Lagrangian neglects the gradients of the field. When these gradients are neglected, the results from Schwinger's proper-time integration (1951) used by Adler (1971) reduce to these results obtained from the Heisenberg-Euler Lagrangian. Baĭer, Milstein & Shaisultanov (1996) have also obtained similar results for arbitrary field strengths (and photon frequencies) using an operator diagram technique.

Baĭer *et al.* and Adler's methods differ in spirit but yield the same results. Baĭer, Katkov & Strakhovenko (1975a) developed the operator diagram technique. In this formalism, the photon splitting matrix element is evaluated with Feynman diagrams (Baĭer, Katkov & Strakhovenko 1975b) using electron propagators in an external field. On the other hand, Adler (1971) calculates the expectation value of the current ($\langle j_\mu(x) \rangle$) order by order in the external photon fields using Schwinger's formalism (1951) and relates this expectation value to the photon-splitting matrix element.

2.5 Photon Splitting Opacities and Application to Neutron Stars

Adler (1971) argues that because of dispersive effects, the process $\| \rightarrow \perp + \perp$, dominates the opacity of photons travelling through a strong field. Therefore, we are interested in the function $C_2(\xi)$ which determines the splitting rate for all magnetic field strengths at photon energies small compared to the mass of the electron. We see immediately from the expansions of C_2 that the opacity has the following behavior for weak and strong fields

$$\kappa\left[\| \rightarrow \perp + \perp\right] = \begin{cases} 0.116\,\mathrm{cm}^{-1} \left(\frac{B \sin\theta}{B_k}\right)^6 \left(\frac{\hbar\omega}{mc^2}\right)^5 & B \ll B_k \\ \\ 0.472\,\mathrm{cm}^{-1} \sin^6\theta \left(\frac{\hbar\omega}{mc^2}\right)^5 & B \gg B_k \end{cases} \tag{2.57}$$

We find, in agreement with the recent result of Baĭer, Milstein & Shaisultanov (1996) and as well as with earlier results (Thompson & Duncan 1995, Baring 1995) that the photon splitting opacity approaches a constant value in the limit of strong fields.

The left panel of Figure 2.2 depicts the opacity for photons with $E = mc^2$ as a function of ξ. Our formulae are not valid for these high-energy photons but for low energies the opacity scales as this quantity times the photon energy to the fifth power. The right panel applies these opacities to neutron stars. Neutron stars are observed to have magnetic fields $\sim 10^{12}$ G (*e.g.* Shapiro & Teukolsky 1983) and a subset of these objects known as magnetars are suspected to have much stronger fields $\sim 10^{16}$ G or larger (Duncan & Thompson 1992). The figure illustrates the energy of photons with a mean-free path of ten kilometers. All parallel-polarized photons with this energy or larger would tranverse an optical depth of one or larger while escaping from the neutron star.

2.6 Conclusion

Because of the asymptotic behavior of the function $C_2(\xi)$, even in immensely large fields, the photons with energies less than 37 keV have opacities less than (10 km)$^{-1}$. This energy corresponds to a temperature of 4×10^8 K, so we must conclude that unless the strong magnetic field of

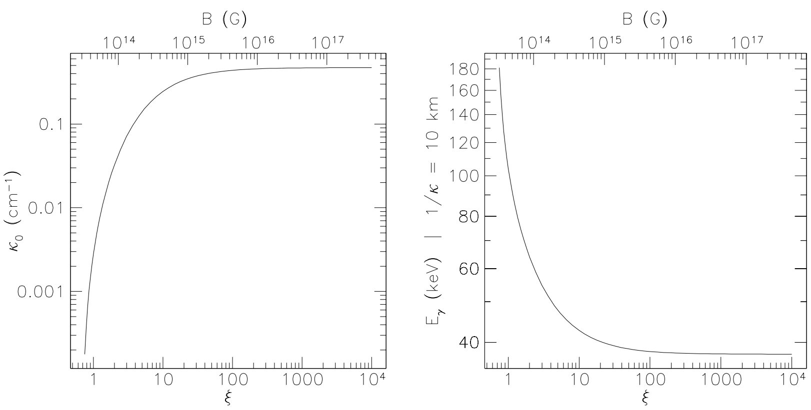

Figure 2.2: The left panel depicts the photon-splitting opacity for photons with $E = mc^2$ as a function ξ and B (upper axis). The right panel shows the energy of photons with a mean-free path for splitting of ten kilometers as a function ξ and B

the neutron star extends over a distance much greater than 10 km, photon splitting affects the thermal radiation of only the youngest neutron stars.

We have derived a closed form expression for the Heisenberg-Euler effective Lagrangian for quantum electrodynamics as a function of the gauge and Lorentz invariant quantities I and K in the limit of small K. We have calculated from this analytic expression the photon-splitting and pair-production rates in the intense field and found them to agree with previous work. Furthermore, the expressions for the dielectric and permeability tensors in an external field derived from our analytic expression also agree with previous results (Heyl & Hernquist 1997c). We expect that these expressions may be applied to a wide variety of problems in strong electromagnetic fields, including Compton scattering, photon-photon scattering, and bremsstrahlung.

Chapter 3

Birefringence and Dichroism of the QED Vacuum

SUMMARY

We use an analytic form for the Heisenberg-Euler Lagrangian to calculate the birefringent and dichroic properties of the vacuum for arbitrarily strong wrenchless fields.

3.1 Introduction

In the presence of a strong external field, the vacuum reacts, becoming magnetized and polarized. The index of refraction, magnetic permeability, and dielectric constant of the vacuum are straightforward to calculate using quantum electrodynamic one-loop corrections (Klein & Nigam 1964a, Klein & Nigam 1964b, Erber 1966, Adler 1971, Berestetskii, Lifshitz & Pitaevskii 1982, Mielnieczuk, Lamm & Valluri 1988). In this paper, we calculate the magnetic permeability and dielectric tensors of an external electric or magnetic field of arbitrary strength in terms of special functions. We combine these general results to calculate the complex-valued index of refraction as a function of field strength.

3.2 The Permeability and Polarizability of the Vacuum

When one-loop corrections are included in the Lagrangian of the electromagnetic field one obtains a non-linear correction term:

$$\mathcal{L} = \mathcal{L}_0 + \mathcal{L}_1 . \tag{3.1}$$

Both terms of the Lagrangian can be written in terms of the Lorentz invariants,

$$I = F_{\mu\nu}F^{\mu\nu} = 2\left(|\mathbf{B}|^2 - |\mathbf{E}|^2\right) \tag{3.2}$$

and

$$K = \left(\frac{1}{2}\epsilon^{\lambda\rho\mu\nu}F_{\lambda\rho}F_{\mu\nu}\right)^2 = -(4\mathbf{E}\cdot\mathbf{B})^2, \tag{3.3}$$

following Heisenberg & Euler (1936). We use Greek indices to count over space and time components $(0,1,2,3)$ and Roman indices to count over spatial components only $(1,2,3)$, and repeated indices imply summation.

Heisenberg & Euler (1936) and Weisskopf (1936) independently derived the effective Lagrangian of the electromagnetic field using electron-hole theory. Schwinger (1951) later rederived the same result using quantum electrodynamics. In Heaviside-Lorentz units, Lagrangian is given by

$$\begin{aligned}
\mathcal{L}_0 &= -\frac{1}{4}I, && (3.4)\\
\mathcal{L}_1 &= \frac{e^2}{hc}\int_0^\infty e^{-\zeta}\frac{\mathrm{d}\zeta}{\zeta^3}\left\{ i\zeta^2\frac{\sqrt{-K}}{4}\times\right. \\
&\quad \frac{\cos\left(\frac{\zeta}{B_k}\sqrt{-\frac{I}{2}+i\frac{\sqrt{-K}}{2}}\right)+\cos\left(\frac{\zeta}{B_k}\sqrt{-\frac{I}{2}-i\frac{\sqrt{-K}}{2}}\right)}{\cos\left(\frac{\zeta}{B_k}\sqrt{-\frac{I}{2}+i\frac{\sqrt{-K}}{2}}\right)-\cos\left(\frac{\zeta}{B_k}\sqrt{-\frac{I}{2}-i\frac{\sqrt{-K}}{2}}\right)} && (3.5)\\
&\quad \left. + |B_k|^2 + \frac{\zeta^2}{6}I\right\}. && (3.6)
\end{aligned}$$

where $B_k = E_k = \frac{m^2c^3}{e\hbar} \approx 1.3\times10^{16}\,\mathrm{V\,cm^{-1}} \approx 4.4\times10^{13}\,\mathrm{G}$.

In the weak field limit Heisenberg & Euler (1936) give

$$\mathcal{L} \approx -\frac{1}{4}I + E_k^2\frac{e^2}{hc}\left[\frac{1}{180E_k^4}\left(I^2-\frac{7}{4}K\right)+\frac{1}{630E_k^6}\left(-I^3+\frac{13}{8}KI\right)\cdots\right] \tag{3.7}$$

We define a dimensionless parameter ξ to characterize the field strength

$$\xi = \frac{1}{E_k}\sqrt{\frac{I}{2}} \tag{3.8}$$

and use the analytic expansion of this Lagrangian for small K derived by Heyl & Hernquist (1997b):

$$\mathcal{L}_1 = \mathcal{L}_1(I,0) + K \left.\frac{\partial \mathcal{L}_1}{\partial K}\right|_{K=0} + \frac{K^2}{2} \left.\frac{\partial^2 \mathcal{L}_1}{\partial K^2}\right|_{K=0} + \cdots \tag{3.9}$$

The first two terms of this expansion are given by

$$\begin{aligned} \mathcal{L}_1(I,0) &= \frac{e^2}{hc}\frac{I}{2}X_0\left(\frac{1}{\xi}\right), & (3.10)\\ \left.\frac{\partial \mathcal{L}_1}{\partial K}\right|_{K=0} &= \frac{e^2}{hc}\frac{1}{16I}X_1\left(\frac{1}{\xi}\right) & (3.11)\end{aligned}$$

where

$$\begin{aligned} X_0(x) &= 4\int_0^{x/2-1} \ln(\Gamma(v+1))\mathrm{d}v + \frac{1}{3}\ln\left(\frac{1}{x}\right) + 2\ln 4\pi - 4\ln A - \frac{5}{3}\ln 2 \\ &\quad - \left[\ln 4\pi + 1 + \ln\left(\frac{1}{x}\right)\right]x + \left[\frac{3}{4} + \frac{1}{2}\ln\left(\frac{2}{x}\right)\right]x^2, & (3.12)\\ X_1(x) &= -2X_0(x) + xX_0^{(1)}(x) + \frac{2}{3}X_0^{(2)}(x) - \frac{2}{9}\frac{1}{x^2} & (3.13)\end{aligned}$$

and

$$\begin{aligned} X_0^{(n)}(x) &= \frac{\mathrm{d}^n X_0(x)}{\mathrm{d}x^n}, & (3.14)\\ \ln A &= \frac{1}{12} - \zeta^{(1)}(-1) \approx 0.2488. & (3.15)\end{aligned}$$

where $\zeta^{(1)}(x)$ denotes the first derivative of the Riemann Zeta function.

We will treat the vacuum as a polarizable medium. In the Heaviside-Lorentz system, the macroscopic fields are given by the generalized momenta conjugate to the fields (Berestetskii, Lifshitz & Pitaevskii 1982)

$$\mathbf{D} = \frac{\partial \mathcal{L}}{\partial \mathbf{E}} = \mathbf{E} + \mathbf{P}, \quad \mathbf{H} = -\frac{\partial \mathcal{L}}{\partial \mathbf{B}} = \mathbf{B} - \mathbf{M}, \quad \mathbf{P} = \frac{\partial \mathcal{L}_1}{\partial \mathbf{E}}, \quad \mathbf{M} = \frac{\partial \mathcal{L}_1}{\partial \mathbf{B}}. \tag{3.16}$$

We define the vacuum dielectric and inverse magnetic permeability tensors as follows (Jackson 1975)

$$D_i = \epsilon_{ij}E_j, \quad H_i = \mu'_{ij}B_j. \tag{3.17}$$

Using the definitions of I and K, we get

$$\epsilon_{ij} = \delta_{ij} - 4\frac{\partial \mathcal{L}_1}{\partial I}\delta_{ij} - 32\frac{\partial \mathcal{L}_1}{\partial K}B_i B_j, \tag{3.18}$$

$$\mu'_{ij} = \delta_{ij} - 4\frac{\partial \mathcal{L}_1}{\partial I}\delta_{ij} + 32\frac{\partial \mathcal{L}_1}{\partial K}E_i E_j. \tag{3.19}$$

If we use the weak-field limit (Equation 3.7), we recover the results of Klein & Nigam (1964a)

$$\epsilon_{ij} = \delta_{ij} + \frac{1}{45\pi}\frac{\alpha}{B_k^2}\left[2(E^2 - B^2)\delta_{ij} + 7B_i B_j\right], \tag{3.20}$$

$$\mu'_{ij} = \delta_{ij} + \frac{1}{45\pi}\frac{\alpha}{B_k^2}\left[2(E^2 - B^2)\delta_{ij} - 7E_i E_j\right] \tag{3.21}$$

where the fine-structure constant, $\alpha = e^2/\hbar c$ in these units.

For wrenchless ($K = 0$) fields of arbitrary strength we use Equation 3.12 and Equation 3.13 to get

$$\epsilon_{ij} = \delta_{ij} + \frac{\alpha}{2\pi}\left\{\left[-2X_0\left(\frac{1}{\xi}\right) + \frac{1}{\xi}X_0^{(1)}\left(\frac{1}{\xi}\right)\right]\delta_{ij} - \frac{1}{\xi^2}\frac{B_i B_j}{B_k^2}X_1\left(\frac{1}{\xi}\right)\right\} + \mathcal{O}\left[\left(\frac{\alpha}{2\pi}\right)^2\right], \tag{3.22}$$

$$\mu'_{ij} = \delta_{ij} + \frac{\alpha}{2\pi}\left\{\left[-2X_0\left(\frac{1}{\xi}\right) + \frac{1}{\xi}X_0^{(1)}\left(\frac{1}{\xi}\right)\right]\delta_{ij} + \frac{1}{\xi^2}\frac{E_i E_j}{E_k^2}X_1\left(\frac{1}{\xi}\right)\right\} + \mathcal{O}\left[\left(\frac{\alpha}{2\pi}\right)^2\right]. \tag{3.23}$$

The expression for μ with only an external magnetic field agrees numerically with the results of Mielnieczuk, Lamm & Valluri (1988).

To examine wave propagation, we must first linearize the relations (Equation 3.16) in the fields of the wave $(\widetilde{\mathbf{E}}, \widetilde{\mathbf{B}})$ (Adler 1971) and obtain a second set of matrices,

$$\widetilde{\epsilon}_{ij} = \frac{\partial^2 \mathcal{L}}{\partial E_i \partial E_j}, \tag{3.24}$$

$$= \delta_{ij} - 4\frac{\partial \mathcal{L}_1}{\partial I}\delta_{ij} + 16\frac{\partial^2 \mathcal{L}_1}{\partial I^2}E_i E_j - \left(64K\frac{\partial^2 \mathcal{L}_1}{\partial K^2} + 32\frac{\partial \mathcal{L}_1}{\partial K}\right)B_i B_j + 128(\mathbf{E}\cdot\mathbf{B})\frac{\partial^2 \mathcal{L}_1}{\partial I \partial K}\left(E_i B_j + E_j B_i\right), \tag{3.25}$$

$$\begin{aligned}
\widetilde{\mu}'_{ij} &= -\frac{\partial^2 \mathcal{L}}{\partial B_i \partial B_j}, \qquad (3.26)\\
&= \delta_{ij} - 4\frac{\partial \mathcal{L}_1}{\partial I}\delta_{ij} - 16\frac{\partial^2 \mathcal{L}_1}{\partial I^2} B_i B_j + \left(64K\frac{\partial^2 \mathcal{L}_1}{\partial K^2} + 32\frac{\partial \mathcal{L}_1}{\partial K}\right) E_i E_j \\
&\quad + 128(\mathbf{E}\cdot\mathbf{B})\frac{\partial^2 \mathcal{L}_1}{\partial I \partial K}\left(E_i B_j + E_j B_i\right). \qquad (3.27)
\end{aligned}$$

We use these matrices in the macroscopic Maxwell equations. To first order, $\widetilde{\mathbf{H}} \| \widetilde{\mathbf{B}}$ and $\widetilde{\mathbf{D}} \| \widetilde{\mathbf{E}}$, so we obtain the wave equation,

$$\nabla^2 \widetilde{\mathbf{E}} - \frac{\widetilde{\epsilon}}{\widetilde{\mu}' c^2}\frac{\partial^2 \widetilde{\mathbf{E}}}{\partial t^2} = 0. \qquad (3.28)$$

and similarly for $\widetilde{\mathbf{B}}$.

In Equation 3.28, $\widetilde{\mu}'$ and $\widetilde{\epsilon}$ are the ratios of the macroscopic to the microscopic fields, *i.e.* $\widetilde{\mathbf{H}} = \widetilde{\mu}'\widetilde{\mathbf{B}}$ The waves travel at a definite velocity $v = c\sqrt{\widetilde{\mu}'/\widetilde{\epsilon}}$ and the index of refraction is $n = \sqrt{\widetilde{\epsilon}/\widetilde{\mu}'}$.

If we take an external magnetic field parallel to the $\hat{3}$ axis, we obtain

$$\begin{aligned}
\widetilde{\epsilon}_{ij} &= \delta_{ij}\left\{1 + \frac{\alpha}{2\pi}\left[-2X_0\left(\frac{1}{\xi}\right) + \frac{1}{\xi}X_0^{(1)}\left(\frac{1}{\xi}\right)\right]\right\} \\
&\quad - \delta_{i3}\delta_{j3}\frac{\alpha}{2\pi}X_1\left(\frac{1}{\xi}\right) + \mathcal{O}\left[\left(\frac{\alpha}{2\pi}\right)^2\right], \qquad (3.29)\\
\widetilde{\mu}'_{ij} &= \delta_{ij}\left\{1 + \frac{\alpha}{2\pi}\left[-2X_0\left(\frac{1}{\xi}\right) + \frac{1}{\xi}X_0^{(1)}\left(\frac{1}{\xi}\right)\right]\right\} \\
&\quad - \delta_{i3}\delta_{j3}\frac{\alpha}{2\pi}\left[X_0^{(2)}\left(\frac{1}{\xi}\right)\xi^{-2} - X_0^{(1)}\left(\frac{1}{\xi}\right)\xi^{-1}\right] \\
&\quad + \mathcal{O}\left[\left(\frac{\alpha}{2\pi}\right)^2\right]. \qquad (3.30)
\end{aligned}$$

In this case, we have the magnetic field of the wave either perpendicular to the plane containing the external magnetic field and the direction of propagation ($\mathbf{k}$), $\perp$ mode, or in that plane, $\|$ mode (Berestetskii, Lifshitz & Pitaevskii 1982). For the $\perp$ mode, we obtain

$$n_\perp = 1 - \frac{\alpha}{4\pi}X_1\left(\frac{1}{\xi}\right)\sin^2\theta + \mathcal{O}\left[\left(\frac{\alpha}{2\pi}\right)^2\right] \qquad (3.31)$$

where θ is the angle between the direction of propagation and the external field. And for the $\|$ mode, we obtain

$$n_\| = 1 + \frac{\alpha}{4\pi}\left[X_0^{(2)}\left(\frac{1}{\xi}\right)\xi^{-2} - X_0^{(1)}\left(\frac{1}{\xi}\right)\xi^{-1}\right]\sin^2\theta + \mathcal{O}\left[\left(\frac{\alpha}{2\pi}\right)^2\right]. \qquad (3.32)$$

The expressions for $n_\|, n_\perp$ obtained here are equivalent to those obtained by Tsai & Erber (1975) through direct calculation of the photon propagator to one-loop accuracy in the presence of the external field.

If we take an external electric field parallel to the $\hat{3}$ axis, we obtain

$$\begin{aligned}\widetilde{\epsilon}_{ij} &= \delta_{ij}\left\{1+\frac{\alpha}{2\pi}\left[-2X_0\left(\frac{1}{\xi}\right)+\frac{1}{\xi}X_0^{(1)}\left(\frac{1}{\xi}\right)\right]\right\} \\ &\quad - \delta_{i3}\delta_{j3}\frac{\alpha}{2\pi}\left[X_0^{(2)}\left(\frac{1}{\xi}\right)\xi^{-2}-X_0^{(1)}\left(\frac{1}{\xi}\right)\xi^{-1}\right] \\ &\quad + \mathcal{O}\left[\left(\frac{\alpha}{2\pi}\right)^2\right], \qquad (3.33)\\ \widetilde{\mu}'_{ij} &= \delta_{ij}\left\{1+\frac{\alpha}{2\pi}\left[-2X_0\left(\frac{1}{\xi}\right)+\frac{1}{\xi}X_0^{(1)}\left(\frac{1}{\xi}\right)\right]\right\} \\ &\quad - \delta_{i3}\delta_{j3}\frac{\alpha}{2\pi}X_1\left(\frac{1}{\xi}\right)+\mathcal{O}\left[\left(\frac{\alpha}{2\pi}\right)^2\right]. \qquad (3.34)\end{aligned}$$

In this case, the propagation modes have the electric field ($\widetilde{\mathbf{E}}$) either in the $\mathbf{k}-\mathbf{E}$ plane ($\|$ mode) or or perpendicular to the plane. For an external electric field, we define

$$\xi = iy = i\frac{E}{E_k} \qquad (3.35)$$

and substitute this into Equation 3.31 and Equation 3.32. This yields indices of refraction

$$\begin{aligned}n_\perp &= 1+\frac{\alpha}{4\pi}X_1\left(\frac{1}{iy}\right)\sin^2\theta+\mathcal{O}\left[\left(\frac{\alpha}{2\pi}\right)^2\right], \qquad (3.36)\\ n_\| &= 1+\frac{\alpha}{4\pi}\left[X_0^{(2)}\left(-\frac{i}{y}\right)y^{-2}-iX_0^{(1)}\left(-\frac{i}{y}\right)y^{-1}\right]\sin^2\theta \\ &\quad +\mathcal{O}\left[\left(\frac{\alpha}{2\pi}\right)^2\right] \qquad (3.37)\end{aligned}$$

where θ again refers to the angle between the direction of propagation and the external electric field.

In the weak-field limit, we have (Heyl & Hernquist 1997b)

$$\begin{aligned}X_1\left(\frac{1}{\xi}\right) &= -\frac{14}{45}\xi^2+\mathcal{O}(\xi^4), \qquad (3.38)\\ X_0^{(2)}\left(\frac{1}{\xi}\right)\xi^{-2}-X_0^{(1)}\left(\frac{1}{\xi}\right)\xi^{-1} &= \frac{8}{45}\xi^2+\mathcal{O}(\xi^4). \qquad (3.39)\end{aligned}$$

An external electric field gives $\xi^2<0$ and an external magnetic field gives $\xi^2>0$, therefore $n_\perp, n_\| > 1$ in the weak-field limit for both cases. Using this limit in Equation 3.32 and Equation 3.31 yields weak-field expressions for the index of refraction in a magnetic field in agreement with earlier work (Adler 1971, Berestetskii, Lifshitz & Pitaevskii 1982).

3.2.1 Series and asymptotic expressions

To calculate the indices of refraction in the weak and strong field limit, we use the expansions of Heyl & Hernquist (1997b). For an external magnetic field, in the weak-field limit ($\xi < 0.5$),

$$\begin{aligned} n_\perp &= 1 + \frac{\alpha}{4\pi}\sin^2\theta\left[\frac{14}{45}\xi^2 - \frac{1}{3}\sum_{j=2}^{\infty}\frac{2^{2j}}{j}\left(\frac{6B_{2(j+1)}}{2j+1} - B_{2j}\right)\xi^{2j}\right] \\ &\quad + \mathcal{O}\left[\left(\frac{\alpha}{2\pi}\right)^2\right], \qquad (3.40) \\ n_\parallel &= 1 - \frac{\alpha}{4\pi}\sin^2\theta\sum_{j=1}^{\infty}\frac{2^{2(j+1)}B_{2(j+1)}}{2j+1}\xi^{2j} + \mathcal{O}\left[\left(\frac{\alpha}{2\pi}\right)^2\right]. \qquad (3.41) \end{aligned}$$

In the strong-field limit ($\xi > 0.5$), we obtain

$$\begin{aligned} n_\perp &= 1 + \frac{\alpha}{4\pi}\sin^2\theta\left[\frac{2}{3}\xi - \left(8\ln A - \frac{1}{3} - \frac{2}{3}\gamma\right)\right. \\ &\quad - \left(\ln\pi + \frac{1}{18}\pi^2 - 2 - \ln\xi\right)\xi^{-1} - \left(-\frac{1}{2} - \frac{1}{6}\zeta(3)\right)\xi^{-2} \\ &\quad \left. - \sum_{j=3}^{\infty}\frac{(-1)^{j-1}}{2^{j-2}}\left(\frac{j-2}{j(j-1)}\zeta(j-1) + \frac{1}{6}\zeta(j+1)\right)\xi^{-j}\right] \\ &\quad + \mathcal{O}\left[\left(\frac{\alpha}{2\pi}\right)^2\right], \qquad (3.42) \\ n_\parallel &= 1 + \frac{\alpha}{4\pi}\sin^2\theta\left[\frac{2}{3} - \frac{\ln\xi + 1 - \ln\pi}{\xi} - \frac{1}{\xi^2}\right. \\ &\quad \left. + \sum_{j=3}^{\infty}\frac{(-1)^{j-1}}{2^{j-2}}\frac{j-2}{j-1}\zeta(j-1)\xi^{-j}\right] + \mathcal{O}\left[\left(\frac{\alpha}{2\pi}\right)^2\right], \qquad (3.43) \end{aligned}$$

where γ is Euler's constant.

For an external electric field, in the weak-field limit ($y < 0.5$) we obtain,

$$
\begin{aligned}
n_\perp &= 1 + \frac{\alpha}{4\pi}\left[\frac{14}{45}y^2 \right. \\
&\quad \left. + \frac{1}{3}\sum_{j=2}^{\infty}\frac{(-1)^j 2^{2j}\left(6B_{2(j+1)} - (2j+1)B_{2j}\right)}{j(2j+1)}y^{2j}\right] \\
&\quad + \mathcal{O}\left[\left(\frac{\alpha}{2\pi}\right)^2\right], \qquad (3.44) \\
n_\parallel &= 1 + \frac{\alpha}{4\pi}\sin^2\theta\sum_{j=1}^{\infty}\frac{(-1)^j 2^{2(j+1)}B_{2(j+1)}}{2j+1}y^{2j} + \mathcal{O}\left[\left(\frac{\alpha}{2\pi}\right)^2\right], \qquad (3.45)
\end{aligned}
$$

and in the strong-field limit ($y > 0.5$)

$$
\begin{aligned}
n_\perp &= 1 + \frac{\alpha}{4\pi}\sin^2\theta\left[-i\frac{2}{3}y + \left(8\ln A - \frac{1}{3} - \frac{2}{3}\gamma\right)\right. \\
&\quad - i\left(\ln\pi + \frac{1}{18}\pi^2 - 2 - \ln(iy)\right)y^{-1} - \left(-\frac{1}{2} - \frac{1}{6}\zeta(3)\right)y^{-2} \\
&\quad \left. + \sum_{j=3}^{\infty}\frac{(-1)^{j-1}}{2^{j-2}}\left(\frac{j-2}{j(j-1)}\zeta(j-1) + \frac{1}{6}\zeta(j+1)\right)(iy)^{-j}\right] \\
&\quad + \mathcal{O}\left[\left(\frac{\alpha}{2\pi}\right)^2\right], \qquad (3.46) \\
n_\parallel &= 1 - \frac{\alpha}{4\pi}\sin^2\theta\left[\frac{2}{3} + i\frac{\ln(iy) + 1 - \ln\pi}{y} + \frac{1}{y^2}\right. \\
&\quad \left. + \sum_{j=3}^{\infty}\frac{(-1)^{j-1}}{2^{j-2}}\frac{j-2}{j-1}\zeta(j-1)(iy)^{-j}\right] + \mathcal{O}\left[\left(\frac{\alpha}{2\pi}\right)^2\right]. \qquad (3.47)
\end{aligned}
$$

From this equation, it is apparent that the index of refraction acquires an imaginary part in strong electric fields.

3.3 Birefringence

In general, the birefringence is quantified by the difference of the indexes of refraction for the two modes of propagation,

$$\begin{aligned} n_\perp - n_\| &= \pm \frac{\alpha}{4\pi} \left[X_0^{(1)}\left(\frac{1}{\xi}\right)\xi^{-1} - X_0^{(2)}\left(\frac{1}{\xi}\right)\xi^{-2} - X_1\left(\frac{1}{\xi}\right)\right] \sin^2\theta \\ &\quad + \mathcal{O}\left[\left(\frac{\alpha}{2\pi}\right)^2\right] \end{aligned} \quad (3.48)$$

where the upper sign is for the magnetized case and the lower for the electrified case. Figure 3.1 depicts the indices of refraction for these two cases.

3.4 Dichroism

The analytic properties of the function $n_\|(\xi)$ can be used to estimate the dichroic properties of a magnetized or electrified vacuum. In a external electric field we have $\xi = iE/E_k = iy$, while in a magnetic field $\xi = B/B_k$. $n_\|(\xi)$ is real for real arguments; however for imaginary ξ, $n_\|(\xi)$ acquires an imaginary part. Classically, this imaginary part may be related to the attenuation length of a plane wave traversing the vacuum

$$l = \frac{2\pi\lambda}{\operatorname{Im} n} \quad (3.49)$$

where λ is the wavelength of the radiation. In quantum field theory, the imaginary part of n is related to the imaginary part of the photon polarization operator and therefore the cross-section for one-photon pair production.

In general the imaginary part for the two polarization modes is

$$\operatorname{Im} n_\perp = \frac{\alpha}{4\pi}\sin^2\theta \operatorname{Im} X_1\left(-\frac{i}{y}\right) + \mathcal{O}\left[\left(\frac{\alpha}{2\pi}\right)^2\right], \quad (3.50)$$

$$\begin{aligned} \operatorname{Im} n_\| &= \frac{\alpha}{4\pi}\sin^2\theta \left[\operatorname{Im} X_0^{(2)}\left(-\frac{i}{y}\right) y^{-2} - \operatorname{Re} X_0^{(1)}\left(-\frac{i}{y}\right) y^{-1}\right] \\ &\quad + \mathcal{O}\left[\left(\frac{\alpha}{2\pi}\right)^2\right]. \end{aligned} \quad (3.51)$$

These are conveniently calculated by evaluating the imaginary part of $X_0(x)$ for imaginary values of x by integrating around the poles of Equation 3.6

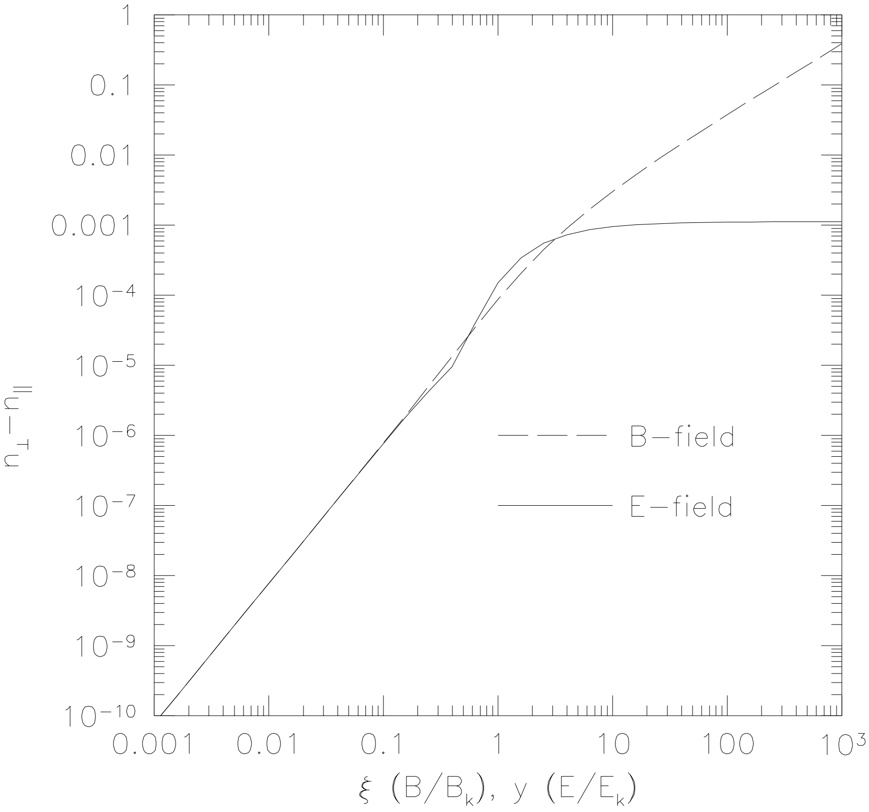

Figure 3.1: The difference between the index of refraction of the parallel and perpendicular polarizations for light traveling through external electric or magnetic fields.

(Heyl & Hernquist 1997b, Itzykson & Zuber 1980),

$$\operatorname{Im} X_0(x) = -\frac{1}{\pi} \sum_{n=1}^{\infty} \frac{e^{-i\pi n x}}{n^2} = -\frac{1}{\pi} e^{-\pi/y} \; {}_{1,1,1}F_{2,2}\left(e^{-\pi/y}\right) \tag{3.52}$$

where F is a generalized hypergeometric function. Using Equation 3.13 to calculate $\operatorname{Im} X_1(x)$, yielding for the indices of refraction,

$$\begin{aligned}
\operatorname{Im} n_\perp &= \frac{\alpha}{4\pi} \sin^2\theta \sum_{n=1}^{\infty} \left(\frac{2}{3}\pi + \frac{1}{n}\frac{1}{y} + \frac{1}{n^2}\frac{2}{\pi} \right) e^{-n\pi/y} \\
&\quad + \mathcal{O}\left[\left(\frac{\alpha}{2\pi} \right)^2 \right], \qquad (3.53) \\
&= \frac{\alpha}{4\pi} \sin^2\theta \left[\frac{2}{3}\pi \left(e^{\pi/y} - 1 \right)^{-1} - \frac{1}{y} \ln\left(1 - e^{-\pi/y}\right) \right. \\
&\quad \left. + \frac{2}{\pi} e^{-\pi/y} \; {}_{1,1,1}F_{2,2}\left(e^{-\pi/y}\right) \right] + \mathcal{O}\left[\left(\frac{\alpha}{2\pi} \right)^2 \right], \qquad (3.54) \\
\operatorname{Im} n_\parallel &= \frac{\alpha}{4\pi} \sin^2\theta \sum_{n=1}^{\infty} \left(\frac{\pi}{y^2} + \frac{1}{n}\frac{1}{y} \right) e^{-n\pi/y} + \mathcal{O}\left[\left(\frac{\alpha}{2\pi} \right)^2 \right], \qquad (3.55) \\
&= \frac{\alpha}{4\pi} \sin^2\theta \left[\frac{\pi}{y^2} \left(e^{\pi/y} - 1 \right)^{-1} - \frac{1}{y} \ln\left(1 - e^{-\pi/y}\right) \right] \\
&\quad + \mathcal{O}\left[\left(\frac{\alpha}{2\pi} \right)^2 \right] \qquad (3.56)
\end{aligned}$$

Figure 3.2 depicts the imaginary part of the index of refraction as a function of field strength.

In the weak-field limit, the imaginary part of the index of refraction is exponentially small as Klein & Nigam (1964b) found. However, our result is larger by a factor of $1/y$ in this limit and is more complicated. The error occurs between their Eq. 5 and Eq. 6. First, they have neglected the real part of the integral, and as in Klein & Nigam (1964a), they have calculated μ'_{ij} and used it as μ_{ij}. These errors are not important for this application. However, their function $\Phi_2(x)$ has not been calculated correctly. By examination of their Eq.6, we see that

$$\frac{\partial \mathcal{L}}{\partial K} = -i \frac{\alpha}{2} \frac{1}{16 I} \Phi_2(x) \tag{3.57}$$

so

$$\Phi_2(x) = -\frac{1}{\pi} \operatorname{Im} X_1 \left(\frac{\pi}{ix} \right) \tag{3.58}$$

which from examination of Equation 3.54 is significantly more complicated than their expression.

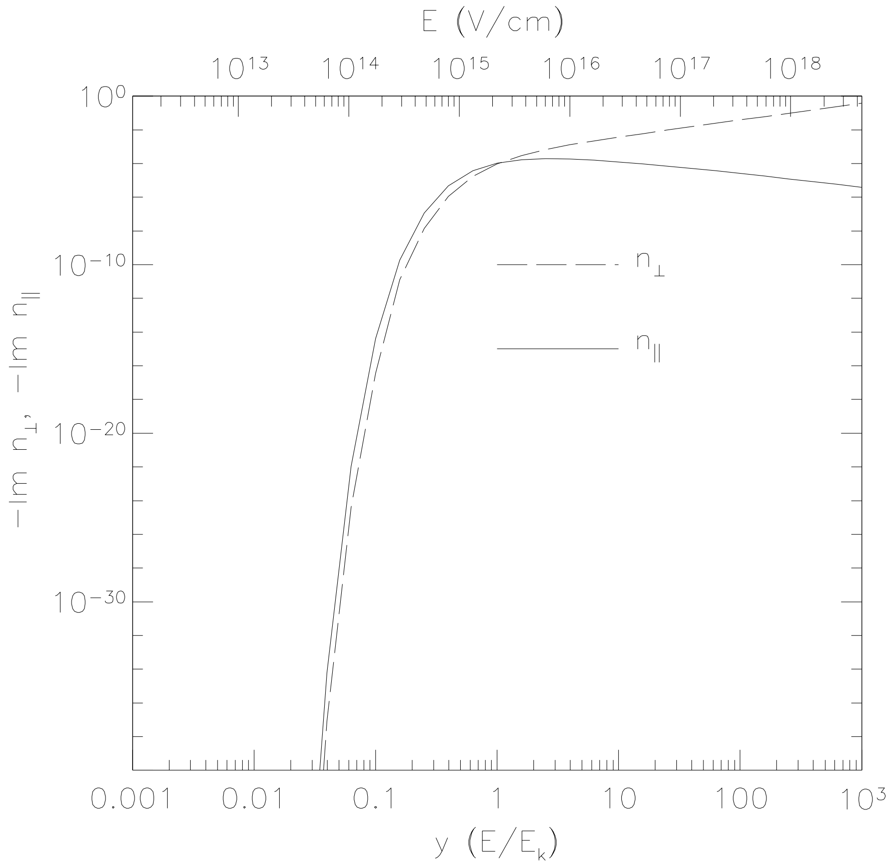

Figure 3.2: The imaginary part of the index of refraction for perpendicular and parallel propagation modes for light traveling through an external electric field.

3.5 Conclusions

Using a closed form expression for the Heisenberg-Euler effective Lagrangian for quantum electrodynamics in wrenchless ($K = 0$) fields, we have calculated general expressions for the index of refraction of a slowly-varying electromagnetic field, and evaluated these expressions for the simple cases of a pure electric or magnetic field. Our results agree with some previous work (Adler 1971, Berestetskii, Lifshitz & Pitaevskii 1982, Mielnieczuk, Lamm & Valluri 1988, Tsai & Erber 1975) in the appropriate limits. We expect these results to be of general utility especially in the study of light propagation in the vicinity of strongly magnetized neutron stars.

Chapter 4

QED Oneloop Corrections to a Macroscopic Magnetic Dipole

SUMMARY

We consider the field equations of a static magnetic field including one-loop QED corrections, and calculate the corrections to the field of a magnetic dipole.

4.1 Introduction

The one-loop corrections of quantum electrodynamics introduce nonlinearities in the equations of the electromagnetic field. These corrections manifest themselves through an index of refraction, electric permittivity and magnetic permeability tensors which are a function of field strength (Tsai & Erber 1975,Heyl & Hernquist 1997c). The vacuum responds to an applied field like a nonlinear paramagnetic substance (Mielnieczuk, Lamm & Valluri 1988). Using an analytic expression for the effective Lagrangian of QED to one-loop order Heyl & Hernquist 1997b, we derive the magnetic magnetic permeability tensor as a function of the applied magnetic field and calculate the one-loop corrections to the field of a macroscopic magnetic dipole.

4.2 The Effects of Non-linearity on the Field Equations

The effective Lagrangian of QED at one-loop order consists of the sum of a linear and a non-linear term

$$\mathcal{L} = \mathcal{L}_0 + \mathcal{L}_1. \tag{4.1}$$

Both terms of the Lagrangian can be written in terms of the Lorentz invariants,

$$I = F_{\mu\nu}F^{\mu\nu} = 2\left(|\mathbf{B}|^2 - |\mathbf{E}|^2\right) \tag{4.2}$$

and

$$K = -\left(\frac{1}{2}\epsilon^{\lambda\rho\mu\nu}F_{\lambda\rho}F_{\mu\nu}\right)^2 = -(4\mathbf{E}\cdot\mathbf{B})^2. \tag{4.3}$$

following Heisenberg & Euler (1936). The Greek indices count over space and time components $(0, 1, 2, 3)$.

Since we are interested in the static properties of a magnetic field, we can take $K = 0$. If we apply the Euler-Lagrange condition to extremize the action, we obtain,

$$\nabla \times \mathbf{H} = 0 \tag{4.4}$$

$$\mathbf{H} = -4\frac{\partial \mathcal{L}}{\partial I}\mathbf{B} \tag{4.5}$$

where the factor of -4 is inserted for later convenience.

Since $\nabla \times \mathbf{H} = 0$, we take $\mathbf{H} = -\nabla\phi$, where ϕ is the magnetic scalar potential. Furthermore, the field $\mathbf{B}$ is derived from a vector potential (*i.e.* $\mathbf{B} = \nabla \times \mathbf{A}$) and so we also have,

$$\nabla \cdot \mathbf{B} = 0. \tag{4.6}$$

If the relationship between $\mathbf{H}$ and $\mathbf{B}$ were linear, this equation would be satisfied by $\nabla^2\phi = 0$. However, we will assume a small non-linearity between the two fields,

$$-4\frac{\partial \mathcal{L}}{\partial I} = \mu_0' + \mu_1'(B^2) \tag{4.7}$$

where μ_0' is a constant and μ_1' a function such that $\mu_1'(B^2) \ll \mu_0'$.

We can invert the relationship between the two fields to first order

$$\mathbf{B} = \left(\mu_0 + \mu_1(H^2)\right)\mathbf{H} \tag{4.8}$$

Now we recast the field equation with the magnetic potential

$$\nabla \cdot \left[\left(\mu_0 + \mu_1(H^2)\right)\nabla\phi\right] = 0, \tag{4.9}$$

write $\phi = \phi_0 + \phi_1$, and solve the equation order by order

$$\begin{aligned}
\nabla^2\phi_0 &= 0 & (4.10)\\
\nabla^2\phi_1 &= \rho_{\text{eff}} = -\nabla\cdot\left[\frac{\mu_1(H^2)}{\mu_0}\nabla\phi_0\right]\\
&= -2\frac{\mu_1^{(1)}(H^2)}{\mu_0}\nabla\phi_0\cdot(\nabla\phi_0\cdot\nabla)\nabla\phi_0 & (4.11)
\end{aligned}$$

where

$$\mu_1^{(1)}(x) = \frac{\mathrm{d}\mu(x)}{\mathrm{d}x}. \tag{4.12}$$

For a magnetic dipole,

$$\begin{aligned}
\phi_0(\mathbf{r}) &= \frac{\mathbf{m}\cdot\mathbf{r}}{|\mathbf{r}|^3} & (4.13)\\
\nabla\phi_0\cdot(\nabla\phi_0\cdot\nabla)\nabla\phi_0 &= 3\frac{\left[5\left(\mathbf{m}\cdot\mathbf{r}\right)^2 + 3|\mathbf{m}|^2|\mathbf{r}|^2\right]\mathbf{m}\cdot\mathbf{r}}{|\mathbf{r}|^{13}} & (4.14)
\end{aligned}$$

or more conveniently in spherical coordinates where we have taken the dipole moment $\mathbf{m}$ to be aligned along the $z-$axis,

$$\begin{aligned}
\phi_0(\mathbf{r}) &= \sqrt{\frac{4\pi}{3}}\frac{m}{r^2}Y_{10}(\theta,\phi) & (4.15)\\
\nabla\phi_0\cdot(\nabla\phi_0\cdot\nabla)\nabla\phi_0 &= 12\sqrt{\frac{\pi}{7}}\frac{m^3}{r^{10}}\left[Y_{30}(\phi,\theta)+\sqrt{21}Y_{10}(\phi,\theta)\right] & (4.16)
\end{aligned}$$

4.3 The Lagrangian to One-Loop Order

Heisenberg & Euler (1936) and Weisskopf (1936) independently derived the effective Lagrangian of the electromagnetic field using electron-hole theory. Schwinger (1951) later rederived the same result using quantum electrodynamics. In Heaviside-Lorentz units, the Lagrangian is given by

$$\mathcal{L}_0 = -\frac{1}{4}I \tag{4.17}$$

$$\mathcal{L}_1 = \frac{e^2}{hc}\int_0^\infty e^{-\zeta}\frac{\mathrm{d}\zeta}{\zeta^3}\left\{ i\zeta^2\frac{\sqrt{-K}}{4}\times \right.$$
$$\frac{\cos\left(\frac{\zeta}{B_k}\sqrt{-\frac{I}{2}+i\frac{\sqrt{-K}}{2}}\right)+\cos\left(\frac{\zeta}{B_k}\sqrt{-\frac{I}{2}-i\frac{\sqrt{-K}}{2}}\right)}{\cos\left(\frac{\zeta}{B_k}\sqrt{-\frac{I}{2}+i\frac{\sqrt{-K}}{2}}\right)-\cos\left(\frac{\zeta}{B_k}\sqrt{-\frac{I}{2}-i\frac{\sqrt{-K}}{2}}\right)} \tag{4.18}$$
$$\left. + |B_k|^2 + \frac{\zeta^2}{6}I\right\}. \tag{4.19}$$

where $B_k = E_k = \frac{m^2c^3}{e\hbar} \approx 2.2 \times 10^{15}\,\mathrm{V\,cm^{-1}} \approx 4.4 \times 10^{13}\,\mathrm{G}$. Dittrich & Reuter (1985) have derived the second-order corrections to the Lagrangian and found them to be in general an order of α smaller than the one-loop corrections regardless of field strength; consequently, the one-loop correction should be adequate for all but the most precise analyses.

In the weak field limit Heisenberg & Euler (1936) give

$$\mathcal{L} \approx -\frac{1}{4}I + E_k^2\frac{e^2}{hc}\left[\frac{1}{180E_k^4}\left(I^2-\frac{7}{4}K\right)+\frac{1}{630E_k^6}\left(-I^3+\frac{13}{8}KI\right)\cdots\right] \tag{4.20}$$

We define a dimensionless parameter ξ to characterize the field strength

$$\xi = \frac{1}{E_k}\sqrt{\frac{I}{2}} \tag{4.21}$$

and use the analytic expression of this Lagrangian for $K = 0$ derived by Heyl & Hernquist (1997b):

$$\mathcal{L}_1(I,0) = \frac{e^2}{hc}\frac{I}{2}X_0\left(\frac{1}{\xi}\right) \tag{4.22}$$

where

$$X_0(x) = 4\int_0^{x/2-1}\ln(\Gamma(v+1))\mathrm{d}v + \frac{1}{3}\ln\left(\frac{1}{x}\right) + 2\ln 4\pi - 4\ln A - \frac{5}{3}\ln 2$$
$$- \left[\ln 4\pi + 1 + \ln\left(\frac{1}{x}\right)\right]x + \left[\frac{3}{4}+\frac{1}{2}\ln\left(\frac{2}{x}\right)\right]x^2 \tag{4.23}$$

where

$$\ln A = \frac{1}{12} - \zeta^{(1)}(-1). \tag{4.24}$$

Here $\zeta^{(1)}(x)$ denotes the first derivative of the Riemann Zeta function.

With the analytic form of the Lagrangian, calculating μ_0' and μ_1' is straightforward and α provides a convenient ordering parameter.

$$\mu_0' = -4\frac{\partial \mathcal{L}_0}{\partial I} = 1 \tag{4.25}$$

$$\mu_1' = -\frac{\alpha}{2\pi}\left[2X_0\left(\frac{1}{\xi}\right) - \frac{1}{\xi}X_0^{(1)}\left(\frac{1}{\xi}\right)\right] \tag{4.26}$$

where $\xi = B/B_k$, and

$$X_0^{(1)}(x) = \frac{\mathrm{d}X_0(x)}{\mathrm{d}x}. \tag{4.27}$$

Inverting this relationship to first order yields,

$$\mu_0 = 1 \tag{4.28}$$

$$\mu_1(H^2) = \frac{\alpha}{2\pi}\left[2X_0\left(\frac{B_k}{H}\right) - \frac{B_k}{H}X_0^{(1)}\left(\frac{B_k}{H}\right)\right] \tag{4.29}$$

$$\mu_1^{(1)}(H^2) = \frac{\alpha}{2\pi}\frac{1}{2B_k^2}\left[\frac{B_k^4}{H^4}X_0^{(2)}\left(\frac{B_k}{H}\right) - \frac{B_k^3}{H^3}X_0^{(1)}\left(\frac{B_k}{H}\right)\right] \tag{4.30}$$

$$= \frac{\alpha}{2\pi}\frac{1}{6B_k^2}\left\{2\frac{B_k^2}{H^2} + 3\frac{B_k^3}{H^3}\left[\ln(4\pi) + 1 + \ln\left(\frac{H}{B_k}\right) - 2\ln\Gamma\left(\frac{1}{2}\frac{B_k}{H}\right)\right] + 3\frac{B_k^4}{H^4}\left[\psi\left(\frac{1}{2}\frac{B_k}{H}\right) - 1\right]\right\} \tag{4.31}$$

where $\psi(x)$ is the digamma function,

$$\psi(x) = \frac{\mathrm{d}\ln\Gamma(x)}{\mathrm{d}x}. \tag{4.32}$$

The expression for μ_1 agrees numerically with the results of Mielnieczuk, Lamm & Valluri (1988). The function $\mu_1^{(1)}(H^2)$ may conveniently be expanded in the weak-field limit ($H < B_k/2$),

$$\mu_1^{(1)}(H^2) = -\frac{\alpha}{2\pi}\frac{8}{B_k^2}\sum_{j=0}^{\infty}\frac{2^{2j}B_{2(j+2)}}{2j+3}\left(\frac{H}{B_k}\right)^{2j} \tag{4.33}$$

where B_j denotes the jth Bernoulli number, and in the strong-field limit ($H > B_k/2$)

$$\mu_1^{(1)}(H^2) = \frac{\alpha}{2\pi}\frac{1}{B_k^2}\left\{\frac{1}{3}\frac{B_k^2}{H^2} - \frac{1}{2}\frac{B_k^3}{H^3}\left[\ln\left(\frac{H}{B_k}\right) + 1 - \ln\pi\right] - \frac{1}{2}\frac{B_k^4}{H^4} - \sum_{j=5}^{\infty}\frac{(-1)^j}{2^{j-3}}\frac{j-4}{j-3}\zeta(j-3)\left(\frac{H}{B_k}\right)^{-j}\right\}. \tag{4.34}$$

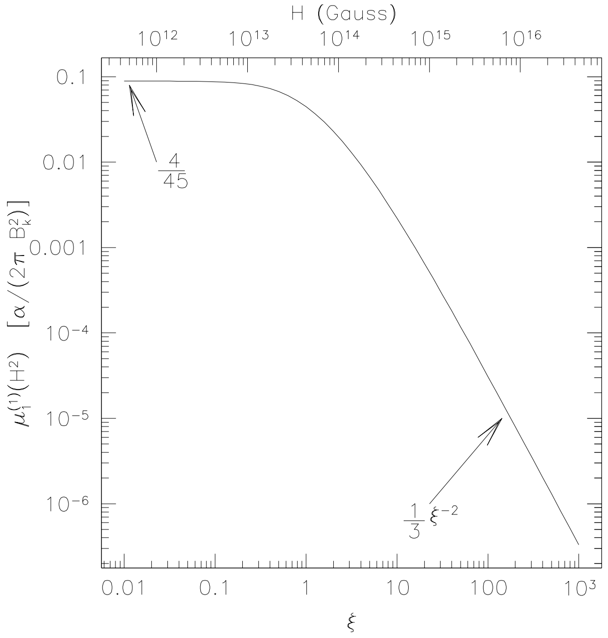

Figure 4.1: $\mu_1^{(1)}(H^2)$ as a function of ξ, H

where we have used the expansions of Heyl & Hernquist (1997b).

As apparent from Figure 4.1, $\mu_1^{(1)}(H^2)$ is constant up to approximately $H = 0.5B_k$ and then begins to decrease quickly as H^{-2}. The existence of these two regimes allows us to find analytic solutions for the correction to the potential (ϕ_1).

4.4 Solving for the first-order correction

4.4.1 Weak-field limit

$\mu_1^{(1)}(H^2)$ is constant as long as $H \ll B_k$. In this regime Equation 4.11 may be solved analytically. Since spherical harmonics are eigenfunctions of the angular component of the Laplacian operator, it is expedient to expand the right-hand side of Equation 4.11 in terms of spherical harmonics (Binney

& Tremaine 1987).

$$\rho_{lm}(r) = \int_0^\pi \sin\theta \mathrm{d}\theta \int_0^{2\pi} \mathrm{d}\phi Y_{lm}^*(\theta,\phi)\rho_{\mathrm{eff}}(r,\theta,\phi) \tag{4.35}$$

With this definition the correction to the potential is given by (Binney & Tremaine 1987)

$$\phi_1(r,\theta,\phi) = -\sum_{l,m} \frac{Y_{lm}(\theta,\phi)}{2l+1}\left[\frac{1}{r^{l+1}}\int_0^r \rho_{lm}(a)a^{l+2}\mathrm{d}a + r^l \int_r^\infty \rho_{lm}(a)\frac{\mathrm{d}a}{a^{l-1}}\right] \tag{4.36}$$

If $\mu_1^{(1)}(H^2)$ is a constant, we see from Equation 4.11 and Equation 4.16 that the expansion given by Equation 4.35 is straightforward

$$\rho_{10}(r) = -24\sqrt{3\pi}\frac{\mu_1^{(1)}}{\mu_0}\frac{m^3}{r^{10}} \tag{4.37}$$

$$\rho_{30}(r) = -24\sqrt{\frac{\pi}{7}}\frac{\mu_1^{(1)}}{\mu_0}\frac{m^3}{r^{10}} \tag{4.38}$$

If we combine these results with Equation 4.36 we see that the interior integral diverges if $\mu_1^{(1)}$ is a constant. This does not present a problem if we insert an inner bound (r_0) to the interior integral. This inner bound is defined as the radius at which either $\mu_1^{(1)}(H^2)$ begins to change (*i.e.* when $H \gtrsim 0.5B_k$) or when the zeroth order potential is no longer given by the dipole formula (*i.e.* at the surface of the object). We obtain

$$\phi_{1,10}(r,\theta,\phi) = \frac{4}{9}\sqrt{3\pi}\frac{\mu_1^{(1)}}{\mu_0}\frac{m^3}{r^2}\left(\frac{3}{r_0^6}-\frac{1}{r^6}\right)Y_{10}(\theta,\phi) \tag{4.39}$$

$$\phi_{1,30}(r,\theta,\phi) = 6\sqrt{\frac{\pi}{7}}\frac{\mu_1^{(1)}}{\mu_0}\frac{m^3}{r^4}\left(\frac{1}{7}\frac{1}{r_0^4}-\frac{1}{11}\frac{1}{r^4}\right)Y_{30}(\theta,\phi). \tag{4.40}$$

These functions describe radially dependent corrections to the dipole and hexapole moments of the object under consideration. If we define the higher moments in analogy to Equation 4.15,

$$\phi_{l0}(r,\theta,\phi) = \sqrt{\frac{4\pi}{2l+1}}\frac{M_{l0}}{r^{(l+1)}}Y_{l0}(\theta,\phi), \tag{4.41}$$

we obtain the following corrections

$$m_1(r) = \frac{2}{3}\frac{\mu_1^{(1)}}{\mu_0}m^3\left(\frac{3}{r_0^6}-\frac{1}{r^6}\right) \tag{4.42}$$

$$M_{30,1}(r) = 3\frac{\mu_1^{(1)}}{\mu_0}m^3\left(\frac{1}{7}\frac{1}{r_0^4}-\frac{1}{11}\frac{1}{r^4}\right). \tag{4.43}$$

To eliminate the dependence on the inner bound, r_0, we assume that the dipole and hexapole moments are known at a radius $r_s > r_0$ and calculate the difference between the known moments at r_s and those measured at infinity.

Substituting the values of μ_0 and $\mu_1^{(1)}$, we obtain,

$$\begin{aligned} m(r=\infty) - m(r=r_s) &= \Delta m = \frac{8}{135}\frac{\alpha}{2\pi} m \left(\frac{m}{r_s^3}\frac{1}{B_k}\right)^2 && (4.44) \\ M_{30}(r=\infty) - M_{30}(r=r_s) &= \Delta M_{30} = \frac{4}{165}\frac{\alpha}{2\pi} m r_s^2 \left(\frac{m}{r_s^3}\frac{1}{B_k}\right)^2 && (4.45) \end{aligned}$$

Both the corrections are given in terms of the magnetic field strength at r_s. Since we have assumed that $\mu_1^{(1)}(H^2)$ is constant near r_s, the field strength at r_s must appreciably be less than B_k for this set of approximations to be valid. Consequently, the correction to the dipole moment is indeed quite small, less than one-thousandth of the "bare" dipole moment. However, there is a correction to the hexapole moment even without a "bare" hexapole moment. Thus radiative corrections generate a hexapole field which is in principle measurable at infinity.

4.4.2 The General Case

In the strong-field limit, we must use the general equation (Equation 4.31) for $\mu_1^{(1)}(H^2)$ because the magnetic field strength varies as a function of θ around the dipole. Before tackling this problem numerically, we can glean several characteristics of the solutions from Equation 4.11 and Equation 4.35. Since for a dipole ρ_{eff} is a odd function of θ and constant with respect to ϕ, the contributions,

$$\rho_{lm}(r) = 0 \text{ if } l \text{ is even or } m \neq 0. \tag{4.46}$$

Furthermore, we can more conveniently write

$$\rho_{lm}(r) = \frac{1}{\mu_0}\frac{\alpha}{2\pi}\frac{1}{B_k^2}\frac{m^3}{r^{10}}\chi_{lm}(\beta) \tag{4.47}$$

where $\chi_{lm}(\beta)$ is a dimensionless function of a dimensionless argument,

$$\beta = \frac{m}{r^3}\frac{1}{B_k}. \tag{4.48}$$

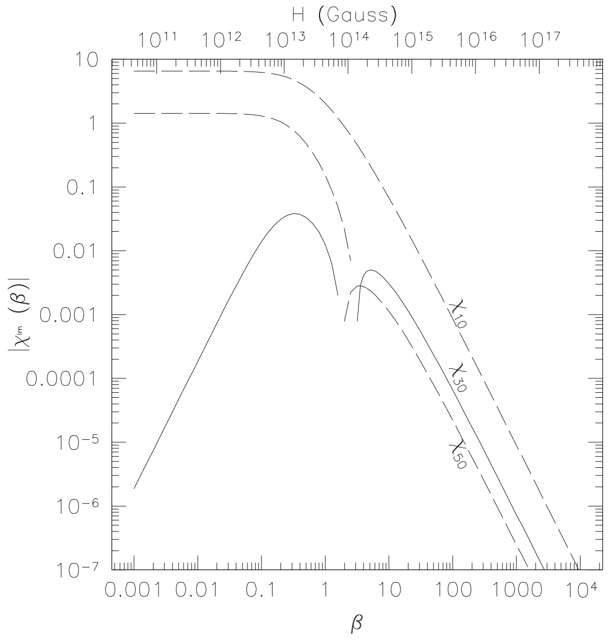

Figure 4.2: $\chi_{lm}(\beta)$ as a function of β, H. The solid lines indicate where $\chi_{lm}(\beta)$ is positive. The dashed lines indicate negative values of the ordinate.

For a dipole,

$$\begin{aligned}\chi_{lm}(\beta) &= -2\int_0^\pi \sin\theta \mathrm{d}\theta \int_0^{2\pi} \mathrm{d}\phi Y_{lm}^*(\theta,\phi) \times \\ & \left(\frac{\alpha}{2\pi}\frac{1}{B_k^2}\right)^{-1}\left(3\cos\theta\left(5\cos^2\theta+3\right)\right)\mu_1^{(1)}\left[\beta^2 B_k^2\left(3\cos^2\theta+1\right)\right] \end{aligned} \quad (4.49)$$

We calculate numerically the functions $\chi_{lm}(\beta)$ for the first three odd harmonics and depict the results in Figure 4.2.

The limiting expressions for the weak-field limit are easily calculated,

$$\chi_{10}(\beta) = \sqrt{3\pi}\left[-\frac{32}{15}+\frac{13312}{1225}\beta^2-\frac{167936}{1225}\beta^4+\mathcal{O}\left(\beta^6\right)\right] \quad (4.50)$$

$$\chi_{30}(\beta) = \sqrt{7\pi}\left[-\frac{32}{105}+\frac{11776}{3675}\beta^2-\frac{323584}{5775}\beta^4+\mathcal{O}\left(\beta^6\right)\right] \quad (4.51)$$

$$\chi_{50}(\beta) = \sqrt{11\pi}\left[+\frac{512}{1617}\beta^2 - \frac{1150976}{105105}\beta^4 + \mathcal{O}\left(\beta^6\right)\right] \tag{4.52}$$

In the strong-field limit, we have the following approximations

$$\chi_{10}(\beta) = -\frac{4}{27}\sqrt{\pi}\left(27\sqrt{3}-4\pi\right)\beta^{-2} + \mathcal{O}\left(\beta^{-3}\right) \tag{4.53}$$

$$\chi_{30}(\beta) = \frac{8}{243}\sqrt{7\pi}\left(81-14\sqrt{3}\pi\right)\beta^{-2} + \mathcal{O}\left(\beta^{-3}\right) \tag{4.54}$$

$$\chi_{50}(\beta) = -\frac{4}{1215}\sqrt{11\pi}\left(1863-340\sqrt{3}\pi\right)\beta^{-2} + \mathcal{O}\left(\beta^{-3}\right) \tag{4.55}$$

The integrals for each spherical-harmonic component of the first-order correction (Equation 4.36) may be recast in terms of integrals over β

$$\phi_1(r,\theta,\phi) = -\frac{1}{3}\frac{m}{r^2}\frac{1}{\mu_0}\frac{\alpha}{2\pi}\beta^2\sum_{l,m}\frac{Y_{lm}(\theta,\phi)}{2l+1}\Bigg[\beta^{(l-7)/3}\int_\beta^{\beta_0}\chi_{lm}(\upsilon)\upsilon^{-(l-4)/3}\mathrm{d}\upsilon + \beta^{-(l+8)/3}\int_0^\beta\chi_{lm}(\upsilon)\upsilon^{(l+5)/3}\mathrm{d}\upsilon\Bigg] \tag{4.56}$$

where the first integral is to be evaluated in the limit as $\beta_0 \to \infty$. Although Equation 4.56 appears to be scale free, the cutoff β_0 has a physical interpretation. Firstly, it can be taken to be the magnetic field strength at the surface of the object. For a point magnetic dipole (*e.g.* an electron), the interpretation is more subtle. As one approaches a point dipole, not only does the field become arbitrarily strong, so do the field gradients. When these gradients become larger in magnitude than B_k/λ_e ($\lambda_e = \hbar/m_e c$, the electron Compton wavelength), the Heisenberg-Euler Lagrangian is no longer applicable; therefore, we do not expect our expressions for ρ_{eff} to be valid arbitrarily close to a point dipole. The radius or field strength at which our expression for ρ_{eff} fails depends on the intrinsic dipole moment of the object (m),

$$r_0 \sim \left(\frac{m}{B_k}\lambda_e\right)^{1/4} \quad \text{or} \quad \beta_0 \sim \left(\frac{m}{B_k}\right)^{1/4}\lambda_e^{-3/4} \tag{4.57}$$

As in the weak-field case, we calculate the shift in the observed multipole moments at infinity relative to the known moments at some inner radius

$r_s > r_0$ or equivalently at some field strength $\beta_s < \beta_0$.

$$\begin{aligned} m_1(0) - m_1(\beta_s) &= -\frac{1}{9} m \frac{1}{\mu_0} \frac{\alpha}{2\pi} \sqrt{\frac{3}{4\pi}} \left[\int_0^{\beta_s} \chi_{10}(\upsilon) \upsilon \mathrm{d}\upsilon \right. \\ & \left. - \frac{1}{\beta_s} \int_0^{\beta_s} \chi_{10}(\upsilon) \upsilon^2 \mathrm{d}\upsilon \right] \end{aligned} \tag{4.58}$$

$$\begin{aligned} M_{30,1}(0) - M_{30,1}(\beta_s) &= -\frac{1}{21} m r_s^2 \frac{1}{\mu_0} \frac{\alpha}{2\pi} \sqrt{\frac{7}{4\pi}} \left[\beta_s^{2/3} \int_0^{\beta_s} \chi_{30}(\upsilon) \upsilon^{1/3} \mathrm{d}\upsilon \right. \\ & \left. - \beta_s^{-5/3} \int_0^{\beta_s} \chi_{30}(\upsilon) \upsilon^{8/3} \mathrm{d}\upsilon \right] \end{aligned} \tag{4.59}$$

$$\begin{aligned} M_{50,1}(0) - M_{50,1}(\beta_s) &= -\frac{1}{33} m r_s^4 \frac{1}{\mu_0} \frac{\alpha}{2\pi} \sqrt{\frac{11}{4\pi}} \left[\beta_s^{4/3} \int_0^{\beta_s} \chi_{50}(\upsilon) \upsilon^{-1/3} \mathrm{d}\upsilon \right. \\ & \left. - \beta_s^{-7/3} \int_0^{\beta_s} \chi_{50}(\upsilon) \upsilon^{10/3} \mathrm{d}\upsilon \right] \end{aligned} \tag{4.60}$$

and in general

$$\begin{aligned} M_{l0,1}(0) - M_{l0,1}(\beta_s) &= -\frac{1}{3(2l+1)} m r_s^{l-1} \frac{1}{\mu_0} \frac{\alpha}{2\pi} \sqrt{\frac{2l+1}{4\pi}} \times \\ & \left[\beta_s^{(l-1)/3} \int_0^{\beta_s} \chi_{l0}(\upsilon) \upsilon^{-(l-4)/3} \mathrm{d}\upsilon \right. \\ & \left. - \beta_s^{-(l+2)/3} \int_0^{\beta_s} \chi_{l0}(\upsilon) \upsilon^{(l+5)/3} \mathrm{d}\upsilon \right] \end{aligned} \tag{4.61}$$

Figure 4.3 depicts the shifts in the moments between the surface of the dipole and infinity.

For the higher moments ($l > 1$), the integrals in Equation 4.56 are well behaved so we need not set a inner bound (β_0) and we can define in general

$$M_{l0,1}(0) = -\frac{1}{3(2l+1)} m \left(\frac{m}{B_k} \right)^{(l-1)/3} \frac{1}{\mu_0} \frac{\alpha}{2\pi} \sqrt{\frac{2l+1}{4\pi}} \int_0^{\infty} \chi_{l0}(\upsilon) \upsilon^{-(l-4)/3} \mathrm{d}\upsilon \tag{4.62}$$

This integral converges for all $l > 1$. For $l = 1$, it diverges logarithmically as $\upsilon \to \infty$.

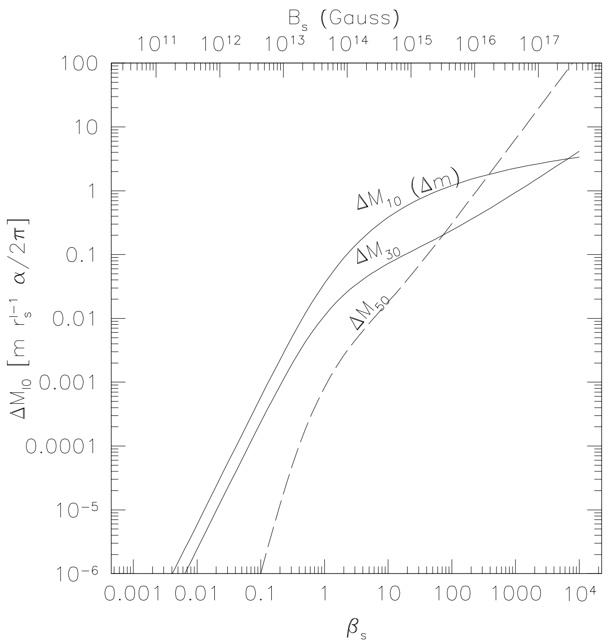

Figure 4.3: The difference in the strength of the multipole moments measured at infinity ($\beta \to 0$) and at the surface, $M_{l0}(0) - M_{l0}(\beta_s)$ (ΔM_{l0}), as a function the strength of the dipole field at the surface, β_s, H_s. The solid lines indicate the moments for which the vacuum acts paramagnetically, *i.e.* $\Delta M_{l0}(\beta_s) > 0$. The dashed lines indicate negative values of the ordinate.

4.5 Conclusions: Application to Neutron Stars

The environment of a neutron star is strongly magnetized; therefore, the one-loop QED corrections may be significant, especially for those neutron stars with ultrastrong surface fields (magnetars) (Duncan & Thompson 1992). Although plasma probably fills this region, QED vacuum corrections dominate the contribution of the plasma to the magnetic permeability (Mészáros 1992).

The structure of the magnetic field at the surface of a neutron star is an important clue to the origin of neutron-star magnetic fields. Several authors have proposed (Blandford, Applegate & Hernquist 1983) that currents in the thin crust generate the observed magnetic fields. In this case, the field structure will be dominated by high-order multipoles with $l \sim \delta r_c / r_* \gg 1$ where δr_c is the thickness of the crust and r_* is the radius of the star (Arons 1993). Arons (1993) argues further that the observed spin-up line for millisecond pulsars constrains the strength of higher-order multipoles at the surface to be no more than 40 % of surface strength of the dipole.

The current results complicate this argument. The location of the observed spin-up line and the value of spin-down index of a pulsar depend on the strength of the various moments of the magnetic field at the light cylinder. Our results show that the vacuum itself may generate higher magnetic moments between the neutron star surface and the light cylinder. Figure 4.4 depicts the fractional contribution of higher magnetic moments to the field strength at the light cylinder as a function of the surface dipole field strength and the pulsar period.

Even for magnetars near their birth, the vacuum adds only a small correction to the field strength at the light cone. Because of the weakness of the QED coupling, the one-loop corrections to otherwise classical descriptions of a magnetic dipole tend to be small for all but the most extreme field strengths.

Observing this effect would be difficult. For a magnetar, measurements of the field strength at two different radii and an estimate of the strength of higher order moments at the surface each to a precision of one part in one-thousand would be required. However, if one could argue that an object had no hexapole or higher-order multipole intrinsically, a measurement of a higher-order multipole far from the object would uncover the effects of one-loop corrections. For example, an electron is intrinsically a magnetic dipole. If one ignores the contribution of terms in the Lagrangian depending on field gradients, one would expect the vacuum surrounding an electron to generate higher order multipole fields. Determining whether this occurs is beyond the scope of this work.

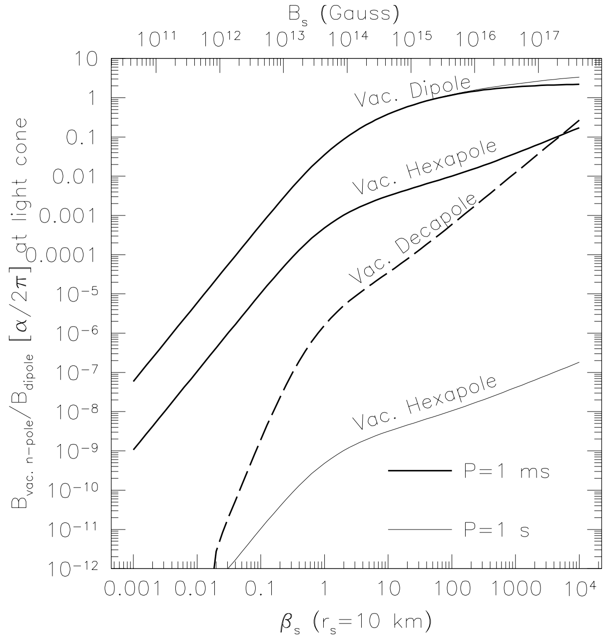

Figure 4.4: The fractional contribution of higher magnetic moments to the field strength at the light cylinder as function of surface dipole field strength for periods of one millisecond and one second. The contribution of the vacuum decapole at the light cone for $P = 1\text{s}$ is too small to be depicted on this graph.

Chapter 5

Testing QED with LIGO

SUMMARY

We propose an experiment using the gravitational wave detector LIGO to measure the photon-photon interaction in quantum electrodynamics. We find that the LIGO testbed interferometer could detect this effect after one week to nine-month integration with a signal to noise ratio ~ 15 *depending on the strength and size of the magnet used.*

5.1 Introduction

Quantum electrodynamics (QED) is one of the most successful physical theories. Its predictions from the lowest energies (Maxwell's equations) to high energies (the anomalous magnetic moment) have been tested with unrivaled precision. However, one of the earliest predictions of QED, the photon-photon interaction (Euler & Kockel 1934), has only been observed through Delbrück scattering (Mietner & Kösters 1933; Wilson 1953) of high-energy photons off of heavy nuclei (see Milstein & Schumacher 1994 for a recent review).

Here, we propose a straightforward experiment to detect the photon-photon interaction more directly by examining the coupling between photons and an external magnetic field (Figure 5.1). For laboratory field strengths the interaction is miniscule and results in an index of refraction $n > 1$ for photons traveling in a vacuum.

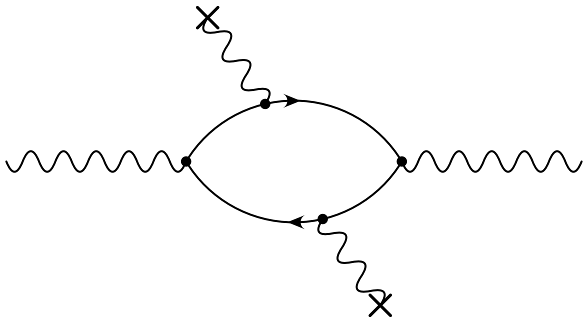

Figure 5.1: The coupling between a photon and an external magnetic field.

5.2 The Experiment

The LIGO interferometer has been designed to detect gravitational radiation by measuring the change in path length between several mirrors induced by a passing gravity wave, by interfering the emission of several lasers traveling down two perpendicular paths. The initial design is sensitive to changes in the path length of $\sim 10^{-19}$ m over the 4-km length of the instrument at a frequency of 200 Hz (Abramovici et al. 1992). At higher frequencies, the photon shot noise increases as the frequency, and at lower frequencies thermal vibrations and seismic activity add uncertainty to the path length.

A magnetic field applied along a section of the light path will induce a change in the light travel time which could be detected as a path length change. To maximize the interaction between the laser photons and the magnetic field, the magnetic field should be directed perpendicular to the direction of propagation and to the magnetic field of the laser radiation. For this geometry, the index of refraction to lowest order in the field strength is given by

$$n - 1 = \frac{\alpha}{4\pi}\frac{14}{45}\left(\frac{B}{B_k}\right)^2 = 9.272 \times 10^{-22}\left(\frac{B}{10T}\right)^2 \tag{5.1}$$

where $\alpha \approx 1/137$ is the fine-structure constant and $B_k = 4.414 \times 10^9$ T. Over a length of four kilometers (the size of the LIGO interferometer), this index of refraction results in an increase in the effective path length ten times larger than the root-mean-square noise in the measured path length of the LIGO Mark II testbed interferometer of 3×10^{-19} m /Hz$^{-1/2}$ near 450

Hz (Abramovici et al. 1996). Unfortunately, it is not practical to magnetize the entire four-kilometer length of one of the legs of LIGO. The change in path length is proportional to the length of path magnetized (l) times the change in the index of refraction,

$$\begin{aligned} \Delta L_{\rm amp} &= (n-1)l = \frac{\alpha}{4\pi}\frac{14}{45}\left(\frac{B}{B_k}\right)^2 l \\ &= 9.272\times 10^{-22}{\rm m}\left(\frac{B}{10T}\right)^2\left(\frac{l}{1\ {\rm m}}\right). \end{aligned} \tag{5.2}$$

The signal-to-noise ratio to measure a change in path length with a characteristic frequency f_c is

$$\frac{S}{N} \simeq \frac{\Delta L_c}{\Delta L_{\rm rms}} = \frac{\Delta L_{\rm amp}\sqrt{n_c}}{\widetilde{\Delta L}(f_c)\sqrt{f_c}} \tag{5.3}$$

where n is the number of cycles observed and $\widetilde{\Delta L}(f)$ is the square root of the power spectral density of Gaussian noise at frequency f (Abramovici et al. 1992). The number of cycles observed n_c is $f_c t$ where t is the duration of the observation. We obtain

$$\frac{S}{N} \simeq \frac{\Delta L_{\rm amp}\sqrt{t}}{\widetilde{\Delta L}(f_c)} = \frac{\alpha}{4\pi}\frac{14}{45}\left(\frac{B}{B_k}\right)^2\frac{l\sqrt{t}}{\widetilde{\Delta L}(f_c)} \tag{5.4}$$

We are free to select f_c to minimize $\widetilde{\Delta L}$. The minimum of $\widetilde{h}$ for the Mark II testbed 40-m interferometer is $\approx 3\times 10^{-19}$ m Hz$^{-1/2}$ at 450 Hz. We find

$$\frac{S}{N} \simeq 15\left(\frac{B}{10\ {\rm T}}\right)^2\left(\frac{l}{1\ {\rm m}}\right)\left(\frac{\widetilde{\Delta L}(f_c)}{3\times 10^{-19}{\rm m\ Hz}^{-1/2}}\right)^{-1}\left(\frac{t}{270\ {\rm d}}\right)^{1/2}. \tag{5.5}$$

This quantity does not depend on the length of the legs of the interferometer but only on the properties of the detector, the laser and the thermal and seismic isolation of the interferometer; consequently, the experiment could be carried out on the 40-meter LIGO test-bed interferometer and with a similar laser and optics achieve the same signal-to-ratio as on the LIGO interferometer itself.

Since LIGO is designed to have several independent beams and detectors, this experiment will not interfere with the normal operations of the instrument, as long as the magnets required to generate the variable 10 T field over 1 m do not interfere with the transmission of the other beams or the vacuum chamber enclosing them.

Unfortunately, the required field geometry cannot be achieved by surrounding the the beam by a compact solenoid which would generate a field parallel to the direction of the laser. QED predicts that the interaction between an external field and a propagating photon is proportional to $\sin^2\theta$ where θ is the angle between the direction of propagation and the field. However, the field geometry is essentially the same as that of a dipole used in a synchrotron. For illustration we estimate the effect using a dipole with the specifications for the Superconducting Super Collider. Each dipole was intended to have a field strength of 6.6 T over a length of 15 m. Each dipole magnet would bend the 20 TeV proton beam 1.5 mrad with a radius of curvature $\sim$ 10 km (Tooker 1994).

It is straightforward to substitute these quantities to obtain a signal-to-noise estimate using a synchrotron magnet

$$\frac{S}{N} \simeq 15 \left(\frac{B}{6.6\ \mathrm{T}}\right)^2 \left(\frac{l}{15\ \mathrm{m}}\right) \left(\frac{\widetilde{\Delta L}(f_c)}{3\times 10^{-19}\mathrm{m\ Hz}^{-1/2}}\right)^{-1} \left(\frac{t}{6\ \mathrm{d}}\right)^{1/2} . \quad (5.6)$$

We see that by using the weaker though much larger magnet the same result could be achieved after a single day's integration.

5.3 Discussion

We have proposed a straightforward experiment using the extant LIGO testbed interferometer and a large synchrotron magnet to measure the nonlinear interaction between a photons and an external field predicted by QED. In contrast to Delbrück scattering, the experiment is performed for photon energies much less than the electron rest mass, and the signal is not modified by other interactions (scattering off of the nuclei themselves or the electrons surrounding them). The proposed experiment would probe the predictions of QED in an unprecedented way.

Chapter 6

Electromagnetic Shocks in Strong Magnetic Fields

SUMMARY

We examine the propagation of electromagnetic radiation through a strong magnetic field using the method of characteristics. Owing to nonlinear effects associated with vacuum polarization, such waves can develop discontinuities analogous to hydrodynamical shocks. We derive shock jump conditions and discuss the physical nature of these non-linear waves

6.1 Introduction

The nonlinear properties of electromagnetic waves traveling through a magnetized vacuum is of particular interest in the study of neutron stars. Heisenberg & Euler (1936) and Weisskopf (1936) first derived nonlinear corrections to the Maxwell equations of the electromagnetic field. Lutzky & Toll (1959) and Zheleznyakov & Fabrikant (1982) applied the weak-field expansion to show that shock waves can develop in the electromagnetic field. Bialynicka-Birula (1981) used the full expression for the nonlinear correction to the Lagrangian to study the generation of harmonics and other nonlinear phenomena in the propagation of EM radiation.

In this paper, we use the method of characteristics to study the evolution of waves governed by an arbitrary Lagrangian and then apply these techniques to the Heisenberg-Euler-Weisskopf-Schwinger Lagrangian (Heisenberg & Euler 1936, Weisskopf 1936, Schwinger 1951). We derive the shock

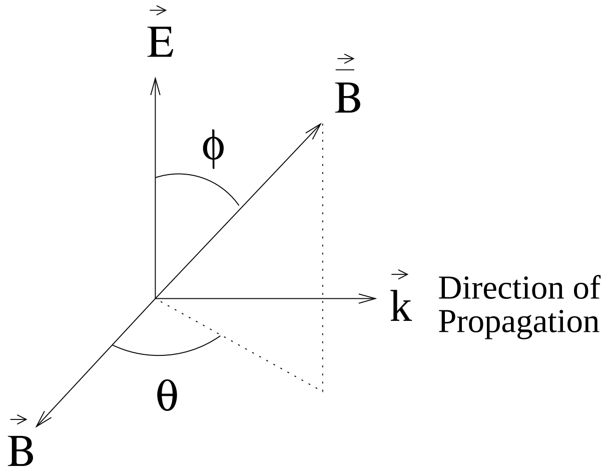

Figure 6.1: Illustration of the field geometry

jump conditions and draw a connection between shock formation and the process of photon coalescence.

6.2 Deriving the Characteristics

We will use the method of characteristics to study the evolution of a disturbance of the electromagnetic field. In general, the relativistic Lagrangian ($\mathcal{L}$) of the electromagnetic field is a function of the two invariants of the field. We follow the notation of Lutzky & Toll (1959) and Heisenberg & Euler (1936) and define

$$I = F_{\mu\nu}F^{\mu\nu} = 2\left(|\mathbf{B}|^2 - |\mathbf{E}|^2\right) \tag{6.1}$$

and

$$K = -\left(\frac{1}{2}\epsilon^{\lambda\rho\mu\nu}F_{\lambda\rho}F_{\mu\nu}\right)^2 = -(4\mathbf{E}\cdot\mathbf{B})^2. \tag{6.2}$$

As illustrated in Figure 6.1, we choose coordinates so that the radiation is polarized in the z-direction and travels along the y-axis toward positive y. The ambient magnetic field makes an angle ϕ with the electric field, and the projection of the magnetic field into $x-y$ plane makes an angle θ with respect to the x-axis (magnetic field of the wave).

With these definitions, the invariants are

$$
\begin{aligned}
I &= 2\left[(\bar{B}\cos\theta\sin\phi + B)^2 + (\bar{B}\sin\theta\sin\phi)^2 + (\bar{B}\cos\phi)^2 - E^2\right] && (6.3)\\
K &= -(4E\bar{B}\cos\phi)^2 && (6.4)
\end{aligned}
$$

where $\bar{B}$ is the strength of the ambient magnetic field, E and B are the strengths of the electric and magnetic fields associated with the radiation.

6.2.1 ϵ, η formalism

We introduce the new coordinates

$$
\begin{aligned}
\epsilon &= y + t\\
\eta &= y - t
\end{aligned} \tag{6.5}
$$

where we set $c \equiv 1$. We characterize the traveling wave by a vector potential with one non-zero component,

$$A_z = \psi(y,t) = \psi(\epsilon,\eta). \tag{6.6}$$

We have assumed that the vector potential has only one independent component which allows us to treat the problem using characteristics. Unfortunately, we cannot follow the interaction between two polarizations which was treated by Bialynicka-Birula (1981).

Using the definition of the vector potential we get

$$
\begin{aligned}
E &= \psi_\eta - \psi_\epsilon\\
B &= \psi_\eta + \psi_\epsilon
\end{aligned} \tag{6.7}
$$

where we have used subscripts to denote partial differentiation. Substituting this into the definitions of I and K, we get

$$
\begin{aligned}
I &= 2(4\psi_\eta\psi_\epsilon + \bar{B}^2 + 2(\psi_\eta + \psi_\epsilon)\bar{B}\cos\theta\sin\phi) && (6.8)\\
K &= -16(\psi_\eta - \psi_\epsilon)^2\bar{B}^2\cos^2\phi. && (6.9)
\end{aligned}
$$

In the (η, ϵ) coordinates Hamilton's principle assumes the simple form (Lutzky & Toll 1959)

$$\frac{\partial}{\partial\epsilon}\left(\frac{\partial\mathcal{L}}{\partial\psi_\epsilon}\right) + \frac{\partial}{\partial\eta}\left(\frac{\partial\mathcal{L}}{\partial\psi_\eta}\right) = 0. \tag{6.10}$$

Since the Lagrangian is a function of I and K alone, we can rewrite this in terms of derivatives of $\mathcal{L}$ with respect to I and K, I and K with respect to ψ_ϵ and ψ_η and finally $\psi_{\epsilon\epsilon}$, $\psi_{\epsilon\eta}$, and $\psi_{\eta\eta}$ by successive applications of the chain rule:

$$
\begin{aligned}
0 &= \frac{\partial \mathcal{L}}{\partial I}\left(\frac{\partial^2 I}{\partial\epsilon\partial\psi_\epsilon}+\frac{\partial^2 I}{\partial\eta\partial\psi_\eta}\right)+\frac{\partial^2\mathcal{L}}{\partial I^2}\left(\frac{\partial I}{\partial\psi_\eta}\frac{\partial I}{\partial\eta}+\frac{\partial I}{\partial\psi_\epsilon}\frac{\partial I}{\partial\epsilon}\right) \qquad (6.11)\\
&\quad+\frac{\partial \mathcal{L}}{\partial K}\left(\frac{\partial^2 K}{\partial\epsilon\partial\psi_\epsilon}+\frac{\partial^2 K}{\partial\eta\partial\psi_\eta}\right)+\frac{\partial^2\mathcal{L}}{\partial K^2}\left(\frac{\partial K}{\partial\psi_\eta}\frac{\partial K}{\partial\eta}+\frac{\partial K}{\partial\psi_\epsilon}\frac{\partial K}{\partial\epsilon}\right)\\
&\quad+\frac{\partial^2\mathcal{L}}{\partial I\partial K}\left(\frac{\partial K}{\partial\epsilon}\frac{\partial I}{\partial\psi_\epsilon}+\frac{\partial I}{\partial\epsilon}\frac{\partial K}{\partial\psi_\epsilon}+\frac{\partial K}{\partial\eta}\frac{\partial I}{\partial\psi_\eta}+\frac{\partial I}{\partial\eta}\frac{\partial K}{\partial\psi_\eta}\right)\\
0 &= a\psi_{\epsilon\epsilon}+b\psi_{\epsilon\eta}+c\psi_{\eta\eta}. \qquad (6.12)
\end{aligned}
$$

where

$$
\begin{aligned}
a &= \frac{\partial^2\mathcal{L}}{\partial I^2}\left(\frac{\partial I}{\partial\psi_\epsilon}\right)^2+\frac{\partial^2\mathcal{L}}{\partial K^2}\left(\frac{\partial K}{\partial\psi_\epsilon}\right)^2+\frac{\partial\mathcal{L}}{\partial I}\frac{\partial^2 I}{\partial\psi_\epsilon^2}+\frac{\partial\mathcal{L}}{\partial K}\frac{\partial^2 K}{\partial\psi_\epsilon^2}\\
&\quad+2\frac{\partial^2\mathcal{L}}{\partial I\partial K}\frac{\partial I}{\partial\psi_\epsilon}\frac{\partial K}{\partial\psi_\epsilon} \qquad (6.13)\\
b &= 2\left[\frac{\partial^2\mathcal{L}}{\partial I^2}\frac{\partial I}{\partial\psi_\eta}\frac{\partial I}{\partial\psi_\epsilon}+\frac{\partial^2\mathcal{L}}{\partial K^2}\frac{\partial K}{\partial\psi_\eta}\frac{\partial K}{\partial\psi_\epsilon}+\frac{\partial\mathcal{L}}{\partial I}\frac{\partial^2 I}{\partial\psi_\eta\partial\psi_\epsilon}+\frac{\partial\mathcal{L}}{\partial K}\frac{\partial^2 K}{\partial\psi_\eta\partial\psi_\epsilon}\right.\\
&\quad\left.+\frac{\partial^2\mathcal{L}}{\partial I\partial K}\left(\frac{\partial I}{\partial\psi_\epsilon}\frac{\partial K}{\partial\psi_\eta}+\frac{\partial I}{\partial\psi_\eta}\frac{\partial K}{\partial\psi_\epsilon}\right)\right] \qquad (6.14)\\
c &= \frac{\partial^2\mathcal{L}}{\partial I^2}\left(\frac{\partial I}{\partial\psi_\eta}\right)^2+\frac{\partial^2\mathcal{L}}{\partial K^2}\left(\frac{\partial K}{\partial\psi_\eta}\right)^2+\frac{\partial\mathcal{L}}{\partial I}\frac{\partial^2 I}{\partial\psi_\eta^2}+\frac{\partial\mathcal{L}}{\partial K}\frac{\partial^2 K}{\partial\psi_\eta^2}\\
&\quad+2\frac{\partial^2\mathcal{L}}{\partial I\partial K}\frac{\partial I}{\partial\psi_\eta}\frac{\partial K}{\partial\psi_\eta} \qquad (6.15)
\end{aligned}
$$

Substituting the definitions of I and K in the field geometry yields

$$
\begin{aligned}
a &= \left[\bar{B}^2\cos^2\theta\sin^2\phi+4\psi_\eta\left(\bar{B}\cos\theta\sin\phi+\psi_\eta\right)\right]\frac{\partial^2\mathcal{L}}{\partial I^2}\\
&\quad-4K\bar{B}^2\cos^2\phi\frac{\partial^2\mathcal{L}}{\partial K^2}-2\bar{B}^2\cos^2\phi\frac{\partial\mathcal{L}}{\partial K}\\
&\quad+16\bar{B}^2\cos^2\phi\left(\bar{B}\cos\theta\sin\phi+2\psi_\eta\right)(\psi_\eta-\psi_\epsilon)\frac{\partial^2\mathcal{L}}{\partial I\partial K} \qquad (6.16)\\
b &= \frac{\partial\mathcal{L}}{\partial I}+2\left[\frac{I}{2}-\left(1-\cos^2\theta\sin^2\phi\right)\bar{B}^2\right]\frac{\partial^2\mathcal{L}}{\partial I^2}\\
&\quad+8K\bar{B}^2\cos^2\phi\frac{\partial^2\mathcal{L}}{\partial K^2}+4\bar{B}^2\cos^2\phi\frac{\partial\mathcal{L}}{\partial K}+2K\frac{\partial^2\mathcal{L}}{\partial I\partial K} \qquad (6.17)
\end{aligned}
$$

$$\begin{aligned}c &= \left[\bar{B}^2\cos^2\theta\sin^2\phi + 4\psi_\epsilon\left(\bar{B}\cos\theta\sin\phi + \psi_\epsilon\right)\right]\frac{\partial^2\mathcal{L}}{\partial I^2} \\ &\quad - 4K\bar{B}^2\cos^2\phi\frac{\partial^2\mathcal{L}}{\partial K^2} - 2\bar{B}^2\cos^2\phi\frac{\partial\mathcal{L}}{\partial K} \\ &\quad + 16\bar{B}^2\cos^2\phi\left(\bar{B}\cos\theta\sin\phi + 2\psi_\epsilon\right)\left(\psi_\epsilon - \psi_\eta\right)\frac{\partial^2\mathcal{L}}{\partial I\partial K}\end{aligned} \quad (6.18)$$

For $\phi = \pi/2$, the equation for the field ψ simplifies considerably,

$$\begin{aligned}0 &= \psi_{\epsilon\epsilon}\left[4\frac{\partial^2\mathcal{L}}{\partial I^2}\left(\psi_\eta^2 + \psi_\eta\bar{B}\cos\theta + \frac{1}{4}\bar{B}^2\cos^2\theta\right)\right] \\ &\quad + \psi_{\epsilon\eta}\left[\frac{\partial\mathcal{L}}{\partial I} + 2\frac{\partial^2\mathcal{L}}{\partial I^2}\left(\frac{1}{2}I - \bar{B}^2\sin^2\theta\right)\right] \\ &\quad + \psi_{\eta\eta}\left[4\frac{\partial^2\mathcal{L}}{\partial I^2}\left(\psi_\epsilon^2 + \psi_\epsilon\bar{B}\cos\theta + \frac{1}{4}\bar{B}^2\cos^2\theta\right)\right]\end{aligned} \quad (6.19)$$

For $\mathcal{L}_{\text{Classical}} = -I/4$, the second derivative of the Lagrangian with respect to I and the all derivatives with respect to K are zero. We obtain $\psi_{\epsilon\eta} = 0$ and recover the result

$$\psi(\epsilon, \eta) = f(\epsilon) + g(\eta) = f(y+t) + g(y-t). \quad (6.20)$$

The terms in this equation correspond physically to ordinary wave propagation in the negative and positive y directions.

Using the quadratic formula, we can factor the differential equation

$$\left(\frac{\partial}{\partial\epsilon} - \rho_+\frac{\partial}{\partial\eta}\right)\left(\frac{\partial}{\partial\epsilon} - \rho_-\frac{\partial}{\partial\eta}\right)\psi = -\psi_\eta\left(\frac{\partial}{\partial\epsilon} - \rho_+\frac{\partial}{\partial\eta}\right)\rho_- \quad (6.21)$$

and

$$\left(\frac{\partial}{\partial\epsilon} - \rho_-\frac{\partial}{\partial\eta}\right)\left(\frac{\partial}{\partial\epsilon} - \rho_+\frac{\partial}{\partial\eta}\right)\psi = -\psi_\eta\left(\frac{\partial}{\partial\epsilon} - \rho_-\frac{\partial}{\partial\eta}\right)\rho_+ \quad (6.22)$$

where

$$\rho_\pm = \frac{-b \pm \sqrt{b^2 - 4ac}}{2a}. \quad (6.23)$$

Looking at Equation 6.21 and Equation 6.22 we define two new coordinates (u, v) such that

$$\epsilon = u + v \text{ and } \eta = -(\rho_+ u + \rho_- v) \quad (6.24)$$

We now define two functions, the Riemann invariants,

$$\psi_+ = \psi_\epsilon - \rho_+\psi_\eta - \int_{v_0}^{v}\psi_\eta\left.\frac{\partial\rho_+}{\partial v}\right|_{v=v'} dv' \quad (6.25)$$

$$\psi_- = \psi_\epsilon - \rho_-\psi_\eta - \int_{u_0}^{u}\psi_\eta\left.\frac{\partial\rho_-}{\partial u}\right|_{u=u'} du' \quad (6.26)$$

which are constant along curves with

$$\frac{\mathrm{d}\eta}{\mathrm{d}\epsilon} = -\rho_\mp(\psi_+, \psi_-; \bar{B}). \tag{6.27}$$

To first order in ψ_η and ψ_ϵ, the field variables of the traveling wave are given in terms of these functions:

$$E = \psi_\eta - \psi_\epsilon = -\frac{(\rho_- - 1)\psi_+ + (\rho_+ - 1)\psi_-}{\rho_- - \rho_+} \tag{6.28}$$

$$B = \psi_\eta + \psi_\epsilon = \frac{(\rho_- + 1)\psi_+ - (\rho_+ + 1)\psi_-}{\rho_- - \rho_+} \tag{6.29}$$

and the characteristic curves are defined in the $y - t$-plane

$$\frac{\mathrm{d}y}{\mathrm{d}t} = \frac{1 - \rho_\mp}{1 + \rho_\mp} = \sigma_\pm. \tag{6.30}$$

Given the specified field configuration, the ψ_+ characteristics travel toward increasing y and the ψ_- ones travel in the opposite direction. We can therefore in this case identify the ψ_+ characteristics with the light travel path

$$\sigma_+ = \frac{1}{n} \tag{6.31}$$

where n is the index of refraction of the magnetized vacuum as discussed in Erber (1966).

In the limit when the electric and magnetic fields due to the radiation may be neglected, we get

$$\rho_\pm = -x \pm \sqrt{x^2 - 1} \tag{6.32}$$

$$\sigma_\pm = -\frac{x + 1 \pm \sqrt{x^2 - 1}}{x - 1 \pm \sqrt{x^2 - 1}} = \mp \frac{\sqrt{x^2 - 1}}{x - 1} \tag{6.33}$$

where

$$x = \left(\frac{\partial \mathcal{L}}{\partial I} + 2\bar{B}^2 \cos^2\theta \sin^2\phi \frac{\partial^2 \mathcal{L}}{\partial I^2} + 4\bar{B}^2 \cos^2\phi \frac{\partial \mathcal{L}}{\partial K} \right) \Bigg/ 2\bar{B}^2 \left(\cos^2\theta \sin^2\phi \frac{\partial^2 \mathcal{L}}{\partial I^2} - 2\cos^2\phi \frac{\partial \mathcal{L}}{\partial K} \right) \tag{6.34}$$

For the weak-field Lagrangian given by Berestetskii, Lifshitz & Pitaevskii (1982),

$$\mathcal{L} = -\frac{1}{16\pi} I + \frac{e^4 \hbar}{180 \times 8\pi^2 m^4 c^7} \left(I^2 - \frac{7}{4} K \right). \tag{6.35}$$

This formalism yields an index of refraction,

$$n = 1 - x^{-1} + \mathcal{O}(x^{-2}) = 1 + \frac{e^4\hbar}{90\pi m^4 c^7}\bar{B}^2(4\cos^2\theta\sin^2\phi + 7\cos^2\phi) \quad (6.36)$$

where we have also used

$$\frac{\partial\mathcal{L}}{\partial I} \gg \bar{B}^2\frac{\partial^2\mathcal{L}}{\partial I^2}, \bar{B}^2\frac{\partial\mathcal{L}}{\partial K}. \quad (6.37)$$

This result agrees with Erber (1966) and Berestetskii, Lifshitz & Pitaevskii (1982).

6.2.2 y, t formalism

The advantage of the ϵ, η formalism is that the field information travels nearly parallel to the coordinate axes; unfortunately, these null axes can obscure the physical processes. The same derivation can proceed similarly for the standard coordinates y, t. In these coordinates the Hamilton's principle assumes the form

$$\frac{\partial}{\partial y}\left(\frac{\partial\mathcal{L}}{\partial B}\right) - \frac{\partial}{\partial t}\left(\frac{\partial\mathcal{L}}{\partial E}\right) = 0. \quad (6.38)$$

where following the previous definitions

$$\psi_y = B \text{ and } \psi_t = -E. \quad (6.39)$$

Taking the partial derivatives again yields an equation of the form,

$$a\psi_{yy} + b\psi_{yt} + c\psi_{tt} = 0 \quad (6.40)$$

where

$$\begin{aligned} a &= \frac{\partial^2\mathcal{L}}{\partial I^2}\left(\frac{\partial I}{\partial B}\right)^2 + \frac{\partial^2\mathcal{L}}{\partial K^2}\left(\frac{\partial K}{\partial B}\right)^2 + 2\frac{\partial^2\mathcal{L}}{\partial I\partial K}\frac{\partial K}{\partial B}\frac{\partial I}{\partial B} + \\ &\quad \frac{\partial\mathcal{L}}{\partial I}\frac{\partial^2 I}{\partial B^2} + \frac{\partial\mathcal{L}}{\partial K}\frac{\partial^2 K}{\partial B^2} &(6.41)\\ &= 4\left[4\left(\bar{B}\cos\theta\sin\phi + B\right)^2\frac{\partial^2\mathcal{L}}{\partial I^2} + \frac{\partial\mathcal{L}}{\partial I}\right] &(6.42)\\ b &= -2\left[\frac{\partial^2\mathcal{L}}{\partial I^2}\frac{\partial I}{\partial E}\frac{\partial I}{\partial B} + \frac{\partial^2\mathcal{L}}{\partial K^2}\frac{\partial K}{\partial E}\frac{\partial K}{\partial B}\right. \\ &\quad + \frac{\partial^2\mathcal{L}}{\partial I\partial K}\left(\frac{\partial K}{\partial E}\frac{\partial I}{\partial B} + \frac{\partial K}{\partial B}\frac{\partial I}{\partial E}\right) + \frac{\partial\mathcal{L}}{\partial I}\frac{\partial^2 I}{\partial E\partial B} \\ &\quad \left. + \frac{\partial\mathcal{L}}{\partial K}\frac{\partial^2 K}{\partial E\partial B}\right] &(6.43) \end{aligned}$$

$$
\begin{aligned}
&= 32E\left(\bar{B}\cos\theta\sin\phi + B\right)\left(\frac{\partial^2\mathcal{L}}{\partial I^2} + 8\frac{\partial^2\mathcal{L}}{\partial I\partial K}\bar{B}^2\cos^2\phi\right) && (6.44)\\
c &= \frac{\partial^2\mathcal{L}}{\partial I^2}\left(\frac{\partial I}{\partial E}\right)^2 + \frac{\partial^2\mathcal{L}}{\partial K^2}\left(\frac{\partial K}{\partial E}\right)^2 + 2\frac{\partial^2\mathcal{L}}{\partial I\partial K}\frac{\partial K}{\partial E}\frac{\partial I}{\partial E}\\
&\quad + \frac{\partial\mathcal{L}}{\partial I}\frac{\partial^2 I}{\partial E^2} + \frac{\partial\mathcal{L}}{\partial K}\frac{\partial^2 K}{\partial E^2} && (6.45)\\
&= 4\Bigg[4E^2\frac{\partial^2\mathcal{L}}{\partial I^2} - \frac{\partial\mathcal{L}}{\partial I} + 8\bar{B}^2\cos^2\phi\,\times\\
&\quad \left(32E^2\bar{B}^2\cos^2\phi\frac{\partial^2\mathcal{L}}{\partial K^2} + 8E^2\frac{\partial^2\mathcal{L}}{\partial I\partial K} - \frac{\partial\mathcal{L}}{\partial K}\right)\Bigg] && (6.46)
\end{aligned}
$$

This equation may be factored yielding

$$\left(\frac{\partial}{\partial y} - \tau_+\frac{\partial}{\partial t}\right)\left(\frac{\partial}{\partial y} - \tau_-\frac{\partial}{\partial t}\right)\psi = -\psi_t\left(\frac{\partial}{\partial y} - \tau_+\frac{\partial}{\partial t}\right)\tau_- \qquad (6.47)$$

and

$$\left(\frac{\partial}{\partial y} - \tau_-\frac{\partial}{\partial t}\right)\left(\frac{\partial}{\partial y} - \tau_+\frac{\partial}{\partial t}\right)\psi = -\psi_t\left(\frac{\partial}{\partial y} - \tau_-\frac{\partial}{\partial t}\right)\tau_+ \qquad (6.48)$$

where

$$\tau_\pm = -\frac{1}{\sigma_\pm} = \frac{-b \mp \sqrt{b^2 - 4ac}}{2a}. \qquad (6.49)$$

where $\sigma_\pm$ are defined as in the previous subsection and τ plays a role analogous to ρ.

As in the (ϵ, η) technique, we define two new coordinates (u, v) such that

$$y = u + v \text{ and } t = -(\tau_+ u + \tau_- v) \qquad (6.50)$$

We now define the Riemann invariants,

$$
\begin{aligned}
\psi_+ &= \psi_y - \tau_+\psi_t - \int_{v_0}^{v}\psi_t\left.\frac{\partial\tau_+}{\partial v}\right|_{v=v'} dv' && (6.51)\\
\psi_- &= \psi_y - \tau_-\psi_t - \int_{u_0}^{u}\psi_t\left.\frac{\partial\tau_-}{\partial u}\right|_{u=u'} du' && (6.52)
\end{aligned}
$$

which are constant along curves with

$$\frac{\mathrm{d}t}{\mathrm{d}y} = -\tau_\mp(\psi_+, \psi_-; \bar{B}). \qquad (6.53)$$

To obtain a cursory understanding of the characteristics of this equation, we expand each of the coefficients about $E, B = 0$ to first order yielding,

$$\begin{aligned} a &= a_0 + a_B \psi_y - a_E \psi_t + \mathcal{O}(B^2) && (6.54)\\ b &= b_0 + b_B \psi_y - b_E \psi_t + \mathcal{O}(B^2) && (6.55)\\ c &= c_0 + c_B \psi_y - c_E \psi_t + \mathcal{O}(B^2). && (6.56) \end{aligned}$$

The coefficients are

$$\begin{aligned} a_0 &= 4\left[4\left(\bar{B}\cos\theta\sin\phi\right)^2 \frac{\partial^2\mathcal{L}}{\partial I^2} + \frac{\partial\mathcal{L}}{\partial I}\right] && (6.57)\\ a_B &= 16\bar{B}\cos\theta\sin\phi\left[3\frac{\partial^2\mathcal{L}}{\partial I^2} + 4\left(\bar{B}\cos\theta\sin\phi\right)^2\frac{\partial^3\mathcal{L}}{\partial I^3}\right] && (6.58)\\ b_E &= 32\bar{B}\cos\theta\sin\phi\left(\frac{\partial^2\mathcal{L}}{\partial I^2} + 8\frac{\partial^2\mathcal{L}}{\partial I\partial K}\bar{B}^2\cos^2\phi\right) && (6.59)\\ c_0 &= -4\left(8\frac{\partial\mathcal{L}}{\partial K}\bar{B}^2\cos^2\phi + \frac{\partial\mathcal{L}}{\partial I}\right) && (6.60)\\ c_B &= -\frac{b_E}{2} && (6.61) \end{aligned}$$

and

$$a_E = b_0 = b_B = c_E = 0. \qquad (6.62)$$

Using this linearization we estimate the magnitude of the inhomogeneous term in Equation 6.47 and Equation 6.48 if we assume $E_t \sim E$ and $B_t \sim B$

$$-\psi_t\left(\frac{\partial}{\partial y} - \tau_\pm\frac{\partial}{\partial t}\right)\tau_\mp = \mathcal{O}(B^2) \qquad (6.63)$$

so we can neglect it to first order.

We estimate the Riemann invariants,

$$\begin{aligned} \psi_+ &= \psi_y - \tau_+\psi_t + \mathcal{O}(B^2) && (6.64)\\ &= B + \tau_+ E + \mathcal{O}(B^2) && (6.65)\\ \psi_- &= \psi_y - \tau_-\psi_t + \mathcal{O}(B^2) && (6.66)\\ &= B + \tau_- E + \mathcal{O}(B^2) && (6.67) \end{aligned}$$

Now taking the limit where E and B themselves may be neglected we have

$$\begin{aligned} \sigma_\pm &= \pm\sqrt{-a_0/c_0}\\ &= \pm\left[\left(4\left(\bar{B}\cos\theta\sin\phi\right)^2\frac{\partial^2\mathcal{L}}{\partial I^2} + \frac{\partial\mathcal{L}}{\partial I}\right) \bigg/ \left(8\bar{B}^2\cos^2\phi\frac{\partial\mathcal{L}}{\partial K} + \frac{\partial\mathcal{L}}{\partial I}\right)\right]^{1/2}\\ &= \mp\frac{\sqrt{x^2-1}}{x-1} && (6.68) \end{aligned}$$

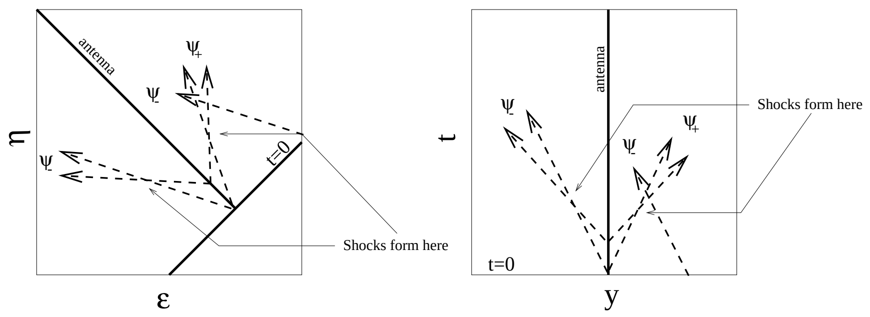

Figure 6.2: Characteristics and Shock Formation

where x is defined in Equation 6.34. We can see from this result that $\tau_+ = -\tau_- + \mathcal{O}(B)$, therefore we have for the two Riemann invariants

$$\psi_\pm = B \pm \tau_+ E + \mathcal{O}(B^2) \tag{6.69}$$

Figure 6.2 depicts how two adjacent characteristic may intersect. Additionally, we see that ψ_- characteristics (*i.e.* lines along which ψ_- is constant) that originate from regions without wave fields cross the ψ_+ characteristics. Therefore, we can argue that $\psi_- = B - \tau_+ E + \mathcal{O}(B^2) = 0$ throughout the region to the right of the antenna because the fields are zero in this region. We can use the same argument for the region to the left of the antenna and find that in general $B = \tau_\pm E + \mathcal{O}(B^2)$ along the $\psi_\pm$ characteristics. Furthermore, to first order, both $\psi_\pm$ are constant along the characteristics; therefore, the slopes of the characteristics which depend only on ψ_+, ψ_- and the constant background field must be constants and the characteristics travel at a constant speed.

Using the figure as a guide, we estimate the distance over which two adjacent characteristics can travel before intersecting is given by

$$\Delta y = c \left(\frac{\partial \tau_\pm}{\partial t} \right)^{-1} = \frac{-2 a_0 \tau_\pm c}{\left(a_B \tau_\pm^2 + c_B \right) B_t - 2 c_B \tau_\pm E_t} \tag{6.70}$$

Where we have use that fact that ψ_+ characteristics travel with velocity $-\tau_- = \tau_+ + \mathcal{O}(B)$.

To work with this equation further, we define an opacity due to shock formation and use $B = \tau_\pm E$. We obtain

$$\kappa \;=\; (\Delta y)^{-1} = \frac{a_B c_0 + c_B a_0}{2 a_0^2 \tau_\pm c} B_t \tag{6.71}$$

$$
\begin{aligned}
&= \pm\frac{a_B c_0 + c_B a_0}{2a_0^2}\sqrt{-\frac{a_0}{c_0}}\frac{B_t}{c} && (6.72)\\
&= \pm 8\bar{B}_B\left(4\frac{\partial^2\mathcal{L}}{\partial I^2}\bar{B}_B^2 + \frac{\partial\mathcal{L}}{\partial I}\right)^{-3/2}\left[\frac{\partial^2\mathcal{L}}{\partial I^2}\frac{\partial\mathcal{L}}{\partial I}\right.\\
&\quad + \left(2\frac{\partial\mathcal{L}}{\partial I}\frac{\partial^2\mathcal{L}}{\partial I\partial K} + 6\frac{\partial^2\mathcal{L}}{\partial I^2}\frac{\partial\mathcal{L}}{\partial K}\right)\bar{B}_E^2 + \left(\frac{\partial\mathcal{L}}{\partial I}\frac{\partial^3\mathcal{L}}{\partial I^3} + \left(\frac{\partial^2\mathcal{L}}{\partial I^2}\right)^2\right)\bar{B}_B^2\\
&\quad \left. + 8\left(\frac{\partial^3\mathcal{L}}{\partial I^3}\frac{\partial\mathcal{L}}{\partial K} + \frac{\partial^2\mathcal{L}}{\partial I^2}\frac{\partial^2\mathcal{L}}{\partial I\partial K}\right)\bar{B}_E^2\bar{B}_B^2\right]\\
&\quad \times\left(8\frac{\partial\mathcal{L}}{\partial K}\bar{B}_E^2 + \frac{\partial\mathcal{L}}{\partial I}\right)^{-1/2}\frac{B_t}{c} && (6.73)
\end{aligned}
$$

where we have defined

$$\bar{B}_B = \bar{B}\cos\theta\sin\phi \text{ and } \bar{B}_E = \bar{B}\cos\phi. \tag{6.74}$$

Where two of these characteristic curves intersect, a shock will form. To move further, we must choose the proper Lagrangian.

6.3 The Non-Linear Lagrangian

Heisenberg & Euler (1936) and Weisskopf (1936) independently derived the effective Lagrangian of the electromagnetic field using electron-hole theory. Schwinger (1951) later rederived the same result using quantum electrodynamics. In rationalized electromagnetic units, the Lagrangian is given by

$$
\begin{aligned}
\mathcal{L} &= -\frac{1}{4}I + \mathcal{L}_1 && (6.75)\\
\mathcal{L}_1 &= \frac{e^2}{hc}\int_0^\infty e^{-\zeta}\frac{\mathrm{d}\zeta}{\zeta^3}\left\{i\zeta^2\frac{\sqrt{-K}}{4}\times\right.\\
&\quad \frac{\cos\left(\frac{\zeta}{B_k}\sqrt{-\frac{I}{2}+i\frac{\sqrt{-K}}{2}}\right) + \cos\left(\frac{\zeta}{B_k}\sqrt{-\frac{I}{2}-i\frac{\sqrt{-K}}{2}}\right)}{\cos\left(\frac{\zeta}{B_k}\sqrt{-\frac{I}{2}+i\frac{\sqrt{-K}}{2}}\right) - \cos\left(\frac{\zeta}{B_k}\sqrt{-\frac{I}{2}-i\frac{\sqrt{-K}}{2}}\right)} && (6.76)\\
&\quad \left. + |B_k|^2 + \frac{\zeta^2}{6}I\right\}. && (6.77)
\end{aligned}
$$

where $E_k = \frac{m^2c^3}{e\hbar}$. In the weak field limit Heisenberg and Euler give

$$\mathcal{L} \approx -\frac{1}{4}I + E_k^2 \frac{e^2}{hc}\left[\frac{1}{180E_k^4}\left(I^2 - \frac{7}{4}K\right) + \frac{1}{630E_k^6}\left(-I^3 + \frac{13}{8}KI\right)\cdots\right] \tag{6.78}$$

We define a dimensionless parameter ξ to characterize the field strength (I)

$$\xi = \frac{1}{E_k}\sqrt{\frac{I}{2}} \tag{6.79}$$

and use the analytic expansion of this Lagrangian for small K derived by Heyl & Hernquist (1997b):

$$\mathcal{L}_1 = \mathcal{L}_1(I,0) + K\left.\frac{\partial \mathcal{L}_1}{\partial K}\right|_{K=0} + \frac{K^2}{2}\left.\frac{\partial^2 \mathcal{L}_1}{\partial K^2}\right|_{K=0} + \cdots \tag{6.80}$$

The first two terms of this expansion are given by

$$\mathcal{L}_1(I,0) = \frac{e^2}{hc}\frac{I}{2}X_0\left(\frac{1}{\xi}\right) \tag{6.81}$$

$$\left.\frac{\partial \mathcal{L}_1}{\partial K}\right|_{K=0} = \frac{e^2}{hc}\frac{1}{16I}X_1\left(\frac{1}{\xi}\right) \tag{6.82}$$

where

$$\begin{aligned} X_0(x) &= 4\int_0^{x/2-1} \ln(\Gamma(v+1))\mathrm{d}v + \frac{1}{3}\ln\left(\frac{1}{x}\right) + 2\ln 4\pi - 4\ln A - \frac{5}{3}\ln 2 \\ &\quad - \left[\ln 4\pi + 1 + \ln\left(\frac{1}{x}\right)\right]x + \left[\frac{3}{4} + \frac{1}{2}\ln\left(\frac{2}{x}\right)\right]x^2 \end{aligned} \tag{6.83}$$

$$X_1(x) = -2X_0(x) + xX_0^{(1)}(x) + \frac{2}{3}X_0^{(2)}(x) - \frac{2}{9}\frac{1}{x^2} \tag{6.84}$$

and

$$X_0^{(n)}(x) = \frac{\mathrm{d}^n X_0(x)}{\mathrm{d}x^n} \tag{6.85}$$

$$\ln A = \frac{1}{12} - \zeta^{(1)}(-1) \approx 0.2488. \tag{6.86}$$

where $\zeta^{(1)}(x)$ is the first derivative of the Riemann Zeta function.

Using these definitions we can derive the various partial derivatives important for shock formation

$$\frac{\partial \mathcal{L}}{\partial I} = -\frac{1}{4} + \frac{e^2}{hc}\left[\frac{1}{2}X_0\left(\frac{1}{\xi}\right) - \frac{1}{4}X_0^{(1)}\left(\frac{1}{\xi}\right)\xi^{-1}\right] \tag{6.87}$$

$$\begin{aligned}
\frac{\partial \mathcal{L}}{\partial K} &= \frac{1}{288}\frac{e^2}{hc}E_k^{-2}\Bigg[-2-\left(18X_0\left(\frac{1}{\xi}\right)-6X_0^{(2)}\left(\frac{1}{\xi}\right)\right)\xi^{-2} \\
&\quad + 9X_0^{(1)}\left(\frac{1}{\xi}\right)\xi^{-3}\Bigg] \qquad (6.88)\\
\frac{\partial^2 \mathcal{L}}{\partial I^2} &= \frac{1}{16}\frac{e^2}{hc}E_k^{-2}\left[-X_0^{(1)}\left(\frac{1}{\xi}\right)\xi^{-3}+X_0^{(2)}\left(\frac{1}{\xi}\right)\xi^{-4}\right] \qquad (6.89)\\
\frac{\partial^2 \mathcal{L}}{\partial I \partial K} &= \frac{1}{384}\frac{e^2}{hc}E_k^{-4}\Bigg[\left(12X_0\left(\frac{1}{\xi}\right)-4X_0^{(2)}\left(\frac{1}{\xi}\right)\right)\xi^{-4} \\
&\quad -\left(3X_0^{(1)}\left(\frac{1}{\xi}\right)+2X_0^{(3)}\left(\frac{1}{\xi}\right)\right)\xi^{-5} \\
&\quad - 3X_0^{(2)}\left(\frac{1}{\xi}\right)\xi^{-6}\Bigg] \qquad (6.90)\\
\frac{\partial^3 \mathcal{L}}{\partial I^3} &= \frac{1}{64}\frac{e^2}{hc}E_k^{-4}\Bigg[3X_0^{(1)}\left(\frac{1}{\xi}\right)\xi^{-5}-3X_0^{(2)}\left(\frac{1}{\xi}\right)\xi^{-6} \\
&\quad - X_0^{(3)}\left(\frac{1}{\xi}\right)\xi^{-7}\Bigg] \qquad (6.91)
\end{aligned}$$

6.4 The Opacity to Shocking

Using the results of the previous section we can expand the opacity (κ) to order e^2/hc, which results in a substantial simplification

$$\begin{aligned}
\kappa &= -32\frac{B_t \bar{B}_B}{c}\left(\frac{\partial^2 \mathcal{L}}{\partial I^2}+\frac{\partial^3 \mathcal{L}}{\partial I^3}\bar{B}_B^2+2\frac{\partial^2 \mathcal{L}}{\partial I \partial K}\bar{B}_E^2\right) \\
&\quad + \mathcal{O}\left[\left(\frac{e^2}{hc}\right)^2\right] \qquad (6.92)
\end{aligned}$$

$$
\begin{aligned}
&= -\frac{B_t \bar{B}_B}{c B_k^2} \frac{e^2}{hc} \Bigg\{ 2 \left[-X_0^{(1)} \left(\frac{1}{\xi}\right) \xi^{-3} + X_0^{(2)} \left(\frac{1}{\xi}\right) \xi^{-4} \right] \\
&\quad + \frac{1}{2} \left(\frac{\bar{B}_B}{B_k}\right)^2 \Bigg[3X_0^{(1)} \left(\frac{1}{\xi}\right) \xi^{-5} - 3X_0^{(2)} \left(\frac{1}{\xi}\right) \xi^{-6} \\
&\quad - X_0^{(3)} \left(\frac{1}{\xi}\right) \xi^{-7} \Bigg] \\
&\quad + \frac{1}{6} \left(\frac{\bar{B}_E}{B_k}\right)^3 \Bigg[\left(12X_0 \left(\frac{1}{\xi}\right) - 4X_0^{(2)} \left(\frac{1}{\xi}\right) \right) \xi^{-4} \\
&\quad - \left(3X_0^{(1)} \left(\frac{1}{\xi}\right) + 2X_0^{(3)} \left(\frac{1}{\xi}\right) \right) \xi^{-5} - 3X_0^{(2)} \left(\frac{1}{\xi}\right) \xi^{-6} \Bigg] \Bigg\} \\
&\quad + \mathcal{O}\left[\left(\frac{e^2}{hc}\right)^2 \right] \qquad (6.93)
\end{aligned}
$$

where we have focused on the propagation of the ψ_+ characteristics. The results for the ψ_- characteristics are identical in magnitude and follow from symmetry.

From the form of Equation 6.73, we see that the opacity is zero for waves traveling with their magnetic field vectors perpendicular to the external field ($\perp$ mode). This result agrees with Bialynicka-Birula's analysis (1981) who found that although a wave in the $\perp$ mode readily generates waves in the $\|$ mode, a wave in the $\perp$ mode does not change to first order. These selection rules result from the CP invariance of QED and may be gleaned from the selection rules for photon splitting (Adler 1971).

Because our analysis tracks the evolution of a single mode, we will calculate the opacity in the limit where the magnetic field of the wave is parallel to the external field. Waves in the $\|$ mode generate higher harmonics in the $\|$ mode but none in the $\perp$ mode. In this limit,

$$
\bar{B}_B = \bar{B} \text{ and } \bar{B}_E = 0 \qquad (6.94)
$$

and Equation 6.73 simplifies further,

$$
\begin{aligned}
\kappa &= \frac{1}{2} \frac{e^2}{hc} \left[X_0^{(1)} \left(\frac{1}{\xi}\right) \xi^{-2} - X_0^{(2)} \left(\frac{1}{\xi}\right) \xi^{-3} + X_0^{(3)} \left(\frac{1}{\xi}\right) \xi^{-4} \right] \frac{1}{c} \frac{B_t}{B_k} \\
&\quad + \mathcal{O}\left[\left(\frac{e^2}{hc}\right)^2 \right] \qquad (6.95)
\end{aligned}
$$

We define a dimensionless auxiliary function $F(\xi)$ to characterize the opacity due to shocking

$$\kappa = -F(\xi)\frac{1}{c}\frac{B_t}{B_k} = -F(\xi) l_B^{-1}. \tag{6.96}$$

We define l_B to be the characteristic length over which the magnetic field of the wave would change by B_k. l_B is positive for sections of the wave where the magnetic field strength increases as its passes a stationary observer, or equivalently in the frame of the wave itself, l_B is positive in sections where the field strength decreases in the direction of propagation.

The function $F(\xi)$ may be expanded in the weak-field limit ($\xi < 0.5$) yielding

$$\begin{aligned} F(\xi) &= -4\frac{e^2}{hc}\frac{1}{\xi}\sum_{j=1}^{\infty} 2^{2j} B_{2(j+1)} \frac{j+1}{2j+1}\xi^{2j} + \mathcal{O}\left[\left(\frac{e^2}{hc}\right)^2\right] && (6.97) \\ &= \frac{e^2}{hc}\left(\frac{16}{45}\xi - \frac{32}{35}\xi^2 + \cdots\right) + \mathcal{O}\left[\left(\frac{e^2}{hc}\right)^2\right] && (6.98) \end{aligned}$$

where B_n denotes the nth Bernoulli number. In the strong-field limit ($\xi > 0.5$), we obtain

$$\begin{aligned} F(\xi) &= \frac{e^2}{hc}\left\{\frac{2}{3}\frac{1}{\xi} + \frac{1}{2}\left(\ln\pi - 2 - \ln\xi\right)\frac{1}{\xi^2}\right. \\ &\qquad \left. + \frac{2}{\xi}\sum_{j=3}^{\infty}\frac{(-1)^{j-1}}{2^j}\frac{4(j-1)-j^2}{j-1}\zeta(j-1)\xi^{-j}\right\} \\ &\qquad + \mathcal{O}\left[\left(\frac{e^2}{hc}\right)^2\right] && (6.99) \end{aligned}$$

where $\zeta(x)$ denotes the Riemann Zeta function and we have used the expansions of Heyl & Hernquist (1997b).

Note from Figure 6.3 that $F(\xi)$ is positive for all field strengths. Thus, from examination of Equation 6.96, we see that the opacity is positive (shocks will develop) in regions where the magnetic field is increasing toward the direction of propagation in the frame of the wave. $F(\xi)$ also reaches a maximum near the critical field strength.

6.5 The Physical Shock: Evolution and Jump Conditions

We expect a shock to develop when and where the value of the Riemann invariant is discontinuous. From Equation 6.67 and using the result $B =$

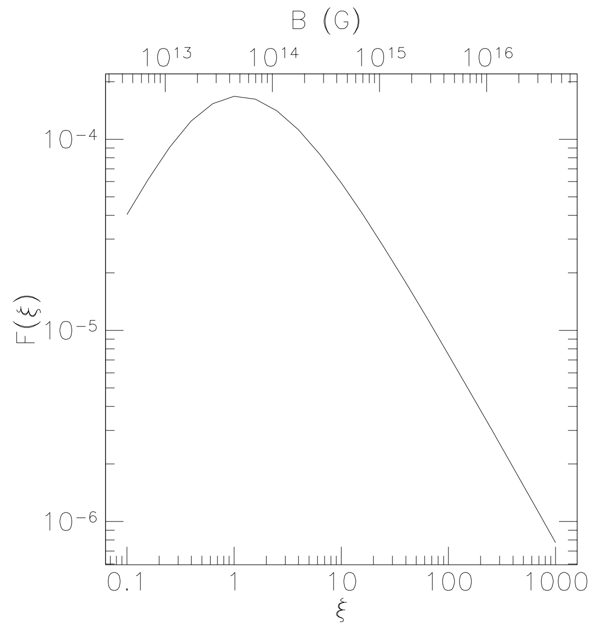

Figure 6.3: The figure depicts the auxiliary function $F(\xi)$ as a function of ξ.

$\tau_\pm E$, we see that the invariants are simply the electric and magnetic field strengths associated with the wave. Figure 6.4 depicts the evolution of the wave. The shock begins to form at an optical depth of one where the field of the wave becomes discontinuous.

As in fluid shocks, dissipative processes prevent the field strengths from becoming double valued. We use the Maxwell equal area prescription (Landau & Lifshitz 1987b) to calculate the shock profile after the characteristic analysis indicates that the field strengths become double valued. We start with a sinusoidal wavefront,

$$B(y,t) = -B_0 \sin(y - \sigma_+ t) = -B_0 \sin \upsilon_0 \tag{6.100}$$

and obtain the following equation for the characteristics

$$\upsilon(\tau) = \upsilon_0 + \tau \sin \upsilon_0 \tag{6.101}$$

in the frame of the wave. Furthermore, for convenience we use the optical depth to shock formation as the time unit.

From Figure 6.4 and Equation 6.101 we see that the wave evolves symmetrically about $\upsilon = \pi$. The position of the shock is given by the location which divides the double-valued regions into equal areas. By symmetry this occurs at $\upsilon = \pi$. The wavefront at $\tau = 2$ is constructed in this manner.

To determine the dissipation of energy by the shock, we calculate the mean power of the wave

$$\begin{aligned} P &= \frac{1}{\pi}\int_0^\pi \sigma_+ B^2 \mathrm{d}\upsilon = \frac{1}{\pi}\sigma_+ B_0^2 \int_0^\pi \sin^2 \upsilon_0 \mathrm{d}\upsilon & (6.102) \\ &= \sigma_+ \frac{B_0^2}{\pi} \int_{\upsilon=0}^{\upsilon=\pi} \sin^2 \upsilon_0 \left(1 + \tau \cos \upsilon_0\right) \mathrm{d}\upsilon_0 & (6.103) \\ &= \sigma_+ \frac{B_0^2}{\pi} \left(\frac{\upsilon_{0,s}}{2} - \frac{1}{4}\sin 2\upsilon_{0,s} + \frac{1}{3}\tau \sin^3 \upsilon_{0,s} \right) & (6.104) \end{aligned}$$

where $\upsilon_{0,s}$ is the smallest solution of

$$\pi = \upsilon_{0,s} + \tau \sin \upsilon_{0,s} \tag{6.105}$$

That is, the shock is located at $\upsilon_s = \pi$. For $\tau \leq 1$ the only real solution to Equation 6.105 is $\upsilon_{0,s} = \pi$. Therefore, before the shock forms the mean power in the wave is simply $\frac{1}{2}\sigma_+ B_0^2$.

Unfortunately, in general this equation can only be solved numerically; however, two limits exist which can be treated analytically. As the shock just begins to develop $\upsilon_0 \approx \upsilon$ near the shock, so $\upsilon_{0,s} \approx \pi$. If we expand

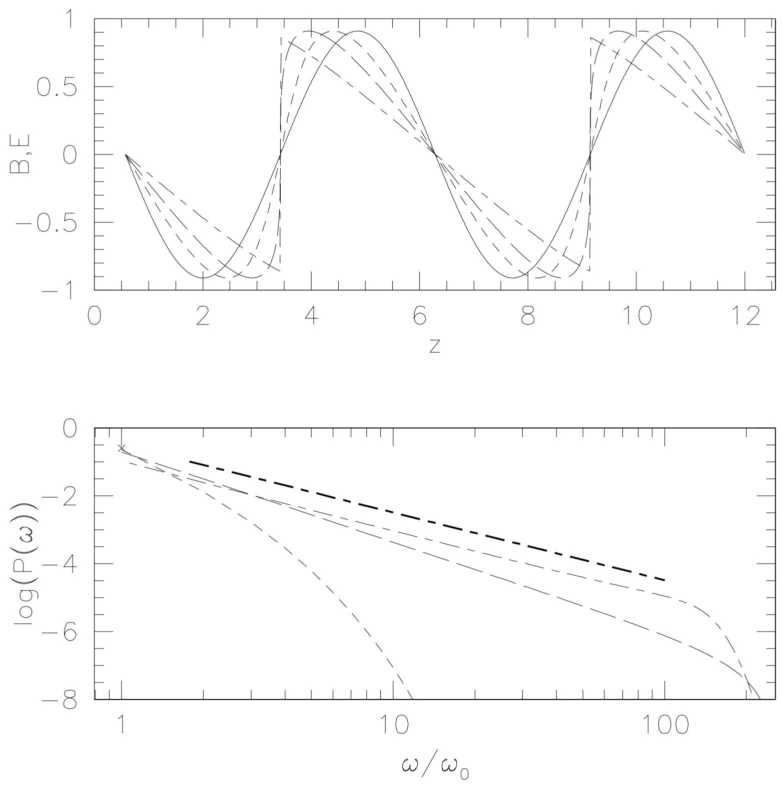

Figure 6.4: Evolution of a wave toward shock formation in the frame of the wave. The upper panel traces the wave in the comoving frame. The lower panel traces the power spectrum of the wave. The successive lines denote original wave, the wave at an optical depth of one-half, at an optical depth of one and at an optical depth of two. The bold line shows a power spectrum of ν^{-2}.

Equation 6.105 about $\upsilon_{0,s} = \pi$, we obtain

$$\upsilon_{0,s} \approx \pi - \sqrt{\frac{6(\tau-1)}{\tau}} \tag{6.106}$$

$$P = \sigma_+ B_0^2 \left[\frac{1}{2} - \frac{8}{5\pi}\sqrt{6}(\tau-1)^{5/2} + \frac{45}{7\pi}\sqrt{6}(\tau-1)^{7/2} + \mathcal{O}(\tau-1)^{9/2} \right] \tag{6.107}$$

We find that as soon as the shock forms at $\tau = 1$, it begins to dissipate energy from the wave. Additionally, the dissipation does not begin abruptly. This first two terms in this expansion are accurate to $\sim 1\%$ for $\tau - 1 \lesssim 0.2$.

At late times, we can find a solution to Equation 6.105 such that $\upsilon_s \approx 0$. Here we obtain

$$\upsilon_{0,s} \approx \frac{\pi}{\tau+1} \tag{6.108}$$

$$P \approx \sigma_+ B_0^2 \frac{\pi^2}{3} \frac{1}{(\tau+1)^2}. \tag{6.109}$$

This expression is accurate to one percent for $\tau > 5$. The upper panel of Figure 6.5 depicts the energy dissipation soon after the shock forms. It is apparent that the dissipation begins smoothly. The lower panel shows the late evolution. The energy of the wave is dissipated within several shock-formation scale-lengths.

In the preceding analysis we have assumed that the field gradients are small both in our linearization and in our selection of the Heisenberg-Euler Lagrangian. Our linearization, specifically the assumption that the gradient of the fields is small relative to the fields breaks down when

$$\lambda_e \frac{\partial B}{\partial z} \sim B \tag{6.110}$$

where λ_e is the Compton wavelength of the electron. The Heisenberg-Euler Lagrangian also breaks down when the field changes by B_k over scales similar to λ_e. In this limit, one must use more powerful techniques, such as the proper-time method (Schwinger 1951) to determine the effective Lagrangian.

When the field changes dramatically over scales similar to λ_e, the wave carries appreciable energy in harmonics with energies greater than $2m_e c^2$ (Figure 6.4). These photons can participate in one-photon pair production (*e.g.* Mészáros 1992), effectively dissipating the wave energy. We estimate

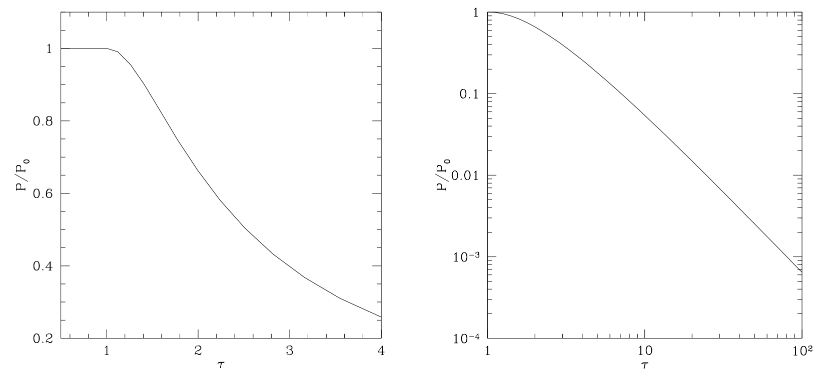

Figure 6.5: The evolution of the power carried by the wave before and after shock formation.

the thickness of the shock to be approximately λ_e. To further understand the properties of the shock, we derive the jump conditions across the shock discontinuity.

We move to the rest-frame of the shock and insist on the continuity of the dual to the field tensor and the energy-momentum tensor:

$$\partial_\nu \mathcal{F}^{\mu\nu} = 0 \text{ and } \partial_\nu \Theta^{\mu\nu} = 0 \tag{6.111}$$

where $\mathcal{F}^{\mu\nu} = \frac{1}{2}\epsilon^{\mu\nu\delta\gamma}F_{\delta\gamma}$ (*e.g.* Landau & Lifshitz 1987a) and

$$\partial_\nu \equiv \frac{\partial}{\partial x^\nu}. \tag{6.112}$$

The first condition follows from the gauge invariance of the fields. The second condition represents the conservation of energy and momentum. These jump conditions are equivalent to those used by Boillat (1972) who insisted that the dual of field tensor be continuous and that the Euler-Lagrange condition be satisfied.

For clarity, in contrast to the analysis of the preceding sections, we examine the energy-momentum and the field tensors of the combined wave and constant background field. Using the techniques outlined in Itzykson & Zuber (1980), we find the energy momentum tensor for non-linear electrodynamics. The canonical tensor ($\widetilde{\Theta}^{\mu\nu}$) is constructed from the Lagrangian by means of a Legendre transformation,

$$\widetilde{\Theta}^{\mu\nu} = \frac{\partial \mathcal{L}}{\partial\left[\partial_\mu A_\rho\right]}\partial^\nu A_\rho - g^{\mu\nu}\mathcal{L} \tag{6.113}$$

where A_ρ is the potential four-vector of the electromagnetic field. We construct the more familiar symmetrized energy-momentum tensor ($\Theta^{\mu\nu}$) by subtracting a total divergence,

$$\begin{aligned}
\Theta^{\mu\nu} &= \frac{\partial \mathcal{L}}{\partial\left[\partial_\mu A_\rho\right]}\partial^\nu A_\rho - g^{\mu\nu}\mathcal{L} - \partial_\rho\left(\frac{\partial \mathcal{L}}{\partial\left[\partial_\mu A_\rho\right]}A^\nu\right) && (6.114)\\
&= \frac{\partial \mathcal{L}}{\partial\left[\partial_\mu A_\rho\right]}\partial^\nu A_\rho - g^{\mu\nu}\mathcal{L} - \frac{\partial \mathcal{L}}{\partial\left[\partial_\mu A_\rho\right]}\partial_\rho A^\nu \\
&\quad - A^\nu\partial_\rho\frac{\partial \mathcal{L}}{\partial\left[\partial_\mu A_\rho\right]} && (6.115)\\
&= \frac{\partial \mathcal{L}}{\partial\left[\partial_\mu A_\rho\right]}F^\nu{}_\rho - g^{\mu\nu}\mathcal{L} && (6.116)
\end{aligned}$$

where the final term of Equation 6.115 is zero by the Euler-Lagrange condition and gauge invariance. Using the definitions of I and K we obtain,

$$\Theta^{\mu\nu} = \left(4\frac{\partial \mathcal{L}}{\partial I}F^{\mu\rho} - 8J\frac{\partial \mathcal{L}}{\partial K}\mathcal{F}^{\mu\rho}\right)F^\nu{}_\rho - g^{\mu\nu}\mathcal{L}. \qquad (6.117)$$

where $J = F_{\mu\nu}\mathcal{F}^{\mu\nu}$.

Simplifying this expression yields,

$$\Theta^{\mu\nu} = -4\frac{\partial \mathcal{L}}{\partial I}F^{\mu\rho}F_\rho{}^\nu - g^{\mu\nu}\left(\mathcal{L} - 2K\frac{\partial \mathcal{L}}{\partial K}\right). \qquad (6.118)$$

which for $\mathcal{L} = -\frac{1}{4}F_{\rho\sigma}F^{\rho\sigma}$, the linear case, yields

$$\Theta^{\mu\nu} = \frac{1}{4}g^{\mu\nu}F_{\rho\sigma}F^{\rho\sigma} + F^{\mu\rho}F_\rho{}^\nu. \qquad (6.119)$$

in agreement with Itzykson and Zuber's (1980) result.

When determining shock jump conditions for a fluid, one calculates the velocity of the discontinuity relative to the rest frame of the fluid. In analogy to a fluid, we can associate the rest frame of the electromagnetic field with the frame in which the energy-momentum tensor is diagonal. This frame exists if either of the two invariants (I and K) is non-zero. In this frame, the electric and magnetic fields are parallel and their magnitudes are given by

$$\begin{aligned}
B^2 &= \frac{1}{4}\left(I + \sqrt{I^2 - K}\right), && (6.120)\\
E^2 &= \frac{1}{4}\left(-I + \sqrt{I^2 - K}\right) && (6.121)
\end{aligned}$$

If we take the fields to point along the x-axis, we obtain

$$\Theta^{00} = -\Theta^{11} = -4\frac{\partial\mathcal{L}}{\partial I}E^2 - \mathcal{L} + 2K\frac{\partial\mathcal{L}}{\partial K}, \tag{6.122}$$

$$\Theta^{22} = \Theta^{33} = -4\frac{\partial\mathcal{L}}{\partial I}B^2 + \mathcal{L} - 2K\frac{\partial\mathcal{L}}{\partial K}. \tag{6.123}$$

To apply this to the geometry of the previous sections (Figure 6.1), we will assume that $K = 0$ and that the shock front is parallel to the $x - z$ plane and traveling toward increasing y.

The geometry leads to the jump conditions:

$$[\Theta^{02}] = 0, [\Theta^{22}] = 0 \text{ and } [\mathcal{F}^{12}] = 0. \tag{6.124}$$

across the shock. We calculate the components of the energy-momentum tensor in the shock frame through a boost. If $K \neq 0$, the Lorentz transformation from the rest frames to the shock frame would include a rotation as well. By boosting the rest frames into the shock frame we get the following jump conditions

$$[\Theta^{02}] = \left[2\gamma^2 v\frac{\partial\mathcal{L}}{\partial I}I\right] = 0 \tag{6.125}$$

$$[\Theta^{22}] = \left[\mathcal{L} - 2\gamma^2\frac{\partial\mathcal{L}}{\partial I}I\right] = 0 \tag{6.126}$$

$$[\mathcal{F}^{12}] = [\sqrt{I/2}\gamma v] = 0 \tag{6.127}$$

where v is the speed that the diagonalizing frame is moving relative to the shock and $\gamma = \left(1 - v^2\right)^{-1/2}$. The three conditions are physically conservation of energy and momentum flux, and the continuity of the electric field parallel to the surface of shock. Analogous jump conditions are given by Landau & Lifshitz (1987b) for relativistic fluid shocks. If we define,

$$e = w - p = -\mathcal{L},\ p = \mathcal{L} - 2\frac{\partial\mathcal{L}}{\partial I}I,\ w = -2\frac{\partial\mathcal{L}}{\partial I}I \text{ and } n = \sqrt{\frac{I}{2}} \tag{6.128}$$

we obtain the following jump conditions

$$[\Theta^{02}] = \left[\gamma^2 v w\right] = 0 \tag{6.129}$$

$$[\Theta^{22}] = \left[p + \gamma^2 v^2 w\right] = 0 \tag{6.130}$$

$$[\mathcal{F}^{12}] = [\gamma v n] = 0 \tag{6.131}$$

Landau & Lifshitz (1987b) give the velocities of the diagonalizing frames relative to the discontinuity

$$v_1 = \sqrt{\frac{p_2 - p_1}{e_2 - e_1}\frac{e_2 + p_1}{e_1 + p_2}} \tag{6.132}$$

$$v_2 = \sqrt{\frac{p_2 - p_1}{e_2 - e_1} \frac{e_1 + p_2}{e_2 + p_1}} \tag{6.133}$$

and the equation of the shock adiabatic

$$\left(\frac{w_1}{n_1}\right)^2 - \left(\frac{w_2}{n_2}\right)^2 + (p_2 - p_1)\left(\frac{w_1}{n_1^2} + \frac{w_2}{n_2^2}\right) = 0 \tag{6.134}$$

where the subscripts 1 and 2 denote conditions on either side of the shock. The equation for the shock adiabatic is automatically satisfied to first order.

Taking Equation 6.132 and Equation 6.133 and assuming that the shock strength is a linear perturbation on the background field we get

$$\begin{aligned}
v_{1,2} &= \sqrt{\left(2I\frac{\partial^2 \mathcal{L}}{\partial I^2} + \frac{\partial \mathcal{L}}{\partial I}\right) \Big/ \frac{\partial \mathcal{L}}{\partial I}} \times \\
&\quad \left\{1 - \frac{1}{2}\Delta I \Big/ \frac{\partial \mathcal{L}}{\partial I}\left[(1 \pm 1)\frac{\partial^2 \mathcal{L}}{\partial I^2} + I\frac{\partial^3 \mathcal{L}}{\partial I^3}\right]\right\} \\
&\quad + \mathcal{O}\left(\frac{B^2}{\bar{B}^2}\right) + \mathcal{O}\left[\left(\frac{e^2}{hc}\right)^2\right], && (6.135) \\
&= \sigma_+ \left[1 + (1 \pm 1)\frac{1 - \sigma^2}{4}\frac{\Delta I}{I} - \frac{1}{2}I\Delta I\frac{\partial^3 \mathcal{L}}{\partial I^3} \Big/ \frac{\partial \mathcal{L}}{\partial I}\right] \\
&\quad + \mathcal{O}\left(\frac{B^2}{\bar{B}^2}\right) + \mathcal{O}\left[\left(\frac{e^2}{hc}\right)^2\right], && (6.136) \\
&= \sigma_+ \left[1 + (1 \pm 1)\frac{1 - \sigma^2}{2}\frac{\Delta B}{\bar{B}} - 4\bar{B}^3\Delta B\frac{\partial^3 \mathcal{L}}{\partial I^3} \Big/ \frac{\partial \mathcal{L}}{\partial I}\right] \\
&\quad + \mathcal{O}\left(\frac{B^2}{\bar{B}^2}\right) + \mathcal{O}\left[\left(\frac{e^2}{hc}\right)^2\right], && (6.137)
\end{aligned}$$

where $\Delta I = I_1 - I_2 > 0, \Delta B = B_1 - B_2 > 0$ and we have used Equation 6.68 to simplify the expression. The upper sign corresponds to the field before the shock passes and the lower sign to the postshocked field. Because both $\frac{\partial^3 \mathcal{L}}{\partial I^3}$ and $\frac{\partial \mathcal{L}}{\partial I}$ are negative we find that $v_2 < \sigma_+$. Furthermore, with the upper sign, the first term linear in ΔI is larger than the second, so $v_1 > \sigma_+$. As a fluid shock, the electromagnetic discontinuity approaches the unshocked field faster than the speed of light in the magnetized vacuum and withdraws from the shocked field subluminally.

6.6 Conclusions

We have derived the characteristic equations for electromagnetic waves in the presence of a strong external magnetic field. By using a analytic expressions for the effective Lagrangian of QED, we have obtained simple expressions to estimate the opacity of waves to shocking for arbitrary magnetic field strengths. After the shock forms, the energy of the disturbance is dissipated with several shock-formation scale lengths. Furthermore, by calculating the shock jump conditions, we find that as shocks in fluids the discontinuities overtake the unshocked field superluminally and recede from the shocked field slower than the speed of light in the magnetized vacuum.

For shocks to form from electromagnetic waves, not only is a strong external field required but also a source of coherent radiation. A prime location for electromagnetic shocks is the vicinity of a neutron star with field strengths approaching and exceeding the critical value and coherent electromagnetic Alfven waves. The study of the nonlinear corrections to the propagation of radiation through a plasma is beyond the scope of this work; however, we expect shock formation to be a hallmark of the nonlinear corrections of quantum electrodynamics and possibly an important process in the energy transmission near neutron stars.

Part II

Magnetic Fields and Atoms

Chapter 7

Magnetically Catalyzed Fusion

SUMMARY

We calculate the reaction cross-sections for the fusion of hydrogen and deuterium in strong magnetic fields as are believed to exist in the atmospheres of neutron stars. We find that in the presence of a strong magnetic field ($B \gtrsim 10^{12}\,G$), the reaction rates are many orders of magnitude higher than in the unmagnetized case. The fusion of both protons and deuterons are important over a neutron star's lifetime for ultrastrong magnetic fields ($B \sim 10^{16}\,G$). The enhancement may have dramatic effects on thermonuclear runaways and bursts on the surfaces of neutron stars.

7.1 Introduction: Atomic Structure in an Intense Magnetic Field

In large magnetic fields a hydrogen atom is compressed both perpendicular and parallel to the field direction. In a sufficiently strong magnetic field ($B \gtrsim 10^{12}$ G), the Schrödinger equation for the dynamics of the electron separates into axial and perpendicular (azimuthal and radial) equations. As the potential is axisymmetric around the direction of the magnetic field, we expect no azimuthal dependence in the ground-state wavefunction of the electron.

In the direction perpendicular to the magnetic field, the wavefunction can be obtained exactly (Landau & Lifshitz 1977). This azimuthal wavefunction is denoted by two quantum numbers n and m. Here we take $n = 0$, as the $n > 0$ solutions are less bound and therefore provide less shielding.

The perpendicular wavefunction has the same form as the Landau wavefunction for an electron in a magnetic field:

$$R_{0m}(\rho, \theta) = \frac{1}{\sqrt{2^{m+1}\pi m! a_H^{m+1}}} \rho^m \exp\left(-\frac{\rho^2}{4a_H^2}\right) e^{im\theta} \tag{7.1}$$

$$R_{0m}^2(\rho) = \frac{(-1)^m}{2\pi m!} \frac{1}{a_H^2} \left(\frac{\mathrm{d}}{\mathrm{d}\beta}\right)^m \left[\exp\left(-\beta\frac{\rho^2}{2a_H^2}\right)\right]\Bigg|_{\beta=1} \tag{7.2}$$

where

$$a_H = \sqrt{\hbar/m_e\omega_H} = \sqrt{\hbar c/|e|H} \tag{7.3}$$

7.1.1 The axial wavefunction

Along the direction of the magnetic field, the electron experiences an effective potential,

$$V_{\mathrm{eff},0m}(z) = \langle R|V(r)|R\rangle = \int_0^\infty -\frac{e^2}{\sqrt{z^2+\rho^2}} R_{0m}^2(\rho) 2\pi\rho \, \mathrm{d}\rho. \tag{7.4}$$

Performing the integral yields

$$\begin{aligned} V_{\mathrm{eff},0m}(z) &= -\frac{e^2}{a_H}\sqrt{\pi/2}\frac{(-1)^m}{m!} \times \\ &\left(\frac{\mathrm{d}}{\mathrm{d}\beta}\right)^m \left[\frac{1}{\sqrt{\beta}} \exp(\beta z^2/2a_H^2) \mathrm{erfc}(\sqrt{\beta}|z|/\sqrt{2}a_H)\right]\Bigg|_{\beta=1} \end{aligned} \tag{7.5}$$

which for large z approaches $-e^2/z$. The Schrödinger equation with this potential is not analytically solvable. We can note certain features of the desired solution. Because, V_{eff} is everywhere finite, both the wavefunction and its first derivative must be continuous. Rather than solve the equation directly, we use a variational principle, which constrains the ground-state wavefunction ($\nu = 0$) along the magnetic field for the given values of n and m. The index ν counts the number of nodes in the axial wavefunction. As with the $n > 0$ states, the $\nu > 0$ states are barely bound compared to the $\nu = 0$ state.

Looking at the radial wavefunction, we take the wavefunction along the z-axis to be a Gaussian as well:

$$Z(z) = \frac{1}{\sqrt[4]{2\pi}\sqrt{a_z}} \exp\left(-\frac{z^2}{4a_z^2}\right) \tag{7.6}$$

We must minimize the integral,

$$I = \langle Z|H_{\rm eff}|Z\rangle = \int_{-\infty}^{\infty} \left[(\hbar^2/2m_e)(\nabla_z Z)^2 + V_{\rm eff} Z^2\right] {\rm d}z \tag{7.7}$$

For this problem the integral is (using the definition of Z and $m = 0$),

$$I = 2\int_0^\infty Z^2 \left[\frac{\hbar^2}{2m_e}\frac{a_H^3 u^2}{4a_z^4} - e^2\sqrt{\pi/2}\exp(u^2/2){\rm erfc}(u/\sqrt{2})\right] {\rm d}u \tag{7.8}$$

where we have substituted $u = z/a_H$. Next, we use the definition of Z,

$$\begin{aligned} I &= 2\Bigg[\frac{\hbar^2}{2m_e}\frac{a_H^3}{4\sqrt{2\pi}a_z^5}\int_0^\infty u^2 \exp\left(-\frac{u^2 a_H^2}{2a_z^2}\right) {\rm d}u \\ &\quad - \frac{e^2}{2a_z}\int_0^\infty \exp(u^2/2)\exp\left(-\frac{u^2 a_H^2}{2a_z^2}\right){\rm erfc}(u/\sqrt{2}){\rm d}u\Bigg]. \end{aligned} \tag{7.9}$$

The first integral is tractable yielding the quantity to be minimized,

$$I = 2\left[\frac{\hbar^2}{16 m_e a_H^2}\frac{1}{\alpha^2} - \frac{e^2}{2a_H}\frac{1}{\alpha}\int_0^\infty \exp\left(\frac{u^2}{2}(1 - 1/\alpha^2)\right){\rm erfc}(u/\sqrt{2})\,{\rm d}u\right], \tag{7.10}$$

with respect to $\alpha = a_z/a_H$. This minimization yields a value of a_z. Table 7.1 lists the results for the minimization for several magnetic field strengths and compares them with the eigenvalues for the energy of the bound state derived by Ruder et al. (1994). Ruder *et al.* use a series of basis functions to solve the Schrödinger equation. Our binding energies fall short of theirs by approximately twenty percent, because we are restricted by our trial wavefunction. We also tried a sum of Gaussians but this added degree of freedom did not yield significantly more tightly bound wavefunctions.

Using the results of the minimization, the electron probability density is

$$\rho(r,z) = \frac{1}{a_H^2 a_z (2\pi)^{3/2}}\exp\left[-\left(\frac{r^2}{2a_H^2} + \frac{z^2}{2a_z^2}\right)\right] \tag{7.11}$$

where we have combined the two Gaussians in a revealing fashion. The quadrapole moment of the distribution is given by $Q = 2a_H^2(\alpha^2 - 1)$. Next we define a quantity

$$n^2 = r^2 + \left(\frac{a_H}{a_z}\right)^2 z^2 = r^2 + \frac{z^2}{\alpha^2} \tag{7.12}$$

and recast the previous equation into the form

$$\rho(r,z) = \frac{1}{a_H^2 a_z (2\pi)^{3/2}}\exp\left(-\frac{n^2}{2a_H^2}\right). \tag{7.13}$$

Table 7.1: The results of the Rayleigh-Ritz minimization. Energies given in Rydbergs (13.6 eV).

	Ruder *et al.*		Our Results			
B (G)	$E_{m=0}$	$E_{m=1}$	$\alpha_{m=0}$	$E_{m=0}$	$\alpha_{m=1}$	$E_{m=1}$
4.7×10^{9}	2.04	1.20	1.14	1.77	1.59	1.15
4.7×10^{10}	4.43	2.93	2.00	4.18	2.65	2.85
4.7×10^{11}	9.45	6.69	3.79	8.91	4.79	6.44
4.7×10^{12}	18.6	13.9	7.77	17.1	9.35	13.0
4.7×10^{13}	-	-	17.3	29.6	20.0	23.6
4.7×10^{14}	-	-	38.1	47.0	46.1	38.1
4.7×10^{15}	-	-	102.	69.6	113.	59.1
4.7×10^{16}	-	-	265.	97.7	288.	84.8

7.1.2 The screening potential

When solving gravitational problems one often looks for electrostatic analogues. Here, we look for a gravitational analogue to an electrostatic problem. The density of the electron is constant on concentric, similar homoemoids. For this density distribution the potential is directly solvable (Binney & Tremaine 1987)

$$\Phi(\vec{x}) = -\pi G \left(\frac{a_2 a_3}{a_1}\right) \int_0^\infty \frac{\psi(\infty) - \psi(m)}{\sqrt{(\tau + a_1^2)(\tau + a_2^2)(\tau + a_3^2)}} \, \mathrm{d}\tau \tag{7.14}$$

where we have the following auxiliary definitions:

$$m^2 = a_1^2 \sum_{i=1}^{3} \frac{x_i^2}{a_i^2 + \tau} \tag{7.15}$$

and

$$\psi(m) = \int_0^{m^2} \rho(m^2) \, \mathrm{d}m^2. \tag{7.16}$$

In our case, we use $G = -e^2$, $a_1 = a_2 = a_H$, $a_3 = a_z$ and

$$\psi(m) = \frac{1}{a_z \pi \sqrt{2\pi}} \left[1 - \exp\left(-\frac{m^2}{2a_H^2}\right)\right]. \tag{7.17}$$

Substituting these results into Equation 7.14 yields

$$\Phi(\vec{x}) = \frac{1}{\sqrt{2\pi}} e^2 \int_0^\infty \frac{\exp\left[-\frac{1}{2}\left(\frac{r^2}{a_H^2+\tau} + \frac{z^2}{a_z^2+\tau}\right)\right]}{(\tau + a_H^2)\sqrt{\tau + a_z^2}} \, \mathrm{d}\tau. \tag{7.18}$$

We change variables to simplify the integral. Using the natural units of the problem, we let $\bar{r} = r/a_H$, $\bar{z} = z/a_H$, and $u = \tau/a_H^2$. This gives the new equation

$$\Phi(\vec{x}) = \frac{e^2}{a_H}\frac{1}{\sqrt{2\pi}}\int_0^\infty \frac{\exp\left[-\frac{1}{2}\left(\frac{\bar{r}^2}{1+u}+\frac{\bar{z}^2}{\alpha^2+u}\right)\right]}{(1+u)\sqrt{\alpha^2+u}}\,\mathrm{d}u \tag{7.19}$$

where we again use the previous definition of α. The potential at the center of the electron cloud $(r = 0, z = 0)$ is given by

$$\Phi(0,0) = \frac{e^2}{a_H}\frac{2}{\sqrt{2\pi}}\frac{\ln\left(\alpha+\sqrt{\alpha^2-1}\right)}{\sqrt{\alpha^2-1}}. \tag{7.20}$$

Moving away from the origin a change of variables is useful when evaluating the integral. Let

$$v = \frac{1}{1+u}. \tag{7.21}$$

The integral becomes

$$\Phi(\vec{x}) = \frac{1}{\sqrt{2\pi}}\frac{e^2}{a_H}\int_0^1 \frac{\exp\left[-\frac{1}{2}\left(\bar{r}^2 v+\bar{z}^2\frac{v}{1+(\alpha^2-1)v}\right)\right]}{\sqrt{(\alpha^2-1)v^2+v}}\,\mathrm{d}v. \tag{7.22}$$

As an example we present results for $B = 9.8 \times 10^{12}$ G. For this field strength $a_H \approx 10^{-12}$ m and $a_z \approx 10^{-11}$ m, so $\alpha = 10$. The range of the nuclear force is approximately 10^{-15} m or $0.001a_H$. Figure 7.1 depicts the potential in units of e^2/a_H for this configuration. The central potential is approximately $0.25e^2/a_H$ and drops quickly in the radial direction. In the axial direction, the potential forms a "core"

The total potential of the electron cloud and the proton may be approximated by the quadrapole formula

$$V(\vec{x}) \approx -\frac{\alpha^2-1}{2}\frac{ea_H^2}{r^3}\left(3\cos^2\phi - 1\right) \tag{7.23}$$

for large separations.

7.1.3 The cloud-cloud potential

When we consider the interaction between the two electron clouds surrounding the protons, we must account not only for their electrical potential but also the antisymmetry of the mutual electron wavefunction. Because of the strong ambient field, we expect that both electron spins will be aligned with

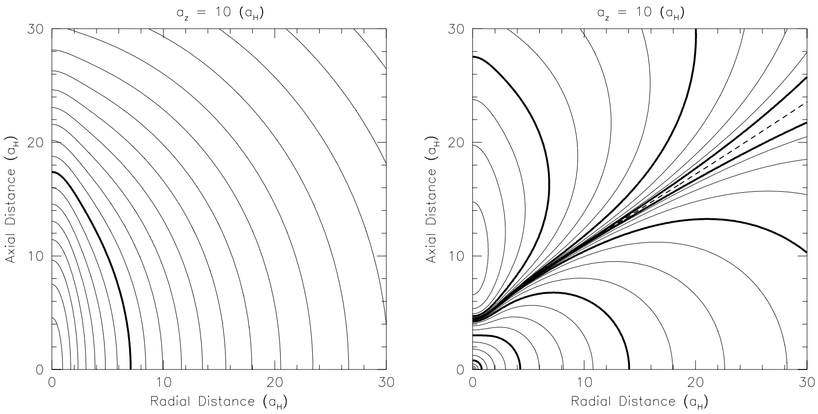

Figure 7.1: The left panel depicts the screening potential as a function of radius and z-position. The right panel shows the total potential experienced by an incoming proton. The dashed contour denotes zero potential. The other contours are logarithmically spaced. In the left panel the bold contour traces a potential of $0.1e^2/a_H$. The contour levels increase toward the center with a spacing of $10^{1/20}$ In the right panel the bold contours trace potentials of $\pm 10^{-4}, 10^{-3} \ldots e^2/a_H$.

the field, so the spatial component of the wavefunction must be antisymmetric. That is,

$$\Psi(\vec{x}_1, \vec{x}_2) = \frac{1}{\sqrt{2}} \left(\psi_1(\vec{x}_1)\psi_2(\vec{x}_2) - \psi_1(\vec{x}_2)\psi_2(\vec{x}_1) \right) \tag{7.24}$$

where

$$\psi_1(\vec{x}) = \sqrt{\rho(\vec{x})} \text{ and } \psi_2(\vec{x}) = \psi_1(\vec{x} - \vec{x}_0) \tag{7.25}$$

with $\rho(\vec{x})$ given by Equation 7.11 and $\vec{x}_0$ is the position of the center of the second electron cloud.

The potential energy of the two electrons is given by (*e.g.* Landau & Lifshitz 1989)

$$\begin{aligned} \Phi_{\rm cc}(\vec{x}_0) &= \int\int \frac{e^2}{|\vec{x}_1 - \vec{x}_2|} |\Psi(\vec{x}_1, \vec{x}_2)|^2 \mathrm{d}^3 x_1 \mathrm{d}^3 x_2 & (7.26) \\ &= A(\vec{x}_0) - J(\vec{x}_0) & (7.27) \end{aligned}$$

where $A(\vec{x}_0)$ and $J(\vec{x}_0)$ are given by

$$A(\vec{x}_0) = \int\int \frac{e^2}{|\vec{x}_1 - \vec{x}_2|} \rho_1(\vec{x}_1)\rho_2(\vec{x}_2) \mathrm{d}^3 x_1 \mathrm{d}^3 x_2 \tag{7.28}$$

$$
\begin{aligned}
J(\vec{x}_0) &= \int\int \mathrm{d}^3x_1 \mathrm{d}^3x_2 \Bigg[\frac{e^2}{|\vec{x}_1 - \vec{x}_2|} \rho_1(\vec{x}_1)\rho_2(\vec{x}_2) \\
&\quad \times \exp\left(-\frac{(x_1 - x_2)x_0 + (y_1 - y_2)y_0}{2a_H^2} - \frac{(z_1 - z_2)z_0}{2a_z^2} \right) \Bigg] \qquad (7.29) \\
&\approx \int\int \mathrm{d}^3x_1 \mathrm{d}^3x_2 \Bigg(\frac{e^2}{|\vec{x}_1 - \vec{x}_2|} \rho_1(\vec{x}_1)\rho_2(\vec{x}_2) \\
&\quad \times \exp\left[-\frac{1}{2} \left(\frac{x_0^2 + y_0^2}{a_H^2} + \frac{z_0^2}{a_z^2} \right) \right] \Bigg) \qquad (7.30) \\
&\approx A(\vec{x}_0) \exp\left[-\left(\frac{r_0^2}{2a_H^2} + \frac{z_0^2}{2a_z^2} \right) \right] \qquad (7.31)
\end{aligned}
$$

where we have used the Gaussian form of $\rho(\vec{x})$ to simplify the expression for $J(\vec{x}_0)$, and to obtain its approximate value we replace $x_1 - x_2$ by x_0 and similarly for the other coordinates.

To calculate the direct term of cloud-cloud potential ($A(\vec{x}_0)$) we will take advantage of the special form of the density distribution given in Equation 7.11. The direct term is in general given by

$$A\left(\vec{x}_0\right) = \int \mathrm{d}^3x_1 \rho\left(\vec{x}_1 - \vec{x}_0\right) \Phi\left(\vec{x}_1\right) \qquad (7.32)$$

which is simply the convolution of the density distribution with the potential. If we perform the Fourier transform of the right-hand side we get

$$A\left(\vec{x}_0\right) = \int \mathrm{d}^3k \widetilde{\rho}\left(\vec{k}\right) \widetilde{\Phi}\left(\vec{k}\right) e^{-i\vec{k}\cdot\vec{x}_0}. \qquad (7.33)$$

Expressing the Poisson equation in Fourier space gives

$$\Phi\left(\vec{x}\right) = -4\pi \int \frac{\mathrm{d}^3k}{(2\pi)^{3/2}} \frac{\widetilde{\rho}\left(\vec{k}\right)}{k^2} e^{-i\vec{k}\cdot\vec{x}}. \qquad (7.34)$$

Because the magnetic field induces the deformation of both electron clouds, the clouds are aligned, and they have the same Fourier transforms; therefore,

$$A\left(\vec{x}_0\right) = -4\pi \int \mathrm{d}^3k \frac{\left[\widetilde{\rho}\left(\vec{k}\right)\right]^2}{k^2} e^{-i\vec{k}\cdot\vec{x}_0}. \qquad (7.35)$$

Because ρ is a three-dimensional Gaussian, so is its Fourier transform; consequently,

$$\left[\widetilde{\rho}\left(\vec{k}\right)\right]^2 = \frac{1}{(2\pi)^{3/2}} \widetilde{\rho}\left(\sqrt{2}\vec{k}\right) \qquad (7.36)$$

Combining Equation 7.35 and Equation 7.36, yields

$$A(\vec{x}_0) = -4\pi \frac{1}{(2\pi)^{3/2}} \int \mathrm{d}^3 k \frac{\widetilde{\rho}\left(\sqrt{2}\vec{k}\right)}{k^2} e^{-i\vec{k}\cdot\vec{x}_0}. \tag{7.37}$$

Performing a change of variables $\vec{l} = \sqrt{2}\vec{k}$ gives

$$A(\vec{x}_0) = -4\pi \frac{1}{\sqrt{2}(2\pi)^{3/2}} \int \mathrm{d}^3 l \frac{\widetilde{\rho}\left(\vec{l}\right)}{l^2} e^{-i\vec{l}\cdot\vec{x}_0/\sqrt{2}}. \tag{7.38}$$

Comparing this equation with Equation 7.34, we get

$$A(\vec{x}_0) = \frac{1}{\sqrt{2}} \Phi\left(\frac{\vec{x}_0}{\sqrt{2}}\right). \tag{7.39}$$

Therefore, the total potential energy between two hydrogen atoms separated by $\vec{x}$ in the magnetic field is given by

$$V(\vec{x}) \approx \frac{e^2}{r} + \frac{1}{\sqrt{2}}\Phi\left(\frac{\vec{x}}{\sqrt{2}}\right)\left(1 - \exp\left[-\left(\frac{r^2}{2a_H^2} + \frac{z^2}{2a_z^2}\right)\right]\right) - 2\Phi(\vec{x}) \tag{7.40}$$

where $\Phi(\vec{x})$ is simply the potential induced by the Gaussian cloud of charge (Equation 7.22).

Far from the atoms ($r \gg \alpha a_H$), the interaction energy may be approximated by the quadrapole-quadrapole energy,

$$V(\vec{x}) \approx \frac{3}{4}\left(\alpha^2 - 1\right)^2 \frac{e^2 a_H^4}{r^5}\left(35\cos^4\phi - 30\cos^2\phi + 3\right). \tag{7.41}$$

where ϕ is the angle relative to the symmetry axis of the atom.

Figure 7.2 and Figure 7.3 depict the total potential energy between two hydrogen atoms in a magnetic field for the same magnetic-field strength as Figure 7.1 ($B = 9.8 \times 10^{12}$G). A comparison of the two figures illustrates that the exchange term provides a slight attractive force between the two electron clouds, because of the anticorrelation of the clouds. At large separations, both potentials are well approximated by the quadrapole-quadrapole formula (Equation 7.41).

7.2 Estimating Reaction Rates

In a fluid state, there will be three possible reaction channels,

- proton-proton dominates in hot, totally ionized gas

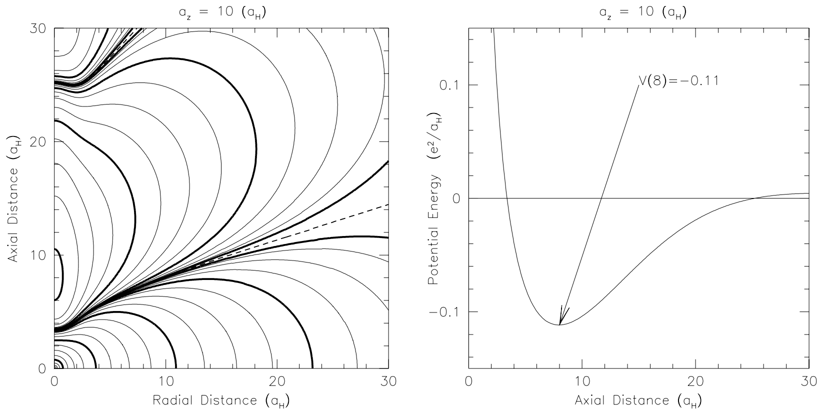

Figure 7.2: The figures depict the total potential energy between two magnetized hydrogen atoms excluding the antisymmetrization energy. For the left panel, the contour spacing is the same as in right panel of Figure 7.1. The right panel illustrates the potential along the axis of the magnetic field.

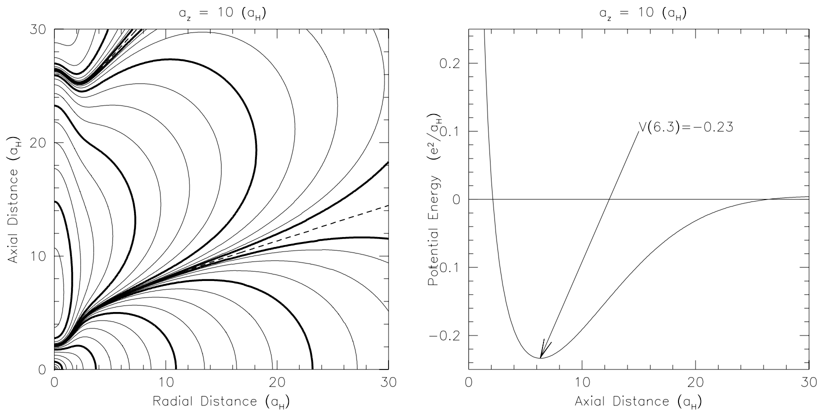

Figure 7.3: The figures depict the total potential energy between two magnetized hydrogen atoms including the antisymmetrization energy. For the left panel, the contour spacing is the same as in right panel of Figure 7.1. The right panel illustrates the potential along the axis of the magnetic field.

- proton-atom dominates in nearly completely ionized gas
- atom-atom dominates in neutral and partially ionized gas

For the first channel, we can use the standard thermonuclear reaction rates (*e.g.* Clayton 1983). For the latter two channels we must include the screening potentials that we calculated in the previous section to determine the potential wall through which the interacting particles must penetrate.

7.2.1 The transmission probability

In the WKB approximation, the probability to traverse through a potential wall is

$$|T|^2 \approx \exp\left(-2\int_{\mathrm{Wall}} \mathrm{d}r\sqrt{\frac{2m}{\hbar^2}\left(V(r)-E\right)}\right) \tag{7.42}$$

$$\approx \exp\left(-2\sqrt{2ma_H}\frac{e}{\hbar}\int_{\mathrm{Wall}} \mathrm{d}u\sqrt{\frac{V(r)-E}{e^2/a_H}}\right) \tag{7.43}$$

$$\approx \exp\left(-26.69B_{12}^{-1/4}\int_{\mathrm{Wall}} \mathrm{d}u\sqrt{\mathcal{V}(u)-\mathcal{E}}\right) \tag{7.44}$$

where B_{12} is the magnetic-field strength in units of 10^{12} G, u is the dimensionless radius r/a_H and $\mathcal{E}$ and $\mathcal{V}$ are the dimensionless energy Ea_H/e^2 and potential.

For the proton-atom channel, the potential includes both that of the nucleus $\mathcal{V} = 1/u$ and the surrounding electron cloud (Equation 7.22). At large distances from the nucleus, $u >> \alpha$, the total potential is well approximated by the quadrapole (Equation 7.23). For the atom-atom channel, the total potential includes contributions from the proton-proton, proton-electron and electron-electron potentials (Equation 7.40), which is well approximated by the quadrapole-quadrapole formula (Equation 7.41) for large separations.

To calculate the transition probability, we use these quadrapole formulae to approximate the potential for $u > 4\alpha$ and for $u < 1/2$, we approximate the potential energy between the electron clouds and the electron clouds and the protons by their central values. This both speeds the calculation and reduces the numerical error.

Figure 7.4 traces the transmission probability for protons to interact with atoms and atoms to interact with atoms at zero relative energy as a function of angle and magnetic field. In the atom-proton case, the protons can most easily penetrate through the mutual potential barrier along

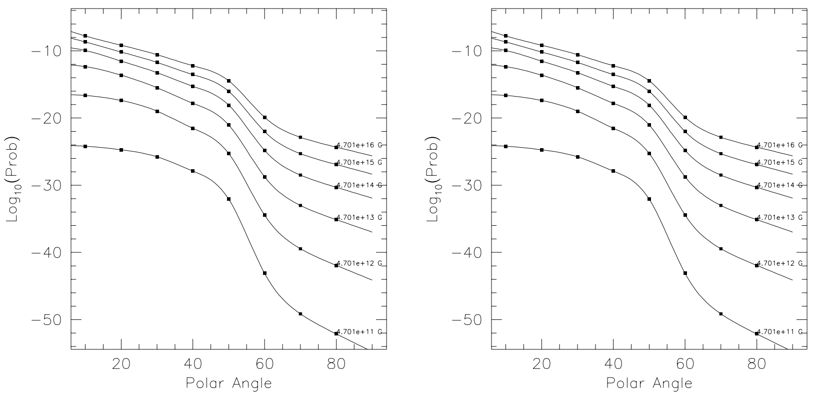

Figure 7.4: The left panel depicts the transmission probability as a function of angle and magnetic field for a proton and an atom to interact at zero relative energy. The right panel depicts the same probability for two atoms. The solid lines trace the probability if the antisymmetrization energy of the electrons is considered. The dashed lines show the probability without antisymmetrization.

the axis of the magnetic field and the penetration probability increases markédly with the strength of the magnetic field. In the atom-atom case, we see that the maximum transmission probability occurs at an angle to the field direction and that with antisymmetrization of the electron density the transmission probability increases dramatically. For the reaction rate estimates that follow we will account for the antisymmetrization energy of the two electron clouds.

To translate this transmission probability into a cross section, we must average $|T|^2$ over a sphere and include the appropriate S-factor for the reaction where $S(E)$ is defined as

$$S(E) = \sigma E |T|^2 \approx S_0(1 + S_1 E) \tag{7.45}$$

In this way, the strong energy dependence of the reaction cross section is removed. For the reaction ${}^1\mathrm{H}(p, e^+\nu)\mathrm{D}$, $S_0 = 4.38 \times 10^{-25}$ MeV-barn and $S_1 = 11.2\ \mathrm{MeV}^{-1}$ at low energies (Bahcall et al. 1982). The reaction of the less abundant deuterons with protons has a much larger S-factor of $S_0 = 2.5 \times 10^{-7}$ MeV-barn and $S_1 = 27.8\ \mathrm{MeV}^{-1}$ (Clayton 1983).

Given these definitions, the reaction proceeds at a rate of

$$r_{12} = (1+\delta_{12})^{-1} n_1 n_2 \langle \sigma v \rangle \tag{7.46}$$

$$= (1+\delta_{12})^{-1} n_1 n_2 \left(\frac{8}{\mu\pi}\right)^{1/2} S_0 (1 + S_1 kT)(kT)^{-1/2} |T|^2 \tag{7.47}$$

where μ is the reduced mass of the reactants, and n_1, n_2 are their number densities. r_{12} has the units of reactions per unit time per unit volume, so we can define a typical timescale for a reactant to be consumed

$$\tau_{12} = n_1 / r_{12}. \tag{7.48}$$

We will use this timescale to assess the effectiveness of the screening in catalyzing the nuclear fusion reactions. We also account for the increasing excitation of the gas as the temperature increases and the onset of thermonuclear reactions above several million degrees.

7.2.2 The ground-state fraction

The screening is much less effective if the electron is in an excited state, so we estimate the fraction of atoms in the ground state by first calculating the ionization equilibrium and then the fraction of neutral atoms in the ground state.

Lai & Salpeter (1995) give the form of the Saha equation for hydrogen atoms, electrons and protons in equilibrium in the presence of a quantizing magnetic field. Throughout this formalism, we use the natural units of the problem, *i.e.* T is the temperature in units of 3.15×10^5 K, M is the mass of the system in units of the electron's mass (1840 for hydrogen and 3670 for deuterium), b is the strength of the magnetic field in units of 2.35×10^9 G and n_g is the number density of the gas in units of $6.76 \times 10^{24}\text{cm}^{-3}$.

We first look at the unexcited hydrogen atom. For the partition function of the ground state in a quantizing magnetic field, Lai & Salpeter (1995) give

$$Z_{\text{ground}}(H) \simeq n_g^{-1/3} \left(\frac{MT}{2\pi}\right)^{1/2} \exp\left(\frac{|E(H)|}{T}\right) Z_\perp \tag{7.49}$$

where $E(H) = -0.16 l^2$ (the ground-state energy of the atom), $l = \ln b$, and

$$Z_\perp = \frac{n_g^{-2/3}}{(2\pi)^2} \int_0^{K_{\perp\max}} 2\pi K_\perp \mathrm{d}K_\perp \exp\left[-\frac{E_\perp(K_\perp)}{T}\right] \tag{7.50}$$

$$Z_\perp \simeq \frac{n_g^{-2/3}}{2\pi} \int_0^{K_{\perp\max}} K_\perp \mathrm{d}K_\perp \exp\left[-\frac{\tau}{2M_\perp T} \ln\left(1 + \frac{K_\perp^2}{\tau}\right)\right] \tag{7.51}$$

$$= n_g^{-2/3} \frac{M_\perp'' T}{2\pi}, \tag{7.52}$$

where $M_\perp = M + \xi b/l$ (with $\xi \simeq 2.8$) and

$$\tau \simeq 0.64\, l\xi b \left[1 + \frac{Ml}{\xi b}\right]^2 . \tag{7.53}$$

Here we have explicitly integrated to $K_{\perp\max}$, so we replace $M'_\perp$ of Lai & Salpeter (1995) with $M''_\perp$,

$$M''_\perp = M'_\perp \left[1 - \left(1 + \frac{K^2_{\perp\max}}{\tau}\right)^{-\tau/2M'_\perp T}\right] \tag{7.54}$$

and $M'_\perp$ is as given by Lai & Salpeter (1995),

$$M'_\perp = M_\perp \left(1 - \frac{2M_\perp T}{\tau}\right)^{-1} . \tag{7.55}$$

As $K_{\perp\max} \to \infty$, $M''_\perp \to M'_\perp$ and we recover the Lai & Salpeter (1995) result. $K_{\perp\max}$ is the upper limit on the perpendicular momentum for the given state. The electron clouds of neighboring atoms should not overlap; otherwise, the gas would become pressure ionized. Therefore, we take the size of the state, $R_K = K_\perp/b < R_g = n_g^{-1/3}$ as the defining condition on $K_{\perp\max}$. We obtain

$$K_{\perp\max} = b n_g^{-1/3}. \tag{7.56}$$

The total partition function of the neutral atom is given by

$$Z(H) = Z_{\rm ground}(H) z_\nu(H) z_m(H) \tag{7.57}$$

where z_ν and z_m are the partition functions for excitations of the ν and m quantum numbers respectively. Lai & Salpeter (1995) argue that the $z_\nu(H) \simeq 1$ as these states are hardly occupied relative to the ionized, $m > 0$ and ground states. For the contribution of the $m > 0$ states to the partition function, they obtain

$$z_m(H) \simeq \left(1 + e^{-b/MT}\right) \sum_{m=0}^{\infty} \frac{M''_{\perp m}}{M''_\perp} \exp\left[-\frac{1}{T}\left(0.16\, l^2 - 0.16\, l_m^2 + m\frac{b}{M}\right)\right], \tag{7.58}$$

where we have several additional auxiliary definitions:

$$l_m = \ln\left(\frac{b}{2m+1}\right), \tag{7.59}$$

and as with ground state we correct for $K_{\perp\max} < \infty$ with

$$M''_{\perp m} = M'_{\perp m} \left[1 - \left(1 + \frac{K^2_{\perp\max}}{\tau}\right)^{-\tau_m/2M'_{\perp m} T}\right] \tag{7.60}$$

and $M'_{\perp m}$ is as given by Lai & Salpeter (1995),

$$M'_{\perp m} = M_{\perp m} \left(1 - \frac{2M_{\perp m}T}{\tau_m}\right)^{-1}. \tag{7.61}$$

$M_{\perp m}$ is given by the following relation

$$1-\frac{M}{M_{\perp m}} \simeq \frac{b}{M}\left[\frac{m+1}{b/M + 0.16\, l_m^2 - 0.16\, l_{m+1}^2} - \frac{m}{b/M + 0.16\, l_{m-1}^2 - 0.16\, l_m^2}\right]. \tag{7.62}$$

and we use the following additional definition

$$\tau_m \simeq 0.64\, l_m (M_{\perp m} - M)\left[1 + \frac{M}{M_{\perp m} - M}\right]^2. \tag{7.63}$$

The ratio of the number of atoms in the ground state to the number of neutral atoms is given by

$$\frac{X_{\text{ground}}(H)}{X(H)} = \frac{Z_{\text{ground}}(H)}{Z(H)} = \frac{1}{z_m(H)}. \tag{7.64}$$

Next we calculate the ionization-recombination equilibrium.

$$\frac{X(H)}{X_p X_e} = \frac{Z(H)}{Z(p)Z(e)} \tag{7.65}$$

$$\simeq n_g \left(\frac{b}{2\pi}\right)^{-2} M''_{\perp} \left(\frac{T}{2\pi}\right)^{1/2} \tanh\left(\frac{b}{2MT}\right) \times \exp\left(\frac{|E(H)|}{T}\right) z_m(H), \tag{7.66}$$

where $X(H) = n(H)/n_g$, $X_p = n_p/n_g$, $X_e = n_e/n_g$ are the number density fractions of the different species.

Combining Equation 7.64 and Equation 7.66 yields the fraction of "shielded" nuclei as a a function of temperature, density and magnetic-field strength. Figure 7.5 depicts the fraction of unexcited hydrogen atoms in the gas as function of temperature for several field strengths and two densities.

7.2.3 Thermonuclear reactions

We parameterize the thermonuclear reaction rates (*e.g.* Clayton 1983) by

$$r_{pp} = 3.06 \times 10^{-37} \text{cm}^3 \text{sec}^{-1} n_p^2 T_6^{-2/3} \exp(-33.71 T_6^{-1/3}) \tag{7.67}$$

$$r_{pD} = 3.28 \times 10^{-19} \text{cm}^3 \text{sec}^{-1} n_p n_D T_6^{-2/3} \exp(-37.11 T_6^{-1/3}). \tag{7.68}$$

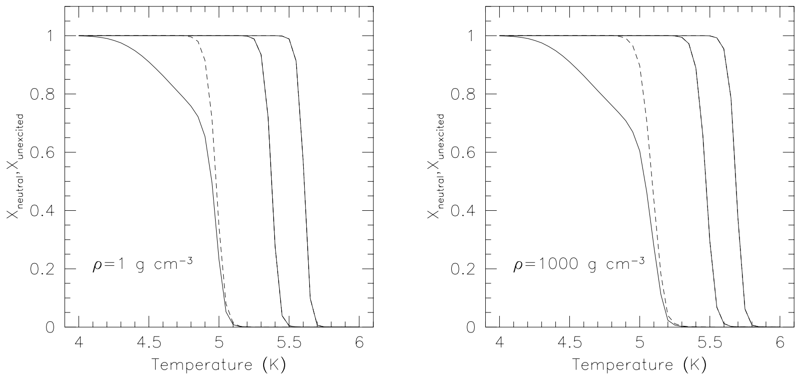

Figure 7.5: The ground-state fraction as a function of temperature, density and magnetic field. The left panel shows the neutral fraction as a dashed line and the unexcited fraction as a solid line for $\rho \sim 1$ g cm^{-3} and $B = 10^{12}, 10^{14}$ and 10^{16} G. The right panel is for a density $\rho \sim 1000$ g cm^{-3}.

The timescale for the exhaustion of a particular reactant becomes

$$\tau_1 = \frac{n_1}{r_{\rm thermo} + r_{\rm magneto}}. \tag{7.69}$$

Figure 7.6 shows the reaction timescale for the consumption of hydrogen and deuterium in the reactions $p(p, e^+\nu)D$ and $D(p,\gamma)^3$He respectively for a magnetic field of 10^{16}G.

Even in this very strong magnetic field, the p-p reaction proceeds only very slowly below temperatures of one million degrees; however, over millions of years, the hydrogen gas would be processed to deuterium and then to helium in such a strong magnetic field. It would provide a steady source of energy, while eroding the storehouse of hydrogen which could potentially fuel a thermonuclear runaway. Relatively, the second reaction proceeds instantly with timescales of less than one year for the interesting range of densities and temperatures.

For the weak fields depicted in Figure 7.7 only the deuterium reaction proceeds at a significant rate.

7.3 Discussion

We find that in strong magnetic fields ($B \gtrsim 10^{12}$ G), the cross-section for nuclear fusion is dramatically larger than in the unmagnetized case. For

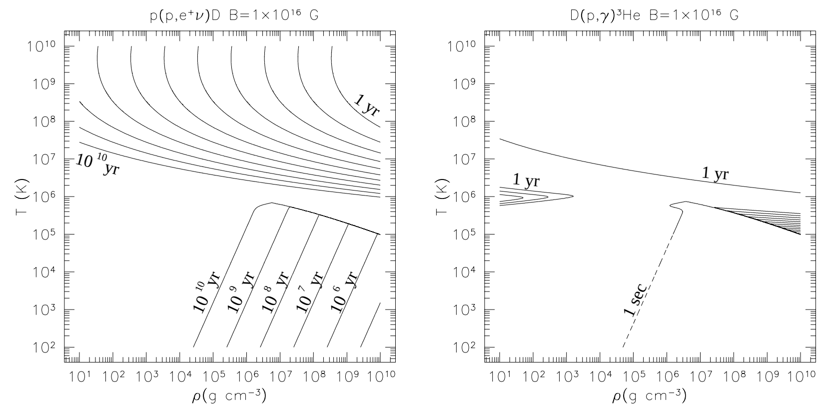

Figure 7.6: The two panels depict the reaction timescale for the reactions $p(p, e^+\nu)D$ and $D(p,\gamma)^3$He for $B = 10^{16}$G over a range of temperatures and densities. The dashed contour traces τ of one second. The solid contours trace loci of timescales ranging from one year to 10^{10} years with a factor of ten in between each contour.

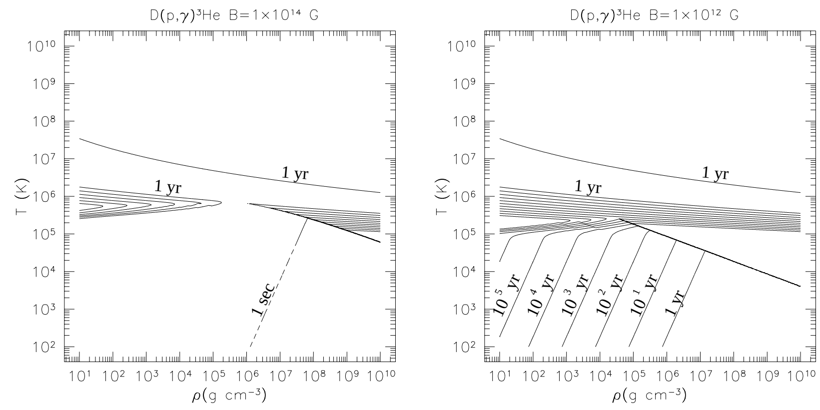

Figure 7.7: The two panes depict the reaction timescale for the reaction $D(p,\gamma)^3He$ for $B = 10^{14}$G and 10^{12}G over a range of temperatures and densities. The dashed contour traces τ of one second. The solid contours trace loci of timescales ranging from one year to 10^{10} years with a factor of ten in between each contour.

these strong fields, deuterons fuse to ^{3}He over short timescales ($\lesssim 10^6$ yr) for the density and temperatures expected on the surface of a neutron star. Because of the inherent weakness of the $p-p$ interaction, the fusion of protons to deuterium is only important over cosmological timescales for ultrastrong fields ($B \gtrsim 10^{16}$ G) in spite of the large enhancement in the cross section of this reaction.

For larger atoms ($Z > 1$), we expect that reaction cross-sections will also be larger in the presence of an intense magnetic field. However, the shielding is unlikely to be as effective as for the $Z = 1$ case, because additional electrons must occupy $m > 0$ levels which are much less effective at screening the nuclear charge.

Chapter 8

Hydrogen and Helium Atoms and Molecules in an Intense Magnetic Field

SUMMARY

We calculate the atomic structure of hydrogen and helium, atoms and molecules in an intense magnetic field, analytically and numerically with a judiciously chosen basis.

8.1 Introduction

The problem of atoms and molecules in a magnetic field is both a classic example of time-independent perturbation theory and a vexing challenge in the study of neutron star and white dwarfs. A sufficiently intense magnetic field cannot be treated perturbatively. The spectra and properties of neutron-star atmospheres depend crucially on magnetic field. Indeed, in the intense magnetic field of a neutron star $B \gtrsim 10^{10}$ G the nucleus rather than the field acts as a perturbation. The electron is effectively confined to move along the magnetic field lines.

This work extends classic analytic work on the one-dimensional hydrogen atom (Loudon 1959; Haines & Roberts 1969) to form the basis of a perturbative treatment of hydrogen in an intense magnetic field. This analytic treatment yields binding energies for $B \gtrsim 10^{12}$ G whose accuracy rivals that of the recent exhaustive treatment of hydrogen in an magnetic field by Ruder et al. (1994) with substantially less computational expense.

We also present a straightforward numerical treatment of the hydrogen atom, the hydrogen molecular ion and the helium atom. The electron wavefunction is expanded in a convenient basis, and the Schrödinger equation may be solved approximately by diagonalizing a suitably calculated matrix. The effective potential between the electrons and between the electrons and the nuclei may be determined analytically, expediting the calculation dramatically.

8.2 The Single Electron Problem

We begin with the problem of a single electron bound by the combined field of an atomic nucleus and strong external magnetic field. The Hamiltonian for the electron is given by

$$H = \frac{\mathbf{P}^2}{2M} - \frac{Ze^2}{r} - \mu \cdot \mathbf{B} \tag{8.1}$$

where we have assumed that the nucleus is infinitely massive, M is the mass of the electron and $\mathbf{P} = \mathbf{p} - e/c\,\mathbf{A}$.

To derive the Schrödinger equation for the electron, we make the replacement $\mathbf{p} = -i\hbar\boldsymbol{\nabla}$. We take the magnetic field to point in the z-direction and choose the gauge where $A_\phi = B\rho/2$, $A_\rho = A_z = 0$ and obtain

$$\left(-\frac{\hbar^2}{2M}\boldsymbol{\nabla}^2 - \frac{i\hbar}{2Mc}B|e|\frac{\partial}{\partial\phi} + \frac{1}{8}\frac{e^2}{Mc^2}B^2\rho^2 - \frac{Ze^2}{r} - \frac{\mu}{s}\sigma_z B - E\right)\psi(1) = 0 \tag{8.2}$$

where 1 denotes the spin and spatial coordinates of the electron *i.e.* $\mathbf{r}_1, \sigma_1$. The spin portion of the wavefunction decouples from the spatial component; therefore, we take the electron spins antialigned with the magnetic field to minimize the total energy, *i.e.* to calculate the ground state.

For $Z = 0$, we recover the equation for a free electron in an external magnetic field which is satisfied by a function of the form

$$\psi_{nmp_z}(\mathbf{r}) = R_{nm}(\rho,\phi)e^{izp_z/\hbar} \tag{8.3}$$

where

$$\begin{aligned} R_{nm}(\rho,\phi) &= \frac{1}{a_H^{|m|+1}|m|!}\left[\frac{(|m|+n)!}{2^{|m|+1}\pi n!}\right]^{1/2} \exp\left(-\frac{\rho^2}{4a_H^2}\right)\rho^{|m|} \times \\ & \quad {}_1F_1(-n, |m|+1, \rho^2/2a_H^2)e^{im\phi}, \end{aligned} \tag{8.4}$$

where $a_H = \sqrt{\hbar/M\omega_H} = \sqrt{\hbar c/|e|B}$ (Landau & Lifshitz 1989), and ${}_1F_1$ is the confluent hypergeometric function.

It is convenient to define a critical field where the energy of the Landau ground state $\hbar\omega_H/2$ equals the characteristic energy of hydrogen e^2/a_0, where the Bohr radius, $a_0 \approx 0.53\mathring{A}$. The transition to the intense magnetic field regime (IMF) occurs at (Canuto & Kelly 1972)

$$B_I = 2m^2 c \left(\frac{e}{\hbar}\right)^3 \approx 4.701 \times 10^9 \text{ G}. \tag{8.5}$$

We will express field strengths in terms of $\beta = B/B_I$.

For $Z \neq 0$, the complete solution may be expanded in a sum of ψ_{nmp_z} since these form a complete set. However, for sufficiently strong fields, one can treat the Coulomb potential as a perturbation and use the ground Landau state with the appropriate m quantum number as the first approximation to the radial wavefunction; this is known as the adiabatic approximation.

Equivalently, the adiabatic approximation assumes that the Coulomb potential does not effectively mix the Landau states, *i.e.*

$$\left|\frac{\langle R_{nm}|V(r)|R_{n'm}\rangle}{E_n - E_n'}\right| \ll 1. \tag{8.6}$$

To determine the validity of the adiabatic approximation we calculate this quantity for the first two Landau states and $m = 0$,

$$\begin{aligned}\left|\frac{\langle R_{00}|V(r)|R_{10}\rangle}{2\alpha^2\beta M c^2}\right| &= \left|\frac{1}{2\alpha^2\beta M c^2}\frac{-Ze^2}{a_H^2}\times\right.\\ &\left.\int_0^\infty \frac{1}{\sqrt{z^2+\rho^2}}\left(1-\frac{\rho^2}{2a_H^2}\right)\exp\left(-\frac{\rho^2}{2a_H^2}\right)\rho\mathrm{d}\rho\right| \qquad (8.7)\\ &\leq \left|\frac{1}{2\alpha^2\beta M c^2}\frac{-Ze^2}{a_H^2}\times\right.\\ &\left.\int_0^\infty \left(1-\frac{\rho^2}{2a_H^2}\right)\exp\left(-\frac{\rho^2}{2a_H^2}\right)\mathrm{d}\rho\right| = \frac{Z}{4}\sqrt{\frac{\pi}{\beta}}. \qquad (8.8)\end{aligned}$$

where $\alpha \approx 1/137$ is the fine structure constant. We find for $\beta = 1000$ ($B = 4.7 \times 10^{12}$ G), that the Coulomb potential mixes the Landau states of hydrogen by at most 1.4 %. For stronger fields, the mixing is even less important.

In the adiabatic approximation, we assume that

$$\psi_{0m\nu}(1) = R_{0m}(\rho,\phi)Z_{m\nu}(z)\chi(\sigma) \tag{8.9}$$

where $Z_{m\nu}(z)$ remains to be determined, ν counts the number of nodes in the z wavefunction, and we expect the axial wavefunctions to be different for different values of the magnetic quantum number m. We will use the notation, $|0m\nu\rangle$, to designate the eigenstates.

For $n = 0$, the functions R_{nm} assume a simple form

$$R_{0m}(\rho,\phi) = \frac{1}{\sqrt{2^{|m|+1}\pi|m|!a_H^{|m|+1}}}\rho^{|m|}\exp\left(-\frac{\rho^2}{4a_H^2}\right)e^{im\phi} \tag{8.10}$$

$$|R_{0m}(\rho,\phi)|^2 = \frac{(-1)^{|m|}}{2\pi|m|!}\frac{1}{a_H^2}\left(\frac{\mathrm{d}}{\mathrm{d}\kappa}\right)^{|m|}\left[\exp\left(-\kappa\frac{\rho^2}{2a_H^2}\right)\right]\Bigg|_{\kappa=1} \tag{8.11}$$

With these assumptions the functions $Z_{\nu m}(z)$ satisfy a one-dimensional Schrödinger equation,

$$(H_z - E)Z = \left[-\frac{\hbar^2}{2M}\frac{\mathrm{d}^2}{\mathrm{d}z^2} + V_{\mathrm{eff},0m}(z) - E_{\nu m}\right]Z_{\nu m}(z) = 0, \tag{8.12}$$

where

$$V_{\mathrm{eff},0m}(z) = \langle R|V(r)|R\rangle = \int_0^\infty -\frac{Ze^2}{\sqrt{z^2+\rho^2}}|R_{0m}(\rho)|^2\,2\pi\rho\,\mathrm{d}\rho. \tag{8.13}$$

Performing the integral yields (Lai, Salpeter & Shapiro 1992; Canuto & Kelly 1972)

$$\begin{aligned} V_{\mathrm{eff},0m}(z) &= -\frac{Ze^2}{a_H}\sqrt{\pi/2}\frac{(-1)^{|m|}}{|m|!}\times \\ &\left(\frac{\mathrm{d}}{\mathrm{d}\kappa}\right)^{|m|}\left[\frac{1}{\sqrt{\kappa}}\exp(\kappa z^2/2a_H^2)\mathrm{erfc}(\sqrt{\kappa}|z|/\sqrt{2}a_H)\right]\Bigg|_{\kappa=1} \end{aligned} \tag{8.14}$$

which for large z approaches $-Ze^2/z$. The Schrödinger equation with this potential is not tractable analytically. We can take one of two paths. First, the potential may be replaced by a simpler yet still accurate function. Second, we attempt to solve the Schrödinger equation numerically.

8.3 Analytic Solution

8.3.1 The Approximate Potential

The potential given in Equation 8.14 for arbitrary m may be approximated to within 30 % over the entire domain by the much simpler form

$$V_{\mathrm{eff},0m}(z) \approx V_{\mathrm{approx},0m}(z) = -\frac{Ze^2}{|z| + k_m a_H} \tag{8.15}$$

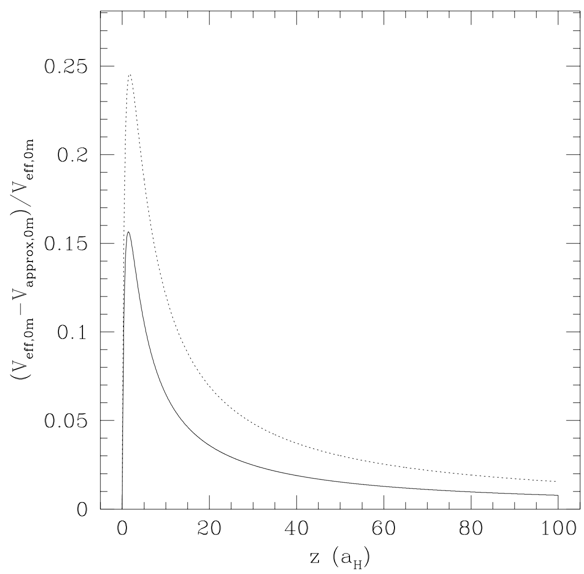

Figure 8.1: The relative difference between the effective potential and the approximated potential. The solid line traces the difference for the $m = 0$ state and the dotted line gives the $m = -1$ state.

where

$$k_m = -\frac{Ze^2}{a_H V_{\text{eff},0m}(0)} = \sqrt{2}\frac{\Gamma(|m|+1)}{\Gamma(|m|+\frac{1}{2})} = \sqrt{\frac{2}{\pi}}\frac{2^{|m|}|m|!}{(2|m|-1)!!} \tag{8.16}$$

The double factorial is defined by $(-1)!! = 1$ and $(2n+1)!! = (2n+1)(2n-1)!!$. For large m, $\frac{1}{2}k_m a_H$ asymptotically approaches $\sqrt{2|m|+1}a_H$, the mean radius of a Landau orbital.

As we see from Figure 8.1, the relative difference between the two expressions is largest near $z = k_m a_H$. For $m = 0$, the difference is greater than 5 % from $z = 0.1$ to $z = 10$. We do not expect this approximation to yield eigenvalues accurate to better than $\sim 10\%$ for wavefunctions peaked in this range.

We obtain the following eigenvalue equation with the approximated potential,

$$\left[-\frac{\hbar^2}{2M}\frac{\mathrm{d}^2}{\mathrm{d}z^2} - \frac{Ze^2}{|z| + k_m a_H} - E_{0m\nu}\right] Z(z) = 0. \tag{8.17}$$

This equation is nearly identical to the Schrödinger equation with a Coulomb potential; therefore, we treat it as a Coulomb problem by using the natural units (Bohr radii for length and Rydbergs for energy),

$$z = \frac{\lambda\!\!\!^{-}_e}{\alpha}\zeta \text{ and } \epsilon = \frac{2E}{\alpha^2 M c^2} \tag{8.18}$$

which yields

$$\left[\frac{\mathrm{d}^2}{\mathrm{d}\zeta^2} + \left(\epsilon + \frac{2Z}{|\zeta| + \zeta_m}\right)\right] Z(\zeta) = 0. \tag{8.19}$$

where $\zeta_m = k_m\sqrt{1/2\beta}$

Again as in the Coulomb problem, we perform the following substitutions

$$n = \frac{1}{\sqrt{-\epsilon}} \text{ and } \xi = \frac{2\zeta}{n}, \tag{8.20}$$

yielding,

$$\left[\frac{\mathrm{d}^2}{\mathrm{d}\xi^2} + \left(-\frac{1}{4} + \frac{nZ}{|\xi| + \xi_m}\right)\right] Z(\xi) = 0. \tag{8.21}$$

This equation may be solved in terms of Whittaker's functions (Abramowitz & Stegun 1970). First, we have

$$\begin{aligned} Z_1(\xi) &= A_\pm M_{nZ,1/2}(|\xi| + \xi_m) \\ &= A_\pm(|\xi| + \xi_m)\ {}_1F_1(1 - nZ, 2, |\xi| + \xi_m) e^{-(|\xi|+\xi_m)/2} \end{aligned} \tag{8.22}$$

where $A_\pm$ are the normalization constants for $\xi > 0$ and $\xi < 0$ respectively. Unless nZ is an integer, these solutions tend to infinity as ξ goes to infinity.

As with the equation for an unmagnetized Coulomb potential, there exists an additional set of solutions. For the three-dimensional Coulomb problem, this solution diverges at the origin and is unphysical. However, here we can obtain a well behaved solution. By the method of reduction of order, we obtain the alternative solutions,

$$\begin{aligned} Z_2(\xi) &= A_\pm W_{nZ,1/2}(|\xi| + \xi_m) \\ &= A_\pm(|\xi| + \xi_m)\ {}_1F_1(1 - nZ, 2, |\xi| + \xi_m) e^{-(|\xi|+\xi_m)/2} \times \\ &\quad \int^{|\xi|+\xi_m} \frac{e^t}{\left(t\ {}_1F_1(1 - nZ, 2, t)\right)^2} \mathrm{d}t. \end{aligned} \tag{8.23}$$

These solutions agree with earlier treatments of the one-dimensional hydrogen atom (Loudon 1959Haines & Roberts 1969). For integer values of nZ, the integral in Equation 8.23 diverges; therefore, the eigenvalues differ from those of the unmagnetized Coulomb potential. Additionally for the unmagnetized Coulomb potential, $\xi_m = 0$ and the prefactor of $(|\xi| + \xi_m)$ is absent. We find that in this case, this wavefunction diverges as ξ^{-1} near the origin and only the counterparts of the states given by Equation 8.22 are physical.

The solutions to Equation 8.17 will be made of a linear combination of Z_1 and Z_2. For a given magnetic quantum number m, the excitations along the magnetic field axis will be denoted by ν with $\nu = 0$ being the ground state. Determining the ground eigenvalue of Equation 8.21 for a given value of ξ_m proceeds in reverse. Since the ground state is even, we have $A_+ = A_-$ and $Z'(0) = 0$. One first selects a value for $0 < nZ < 1$. To have the correct behavior as $z \rightarrow \infty$, we perform the integral of Equation 8.23 from $|\xi| + \xi_m$ to ∞ and calculate $Z_{m0}(\xi)$ for $\xi_m = 0$.

With the calculated function, one can determine where $Z'_{m0}(\xi) = 0$ and use this as the value of ξ_m corresponding to the eigenvalue nZ. The value of ξ_m is simply related to the field strength,

$$\beta = \frac{2k_m^2}{\xi_m^2}(-\lambda) \tag{8.24}$$

8.3.2 First-order Binding Energies

As an example we take $Z = 1$ and $n = 1/\sqrt{15.58}$. This corresponds to a bound state ($|000\rangle$) with an energy of 15.58 Ry. We find $\xi_0 = 0.141$ which yields $\beta = 1000$. For $\beta = 1000$, Ruder et al. (1994) obtain a binding energy for the $m = 0, \nu = 0$ state of 18.60986 Ry. However, it is straightforward to improve upon our estimate of the binding energy by treating the small difference between the approximate and effective potential as a perturbation. We obtain

$$E_{m0}^{(1)} = \langle Z_{m0} | H' | Z_{m0} \rangle \tag{8.25}$$

where $H' = V_{\text{eff}} - V_{\text{approx}}$. We then obtain the binding energy to first order of 18.48 Ry for $\beta = 1000$.

This technique may also be applied to states with $m < 0$ by using the appropriate value for k_m in Equation 8.17. For example, also for $\beta = 1000$ and $m = -1$ ($|0-10\rangle$), we obtain the zeroth order binding energy of 10.45 Ry and the first-order corrected value of 13.71 Ry compared to the result of Ruder et al. (1994) of 13.90394 Ry. Since Equation 8.15 is a better approximation to the effective potential for electrons in the $m = 0$ state than in $m > 0$ states we obtain eigenvalues to first order within 0.7 % of

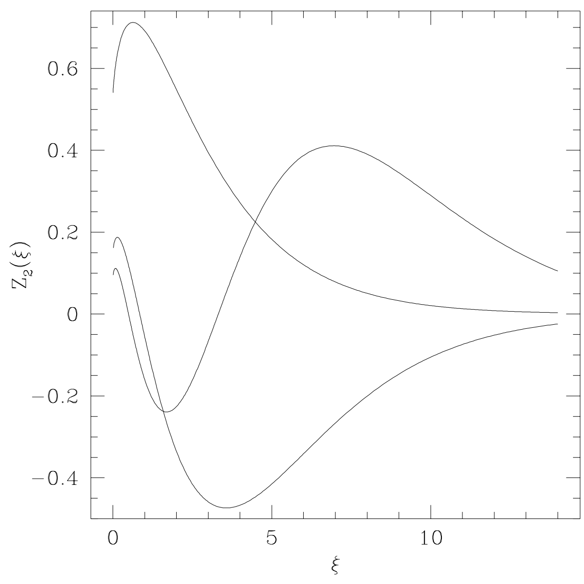

Figure 8.2: The function $Z_2(\xi)$ for $\xi_0 = 0$ for $nZ = 1/2, 3/2, 5/2$.

the fully numerical treatment for $\beta \geq 1000$ for these states (compared to within 1.4 % for $m = -1$ states).

To calculate the wavefunctions with $\nu > 0$, we calculate $Z_2(\xi)$ for $nZ > 1$ and use the first extremum or zero of $Z_2(\xi)$ as the value of ξ_0 for the even and odd solutions respectively. Figure 8.2 depicts $Z_2(\xi)$ for several values of nZ. For nZ between k and $k+1$, $Z_2(x)$ has k zeros and $k+1$ extrema. Therefore, we find that the $\nu > 0$ states have zeroth-order binding energies of fractions of a Rydberg. The calculation of $Z_2(\xi)$ is complicated by the fact that the function $Z_1(\xi)$ also has zeros in the range of integration from ξ to ∞ which make Equation 8.23 ill defined. To pass over the singularities in the integrand, we integrate the differential equation 8.21 directly.

For smaller values of nZ in the range k to $k+1$, the first zeros and extrema approach $\xi = 0$. Therefore, for larger values of β, the zeroth order eigenvalues of the $\nu > 0$ spectrum approach the Bohr energies. The energies of the odd states approach the Bohr energies from below (*i.e.* they are more weakly bound), and the even states with the same number of nodes are yet more weakly bound (Haines & Roberts 1969).

Our first-order adiabatic approximation is less accurate for smaller field strengths. For $\beta = 100$ and $m = 0$ ($|000\rangle$), we obtain a first-order corrected eigenvalue of 9.348 Ry compared to the numerically derived value of 9.4531 Ry (a difference of 1.1 %). However, for fields of $B > 5 \times 10^{11}$ G, the wavefunctions and binding energies derived in this section for $m < 3$ and arbitrary ν are sufficiently accurate for all but the most precise analyses.

8.3.3 Perturbed Wavefunctions

To obtain first order corrections to the wavefunctions $Z_{m\nu}$ and second order corrections to the binding energies, we follow the standard techniques for time-independent perturbation theory (Bransden & Joachain 1989). We must calculate the following quantities

$$H'_{\nu\mu} = \langle Z_{m\nu} | H' | Z_{m\mu} \rangle \tag{8.26}$$

for a particular value of β. Since both V_{eff} and V_{approx} are symmetric about $z = 0$, $H'_{\nu\mu}$ is zero for ν odd and μ even.

We obtain

$$Z^{(1)}_{m\nu} = \sum_{\mu \neq \nu} \frac{H'_{\mu\nu}}{E^{(0)}_\nu - E^{(0)}_\mu} Z^{(0)}_{m\mu} \tag{8.27}$$

and

$$E^{(2)}_{m\nu} = \sum_{\mu \neq \nu} \frac{|H'_{\mu\nu}|^2}{E^{(0)}_\nu - E^{(0)}_\mu} \tag{8.28}$$

For $\beta = 1000$, the mixing among the ν states is on the order of a few percent. The second order corrections to the binding energies for the ground ($\nu = 0$) state is 10^{-3} times the first order correction. For the excited states with $\nu < 6$ the second order correction is less than six percent of the first-order correction; we quote the binding energies to first order for the several of the most bound levels of hydrogen for $\beta \geq 1000$ in Table 8.1 and depict the wavefunctions to zeroth order for $\beta = 1000$ in Figure 8.3.

8.4 Numerical Solution

8.4.1 The Basis Set

We can make substantial progress by carefully selecting a basis to expand the solutions $Z_{\nu m}$. Specifically, we choose

$$Z_{\mu m}(z) = \sum_{k=0}^{\infty} A_{\mu m k} \mathcal{G}_k(z) \tag{8.29}$$

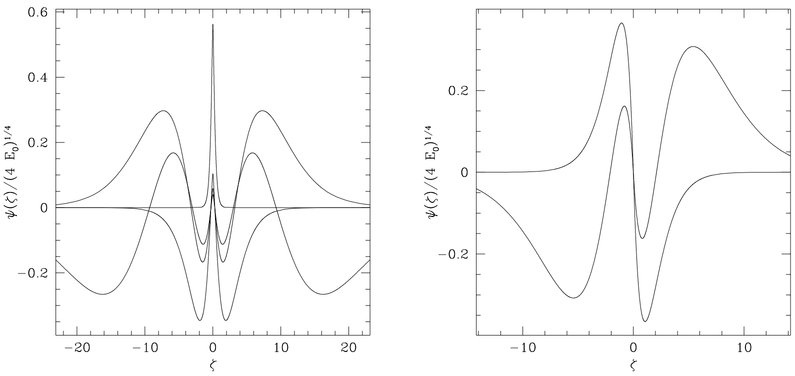

Figure 8.3: The axial wavefunctions of hydrogen in an intense magnetic field (analytic calculation) for $\beta = 1000$. The left panel depicts the first four even states with axial excitations ($|000\rangle, |002\rangle, |004\rangle, |006\rangle$). The right panel shows the first two odd states ($|001\rangle, |003\rangle$).

Table 8.1: The zeroth and first-order binding energies of hydrogen in an intense magnetic field in Rydberg units

	$\|000\rangle$		$\|0-10\rangle$		$\|0-20\rangle$	
β	E_0	E_1	E_0	E_1	E_0	E_1
1×10^3	15.58	18.48	10.45	13.71	8.779	11.76
2×10^3	18.80	22.26	12.81	16.73	10.83	14.46
5×10^3	23.81	28.09	16.57	21.51	14.12	18.73
1×10^4	28.22	33.19	19.94	25.73	17.10	22.55
2×10^4	33.21	38.91	23.81	30.53	20.56	26.93
5×10^4	40.75	47.49	29.76	37.81	25.91	33.61
1×10^5	47.20	54.76	34.95	44.08	30.60	39.40

	$\|001\rangle$		$\|002\rangle$	
β	E_0	E_1	E_0	E_1
1×10^3	0.9401	0.9888	0.5841	0.6215
2×10^3	0.9559	0.9935	0.6062	0.6322
5×10^3	0.9710	0.9970	0.6329	0.6560
1×10^4	0.9790	0.9983	0.6518	0.6730
2×10^4	0.9849	0.9990	0.6684	0.6880
5×10^4	0.9903	0.9996	0.6885	0.7060
1×10^5	0.9931	0.9998	0.7027	0.7188

where

$$\mathcal{G}_k(z) = \frac{1}{(2\pi)^{1/4}\sqrt{a_Z 2^k k!}} H_k\left(\frac{z}{\sqrt{2}a_Z}\right) \exp\left(-\frac{z^2}{4a_Z^2}\right). \tag{8.30}$$

$H_k(z)$ are the Hermite polynomials which are orthogonal on the interval $-\infty$ to ∞ with the weighting function $\exp(-z^2)$. The $\mathcal{G}_k$ are the solutions to the Schrödinger equation for a harmonic oscillator potential; consequently, they provide a complete set for expanding the functions $Z_{\nu m}(z)$.

To obtain the coefficients in the expansion, we calculate the matrix

$$M_{kl} = \langle \mathcal{G}_k | H_z | \mathcal{G}_l \rangle \tag{8.31}$$

which is a function of a_Z and the azimuthal state given by m. We calculate this matrix for $k, l < N$ ($N = 5 - 50$) and diagonalize it. The eigenvalues of this matrix (λ_ν) are $E_{\nu m}$, and the eigenvectors are the coefficients $A_{\nu m k}$ in Equation 8.29. Additionally, the functions $Z_{\nu m}(z)$ and $\mathcal{G}_k(z)$ have definite parity; consequently, for even parity solutions to Equation 8.12, only the elements of M_{kl} with k and l even need to be calculated. This reduces the size of the matrix from N^2 to $N^2/4$.

Because the number of basis functions used is not infinite, we cannot expect the expansion to span the Hilbert space of solutions to Equation 8.12. To estimate the solution, we vary a_Z to minimize the eigenvalue λ_ν corresponding to the bound state that we are interested in. By using an expansion of the form Equation 8.29, the binding energies and wavefunctions may be estimated for excited states along the z-axis.

Although the functions $\mathcal{G}_k$ satisfy a much different equation from Equation 8.12, if sufficiently many Gauss-Hermite functions are included, we can obtain highly accurate eigenvalues and eigenvectors. For the ground state ($|000\rangle$) with the first 31 $\mathcal{G}_k$, we obtain a binding energy of 18.5579 Ry at $\beta = 1000$, within a factor of 3×10^{-3} of the result of Ruder *et al.* , 18.60986 Ry. The results are equally accurate for the first excited state ($|001\rangle$); however, states with more nodes require additional terms in the expansion to achieve the same accuracy. Figure 8.4 compares the zeroth-order analytic wavefunction with the numerical wavefunction determined by this technique.

Obtaining an additional few parts per thousand in accuracy can only justify a portion of the additional computation required for this numerical technique; however, this technique may be applied to solve the Schrödinger equation for potentials more complicated than Equation 8.14.

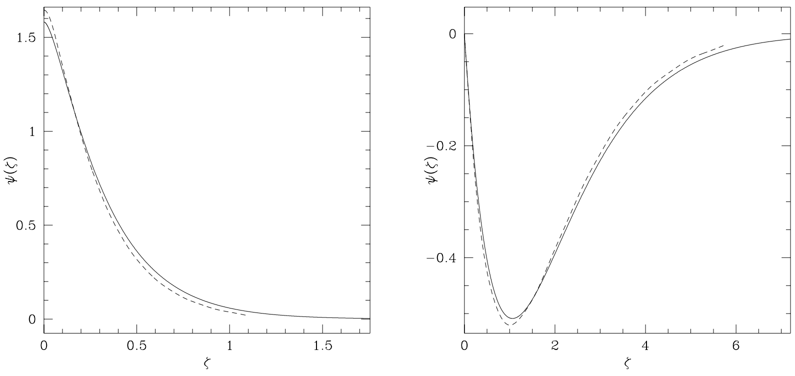

Figure 8.4: A comparison of numerical and analytic wavefunctions for hydrogen. Both panels are for $\beta = 1000$. The left panel displays the state $|000\rangle$, and the right shows $|001\rangle$. The dashed line traces the numerical results with the first 31 $\mathcal{G}_k$. The solid line traces the zeroth-order analytic solutions.

8.4.2 The H_2^+ molecule

Before proceeding to the multi-electron problem, we study the binding energy of the H_2^+ molecule in an intense magnetic field. This system retains the symmetry under parity of hydrogen, so the numerical technique may be applied directly with only two alterations.

The effective potential is now given by

$$V_{\text{eff},0m,\text{H}_2^+}(z) = V_{\text{eff},0m}(z+a) + V_{\text{eff},0m}(z-a) \tag{8.32}$$

and we must vary the internuclear separation $2a$ to find the minimum binding energy for the entire system (the Born-Oppenheimer approximation, *e.g.* Bransden & Joachain 1989). We find the ground state, $|000\rangle$, at $\beta = 1000$ has a binding energy of 28.3457 Ry, compared to the Le Guillou & Zinn-Justin (1984) result of 28.362 Ry. The internuclear separation is $0.1818a_0$; Le Guillou & Zinn-Justin (1984) find $0.181a_0$. Figure 8.5 depicts the wavefunctions of the ground and first excited state $|0-10\rangle$ for H_2^+.

The accuracy of our analysis of H_2^+ is insufficient to determine if the ungerade state is slightly bound or unbound relative to a hydrogen atom plus a proton. However, in the magnetic case, the electron may be excited into the $|0m0\rangle$ states whose axial wavefunctions are similar to that of the $|000\rangle$ state. The $|0-10\rangle$ state is much less bound at 20.4252 Ry than the $|000\rangle$ state (compared to 18.5579 Ry for the H+p system). For stronger

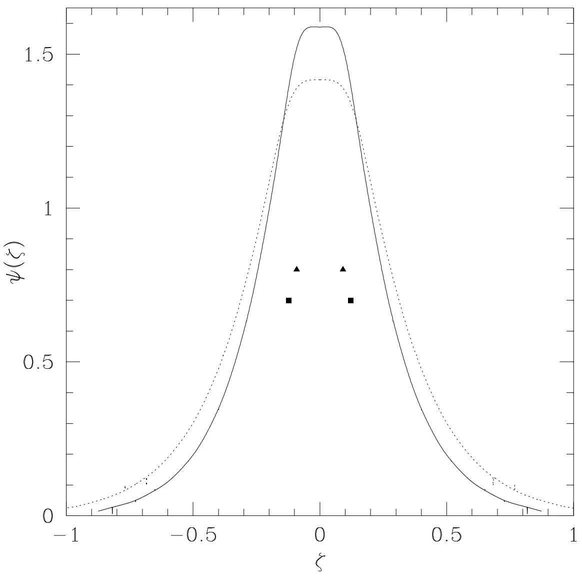

Figure 8.5: The ground and first-excited state of H_2^+. The solid line traces $|000\rangle$, and the dashed line follows $|0-10\rangle$. The triangles give the positions of the protons for the ground state and the squares for the excited state.

Table 8.2: The binding energy of H_2^+ in an intense magnetic field. The values have been derived numerically and the final column gives the numerically derived binding energy of the ground state of H for comparison.

	H_2^+		H
β	$\|000\rangle$	$\|0-10\rangle$	$\|000\rangle$
1×10^3	28.35	20.43	18.57
2×10^3	35.04	25.63	22.37
5×10^3	45.77	34.08	28.25
1×10^4	55.37	41.83	33.37
2×10^4	66.56	50.86	39.11
5×10^4	83.45	64.95	47.70
1×10^5	98.27	77.38	54.96

fields, the $|0-20\rangle$ and more excited states are bound relative to the H+p system.

Table 8.2 depicts the numerical results for the ground and first excited state of H_2^+ in an intense magnetic field. The ratio of the binding energies of the $|000\rangle$ and $|0-10\rangle$ for H_2^+ is approximately equal to the ratio the energies of the same states of hydrogen and the same magnetic field strength. This observation provides a quick way to estimate the energies of the excited states of H_2^+ from the binding energy of the ground state.

Table 8.3 presents results calculated for different values of magnetic field. Our values differ by less than 0.5 % for $B \geq 10^{12}$ G and by $\sim 1\%$ for the two weaker fields considered. We see that the first excited state of H_2^+ becomes bound relative to hydrogen atom and a proton at $B \approx 10^{12}$ G. Furthermore, a comparison of Table 8.3 with Table 3 of Lopez, Hess & Turbiner (1997) shows that the ungerade state is unbound for $B \geq 10^{11}$ G.

8.5 The Multiple Electron Problem

To calculate the atomic structure of multi-electron atoms, we employ a single-configuration Hartree-Fock technique. Specifically, we assume that the multi-electron wavefunction is given by a single Slater determinant of one-electron wavefunctions. These wavefunctions are varied to minimize the total energy of the system given the constraint that each one-electron wavefunction remains normalized.

This minimization results in the following eigenvalue equations for the

Table 8.3: The binding energy of H_2^+ in an intense magnetic field for comparison with the results of Lopez, Hess & Turbiner (1997).

	H_2^+		H
B (G)	$\|000\rangle$	$\|0-10\rangle$	$\|000\rangle$
1×10^{11}	7.347	4.880	5.611
5×10^{11}	13.37	9.188	9.568
1×10^{12}	17.05	11.88	11.87
2×10^{12}	21.53	15.25	14.58
5×10^{12}	28.89	20.85	18.89
1×10^{13}	35.69	26.14	22.74

individual wavefunctions,

$$F(1)\psi_i(1) = \epsilon_i\psi_i(1) \tag{8.33}$$

where 1 denotes the spin and spatial coordinates of the electron *i.e.* $\mathbf{r}_1, \sigma_1$.

The operator $F(1)$ is the sum of a kinetic and potential energy term

$$F(1) = H_0(1) + V(1) \tag{8.34}$$

where the kinetic term is given by the one-particle Schrödinger equation of an electron in the Coulomb field of the nucleus.

The potential energy consists of a direct and exchange interaction with the other electrons

$$V(1) = \sum_j [J_j(1) - K_j(1)] \tag{8.35}$$

where

$$J_j(1)\psi_i(1) = \left[\int d\tau_2 \psi_j^*(2)\left(\frac{e^2}{r_{12}}\right)\psi_j(2)\right]\psi_i(1) \tag{8.36}$$

$$K_j(1)\psi_i(1) = \left[\int d\tau_2 \psi_j^*(2)\left(\frac{e^2}{r_{12}}\right)\psi_i(2)\right]\psi_j(1) \tag{8.37}$$

Rather than solve the eigenvalue equations directly, we calculate the total energy of the system given a set of wavefunctions and minimize this energy by varying the parameters of the wavefunctions.

In a sufficiently strong magnetic field, these equations for the atomic structure become approximately separable in cylindrical coordinates. With this in mind, we take the trial wavefunctions to be of the form

$$\psi_i(1) = Z(z)R(\rho,\phi)\chi(\sigma). \tag{8.38}$$

Since we are looking for the ground state of these atoms, we take all the electron spins antialigned with the field and the radial wavefunction to be given by $n = 0$ Landau states with each electron occupying a different m state. We obtain

$$\psi_i(1) = Z_i(z) R_{0m_i}(\rho, \phi) \chi_{-\frac{1}{2}}(\sigma) \tag{8.39}$$

where

$$R_{0m}(\rho, \phi) = \frac{1}{\sqrt{2\pi |m|!}} \frac{1}{a_H} \exp\left(-\frac{\rho^2}{4a_H^2}\right) \left(\frac{\rho}{\sqrt{2} a_H}\right)^{|m|} e^{im\phi} \tag{8.40}$$

and $a_H = \sqrt{\hbar c/|e|B}$. We suppress the spin portion of the wavefunction and use the natural length and energy units of the problem $a_H, e^2/a_H$.

The total energy of the system is given by

$$E = \sum_i \langle \psi_i(1) | F(1) | \psi_i(1) \rangle . \tag{8.41}$$

To expedite the calculation we can integrate over the known wavefunctions in the ρ and ϕ coordinates. Specifically, we begin with the integral over ϕ in the potential energy terms

$$\begin{aligned} \langle \psi_i(1) | J_j(1) | \psi_i(1) \rangle &= e^2 \int \rho_1 d\rho_1 dz_1 Z_i^*(z_1) R_{0m_i}^*(\rho_1) Z_i(z_1) R_{0m_i}(\rho_1) \times \\ &\quad \int \rho_2 d\rho_2 dz_2 Z_j^*(z_2) R_{0m_j}^*(\rho_2) Z_j(z_2) R_{0m_j}(\rho_2) \times \\ &\quad f(\rho_1, \rho_2, z_1 - z_2) \qquad (8.42) \\ \langle \psi_i(1) | K_j(1) | \psi_i(1) \rangle &= e^2 \int \rho_1 d\rho_1 dz_1 Z_i^*(z_1) R_{0m_i}^*(\rho_1) Z_j(z_1) R_{0m_j}(\rho_1) \times \\ &\quad \int \rho_2 d\rho_2 dz_2 Z_j^*(z_2) R_{0m_j}^*(\rho_2) Z_i(z_2) R_{0m_i}(\rho_2) \times \\ &\quad g(m_i - m_j, \rho_1, \rho_2, z_1 - z_2) \qquad (8.43) \end{aligned}$$

where

$$\begin{aligned} f(\rho_1, \rho_2, z_1 - z_2) &= \int d\phi_1 \int d\phi_2 \times \\ &\quad \frac{1}{\sqrt{\rho_1^2 + \rho_2^2 + (z_1 - z_2)^2 - 2\rho_1 \rho_2 \cos(\phi_1 - \phi_2)}} \end{aligned} \tag{8.44}$$

$$g(m_i - m_j, \rho_1, \rho_2, z_1 - z_2) = \int d\phi_1 \int d\phi_2 \times \frac{e^{i(m_j - m_i)(\phi_1 - \phi_2)}}{\sqrt{\rho_1^2 + \rho_2^2 + (z_1 - z_2)^2 - 2\rho_1\rho_2\cos(\phi_1 - \phi_2)}} \tag{8.45}$$

The expressions for the functions f and g may be simplified by the substitution $\phi_1 - \phi_2 = 2(\beta + \pi/2)$ and the definition

$$k^2 = \frac{4\rho_1\rho_2}{(\rho_1 + \rho_2)^2 + (z_1 - z_2)^2} \tag{8.46}$$

resulting in

$$f(\rho_1, \rho_2, z_1 - z_2) = \frac{8\pi}{\sqrt{(\rho_1 + \rho_2)^2 + (z_1 - z_2)^2}} \times \int_0^{\pi/2} d\beta \frac{1}{\sqrt{1 - k^2 \sin^2\beta}} \tag{8.47}$$

$$= \frac{8\pi}{\sqrt{(\rho_1 + \rho_2)^2 + (z_1 - z_2)^2}} F\left(\frac{\pi}{2}, k\right) \tag{8.48}$$

$$g(m_i - m_j, \rho_1, \rho_2, z_1 - z_2) = \frac{8\pi}{\sqrt{(\rho_1 + \rho_2)^2 + (z_1 - z_2)^2}} \times \int_0^{\pi/2} d\beta \frac{e^{2i(m_j - m_i)(\beta + \pi/2)}}{\sqrt{1 - k^2 \sin^2\beta}} \tag{8.49}$$

$$= \frac{8\pi}{\sqrt{(\rho_1 + \rho_2)^2 + (z_1 - z_2)^2}} \times \int_0^{\pi/2} d\beta \frac{\cos(2(m_j - m_i)(\beta + \pi/2))}{\sqrt{1 - k^2 \sin^2\beta}} \tag{8.50}$$

where $F\left(\frac{\pi}{2}, k\right)$ is the complete Legendre elliptic integral of the first kind. The imaginary portion of the integral for g must be zero since the Hamiltonian is hermitian (i.e. unitarity). This may be seen by expanding the denominator in powers of $\sin^2\beta$ and multiplying this series by $i\sin(2(m_i - m_j)(\beta + \pi/2))$. The integral of this term is zero.

Numerical Recipes (Press et al. 1988) provides routines to efficiently calculate $F\left(\frac{\pi}{2}, k\right) = \texttt{cel}(\sqrt{1 - k^2}, 1, 1, 1)$ (unfortunately, this routine is absent from the latest edition). Furthermore, for $|m_i - m_j| = 1$, we can use the same routine to calculate g,

$$g(\pm 1, \rho_1, \rho_2, z_1 - z_2) = \frac{8\pi}{\sqrt{(\rho_1+\rho_2)^2 + (z_1 - z_2)^2}} \texttt{cel}(\sqrt{1-k^2}, 1, -1, 1). \tag{8.51}$$

For $|m_i - m_j| > 1$, we must perform the integral numerically.

Furthermore, we can gain insight on both the functions f and g by expanding them in the limit of large $\Delta z = |z_i - z_j|$.

$$\begin{aligned}
f(\rho_1, \rho_2, z_1 - z_2) &= (2\pi)^2 \Bigg[\frac{1}{\Delta z} - \frac{1}{2} \frac{\rho_1^2 + \rho_2^2}{\Delta z} + \frac{3}{8} \frac{\rho_1^4 + 4\rho_1^2\rho_2^2 + \rho_2^4}{\Delta z^5} \\
&\quad - \frac{5}{16} \frac{\rho_1^6 + 9\left(\rho_1^4\rho_2^2 + \rho_1^2\rho_2^4\right) + \rho_2^6}{\Delta z^7} \\
&\quad + \frac{35}{128} \frac{\rho_1^8 + 16\left(\rho_1^6\rho_2^2 + \rho_1^2\rho_2^6\right) + 36\rho_1^4\rho_2^4 + \rho_2^8}{\Delta z^9} \\
&\quad + \mathcal{O}\left(\frac{1}{\Delta z^{11}}\right) \Bigg] &(8.52) \\
g(0, \rho_1, \rho_2, z_1 - z_2) &= f(0, \rho_1, \rho_2, z_1 - z_2) &(8.53) \\
g(\pm 1, \rho_1, \rho_2, z_1 - z_2) &= (2\pi)^2 \Bigg[\frac{1}{2} \frac{\rho_1\rho_2}{\Delta z^3} - \frac{3}{4} \frac{\rho_1\rho_2^3 + \rho_1^3\rho_2}{\Delta z^5} \\
&\quad + \frac{15}{16} \frac{\rho_1\rho_2^5 + 3\rho_1^3\rho_2^3 + \rho_1^5\rho_2}{\Delta z^7} \\
&\quad - \frac{35}{32} \frac{\rho_1\rho_2^7 + 6\left(\rho_1^5\rho_2^3 + \rho_1^3\rho_2^5\right) + \rho_1^7\rho_2}{\Delta z^9} \\
&\quad + \mathcal{O}\left(\frac{1}{\Delta z^{11}}\right) \Bigg] &(8.54) \\
g(\pm 2, \rho_1, \rho_2, z_1 - z_2) &= (2\pi)^2 \Bigg[\frac{3}{8} \frac{\rho_1^2\rho_2^2}{\Delta z^5} - \frac{15}{16} \frac{\rho_1^2\rho_2^4 + \rho_1^4\rho_2^2}{\Delta z^7} \\
&\quad + \frac{105}{64} \frac{\rho_1^6\rho_2^2 \frac{8}{3}\rho_1^4\rho_2^4 + \rho_1^2\rho_2^6}{\Delta z^9} \\
&\quad - \frac{315}{128} \frac{\rho_1^2\rho_2^8 + 5\left(\rho_1^4\rho_2^6 + \rho_1^6\rho_2^4\right) + \rho_1^8\rho_2^2}{\Delta z^{11}} \\
&\quad + \mathcal{O}\left(\frac{1}{\Delta z^{13}}\right) \Bigg] &(8.55)
\end{aligned}$$

$$\begin{aligned} g(\pm 3, \rho_1, \rho_2, z_1 - z_2) &= (2\pi)^2 \left[\frac{5}{16} \frac{\rho_1^3 \rho_2^3}{\Delta z^7} - \frac{35}{32} \frac{\rho_1^5 \rho_2^3 + \rho_1^3 \rho_2^5}{\Delta z^9} \right. \\ &\qquad \left. + \mathcal{O}\left(\frac{1}{\Delta z^{11}} \right) \right] \qquad (8.56) \\ g(\pm 4, \rho_1, \rho_2, z_1 - z_2) &= (2\pi)^2 \left[\frac{35}{128} \frac{\rho_1^4 \rho_2^4}{\Delta z^9} + \mathcal{O}\left(\frac{1}{\Delta z^{11}} \right) \right] \qquad (8.57) \end{aligned}$$

and in general

$$g(\pm \Delta m, \rho_1, \rho_2, z_1 - z_2) \propto \frac{(\rho_1 \rho_2)^{\Delta m}}{\Delta z^{2\Delta m + 1}} \qquad (8.58)$$

to leading order in $1/\Delta z$.

In the limit of large Δz, the integrals over the radial wavefunctions may evaluated using these expansions. This calculation is speeded by the observation that

$$\int 2\pi \rho d\rho R_{0m_1}(\rho) R_{0m_2}(\rho) \rho^n = \sqrt{\frac{2^n}{|m_1|!|m_2|!}} \Gamma\left(\frac{|m_1| + |m_2| + n}{2} + 1 \right) \qquad (8.59)$$

which may be proven by using the normalization condition of the functions $R_{0m}(\rho)$ and analytically continuing the factorial function with the Gamma function. For $\Delta z < 10$ we have numerically integrated the functions f and g over the various pairs of Landau states.

After the integration over the radial and angular coordinates, the energy may now be written as expectation values of operators acting on the $Z(z)$ wavefunction. Since each electron is assumed to be in a particular Landau m level, we can calculate an effective potential energy between the electron and the nucleus by integrating over ρ, ϕ. The potential is given by Equation 8.13.

The calculational strategy is similar to the single electron case. The quantum numbers ν, m for each electron are chosen ahead of time, and the wavefunction $Z(z)$ is expanded as Equation 8.29 with each electron having is own variable value of a_Z. For each electron i, the matrix

$$(M_i)_{kl} = \langle \mathcal{G}_k | F(i) | \mathcal{G}_l \rangle \qquad (8.60)$$

is calculated.

The added complication is that the diagonalization of the matrices M_i must proceed iteratively. For the given values of a_Z, the matrices are first calculated assuming that the other electrons ($j \neq i$) have $A_k = 1$ for $k = \nu_j$. Then each electron's matrix is diagonalized and the ν_ith eigenvector is used

Table 8.4: The binding energy of He, HHe^+ and HHe in an intense magnetic field. The number in parenthesis gives the number of free parameters in each variational model. The electrons occupy the most tightly bound states, $|0m0\rangle$, *e.g.* $|000\rangle$, $|0-10\rangle$ and $|0-20\rangle$ for HHe. The values have been derived numerically and the final column gives the numerically derived binding energy of the ground state of H for comparison.

β	He (6)	HHe^+ (5)	HHe (7)	H (25)
1×10^2	32.47	35.75	42.59	9.383
2×10^2	40.98	45.95	54.25	11.64
5×10^2	54.95	63.07	73.36	15.28
1×10^3	67.85	79.24	90.89	18.57
2×10^3	83.00	98.55	111.3	22.37
5×10^3	106.9	129.7	143.1	28.25
1×10^4	127.8	157.5	168.0	33.37
2×10^4	151.6	189.7	193.1	39.11
5×10^4	187.6	239.6		47.70
1×10^5	218.4	282.5		54.96

to calculate the interelectron potential for the next iteration. The matrices converge after $\sim 5-10$ iterations. Next, the values of a_Z for each electron are varied to minimize the total energy of the configuration.

For brevity, we discuss the ground state energies and wavefunctions for H_2, He and HHe as a function of field strength for $\beta \geq 1000$. Since we are interested in the ground states of these species we set $\nu = 0$ for all the electrons and assign the electrons consecutive m quantum numbers beginning with $m = 0$. Because none of the electrons have axial excitations, we are interested in only the most negative eigenvalue of the electron matrices. This eigenvalue is more efficiently determined by varying the coefficients in Equation 8.29 directly than by diagonalizing the electron matrices iteratively.

Table 8.4 gives the binding energies of the most tightly bound states of H_2, He, HHe and H calculated numerically using the variational method. The energies for H are within 1.1 % of the values quoted by Ruder et al. (1994) for weakest field strength common between the two studies. For the stronger fields, the agreement is even closer. For He the energies are within 2.5 % of the values of Ruder *et al.* for the fields that overlap.

We also computed the binding energies of H_2 and H^- and compared the results with the values found by Lai, Salpeter & Shapiro (1992). We interpolated the Lai *et al.* results using a cubic spline with $\ln\beta$ as the independent variable. The binding energies for H_2 were within $0.6 - 3\%$ of the Lai *et al.* results. The agreement for H^- was poorer ranging from $2 - 7\%$. The results for H and H_2^+ (Table 8.2) agree to within 0.9% of the Lai *et al.* values.

We compare these interpolated results with the results for the species He, HHe and HHe^+ to find that the reaction

$$\mathrm{H} + \mathrm{He} \rightarrow \mathrm{HHe} \tag{8.61}$$

is exothermic over the range of field strengths considered. However, if there is sufficient hydrogen present, the species HHe would quickly be consumed by the exothermic reaction

$$\mathrm{H} + \mathrm{HHe} \rightarrow \mathrm{He} + \mathrm{H}_2 \tag{8.62}$$

for these field strengths, unless

$$\mathrm{H} + \mathrm{HHe} \rightarrow \mathrm{H}_2\mathrm{He} \tag{8.63}$$

is sufficiently exothermic (the binding energy and configuration of H_2He is beyond the scope of this paper). The potential production channels for HHe^+,

$$\begin{aligned} \mathrm{He} + \mathrm{H}_2 &\rightarrow \mathrm{HHe}^+ + \mathrm{H}^-, & (8.64)\\ \mathrm{He} + \mathrm{H}_2^+ &\rightarrow \mathrm{HHe}^+ + \mathrm{H} \text{ and} & (8.65)\\ \mathrm{He} + \mathrm{H} &\rightarrow \mathrm{HHe}^+ + \mathrm{e}^- & (8.66)\end{aligned}$$

are endothermic over the range of field strengths considered. We therefore conclude that at least for hydrogen and helium, atoms in an intense magnetic field are far more cohesive than adhesive.

8.6 Conclusions

We have developed both an analytic and a convenient numerical technique to accurately calculate the properties of simple atoms and molecules in an intense magnetic field. The calculations presented here complement the earlier work. We examine two compounds (HHe and HHe^+) in addition to the species studied earlier which may form in the intensely magnetized outer layers of a neutron star. Additionally, our technique finds both tightly bound and excited states efficiently and accurately which is necessary to calculate the radiative transfer of the neutron star atmosphere.

The properties of the lowest density layers of a neutron star's crust determine the spectral characteristics of the radiation expected from the star. One possibility is that linear chains of atoms form in the surface layers (Ruderman 1974; Chen, Ruderman & Sutherland 1974; Flowers et al. 1977; Müller 1984; Neuhauser, Koonin & Langanke 1987; Lai, Salpeter & Shapiro 1992), and the atmosphere condenses at finite density. We find that the reactions between hydrogen and helium are unlikely to affect the formation of hydrogen or helium chains unless the formation of hydrogen-helium hybrid chains is favored.

If the envelope is truncated at sufficiently high density, the thermal isolation can be substantially reduced (Hernquist 1985). Furthermore, the composition of the outermost layers determines the spectra from the neutron star (*e.g.* Pavlov et al. 1994; Pavlov et al. 1996; Zavlin, Pavlov & Shibanov 1996; Rajagopal, Romani & Miller 1997). Without understanding magnetized chemistry in neutron-star atmospheres, is difficult to interpret observations of these objects.

Part III

Magnetic Fields and Heat Transfer

Chapter 9

Almost Analytic Models of Ultramagnetized Neutron Star Envelopes

SUMMARY

Recent ROSAT measurements show that the x-ray emission from isolated neutron stars is modulated at the stellar rotation period. To interpret these measurements, one needs precise calculations of the heat transfer through the thin insulating envelopes of neutron stars. We present nearly analytic models of the thermal structure of the envelopes of ultramagnetized neutron stars. Specifically, we examine the limit in which only the ground Landau level is filled. We use the models to estimate the amplitude of modulation expected from non-uniformities in the surface temperatures of strongly magnetized neutron stars. In addition, we estimate cooling rates for stars with fields $B \sim 10^{15} - 10^{16}$ G which are relevant to models that invoke "magnetars" to account for soft γ-ray emission from some repeating sources.

9.1 Introduction

Since the launch of the ROSAT satellite, our knowledge of isolated neutron stars has expanded into new realms. Before ROSAT, neutron stars were unique objects in astronomy. Although they had been observed over a range of energies from radio to ultra-high-energy gamma rays, and had been evoked to power a variety of astrophysical objects from pulsars to soft

Table 9.1: Several pulsars with observed surface blackbody emission

Pulsar	References
PSR J0437-4715	Becker & Trümper 1993
PSR 0630+18 (Geminga)	Halpern & Holt 1992, Halpern & Ruderman 1993, Halpern & Wang 1997
PSR 0656+14	Finley, Ögelman & Kiziloglu 1992, Anderson et al. 1993, Greiveldinger et al. 1996, Possenti, Mereghetti & Colpi 1996
PSR 0833-45 (Vela)	Ögelman, Finley & Zuckerman 1993
PSR 1055-52	Ögelman & Finley 1993, Greiveldinger et al. 1996
PSR 1929+10	Yancopoulos, Hamilton & Helfand 1994

X-ray repeaters and gamma-ray bursts, one could not argue unequivocally that a single photon from the surface of a neutron star had ever been detected.

For the first time, we have direct evidence for radiation from the surfaces of neutron stars. More than a dozen such sources have been detected by ROSAT (*e.g.* Ögelman 1995), and more than ten have been fitted with spectra. The spectra divide the objects into two classes: 1) objects with hard spectra whose X-ray emission is best attributed to the magnetosphere, and 2) neutron stars whose soft flux is well-described by a blackbody spectrum. Table 9.1 lists several of those that fall into the second group with pertinent references.

Two component models characterize the X-ray spectra of these objects. The soft component is typically a blackbody, and the hard component is either a blackbody or power-law. Furthermore, the temperatures inferred for the soft components agree with theoretical cooling curves at the characteristic ages of the stars. If this interpretation is correct, the observations provide a direct probe of the structure of cooling neutron stars. (Halpern & Ruderman 1993 provide an alternative explanation for the soft emission from Geminga).

Additionally, the observations show that the thermal radiation is modulated at the rotation period of the neutron stars. Although the time variation of the flux is small, with the count rates varying by 10%–30% from their average values, this modulation is important because the thermal flux from a star emitting isotropically would be constant. A strong magnetic can modulate the thermal flux through several physical effects:

1. Anisotropic heat conduction in the outer layers of the star (the envelope) will result in non-uniform temperatures on the stellar surface, with the magnetic poles being warmer than the equatorial regions.

2. Anisotropic radiative transfer in the atmosphere of the neutron star will produce spectra whose shapes vary with the local inclination of the field and the line of sight.

3. QED processes in the magnetosphere which depend on the local strength of the field, such as photon splitting, can alter the spectrum.

4. The magnetosphere channels accreted particles onto the polar regions, heating the stellar surface non-uniformly and mimicking the effects of anisotropic heat conduction in the envelope.

All of these effects must be considered to compare model spectra with the observations. As a first step, we focus on item (1), which is required to understand effects (2) and (3). Although particle bombardment of the surface is likely to contribute to the observed fluxes, as a first approximation we assume that this effect contributes mainly to the harder components of the observed spectra and has little effect on the soft blackbody components.

To a very good approximation, neutron stars are isothermal spheres insulated from their environments by a thin outer layer which contains negligible heat capacity and all of the temperature gradient. These properties make neutron stars almost unique among astrophysical objects which tend to have a gradual temperature gradient from the surface to the center. Instead, in this respect these exotic objects are more akin to everyday objects such as buildings and ovens which effectively insulate an isothermal interior with concentrated insulation at the interface with the exterior.

We proceed in the spirit of Gudmundsson, Pethick & Epstein (1982) and concentrate our analysis on this thin region insulating the bulk of the neutron star. The envelope is customarily defined to extend from zero density to $\rho \sim 10^{10}$ g/cm^3, and its thickness (h_E) is of the order of tens of meters, very small compared to the radius of the star, $R \sim 10$ km. By limiting the analysis, we focus on how various physical processes affect the thermal structure of the envelope and the relationship between the core temperature and the flux emitted at the surface. An alternative point of view is to combine the envelope calculation with an estimate of the cooling rate due to neutrinos and the total heat capacity of the neutron star, yielding theoretical cooling curves (*e.g.* Tsuruta et al. 1972, Nomoto & Tsuruta 1981, Glen & Sutherland 1980, Van Riper & Lamb 1981)

Several authors have made much progress in understanding the properties of neutron star envelopes with and without magnetic fields. Gudmundsson, Pethick & Epstein (1982) numerically calculate the thermal structure for unmagnetized envelopes, and Hernquist & Applegate (1984) present analytic models for the $B = 0$ case. Tsuruta (1979), Glen & Sutherland (1980), Van Riper & Lamb (1981) and Urpin & Yakovlev (1980) calculate the luminosity observed at infinity as a function of the core temperature for several magnetic field strengths less than 10^{14} G, including the zero-field case. Hernquist (1985) calculates the thermal structure of envelopes for $B \leq 10^{14}$ G for transport along the field, using the electron conductivities of Hernquist (1984) which account for the quantization of electron energies in the magnetic field in a relativistic framework. We will use these conductivities in the present work; therefore, Hernquist (1985) provides a natural benchmark.

Van Riper (1988) builds upon the Hernquist (1985) results by exploring various assumptions concerning the properties of the envelope at low densities and calculating profiles for many field strengths ($B < 10^{14}$ G) and core temperatures. Again, these calculations are limited to conduction along the field. Schaaf (1990a), using the electron conductivities calculated in Schaaf (1988), calculates the thermal structure in two dimensions for $B \lesssim 10^{11}$ G. Above a field strength of 10^{12} G, the calculations are not considered reliable. Finally, Shibanov et al. (1995) present the temperature distribution as a function of magnetic colatitude for $B = 10^{12}$ G from a numerical solution to the two-dimensional thermal structure equation in a plane-parallel approximation.

The current work complements the previous ones by extending the results to stronger field strengths (10^{14} G $\leq B \leq 10^{16}$ G) in a semi-analytical fashion. We apply the approach of Hernquist & Applegate (1984) in the limit of a strongly magnetized envelope, and then justify and use the plane-parallel approximation to solve the two-dimensional structure equation. We derive separable thermal structure equations in the high and low temperature limits for both liquid and solid material. We calculate the thermal structure in terms of simple (although analytically intractable) integrals.

The plane-parallel approximation has the second important advantage that the detailed field configuration separates from the thermal structure problem. Assuming that is is correct, we can synthesize the results for any field distribution $B(\theta, \phi)$ as long as B is not too inhomogeneous on the scale of the envelope thickness.

We find that the emission from a given surface element is a simple function of the location of the element. Using this functional form, we derive light curves and time-dependent spectra including general relativistic effects. Although we closely follow the formalism of Page (1995), we calculate the two-dimensional thermal structure of the envelope and present results for several field strengths and fluxes. We internally verify and justify the geometric simplification used to translate our results into observables.

9.2 Preliminaries

In extremely intense magnetic fields, the Landau energy ($\hbar\omega_B$) of an electron will typically exceed its thermal energy. In these strong fields, the quantization of the electron energy determines the structure of the electron phase space and must be taken into account in calculating the thermodynamics of the electron gas.

To quantify the strength of the magnetic field we define

$$\beta = \frac{\hbar\omega_B}{m_e c^2} = \frac{\hbar|e|}{m_e^2 c^3} B. \tag{9.1}$$

Here $\beta = 1$ corresponds to a field of 4.414×10^{13} Gauss and ω_B is the non-relativistic electron gyrofrequency.

The chemical potential and temperature of the electrons can be expressed similarly as

$$\zeta = \frac{\mu}{m_e c^2} \text{ and } \tau = \frac{kT}{m_e c^2}. \tag{9.2}$$

Throughout this paper we use relativistic expressions for the energy and chemical potential, including the electron rest mass.

In an extremely strong magnetic field, the quantization of electron energies into Landau levels restricts the phase space of the otherwise free electron gas (Hernquist 1985), and its thermodynamic properties are given by

$$n_e = \frac{\beta}{2\pi^2} \int_1^\infty d\gamma f(\gamma)\gamma \sum_{n=0}^{n_{\max}} \frac{g_n}{\alpha_n} \left(\frac{1}{\lambda\!\!\!^{-}_e{}^3} \right), \tag{9.3}$$

$$P_e = \frac{\beta}{2\pi^2} \int_1^\infty d\gamma f(\gamma) \sum_{n=0}^{n_{\max}} g_n \alpha_n \left(\frac{m_e c^2}{\lambda\!\!\!^{-}_e{}^3} \right), \tag{9.4}$$

$$\frac{\partial \rho}{\partial \zeta} = -\frac{\beta}{2\pi^2} \int_1^\infty d\gamma \frac{\partial f}{\partial \gamma} \gamma \sum_{n=0}^{n_{\max}} \frac{g_n}{\alpha_n} \left(\frac{m_u}{Y_e} \frac{1}{\lambda\!\!\!^{-}_e{}^3} \right), \tag{9.5}$$

$$\frac{\partial \rho}{\partial \tau} = -\frac{\beta}{2\pi^2} \int_1^\infty d\gamma \frac{\partial f}{\partial \gamma} \gamma \frac{\gamma - \zeta}{\tau} \sum_{n=0}^{n_{\max}} \frac{g_n}{\alpha_n} \left(\frac{m_u}{Y_e} \frac{1}{\lambda\!\!\!^{-}_e{}^3} \right), \tag{9.6}$$

$$S_e = -\frac{\beta}{2\pi^2} \int_1^\infty d\gamma \frac{\partial f}{\partial \gamma} \frac{\gamma - \zeta}{\tau} \sum_{n=0}^{n_{\max}} g_n \alpha_n \left(\frac{k}{\lambda\!\!\!^{-}_e{}^3} \right) \tag{9.7}$$

where

$$
\begin{aligned}
n_{\max} &= \frac{\gamma^2-1}{2\beta} && (9.8)\\
\alpha_n^2 &= \gamma^2 - 2n\beta - 1, && (9.9)\\
f(\gamma) &= \frac{1}{1+\exp\left[(\gamma-\zeta)/\tau\right]}, && (9.10)\\
Y_e &= \frac{Z}{A} && (9.11)
\end{aligned}
$$

and $g_n = 2 - \delta_{n0}$ is the degeneracy of the Landau level, $\lambdabar_e$ is the electron Compton wavelength, m_u is the atomic mass unit, and Z and A are the mean atomic number and mean atomic mass of the material. For partially ionized matter, Y_e is given by the product of Z/A and the ionized fraction.

In the degenerate limit, electron conduction transfers energy through the envelope. For a liquid, electron-ion collisions hamper this flow. In the solid state, electron-phonon collisions provide the resistance. Additionally, heat flux is greatly restricted perpendicular to the magnetic field lines; consequently, we have an anisotropic thermal conductivity ($\boldsymbol{\kappa}$) tensor. In the absence of a electric current, we obtain (Hernquist 1984)

$$\boldsymbol{\kappa} = \boldsymbol{\gamma} - T\boldsymbol{\lambda}\cdot(\boldsymbol{\sigma})^{-1}\cdot\boldsymbol{\lambda} \tag{9.12}$$

where $\boldsymbol{\gamma}$, $\boldsymbol{\lambda}$ and $\boldsymbol{\sigma}$ are the thermal conductivity, thermoelectric and electrical conductivity tensors respectively.

If we take the field to point along the z direction locally,

$$
\begin{aligned}
\begin{pmatrix}\sigma_{zz}\\ \lambda_{zz}\\ \gamma_{zz}\end{pmatrix} &= -\frac{\beta}{2\pi^2}\int_1^\infty \frac{\partial f}{\partial\gamma}\begin{pmatrix} e^2\\ -|e|k(\gamma-\zeta)/\tau\\ km_ec^2(\gamma-\zeta)^2/\tau\end{pmatrix}\phi(\nu;\beta)d\gamma\\
&\quad\times\left(\frac{1}{\hbar\lambdabar_e{}^2}\frac{1}{\sigma_0 n_i}\right) && (9.13)\\
\begin{pmatrix}\sigma_{yy}\\ \lambda_{yy}\\ \gamma_{yy}\end{pmatrix} &= -\frac{1}{2\pi^2}\int_1^\infty \frac{\partial f}{\partial\gamma}\begin{pmatrix} e^2\\ -|e|k(\gamma-\zeta)/\tau\\ km_ec^2(\gamma-\zeta)^2/\tau\end{pmatrix}Q(\nu;\beta)d\gamma\\
&\quad\times\left(\frac{\hbar}{\sigma_0 n_i}\right) && (9.14)
\end{aligned}
$$

where $\nu = \gamma/\beta$, n_i is the number density of ions (n_e/Z), σ_0 is the scattering cross section and ϕ and Q are perturbations to the distribution function and the diagonal component of the density matrix $f_{ns}(p_z, y_B)$, summed over Landau level n and spin s (Hernquist 1984).

9.3 The Low-Temperature, Strong-Field Regime

We are specifically interested in the low temperature limit ($\tau \ll \zeta - 1$) and the regime in which only one Landau level is filled ($\zeta < \sqrt{2\beta+1}$). For neutron stars with $\beta \gtrsim 1$, this limit applies to the regions that most effectively insulate the isothermal core of the star.

In this regime we obtain,

$$
\begin{aligned}
n_e &= \frac{\beta}{2\pi^2}\sqrt{\zeta^2-1}\left(\frac{1}{\lambda\!\!\!^{-}{}_e^{\,3}}\right) && (9.15)\\
\kappa_{zz} &= \frac{1}{6}\beta\tau\frac{1}{n_i \lambda\!\!\!^{-}{}_e^{\,3}}\phi(\zeta;\beta)\left(\frac{ck}{\sigma_0}\right) && (9.16)\\
\kappa_{yy} &= \frac{1}{6}\tau Q(\zeta;\beta)\left(\frac{n_i\sigma_0 ck}{\lambda\!\!\!^{-}{}_e}\right). && (9.17)
\end{aligned}
$$

Also, Yakovlev (1984) has calculated the function ϕ in this limit, and we apply the formalism of Hernquist (1984) to calculate the function Q analytically for electron-ion and electron-phonon scattering.

9.3.1 Electron-ion Scattering

Electron-ion scattering dominates the resistance to electron conduction in the liquefied regions of the neutron-star envelope. The scattering cross section is

$$\sigma_0 = \frac{\pi Z^2\alpha^2}{\beta^2}\lambda\!\!\!^{-}{}_e^{\,2} \tag{9.18}$$

where $\alpha \approx 1/137$ is the fine-structure constant and

$$
\begin{aligned}
\phi_{ei}(\gamma;\beta) &= \frac{1}{8}w\left[\frac{1}{w+a_d} - \exp(w+a_d)E_1(w+a_d)\right]^{-1}, && (9.19)\\
Q_{ei}(\gamma;\beta) &= \frac{1}{\alpha_0^2}\Big\{\left[\beta(a_d+1)+2\alpha_0^2\right]\exp(w+a_d)E_1(w+a_d)\\
&\quad +\beta(a_d+1)\gamma^2 e^{a_d}E_1(a_d) - \beta(\gamma^2+1)\Big\} && (9.20)
\end{aligned}
$$

where

$$
\begin{aligned}
w &= \frac{2\alpha_0^2}{\beta}, && (9.21)\\
a_d &= 0.15\left(\frac{\alpha_0^2}{2\beta}\right)^{1/3}, && (9.22)
\end{aligned}
$$

and $E_n(x)$ is an exponential integral which is easily calculated and is defined by

$$E_n(x) = \int_1^\infty \frac{e^{-xt}}{t^n} dt, \quad x \geq 0, \quad n = 0, 1, \ldots \tag{9.23}$$

9.3.2 Electron-phonon Scattering

In the solid state, electrons scatter off of phonons which impedes the flow of heat. The scattering off of impurities may also be important at even lower temperatures (Yakovlev & Urpin 1980). As we are studying envelopes with effective temperatures $\sim 10^6$ K, we neglect this effect.

The results for electron-phonon scattering are relatively simple. We obtain

$$\sigma_0 = \frac{\alpha u_{-2}}{2} \frac{\tau}{\beta} \left(\frac{1}{n_i \lambda\!\!\!^{-}_e{}^3} \right) \lambda\!\!\!^{-}_e{}^2, \tag{9.24}$$

$$\phi_{ep}(\gamma; \beta) = \frac{1}{8} w \left[e^w E_1(w) \right]^{-1}, \tag{9.25}$$

$$Q_{ep}(\gamma; \beta) = \beta + \frac{4}{w} - 2e^w E_1(w) \tag{9.26}$$

and we take $u_{-2} \approx 13$ (Yakovlev & Urpin 1980, Potekhin & Yakovlev 1996) for a body-centered cubic lattice.

The expressions for ϕ and Q presented in this and the previous subsection are valid for any temperature for $\gamma < \sqrt{2\beta + 1}$ (or equivalently $w < 4$).

9.3.3 Degenerate Structure Equations

If we assume that the pressure is supplied by the electrons alone, the general relativistic equations of thermal structure in the plane-parallel approximation assume the simple form

$$\frac{\mathrm{d}T}{\mathrm{d}\mu} = \frac{F}{g_s} \frac{Y_e}{m_u} \frac{1}{\kappa} \frac{1}{1 - F S_e / g_s \rho \kappa} \tag{9.27}$$

$$\frac{\mathrm{d}\mu}{\mathrm{d}z} = \frac{m_u}{Y_e} g_s \left(1 - \frac{F}{g_s} \frac{S_e}{\rho \kappa} \right) \tag{9.28}$$

where we have neglected the thickness of the envelope ($h_E \sim 100\,\mathrm{m}$) relative to the stellar radius (R). Here F and g_s are the flux and the acceleration of gravity as measured at the surface, respectively. In the absence of a magnetic field, this plane-parallel approximation introduces errors of the order $R_s h_E / R^2 \approx 0.6\%$ where $R_s = 2GM/c^2$ (Gudmundsson, Pethick &

Epstein 1982). To understand the potential errors of this plane-parallel treatment in the presence of a magnetic field, we compare the results of Shibanov et al. (1995) with those of Schaaf (1990a). Although Shibanov et al. (1995) use a one-dimensional treatment, their results agree with those of two-dimensional treatment by Schaaf (1990a) for several surface temperatures and a magnetic field of 10^{12} G. In stronger magnetic fields, conduction perpendicular to the magnetic field is even less important, and we expect the one-dimensional treatment to be even more accurate.

To estimate the errors in using the plane-parallel treatment in the presence of the magnetic field, we examine the thermal structure equation in two dimensions (Schaaf 1990a)

$$\begin{aligned} \boldsymbol{\nabla}\cdot\boldsymbol{F} &= -\frac{e^{-\Lambda_s}}{r^2}\frac{\partial}{\partial r}\left[r^2\kappa_{11}e^{-\Lambda_s}\frac{\partial T}{\partial r}+r\kappa_{12}\frac{\partial T}{\partial\theta}\right] \\ &\quad -\frac{1}{r\sin\theta}\frac{\partial}{\partial\theta}\left[\sin\theta\left(\kappa_{21}e^{-\Lambda_s}\frac{\partial T}{\partial r}+\frac{\kappa_{22}}{r}\frac{\partial T}{\partial\theta}\right)\right]=0, \end{aligned} \tag{9.29}$$

where θ is an angle along the surface of star, specifically the magnetic colatitude,

$$e^{-\Lambda_s}=\sqrt{1-\frac{R_s}{R}}, \tag{9.30}$$

and the κ_{ij} are the components of the thermal conduction tensor, where 1 denotes the radial direction and 2 denotes the tangential direction. The components of $\boldsymbol{\kappa}$ are found by rotating the tensor calculated in the previous section so that the z-direction coincides with the radial direction here. This gives

$$\kappa_{11} = \kappa_{yy}\sin^2\psi+\kappa_{zz}\cos^2\psi, \tag{9.31}$$

$$\kappa_{22} = \kappa_{yy}\cos^2\psi+\kappa_{zz}\sin^2\psi, \tag{9.32}$$

$$\kappa_{12}=\kappa_{21} = (\kappa_{yy}-\kappa_{zz})\sin\psi\cos\psi, \tag{9.33}$$

where ψ is the angle between the local field direction and the radial direction. For a uniformly magnetized neutron star $\psi=\theta$; for a dipole field, $\cot\psi = 2\cot\theta$ (Greenstein & Hartke 1983), or more conveniently

$$\cos^2\psi=\frac{4\cos^2\theta}{3\cos^2\theta+1}. \tag{9.34}$$

If we assume that the components of the thermal conduction matrix ($\boldsymbol{\kappa}$) are of the same order and take the maximum temperature gradient to be $T_c - T_{\rm eff} \sim T_c$ radially over the thickness of the envelope, h_E, or tangentially over one radian, we obtain

$$\frac{\partial T}{\partial \theta} \sim T_c \ll e^{-\Lambda_s} r \frac{\partial T}{\partial r} \sim e^{-\Lambda_s} R \frac{T_c}{h_E} \sim 10^2 T_c \tag{9.35}$$

where T_c is the core temperature. We find that neglecting derivatives with respect to angle does not dramatically increase the error relative to the unmagnetized plane-parallel case.

However, this argument does not apply for θ close to $\pi/2$ (*i.e.* where the magnetic field lines are parallel to the surface for a uniform or dipole field). Here,

$$\kappa_{22} = \kappa_{zz} \gg \kappa_{11} = \kappa_{yy}. \tag{9.36}$$

If we reexamine the error analysis for $\psi \approx \pi/2$ we find that relevant quantities to compare are

$$\kappa_{22} \frac{\partial^2 T}{\partial \theta^2} \text{ and } \kappa_{11} r^2 e^{-2\Lambda_s} \frac{\partial^2 T}{\partial r^2}. \tag{9.37}$$

The tangential transport will exceed the radial transport if

$$\cos^2 \psi < e^{2\Lambda_s} \frac{h_E^2}{R^2} - \frac{\kappa_{yy}}{\kappa_{zz}} \tag{9.38}$$

Comparing these values we find that if $\kappa_{zz} \gtrsim 10^4 \kappa_{yy}$, the one-dimensional treatment will break down near $\psi = \pi/2$; otherwise, the plane-parallel treatment is adequate even at $\psi = \pi/2$.

For regions where the magnetic field lines are not nearly parallel to the surface, the plane-parallel approximation works well; consequently even for an arbitrary field geometry, because the envelope is thin, we ignore $\partial/\partial\theta$ terms in the structure equation compared to $r\partial/\partial r$ terms and focus on radial heat flow. With these assumptions, we have (Schaaf 1990a)

$$\kappa = \kappa_{11} = \kappa_{zz} \cos^2 \psi + \kappa_{yy} \sin^2 \psi. \tag{9.39}$$

In the low-temperature limit, we obtain the dimensionless equation

$$\frac{\mathrm{d}\tau}{\mathrm{d}\zeta} = \left(Y_e \frac{F}{m_u g_s} \frac{{\lambda\!\!\!^{-}}_e{}^2}{c} \right) \left(\frac{ck}{{\lambda\!\!\!^{-}}_e{}^2} \frac{1}{\kappa} \right) \tag{9.40}$$

where the dimensionless flux is given by

$$\left(Y_e \frac{F}{m_u g_s} \frac{{\lambda\!\!\!^{-}}_e{}^2}{c} \right) = 7.83 \times 10^{-3} \frac{Z_{26}}{A_{56}} \frac{T_{\mathrm{eff},6}^4}{g_{s,14}}, \tag{9.41}$$

where $Z_{26} = Z/26$, $A_{56} = A/56$, $T_{\rm eff,6} = T_{\rm eff}/10^6$ K, and $g_{s,14} = g_s/10^{14}$ cm/s^2. $T_{\rm eff}$ is the effective blackbody temperature of the neutron star photosphere again as measured at the surface, which we take to be located at an optical depth of 2/3.

For Equation 9.40 to be separable for an arbitrary geometry, κ_{zz} and κ_{yy} must depend on τ in the same fashion. For electron-ion scattering this is the case, so we can hope to find a simple analytic solution to the structure equation. Unfortunately, since the cross-section for electrons to scatter off of phonons depends explicitly on temperature (Equation 9.24), in the solid state the structure equation is separable only where the field is either purely radial or tangential.

In the liquid state, we obtain the following structure equation,

$$\begin{aligned}\tau\frac{\mathrm{d}\tau}{\mathrm{d}\zeta} &= \left(Y_e \frac{F}{m_u g_s}\frac{\lambda\!\!\!^-_e}{c}^2\right)\left[\cos^2\psi \frac{\pi}{3}\frac{\beta^2}{Z\alpha^2}\frac{\phi_{ei}(\zeta;\beta)}{\sqrt{\zeta^2-1}}\right. \\ &\quad \left. + \frac{\sin^2\psi}{12\pi}\frac{Z\alpha^2}{\beta}Q_{ei}(\zeta;\beta)\sqrt{\zeta^2-1}\right]^{-1} \end{aligned} \tag{9.42}$$

In the solid state for electron-phonon scattering, we obtain

$$\frac{\mathrm{d}\tau}{\mathrm{d}\zeta} = \left(Y_e \frac{F}{m_u g_s}\frac{\lambda\!\!\!^-_e}{c}^2\right)\left[\frac{1}{3}\frac{\beta^2}{\alpha u_{-2}}\phi_{ep}(\zeta;\beta)\right]^{-1}, \ \psi = 0 \tag{9.43}$$

$$\tau^2\frac{\mathrm{d}\tau}{\mathrm{d}\zeta} = \left(Y_e \frac{F}{m_u g_s}\frac{\lambda\!\!\!^-_e}{c}^2\right)\left[\frac{1}{12}\frac{\alpha u_{-2}}{\beta}Q_{ep}(\zeta;\beta)\right]^{-1}, \ \psi = \frac{\pi}{2} \tag{9.44}$$

9.4 The High Temperature Regime

In the nondegenerate regime we assume that most of the heat is transported by photons and that free-free absorption provides the opacity. We take the unmagnetized thermal conductivity to be of the Kramer's form (Silant'ev & Yakovlev 1980),

$$\kappa^{(F)}_{\beta=0} = \kappa_0 \frac{T^{13/2}}{\rho^2} \tag{9.45}$$

where

$$\kappa_0 = \frac{1}{2.947}\frac{c_7}{\pi\sqrt{2\pi}}\frac{\sigma c k^{7/2} m_u^2 m_e^{3/2}}{e^6\hbar^2}\frac{A^2}{Z^3} \tag{9.46}$$

$$= \frac{16\sigma}{3}m_u\frac{196.5}{24.59}\frac{A^2}{Z^3}\frac{\mathrm{g}}{\mathrm{cm^5 K^{7/2}}}, \tag{9.47}$$

$c_7 = 316.8$ and σ is the Stefan-Boltzmann constant. The factor of 2.947 scales the results of Silant'ev & Yakovlev (1980) to agree with the results of Cox & Giuli (1968) (for discussion see Hernquist 1985).

Electron-scattering may also play a role in the nondegenerate regime. To simplify the calculation, we neglect its contribution and verify that it is indeed negligible. We take it to be given by (Silant'ev & Yakovlev 1980)

$$\kappa^{(T)}_{\beta=0} = \frac{16\sigma}{3\sigma_T}\frac{m_u}{Y_e}\frac{T^3}{\rho} \tag{9.48}$$

where σ_T is the Thompson cross section.

To determine which process dominates the heat transport, we take the ratio of the opacities for the two mechanisms (*e.g.* Van Riper 1988). The opacity is defined by

$$\widetilde{\kappa} = \frac{16\sigma}{3}\frac{T^3}{\rho\kappa} \tag{9.49}$$

The ratio of these contributions is given by

$$\begin{aligned}\frac{\widetilde{\kappa}^{(F)}_{\beta=0}}{\widetilde{\kappa}^{(T)}_{\beta=0}} &= \frac{\kappa^{(T)}_{\beta=0}}{\kappa^{(F)}_{\beta=0}} = 2.947\frac{16\pi\sqrt{2\pi}}{3c_7}\frac{Z^2}{A}\frac{e^6\hbar^2}{m_u\sigma_T c k^{7/2} m_e^{3/2}}\frac{\rho}{T^{7/2}} && (9.50)\\ &= 2.28\times 10^3\frac{Z_{26}^2}{A_{56}}\frac{\rho_0}{T_6^{7/2}} && (9.51)\end{aligned}$$

where $\rho_0 = \rho/1\ \mathrm{g\ cm}^{-3}$ In the next subsection, we find that this ratio is large throughout the non-degenerate portion of the envelope.

We parameterize the effects of the magnetic field by the anisotropy factor for free-free scattering, which dominates the opacity through the nondegenerate portion of the envelope (Pavlov & Yakovlev 1977, Silant'ev & Yakovlev 1980),

$$\kappa = \kappa_{\mathrm{unmagnetized}}\eta_{ff}(b,\psi) \tag{9.52}$$

(Silant'ev and Yakovlev used ζ where we use η). The function η consists of parallel and perpendicular contributions

$$\eta_{ff}(b,\psi) = \cos^2\psi\eta_{ff,\parallel}(b) + \sin^2\psi\eta_{ff,\perp}(b), \tag{9.53}$$

where $b = \beta/\tau$.

In weak and intermediate fields, the auxiliary functions are tabulated by Silant'ev & Yakovlev (1980).

For $b \gg 7$, the functions are given by (Pavlov & Yakovlev 1977)

$$\eta_{ff,\parallel}(b) = \frac{2}{3}qb^2\frac{1}{2(\xi-1)^2}\left[\xi + 2 - 3\sqrt{\frac{\xi}{|\xi-1|}}F(\xi)\right], \tag{9.54}$$

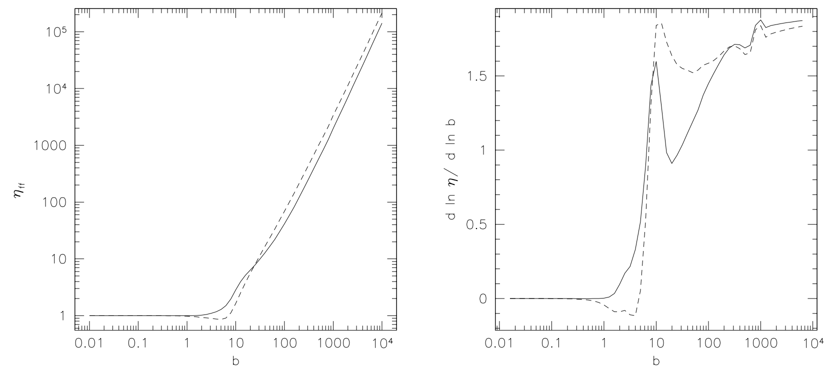

Figure 9.1: The left panel depicts the function η_{ff} *i.e.* the ratio of the magnetized to the unmagnetized free-free conductivity as a function of $b = \beta/\tau$ for parallel (solid line) and perpendicular (dashed line) transport. The right panel traces the logarithmic derivative of η_{ff}. We see that for large b (strong magnetic fields), η_{ff} is well approximated by a power law.

$$\eta_{ff,\perp}(b) \quad = \quad \frac{2}{3} q b^2 \frac{1}{4(\xi-1)^2} \left[2\xi - 5 + 3 \frac{F(\xi)}{\sqrt{\xi|\xi-1|}} \right], \tag{9.55}$$

with $q = 0.0214$ (Silant'ev & Yakovlev 1980). The parameter ξ is given by

$$\xi = \frac{1}{2} \left[\ln\left(\frac{1}{5} b\right) - \gamma_{\mathrm{Euler}} - 1 \right] \tag{9.56}$$

with $\gamma_{\mathrm{Euler}} = 0.577216$, and the function,

$$F(\xi) = \begin{cases} \arctan\left(\sqrt{\frac{1-\xi}{\xi}}\right) & \xi < 1 \\ \frac{1}{2} \ln\left(\frac{\sqrt{\xi}+\sqrt{\xi-1}}{\sqrt{\xi}-\sqrt{\xi-1}}\right) & \xi \geq 1. \end{cases} \tag{9.57}$$

We use these strong field results to extrapolate beyond the tabulated values in Silant'ev & Yakovlev (1980); *i.e.* for $b > 1000$. For $b < 1000$ we use the results of Silant'ev & Yakovlev (1980). The functions $\eta_{ff,\parallel}$ and $\eta_{ff,\perp}$ and their logarithmic derivatives are shown in Figure 9.1.

9.4.1 Non-degenerate Structure Equation

We follow the method of Hernquist & Applegate (1984), but we do not require that the conductivity be a power law in ρ and T.

In the non-degenerate regime, the thermal structure equation of the envelope is

$$\frac{\mathrm{d}T}{\mathrm{d}P} = \frac{F}{g_s}\frac{1}{\rho\kappa} \tag{9.58}$$

and we consider an unmagnetized conductivity which is a power law as Equation 9.45

$$\kappa = \kappa_0 \frac{T^\delta}{\rho^\alpha}. \tag{9.59}$$

Even in an intense magnetic field, in the nondegenerate regime, the pressure is given by the ideal gas law (Blandford & Hernquist 1982)

$$P = \frac{Y_e}{m_u}\rho k T. \tag{9.60}$$

We combine Equations 9.58–9.60 with Equations 9.45 and 9.52, yielding

$$\frac{\mathrm{d}T}{\mathrm{d}P} = \frac{F}{g_s}\frac{1}{\kappa_0}\left(\frac{m_u}{Y_e k}\right)^{\alpha-1} \frac{P^{\alpha-1}}{\eta_{ff}(b,\psi)T^{\alpha+\delta-1}}. \tag{9.61}$$

As for the structure equations in the degenerate limit, this equation is separable, yielding $\rho(T)$. Because η_{ff} depends on T through the argument b, the relation between T and P need not be a power law as in the unmagnetized case. In the limit that $\eta_{ff} = 1$, the result of Hernquist & Applegate (1984) obtains.

More generally, if we take, η_{ff} to be a power law $\propto b^{-2}$ (*e.g.* Tsuruta et al. 1972) which is approximately true for $b \to \infty$ as can be seen in Figure 9.1, we can immediately use the results of Hernquist & Applegate (1984) to obtain that the conductivity is constant through the nondegenerate envelope:

$$\kappa = \frac{\alpha+\delta-2}{\alpha}\frac{F}{g_s}\frac{Y_e k}{m_u} \tag{9.62}$$

$$= 7.07 \times 10^{13} \frac{Z_{26}}{A_{56}} \frac{T_{\mathrm{eff},6}^4}{g_{s,14}} \frac{\mathrm{erg}}{\mathrm{K\ cm\ s}} \tag{9.63}$$

for $\alpha = 2$ and $\delta = 6.5$ as in Equation 9.45. If we equate this result with our assumed conductivity and solve for T, we find that the solution follows

$$T = \left(\frac{\kappa}{a_\beta \kappa_0}\right)^{1/(\delta-2)} \rho^{\alpha/(\delta-2)} = 10^6\mathrm{K}\left(\frac{\rho}{\rho_{T_6}}\right)^{4/9} \tag{9.64}$$

where

$$a_\beta = \frac{2}{3} q \left(\frac{\beta m_e c^2}{k} \right)^2 \frac{1}{\ln b_{\rm Typical}} \tag{9.65}$$

$$\rho_{T_6} = 71.3 \text{ g cm}^{-3} \frac{\beta}{\sqrt{\ln b_{\rm Typical}}} A_{56}^{3/2} Z_{26}^{-2} T_{\rm eff,6}^{-2} g_{s,14}^{1/2}, \tag{9.66}$$

and $b_{\rm Typical}$ is a typical value of β/τ in the envelope, $b_{\rm Typical} \approx 6 \times 10^3 \beta$. One should note that for free-free scattering in the weak-field limit, $T \propto \rho^{4/13}$.

With Equation 9.64, we can calculate the density at the onset of degeneracy. We will assume that at the onset of degeneracy the electron density is given by Equation 9.15 and that $\tau \approx \zeta - 1$. This yields

$$\rho_{\rm ND/D} = 3.92 \times 10^5 \text{ g cm}^{-3} \beta (\ln b_{\rm Typical})^{1/7} A_{56}^{6/7} Z_{26}^{-5/7} T_{\rm eff,6}^{4/7} g_{s,14}^{-1/7}. \tag{9.67}$$

Also, by combining Equation 9.64 with Equation 9.51, we find that the ratio of opacities along the solution is given by

$$\frac{\widetilde{\kappa}_{\beta=0}^{(F)}}{\widetilde{\kappa}_{\beta=0}^{(T)}} = 1.74 \times 10^6 \rho_0^{-5/9} \left(\frac{\beta}{\sqrt{\ln b_{\rm Typical}}} \right)^{14/9} A_{56}^{4/3} Z_{26}^{-10/9} T_{\rm eff,6}^{-28/9} g_{s,14}^{7/9}. \tag{9.68}$$

Since this ratio increases with decreasing density, we only need to estimate it at the maximum density for the solution, *i.e.* the density at the onset of degeneracy

$$\left. \frac{\widetilde{\kappa}_{\beta=0}^{(F)}}{\widetilde{\kappa}_{\beta=0}^{(T)}} \right|_{\rm ND/D} = 1.36 \times 10^3 \beta (\ln b_{\rm Typical})^{-6/7} A_{56}^{6/7} Z_{26}^{-5/7} T_{\rm eff,6}^{-24/7} g_{s,14}^{6/7}. \tag{9.69}$$

For $B = 10^{14}$ G this ratio is greater than one for $T_{\rm eff} < 5.9 \times 10^6$ K, which is larger than the effective temperatures considered here. Furthermore, this is a conservative estimate of this ratio because generally we cut off the nondegenerate solution where degenerate electrons begin to dominate the heat conduction. In unmagnetized envelopes this occurs where the gas is mildly degenerate (Hernquist & Applegate 1984). We find that this is also the case for strongly magnetized envelopes.

9.5 Calculations

9.5.1 Strategy

We have found that the heat transfer equation is not solvable analytically, but it is separable in several cases. For the liquid and degenerate region of the envelope the solution may be calculated once for each field strength and geometry, and scaled to reflect the magnitude of the heat flux and shifted to fit the temperature at the low density edge of the region. We can apply this same strategy in the solid state only for the case of a purely radial or azimuthal field. Otherwise, for the solid region, the temperature as a function of chemical potential will depend on the flux and boundary conditions in a more complicated way; consequently, the solution must be recalculated for each value of the flux.

The general strategy is as follows:

1. Use the radiative zero solution for the given flux to determine the temperature and density at which degenerate electrons begin to dominate the heat conduction.

2. Determine the phase of the material at this depth in the envelope.

3. Calculate the appropriate (liquid or solid) solution for the boundary conditions determined by the radiative zero solution through the non-degenerate portion of the envelope.

4. Determine if the solution crosses a phase transition. We define the melting curve as follows (Slattery, Doolen & DeWitt 1980)

$$\Gamma \equiv \frac{(Ze)^2}{r_i kT} = \frac{Z^{5/3}\alpha}{\tau}\left(\frac{2}{3\pi}\beta\right)^{1/3}\left(\zeta^2-1\right)^{1/6} = \Gamma_m \approx 171 \qquad (9.70)$$

   where the second equality obtains in the degenerate limit when only one Landau level is filled. We have defined, r_i, the radius of the Wigner-Seitz cell, by $n_i 4\pi r_i^3/3 = 1$ where n_i is the number density of ions.

5. With the temperature and density at the phase change, continue the solution until the lowest Landau level is completely filled (*i.e.* $\zeta = \sqrt{2\beta+1}$). We will denote the temperature and density at this point by $T_{\rm max}$ and $\rho_{\rm max}$, respectively.

From the generic shape of the solutions (Equation 9.64), the envelope is solid at the lowest densities regardless of field strength (as long as $\beta \gg \tau$) and flux. The envelope may pass through a phase change in the nondegenerate regime. In the degenerate regime, for parallel transport, the envelope tends to be solid at the highest densities, while for perpendicular transport, it tends to be liquid. Therefore, in general, in the degenerate envelope, the matter may pass through a single phase change either liquid-to-solid for parallel transport or solid-to-liquid for perpendicular transport.

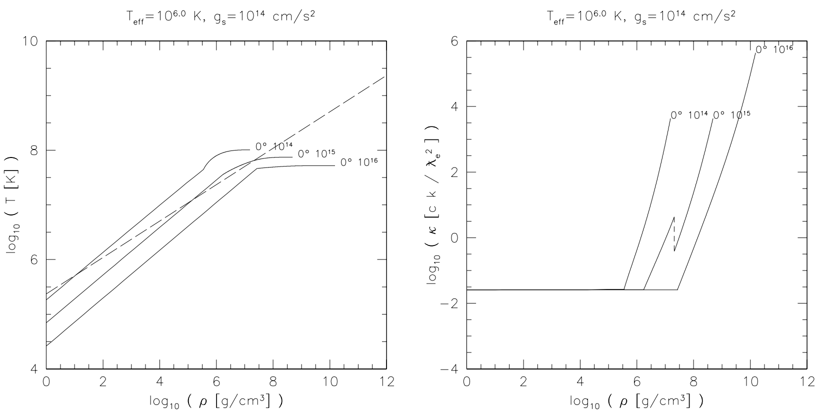

Figure 9.2: Thermal structure of a strongly magnetized neutron star envelope for a radial field. The left panel traces the temperature-density relation with $B = 10^{14}, 10^{15}, 10^{16}$ G and effective surface temperature of 10^6 K. The right panel traces the conductivity through the envelope. The constant conductivity solution appropriate for a purely power-law conductivity law works well through the nondegenerate regime. In the left panel, liquid phase exists above the dashed curve, and solid phase exists below.

9.5.2 Results for the separable structure equations

As described earlier, in the low-temperature limit when only one Landau level is filled the structure equation is simple and may be integrated for a given field strength and geometry and the boundary conditions and the dependence on the flux may be satisfied after the numerical solution is obtained.

Given these numerical results, it is straightforward to calculate the core temperature for a given surface temperature and flux. However, before fixing the boundary conditions, we can note several general features of the results. First, for transport along the magnetic field, the envelope becomes nearly isothermal at $\zeta - 1 \sim 0.1$ regardless of the magnetic field strength. However, for transport perpendicular to the field, the temperature rises steadily throughout the range of applicability of this formalism.

Parallel Transport In Figure 9.2 we present results for the degenerate and non-degenerate regime for several magnetic fields with an effective surface temperature of 10^6 K. In the nondegenerate regime the temperature solution follows the power-law given in Equation 9.64 and the *conductivity* is nearly constant. In the degenerate regime, the conductivity increases dramatically and the *temperature* remains nearly constant. For the solution with $B = 10^{15}$ G, the discontinuity in the conductivity at the phase transition is apparent. The results for 10^{14} G qualitatively agree with the results of Hernquist (1985) for this field strength. Quantitatively however, we find that the conductivity in the nondegenerate regime is thirty percent lower than the earlier result of 10^{14} erg/(K cm s) and is given by Equation 9.63. As the magnetic field strength increases, we find that the core temperature (or here the temperature at which the first Landau level is filled) decreases. This effect results from the increased conductivity in the nondegenerate regime where κ is approximately proportional to β^2 and the degenerate regime where the quantization of the electron phase space increases the conductivity above the zero-field values.

We take advantage of the simplicity of this analytic technique when calculating the thermal structure for hotter and cooler surface temperatures. We do not need to reintegrate the structure equations themselves. All that is required is to recalculate the boundary conditions at the nondegenerate-degenerate interface and the liquid-solid phase transition. Some representative results are shown in Figure 9.3. Again we find qualitative agreement with Hernquist (1985). In the nondegenerate regime, the increased or decreased flux mimics the effect of changing the field strength depicted in Figure 9.2.

We compare the various results by determining the temperature at the following densities: $\rho = 1.5 \times 10^7$, 4.7×10^8 and 1.5×10^{10} g/cm^3. These are the densities at which the lowest Landau level fills for field strengths of 10^{14}, 10^{15} and 10^{16} G. Moreover, since the matter is nearly isothermal at higher densities, these temperatures are close to the core temperature, at least for parallel transport. By fitting the results of the calculations, we find that at the lowest density:

$$T(\rho = 1.5 \times 10^7 \mathrm{g/cm}^3) \propto \beta^{-0.19} \left(\frac{F}{g_s}\right)^{0.35} \tag{9.71}$$

and at both the higher densities

$$T(\rho = 4.7 \times 10^8 \mathrm{g/cm}^3, 1.5 \times 10^{10} \mathrm{g/cm}^3) \propto \beta^{-0.16} \left(\frac{F}{g_s}\right)^{0.43} . \tag{9.72}$$

Figure 9.4 compares the numerical results with the best-fit power-law relations.

Perpendicular Transport Modeling the transition between photon and electron heat transport is qualitatively different for transport perpendicular to the field lines. In the parallel case, the conductivity from electrons

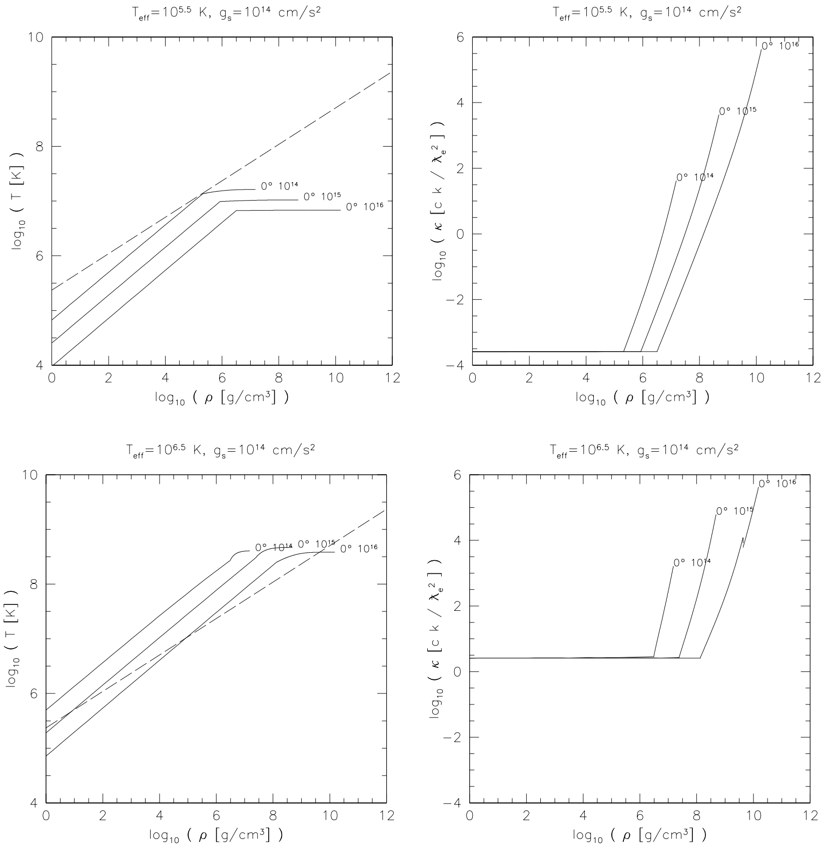

Figure 9.3: Same as Figure 9.2 but for different effective temperatures.

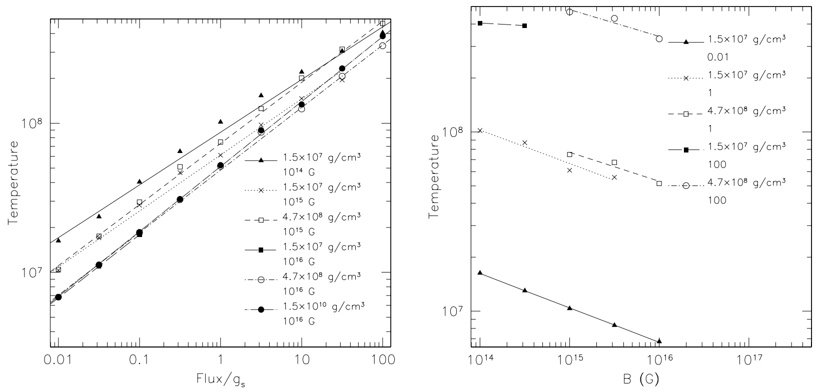

Figure 9.4: The left panel depicts the temperature-flux relation for several field strengths and densities. F/g_s is given in units of $\sigma(10^6 K)^4/10^{14}$ cm/s^2. The right panel depicts the temperature-magnetic-field relation. The symbols show the calculated data points and the lines are the best-fit power law functions to the data.

typically increases rapidly with density, and the transition from photon to electron-dominated heat transport is abrupt. For perpendicular transport, the function Q decreases with energy, and therefore the conductivity decreases with density for fixed temperature. In this case the transition is more subtle. Fortunately, the solution does not depend strongly on how this transition is treated, so we choose to employ $\zeta - 1 > \tau$ to delineate the region where electron conduction dominates. The conductivity is not continuous across this transition as is apparent in Figure 9.5.

We varied the definition of the non-degenerate-degenerate interface and found that it had little effect on the $T_{\rm max} - T_{\rm eff}$ relation. Figure 9.6 shows how the solution changes if we move the interface to a factor of ten higher or lower temperature (*i.e.* $\zeta - 1 > 10\tau$ and $\zeta - 1 > \tau/10$). Although near the interface the solutions differ dramatically, at higher densities the choice has little effect. The boundary condition at the transition is unimportant for perpendicular transport, because the temperature rises quickly with density, and the solution quickly "forgets" the boundary conditions, in a manner analogous to the convergence of the radiative zero solution to the true solution in stellar atmospheres (*e.g.* Schwarzschild 1965). This is in contrast to the case where $\psi \neq \pi/2$ where the material quickly becomes isothermal in the degenerate regime.

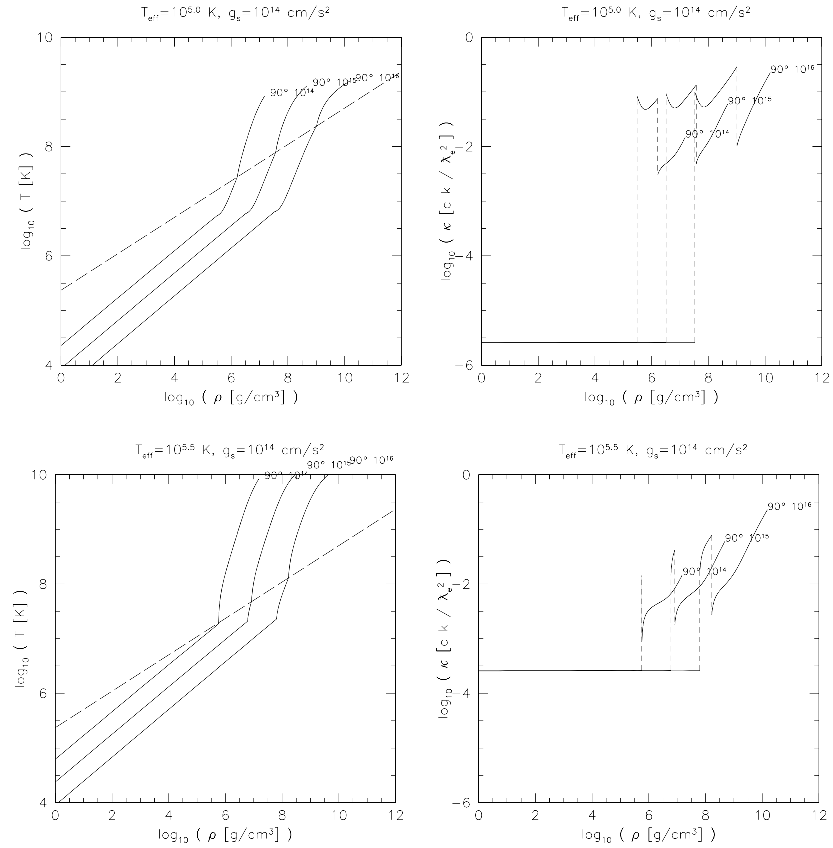

Figure 9.5: Same as Figure 9.3 for the perpendicular case.

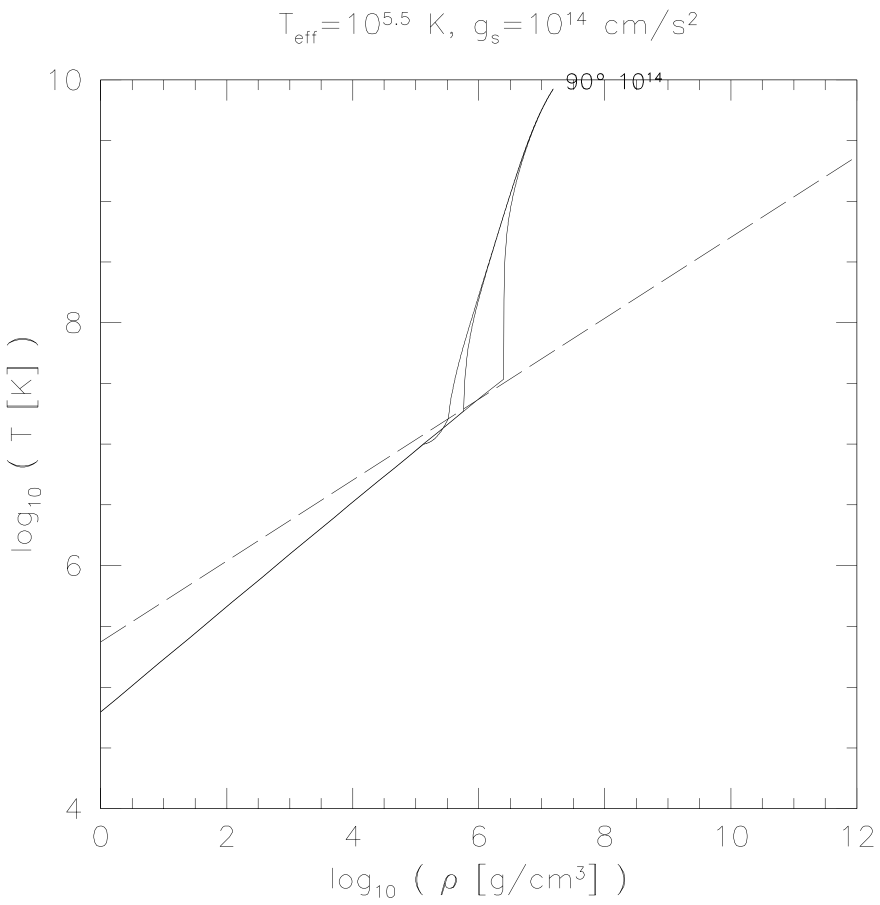

Figure 9.6: The dependence of the envelope solution for transport perpendicular to the magnetic field upon the definition of the non-degenerate-degenerate interface. We have calculated the location of the interface for $(\zeta - 1)/\tau = 0.1, 1, 10$ from left to right.

Table 9.2: Results of the Two Dimensional Calculations

Field Strength [G]	$T_{\rm eff}(\psi = 0)$ [K]	$T_{\rm max}(\zeta = \sqrt{2\beta + 1})]$ [K]
10^{14}	1.07×10^6	1.12×10^8
10^{15}	3.16×10^6	4.79×10^8
10^{16}	5.06×10^6	8.13×10^8

We find that for a given effective temperature the core temperature is much higher where the heat must travel perpendicularly to the field lines. Furthermore, we find that for stronger field strengths the effect is more pronounced.

Effective Temperature Distributions To find the effective temperature as a function of angle with respect to the magnetic field we vary the effective temperature as a function of angle until the temperature where the first Landau level fills is constant for the various angles. Unfortunately, where the magnetic field is neither radial or tangential we only have solutions in the non-degenerate and liquid degenerate regimes. Therefore, for acute angles we must select fluxes such that the degenerate solution is entirely in the liquid regime. For the more strongly magnetized envelopes we can follow the solution to higher densities; consequently, we must use larger effective temperatures for the stronger magnetic fields. Table 9.2 summarizes the parameters for the calculations.

Figure 9.7 depicts the results for $B = 10^{14}$ and 10^{16} G. For all but the perpendicular case, the envelope has become nearly isothermal by the density where the first Landau level fills.

Figure 9.8 shows the flux as a function of angle for all of the two-dimensional calculations. The agreement between the flux distribution and a simple $\cos^2 \psi$ law is striking. Greenstein & Hartke (1983) have argued that if the conductivity is constant through the envelope, the flux will follow a distribution of the form $A \cos^2 \psi + B \sin^2 \psi$. Although in the nondegenerate regime the conductivity along a $T(\rho)$ solution is nearly constant, in the degenerate regime it varies by several orders of magnitude. Furthermore, the nondegenerate layers do not throttle the heat flux; if they did, one would expect little variability, as the conductivity parallel and perpendicular to the field are nearly equal in the strong field limit (Figure 9.1).

We look to the degenerate structure equation for the liquid state to explain the remarkable agreement with a $\cos^2 \psi$ distribution. From examination of Equation 9.42, we see that if the conductivity transverse to the

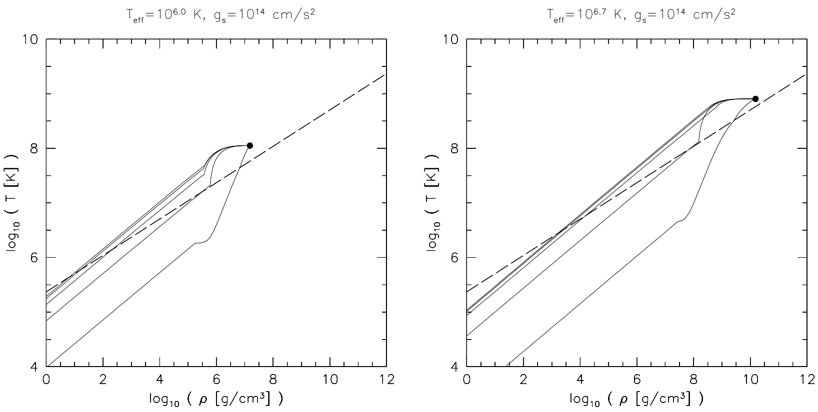

Figure 9.7: The left panel shows the temperature structure of the envelope as a function of density for $B = 10^{14}$ G and $T_{\rm eff} = 1.07 \times 10^6$ K at $\psi = 0$. From top to bottom, the results are for $\psi = 0°, 30°, 60°, 85°, 90°$ where ψ is the angle between the magnetic field and the radial direction. The right panel depicts the temperature structure for $B = 10^{16}$ G and $T_{\rm eff} = 5.06 \times 10^6$ K at $\psi = 0$. The solutions are constrained to have the same temperature at the density where the first Landau level fills (denoted by the bold circle). In both panels, liquid phase exists above the dashed curve, and solid phase exists below.

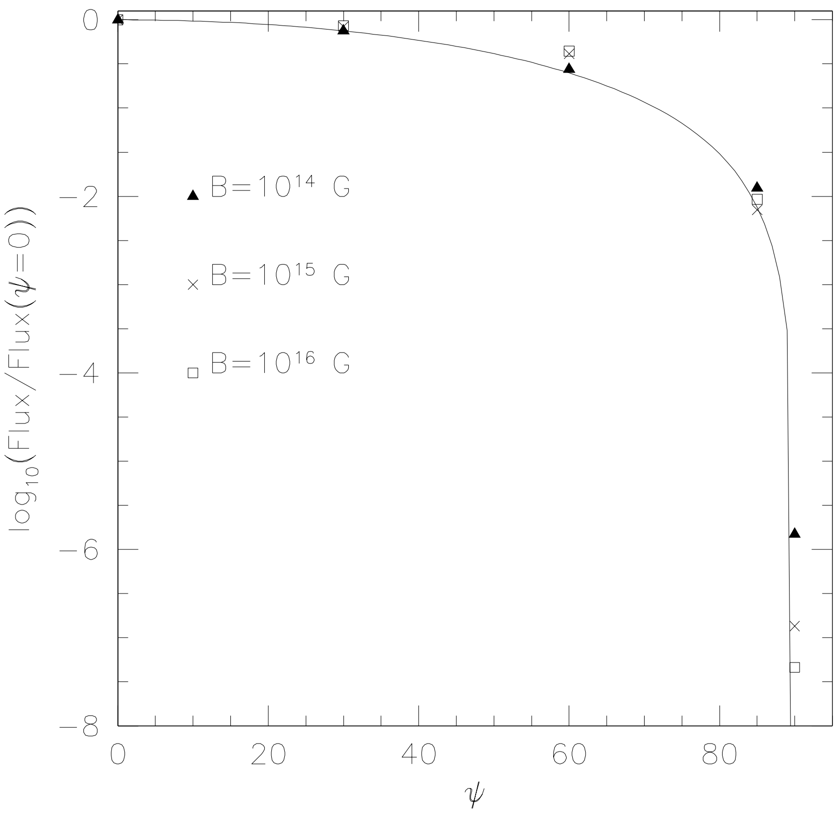

Figure 9.8: Flux as a function of angle for $B = 10^{14}, 10^{15}$ and 10^{16} G. The solid curve is $\cos^2 \psi$.

field is neglected, we can make the replacement

$$F \rightarrow F \cos^2 \psi \tag{9.73}$$

and recover the structure equation for $\psi = 0$. We determine where this approximation is valid by comparing the transverse and parallel components of the conductivity tensor

$$\frac{\kappa_{yy,ei}}{\kappa_{zz,ei}} = \frac{Z^2\alpha^4}{4\pi^2\beta^3}(\zeta^2-1)\frac{Q_{ei}(\zeta;\beta)}{\phi_{ei}(\zeta;\beta)} = 8.22 \times 10^{-11}\frac{Z_{26}^4}{A_{56}^2 B_{14}^5}\rho_6^2\frac{Q_{ei}(\zeta;\beta)}{\phi_{ei}(\zeta;\beta)}. \tag{9.74}$$

At first glance, it appears that the transverse conductivity is negligible throughout the degenerate regime. However, the functions Q_{ei} and ϕ_{ei} complicate the discussion. Specifically, $\phi_{ei} \rightarrow 0$ and $Q_{ei} \rightarrow \infty$ as $\zeta \rightarrow 1$; therefore, transverse conduction is likely to be important in the nonrelativistic portion of the degenerate envelope. Figure 9.7 shows that this is indeed the case. For $B = 10^{14}G$, the solutions for $\psi < \pi/2$ are nearly identical for $\rho > 10^{6.5}$ g/cm^3 or $\zeta > 1.1$. As ζ approaches unity, the ratio of the conductivities increases without bound, the transverse conductivity may no longer be neglected, and the runs of temperature with density begin to diverge.

Empirically, we find that in the region of the envelope which most effectively throttles the flux, the transverse conductivity may be neglected for $\psi < \pi/2$ without introducing significant error.

9.5.3 Observed Flux Distribution

We follow the technique outlined by Page (1995) to calculate the observed fluxes. However, unlike Page (1995) we evaluate the double integrals over the visible portion of the neutron star surface directly. We use the $\cos^2\psi$ rule to calculate the photon distribution function at the surface, and so we do not define a grid of precalculated distribution functions as does Page (1995).

As a first approximation, we focus on the variation of the observed bolometric flux with the angle φ of the line of sight with the magnetic dipole axis. This angle is a function of the phase angle (γ), the inclination of the dipole to the rotation axis (α) and the line of sight to the rotation axis (ζ)

$$\cos\varphi = \cos\zeta\cos\alpha + \sin\zeta\sin\alpha\cos\gamma \tag{9.75}$$

(Greenstein & Hartke 1983). For simplicity, in the discussion that follows we will take $\alpha = \zeta = \pi/2$; therefore $\varphi = \gamma$ and we refer to $\varphi = 0, \pi$ as on-phase and $\varphi = \pi/2, 3\pi/2$ as off-phase.

We repeat the calculation for several values of the stellar radius (with fixed mass) to determine the effects of general relativity on the light curves: gravitational redshift and the deflection of null geodesics (self-lensing, or more concisely "lensing").

To quantify the effect of gravitational lensing on the light curves of magnetized neutron stars, we calculate the mean value of the bolometric flux emitted by the surface over the visible region of the star. We assume that the flux at a given location on the surface is proportional to $\cos^2\psi$ where ψ is the angle between the radial direction and the magnetic field.

For clarity, we treat the gravitational redshift separately. Figure 9.9 depicts the ratio of the mean value of the flux over the visible portion of the star to the flux that would be emitted if the magnetic field were normal to the surface throughout (*i.e.* an isotropic temperature distribution).

In the limit of infinite radius, *i.e.* if lensing is unimportant, we find that for a uniform field

$$\bar{f}(\varphi=0)=\frac{1}{2}f(\psi=0) \text{ and } \bar{f}(\varphi=\pi/2)=\frac{1}{4}f(\psi=0). \tag{9.76}$$

For a dipole field, the calculation is slightly more complicated. First, we used Equation 9.34 to determine the angle of the field with respect to the radial direction. Secondly from equations 9.71 and 9.72, we find that the emergent flux is a function of the field strength. For a dipole configuration, the magnitude of the field varies as

$$\beta \propto \sqrt{3\cos^2\theta+1} \tag{9.77}$$

along the surface of the star. Since we are most interested in fixing the internal temperature at high densities we assume that the flux is proportional to $B^{0.4}$ from Equation 9.72 which reduces the flux for $\theta\sim\pi/2$ further beyond the $\cos^2\psi$ rule. We obtain

$$\bar{f}(\varphi=0)=0.663f(\psi=0) \text{ and } \bar{f}(\varphi=\pi/2)=0.393f(\psi=0). \tag{9.78}$$

If we did not include the effect that the flux is a function of field strength as well as orientation we would have obtained 0.717 and 0.444 for the above values.

We find that the mean flux is greater for the dipole configuration than for a uniform field for all viewing angles if $R/R_s<5$, and that the variation in the light curve is generally smaller. We have taken $M_{\rm NS}=1.4{\rm M}_\odot$, yielding a Schwarzschild radius, R_s, of 4.125 km. The theoretical predictions for the radius of a $1.4{\rm M}_\odot$ neutron star range from 6.5 km to 14 km (Thorsson, Prakash & Lattimer 1994; Pandharipande 1971; Wiringa, Fiks

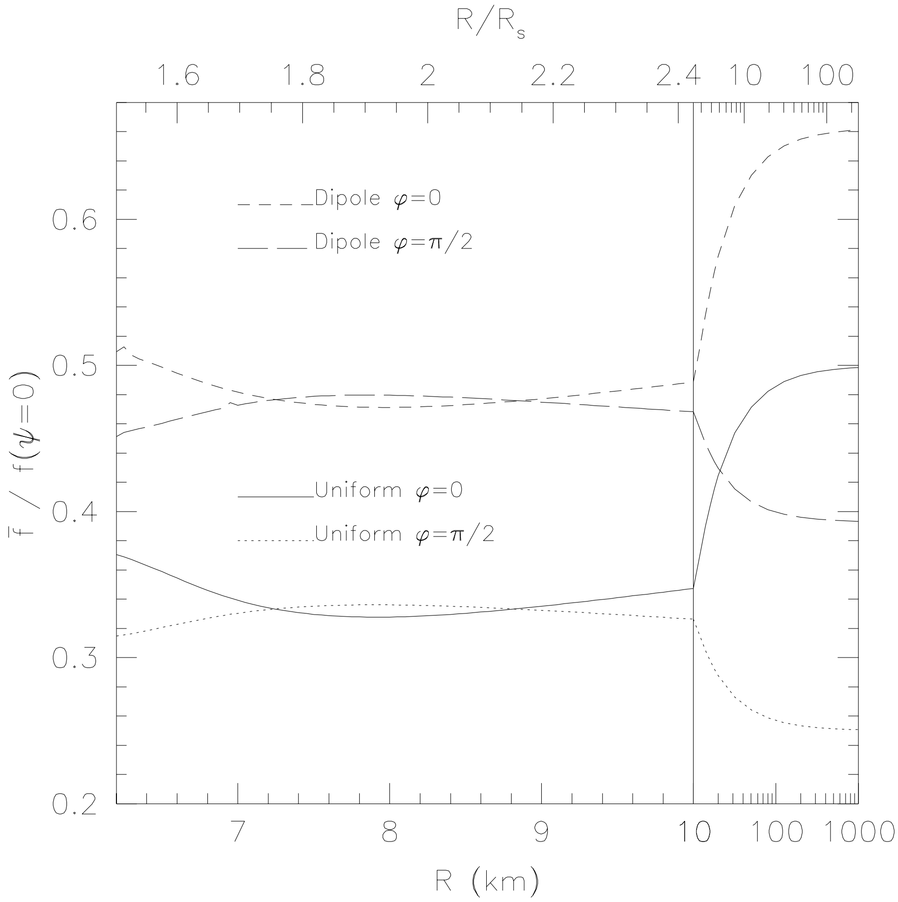

Figure 9.9: The average of the bolometric flux over the visible portion of the neutron star for $\varphi = 0, \pi/2$. The upper pair is for a dipole, and the lower is a uniform field configuration.

& Fabrocini 1988), depending on the details of the equation of star at supernuclear densities.

As Page (1995) found, lensing dramatically reduces the variation of the observed flux with phase by making more than half the surface visible at any time. Interestingly, for the range of radii 7.248 – 8.853 km, we find that the flux is greater when the magnetic poles are located perpendicular to the line of sight. For this range of radii over 90% of the surface is visible. Emission from both of the hotspots reaches the observer leading to a larger flux. For radii less than 7.248 km the entire surface is visible and again the peaks are on phase. Page (1995) found a similar effect for the same range of radii.

The emitted spectra from the visible portion of the neutron-star surface is the sum of blackbody spectra of various temperatures. To determine the emitted spectra, we calculate the distribution of blackbody temperatures on the surface; *i.e.* we estimate the distribution function $\mathrm{d}\bar{f}/\mathrm{d}T_{\mathrm{eff}}$. With this distribution function, it is straightforward to calculate the emergent spectrum averaged over the visible portion of the surface as

$$\bar{f}_\omega = \int_0^\infty \frac{\mathrm{d}\bar{f}}{\mathrm{d}T_{\mathrm{eff}}} \frac{1}{\sigma T_{\mathrm{eff}}^4} \frac{\hbar}{4\pi^2 c^2} \frac{\omega^3}{\exp(\hbar\omega/kT) - 1} dT_{\mathrm{eff}}. \tag{9.79}$$

The factor of $\sigma T_{\mathrm{eff}}^4$ converts the flux to an effective area of emission ($\bar{A}$). The calculation of $\mathrm{d}\bar{f}/\mathrm{d}T_{\mathrm{eff}}$ is numerically more tractable than $\mathrm{d}\bar{A}/\mathrm{d}T_{\mathrm{eff}}$ and allows us to account for the total energy emitted more reliably.

We calculate $\mathrm{d}\bar{f}/\mathrm{d}T_{\mathrm{eff}}$ in similar fashion to $\bar{f}$. To expedite the calculation, we note that given the $\cos^2\psi$ rule the neutron star surface has a limited range of effective temperatures, specifically between 0 and $T_{\mathrm{eff}}(\psi = 0)$. Consequently we define

$$\widetilde{T} = \frac{T_{\mathrm{eff}}}{T_{\mathrm{eff}}(\psi = 0)} \tag{9.80}$$

$$\frac{\mathrm{d}\bar{f}}{\mathrm{d}\widetilde{T}} = \frac{\mathrm{d}\bar{f}}{\mathrm{d}T_{\mathrm{eff}}} T_{\mathrm{eff}}(\psi = 0). \tag{9.81}$$

For observations on-phase ($\varphi = 0$) and without lensing ($R \rightarrow \infty$), the flux-weighted temperature distribution can be calculated directly if the envelope is uniformly magnetized. It is given by

$$\frac{\mathrm{d}\bar{f}}{\mathrm{d}\widetilde{T}} = 4\widetilde{T}^7 f(\psi = 0). \tag{9.82}$$

The result for the dipole cannot be written explicitly and is not illustrative.

For a general geometry ($\varphi \neq 0$), we expand this function in an orthonormal basis on the interval 0 to 1. Specifically, we assume that for $0 \leq \widetilde{T} \leq 1$

$$\frac{\mathrm{d}\bar{f}}{\mathrm{d}\widetilde{T}} = \sum_{l=0}^{\infty} A_l Q_l(\widetilde{T}) \tag{9.83}$$

and zero otherwise, where

$$Q_l(\widetilde{T}) = \sqrt{2l+1} P_l(2\widetilde{T} - 1). \tag{9.84}$$

The $P_l(x)$ are the Legendre polynomials. From the properties of these orthonormal functions, we have $A_0 = \bar{f}$, and A_l is calculated by inserting the weighting function $Q_l(\widetilde{T})$ into the integrands in the calculation for $\bar{f}$. We recall that we have assumed, $\widetilde{T} = \cos^{1/2}\psi$

Using an orthonormal basis dramatically speeds the calculation of the distribution. Additionally, because the $P_l(x)$ are polynomials, it is straightforward to calculate conventional statistics of the distribution

$$\left\langle \widetilde{T} \right\rangle = \frac{1}{\bar{f}} \int_0^1 \widetilde{T} \frac{\mathrm{d}\bar{f}}{\mathrm{d}\widetilde{T}} d\widetilde{T} = \frac{\sqrt{3}}{6}\frac{A_1}{A_0} + \frac{1}{2} \tag{9.85}$$

$$\left\langle \widetilde{T}^2 \right\rangle = \frac{\sqrt{5}}{30}\frac{A_2}{A_0} + \frac{\sqrt{3}}{6}\frac{A_1}{A_0} + \frac{1}{3}. \tag{9.86}$$

Unfortunately, with this basis is impossible to insist that distribution is everywhere non-negative, *i.e.* that no temperatures contribute negative flux. However, if a sufficiently large number of A_l are calculated, the intervals where $\mathrm{d}\bar{f}/\mathrm{d}\widetilde{T} < 0$ can be made to be arbitrarily small and to have an arbitrarily small contribution to the total flux. We compare the results of the expansion with Equation 9.82 and find that the maximum relative error in the expansion coefficients between the two techniques is approximately 9×10^{-5}.

Figure 9.10 depicts the results of this calculation for four values of the stellar radius with $\varphi = 0, \pi/2$. In the left panel, we see in the absence of general relativistic effects that when the neutron star is off-phase more flux is produced at lower blackbody temperatures than when the magnetic dipole is pointing toward the observer. For the smallest radius considered ($R = 6.25$ km), the entire surface of the neutron star is visible and a large portion of the front hemisphere has a second image. In this case, both the flux-weighted temperature distributions at $\varphi = 0$ and $\pi/2$ are peaked at the maximum effective temperature. However, the distribution off-phase has a more well populated tail extending toward lower temperatures than on-phase.

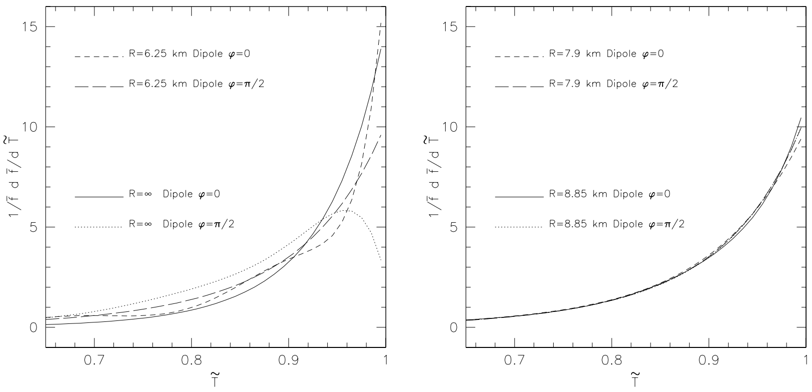

Figure 9.10: The fractional distribution of observed flux as function of the surface blackbody temperature. The left panel depicts the distribution for the minimal ($R/R_s = 1.52$) and maximal radii ($R = \infty$) considered. The right panel depicts the distribution at a radii where $\bar{f}(\varphi = 0) = \bar{f}(\varphi = \pi/2)$ ($R = 8.85$ km) and where the off-phase peaks are maximized ($R = 7.9$ km). All the curves are normalized to have an integral of unity from $\widetilde{T} = 0$ to 1

The right panel depicts a value of the stellar radius ($R = 8.85$ km) where there is practically no variation of $\bar{f}$ with phase. Additionally, we see that the flux-weighted temperature distributions are nearly constant with phase. Also depicted is the temperature distributions for $R = 7.9$ km, the radius where the off-phase peaks are maximized. Here again, the distributions do not change appreciably with phase. We conclude that for $7 \lesssim R \lesssim 9$ km, it would be difficult to detect variation of the spectra with phase, if the neutron star surface indeed radiates as a blackbody.

To calculate the spectra themselves, it is convenient to define the following functions,

$$\mathcal{F}_l(\widetilde{\omega}) = \frac{15}{\pi^4}\widetilde{\omega}^3 \int_0^1 Q_l(\widetilde{T}) \frac{1}{\widetilde{T}^4} \frac{1}{\exp(\widetilde{\omega}/\widetilde{T}) - 1} d\widetilde{T}, \tag{9.87}$$

where $\widetilde{\omega} = \hbar\omega / kT_{\rm eff}(\psi = 0)$, so that

$$\bar{f}_\omega(\omega) = \frac{\hbar}{kT_{\rm eff}(\psi = 0)} \sum_{l=0}^{\infty} A_l \mathcal{F}_l \left(\frac{\hbar\omega}{kT_{\rm eff}(\psi = 0)} \right). \tag{9.88}$$

Since A_l has units of flux, we obtain the correct units of flux-time for $\bar{f}_\omega$.

To convert to the observed spectra, we must account for gravitational redshift and interstellar absorption; we obtain (Page 1995)

$$f_\omega^{\rm observed}(\omega) = \bar{f}_\omega(e^{-\Lambda_s}\omega)e^{-\Lambda_s}\frac{R_\infty^2}{D^2}e^{-N_H\sigma(\omega)} \tag{9.89}$$

where

$$R_\infty \equiv R e^{\Lambda_s} \tag{9.90}$$

where $e^{-\Lambda_s}$ is given in Equation 9.30. The final term accounts for interstellar absorption and D is the distance to the neutron star. For $\sigma(E)$ we use the Morrison & McCammon (1983) cross-sections.

Figure 9.11 depicts the spectra in the ROSAT energy range for two neutron stars. Each of the spectra (light curves) is well fit by a blackbody (heavy curves) at the mean effective temperature with an additional hard component. The mean effective temperature ($T_{\rm mean}$) is defined by

$$\int f_\omega^{\rm observed}(\omega)d\omega = \sigma T_{\rm mean}^4\frac{R_\infty^2}{D^2} \tag{9.91}$$

for $N_H = 0$, *i.e.* it is the equivalent blackbody temperature that accounts for all of the energy emitted from the neutron star surface. The hard component is most significant when the star is observed at right angles to the magnetic axis, and originates from the portions of the hot polar caps that are visible even when the star is off-phase.

In Appendix 9.A, we present two `XSPEC` models which are available over the WWW. With these models, one may simulate observations from various x-ray instruments to estimate the observed pulsed fractions for the models discussed in this section. We present an example in Figure 9.13.

9.5.4 Neutron Star Cooling

We can use the results of the preceding sections to determine the effects of the magnetic field on neutron star cooling rates. Specifically, we take the ratio of the total flux from the surface with and without a magnetic field for the same core temperature. We have used the results of Hernquist & Applegate (1984). To determine the core temperature for a given flux we combine their equations (4.7) and (4.8), switching from the first relation to the second when the surface effective temperature drops below 4.25×10^5 K. The results do not depend qualitatively on whether equation (4.7) or (4.8) of Hernquist & Applegate (1984) is used.

To compare our calculated temperature-flux relation with the results for isotropic heat transport, we multiply the fluxes for the magnetized envelopes by 0.4765 to account for a dipole field configuration. Additionally,

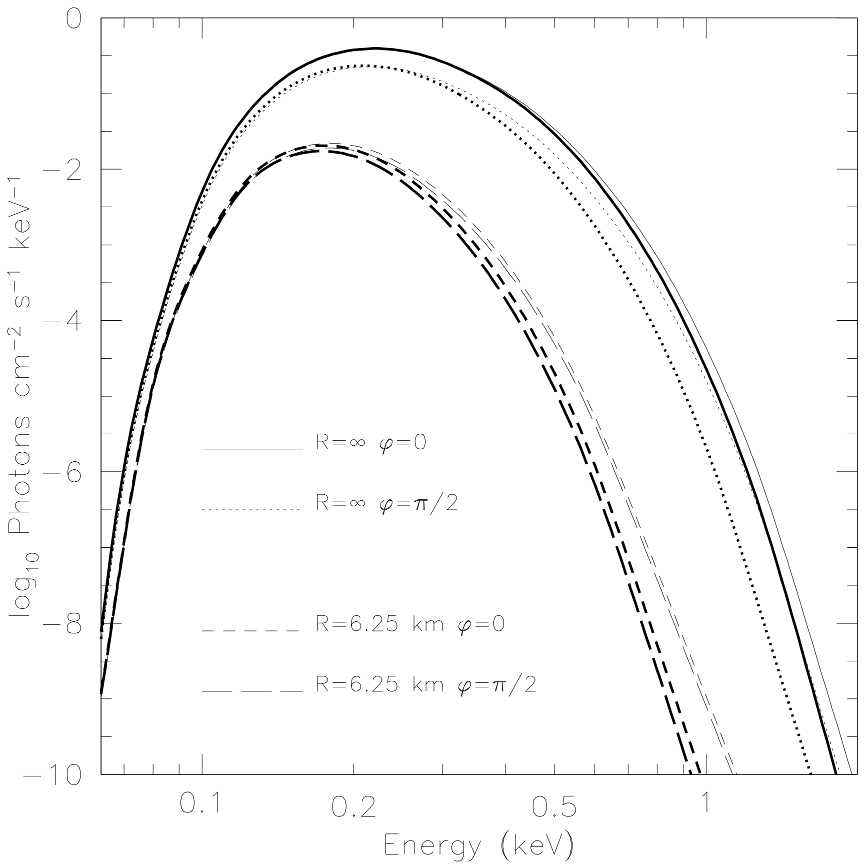

Figure 9.11: The observed spectra from a neutron star with $T_{\rm eff}(\psi = 0) = 7.5 \times 10^5$ K from a distance of 250 pc with an intervening absorption column of $N_H = 10^{20} \mathrm{cm}^{-2}$. The light curves show the spectra, and the heavy curves show blackbody spectra at the mean effective temperature of the neutron star. For the $R = \infty$ model, we have taken $R/R_s \to \infty$ while $R = 20$ km to give the surface area of the neutron star, while neglecting general relativistic effects.

we assume in our calculations that the envelope is isothermal above the density ($\rho_{\max}$) at which the first Landau level fills and use the temperature ($T_{\max}$) at this density to estimate the flux in the unmagnetized case. Only for the strongest field strength considered ($B = 10^{16}$ G) do our analytic calculations extend to the core density assumed by Hernquist & Applegate (1984) of 10^{10} g/cm^3; however, we do not expect the results to be strongly sensitive to this cutoff density as our solutions (for $\psi \neq \pi/2$) are nearly isothermal at high densities.

Figure 9.12 depicts the results of this comparison. We find that for the weakest field strength considered ($B = 10^{14}$ G), the magnetic field has little effect on the total luminosity of the star. However, for cooler core temperatures and stronger magnetic fields, the difference in the luminosities can be up to a factor of ten. The flux ratio is sensitive to the core temperature because Equations 9.71 and 9.72 have a slightly different power-law index than the model assumed for the unmagnetized envelope (0.392). The inflection in each of the curves occurs when the material near non-degenerate-degenerate interface melts as the core temperature increases. All the curves swing upward for high values of $T_{\max}$ because for high fluxes (*i.e.* high core temperatures) our assumption that the temperature is constant for $\rho > \rho_{\max}$ no longer holds.

Because strongly magnetized neutron stars emit significantly more flux, we expect that the thermal history of magnetars should be dramatically different from that of neutron stars with weaker magnetic fields. We discuss this issue further in a subsequent paper (Heyl & Hernquist 1997e).

9.6 Discussion

We have presented an analytic technique for calculating the thermal structure of ultramagnetized neutron star envelopes. We use the exact thermal conductivities in an intense magnetic field of Silant'ev & Yakovlev (1980) and Hernquist (1984) in the non-degenerate and degenerate regimes, respectively. We make two simplifying approximations. We assume that the interface between degenerate and non-degenerate material is abrupt. Hernquist (1985) numerically calculated the thermal structure for $B = 10^{14}$ G without this assumption. Our agreement with this earlier result shows that an abrupt interface is a good approximation. Secondly, we use a standard simplification in the study of stellar atmospheres which is to use the radiative zero solution to fix the outer boundary condition (Schwarzschild 1965). Because the equation for the thermal structure in the outermost layers is qualitatively similar to the relation for an unmagnetized envelope, we conclude that as in the unmagnetized case (Hernquist & Applegate 1984), this

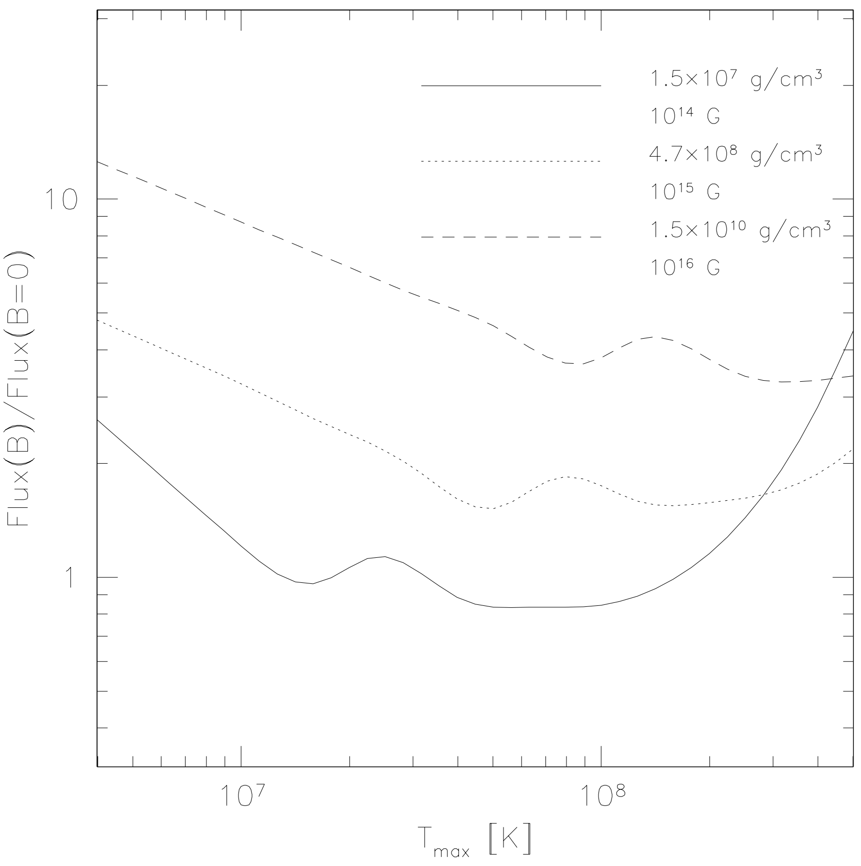

Figure 9.12: The ratio of fluxes in magnetized envelopes to those in unmagnetized ones. We have assumed that the envelope is isothermal above the densities given in the legend to estimate the unmagnetized fluxes.

is also an accurate approximation.

Because the derived thermal structure equations are separable and simple to integrate, one may quickly calculate the thermal structure up to the density at which the first Landau level fills for several field strengths, geometries and intensities of the transmitted flux. With the calculated grid of models, we find that the relation between transmitted flux, field strength and core temperature is well approximated by a power-law. Additionally, because for much of the degenerate envelope, the conductivity along the magnetic field is much larger than perpendicular to it, the transmitted flux is proportional to $\cos^2\psi$, where ψ is the angle between the field and the radial direction. Greenstein & Hartke (1983) justified this relationship when the conductivity is constant through the envelope. However, this justification does not apply in the degenerate regime which throttles the heat flux and where the conductivity varies by several orders of magnitude. Shibanov et al. (1995) also found that this relationship holds for weaker fields in their purely numerical treatment of the thermal structure.

If this $\cos^2\psi$ rule is combined with a model atmosphere, we can calculate the observed flux, by integrating over the neutron star surface and accounting for deflection of the light paths by the neutron star's gravitational field. We choose a blackbody atmosphere which has the added advantage that the spectra shift and scale simply as a function of surface temperature. We find that the observed spectra integrated over the visible portion of the surface exhibit a hard component in addition to the best-fitting blackbody. Since our calculated spectra agree quantitatively with those of Page (1995) for a given maximum surface temperature and stellar radius, we find a similar pulsed fraction of approximately 10% for theoretically acceptable radii of $1.4\mathrm{M}_\odot$ neutron stars of $6.5 - 14$ km (Thorsson, Prakash & Lattimer 1994; Pandharipande 1971; Wiringa, Fiks & Fabrocini 1988). Although the observed pulsed fractions are often as large as 30%–50% (Yancopoulos, Hamilton & Helfand 1994; Halpern & Wang 1997), it may not be necessary to resort to unrealistic large stellar radii or multipole components of the magnetic field (*e.g.* Page & Sarmiento 1996). A more realistic treatment of the atmosphere may be sufficient to explain the large pulsed fractions.

Pavlov et al. (1994) argue that in addition to the transmission of heat through the envelope, the emission at the surface is also strongly anisotropic. Anisotropic emission can naturally produce large pulsed fractions even when the temperature on the surface is uniform (Zavlin et al. 1995, Shibanov et al. 1995). Additionally, the composition of the atmosphere may have a profound effect on the emergent radiation. A magnetized iron atmosphere produces substantial limb darkening for $\psi \sim \pi/2$, and the decrement is strongest at high energies (Rajagopal, Romani & Miller 1997). It is straightforward to graft these atmospheres onto the thermal envelopes calculated here to obtained the observed time-dependent spectra for a variety of realistic neutron star models. These effects may be sufficient to account for the large observed pulsed fractions.

The calculation of the thermal structure itself suggests several avenues for further work. Presently, these models are the only ones available for $B > 10^{12}$ G for conduction oblique to the field lines, and for $B > 10^{14}$ G, the only ones for oblique or parallel transport. A natural route is to extend these analytic models to weaker fields. The calculation of the structure in the non-degenerate regime is independent of field strength, and the degenerate calculation is valid until the first Landau level fills. As the first Landau level fills, both of the functions ϕ and Q are ill behaved, upsetting the Sommerfeld expansion used to derive Equations 9.19 and 9.20, and 9.25 and 9.26; consequently, whenever $\zeta = \sqrt{1 + 2n\beta}$ for $n = 0, 1, 2, \ldots$, a well-defined low-temperature limit for the degenerate conductivities does not exist.

However, as long as the temperature does not approach the spacings between the Landau levels ($\tau \ll \beta$), we can derive separable, although more complicated, thermal structure equations for regions where the uppermost occupied Landau level is neither nearly full nor nearly empty. Potekhin & Yakovlev (1996) present practical formulae for the functions ϕ_{ep} and ϕ_{ei} for arbitrary field strengths and Landau levels, and for transverse conduction the results of Hernquist (1984) are applicable for $B \leq 10^{14}$ G and the lowest thirty Landau levels. Regions where $\zeta \approx \sqrt{1 + 2n\beta}$ must be treated separately either numerically or as an abrupt interface. It is likely that the specific treatment of these regimes would have little effect on the core-temperature-flux relation for the envelope.

A distinct approach is to treat the entire problem numerically, which would allow us to estimate directly the possible errors that our simplifying assumptions introduce and would alleviate the problem of how to treat the regions where $\zeta \approx \sqrt{1 + 2n\beta}$ by passing it on to the computer. Again, numerical models for transverse conduction are not available for field strengths exceeding 10^{12} G, so this would a valuable exercise.

9.7 Conclusions

We derive nearly analytic models for the thermal structure of neutron star envelopes with $B \geq 10^{14}$ G and apply these models to calculate the distribution of effective temperature on the surface of the neutron star for several core temperatures and magnetic field strengths. We find that the relation between transmitted flux, core temperature and field strength may be approximated by a power law and that the effective temperature is proportional to $\cos^{1/2}\psi$ where ψ is the angle between the radial direction and the local direction of the magnetic field. Using the geometric result, we calculate the observed spectra as a function of viewing angle including the effects of general relativity for dipole and uniform field configurations. We extend the conclusions of previous work. If the surface is assumed to radiate as a blackbody and neutron stars have radii within the currently accepted range, the anisotropic heat transport induced by a dipole field configuration is insufficient to produce the observed pulsed fractions even for ultramagnetized envelopes.

Several avenues for additional study stand out. The assumption of blackbody emission from the surface should be relaxed. More realistic atmospheres may be grafted onto these models in a straightforward manner. A more subtle issue to explore is how to extend these calculations to weaker fields where several Landau levels may be filled in the degenerate portion of the envelope.

9.A Appendix : XSPEC Models

Rather than present results for specific instruments and band passes, we supply our results in machine-readable form. We have calculated neutron star spectra for several values of R/R_s, and $\varphi = 0, \pi/2$. We assume a dipole field configuration and the $\cos^2\psi$ rule. The model is calculated for

$$T_{\mathrm{eff},\infty}(\psi = 0) = T_{\mathrm{eff}}(\psi = 0)\sqrt{1 - \frac{R_s}{R}} = 10^6\mathrm{K} \tag{9.92}$$

where $R_s = 2GM/c^2$. $T_{\mathrm{eff},\infty}(\psi = 0)$ may be varied by applying a redshift and renormalization to the spectra. For ease of use by the x-ray astronomy community, we have created `XSPEC` table models with the data.

Within `XSPEC`, the models may be convolved with the response matrix for various x-ray instruments and compared with observed spectra. By using the redshift (z) and normalization (K) parameters we may obtain models for different effective temperatures and radii:

$$K = \left(\frac{R_{\infty,\mathrm{km}}}{D_{10}}\right)^2 \left(\frac{T_{\mathrm{eff},\infty}}{10^6\ \mathrm{K}}\right)^3 \tag{9.93}$$

$$z = \frac{10^6\ \mathrm{K}}{T_{\mathrm{eff},\infty}} - 1 \tag{9.94}$$

where $R_{\infty,\mathrm{km}}$ is the source radius in km as observed at infinity, *i.e.*

$$R_\infty = Re^{\Lambda_s} = R\left(1 - \frac{R_s}{R}\right)^{-1/2} \tag{9.95}$$

from Equation 9.90 and D_{10} is the distance to the neutron star in units of 10 kpc. This particular choice is consistent with the definition of the `bbodyrad` model in `XSPEC`.

Each additive model contains the single interpolation parameter R_s/R which ranges from 0 to 0.6601. As an illustration Figure 9.13 depicts one of the models convolved with the ROSAT PSPC response function for $R/R_s \to \infty$, $R = 20$ km and $D = 250$ pc with $N_H = 10^{20}$ cm^{-2}. Here, we have used the `wabs` model to calculate the interstellar absorption which assumes the Morrison & McCammon (1983) cross-sections.

The errorbars are calculated for an exposure of 10^4 seconds. For these parameters, the variation of the thermal flux with phase is apparent in the spectra. However, as we saw in the previous sections as R/R_s decreases, the variation in the thermal flux weakens.

The table models are available at the following URLs:
`http://www.ucolick.org/~jsheyl/analytic_ns/p0.fits` for $\varphi = 0$
`http://www.ucolick.org/~jsheyl/analytic_ns/p90.fits` for $\varphi = \pi/2$.

The `XSPEC` software itself is available at
`ftp://legacy.gsfc.nasa.gov/software/xanadu/`,
and an online manual is provided at
`http://www.merate.mi.astro.it/~xanadu/xspec/u_manual.html`.

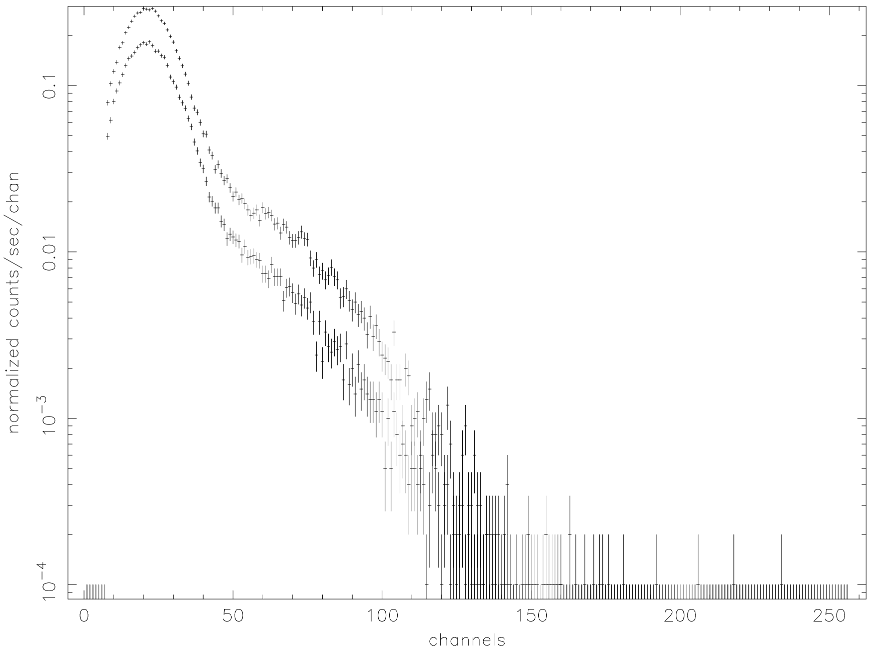

Figure 9.13: The calculated model spectra convolved with the ROSAT PSPC response matrix for $\varphi = 0$ (upper points) and $\varphi = \pi/2$ (lower points). The model parameters are described in the text. The errorbars are for an exposure of 10^4 s.

Chapter 10

Numerical Models of Neutron Star Envelopes

SUMMARY

The analytic study of neutron star envelopes presented in the previous chapter is only applicable for neutron stars that are cold enough and have sufficiently strong magnetic fields. Here, we present a numerical algorithm to calculate the thermal structure of neutron star envelopes without the assumptions made earlier. Unlike earlier work, we present envelope models in two dimensions which precisely account for the quantization of the electron phase space. Both dipole and uniformly magnetized envelopes are considered.

10.1 Introduction

Although analytic studies of neutron star envelopes can well characterize the emission from cooling neutron stars, especially those with sufficiently weak or sufficiently strong fields, most potentially observable neutron stars have field strengths in neither of these limits and high core temperatures which invalidate the low-temperature approximation used in the previous chapter.

The analytic technique outlined earlier assumes that the only the first Landau level is filled, the transition for the highly non-degenerate regime to the highly degenerate regime is abrupt and that either electrons or photons dominate the heat transfer. In the calculations is this chapter, all three of these assumptions are relaxed, and the equations of thermal structure integrated using the opacity that approach those used in Chapter 9 in the low and high temperature limits (Pavlov & Yakovlev 1977, Silant'ev & Yakovlev 1980, Hernquist 1984).

In Chapter 9 several two dimensional models of neutron-star envelopes were presented. Unfortunately, the separation of the structure equation required that the two-dimensional models be restricted to the case where the entire degenerate portion of the envelope is the liquid state. Here, because the equations are solved numerically, this restriction is not important. We construct several uniformly magnetized envelopes whose surface emission follows the $\cos^2\psi$ rule outlined earlier and verify that this distribution yields a uniform core temperature more generally. These two-dimensional results are compared with those of Schaaf (1990a) and extended to include envelopes with a dipole field structure.

Although it would be straightforward to examine additional effects such as Coulomb corrections (*e.g.* Van Riper 1988, Thorolfsson et al. 1997), for clarity and brevity only the processes included in Chapter 9 are incorporated and the effects of the approximating assumptions determined.

10.2 The Physical Description of the Envelope

Because the assumptions made in the preceding chapter will be relaxed, it is important to present the complete equations governing the thermal structure of neutron star envelopes. Again as argued earlier a plane-parallel treatment is suitable for the problem. Again the following set of dimensionless units will be used

$$\beta = \frac{\hbar\omega_B}{m_e c^2} = \frac{\hbar|e|}{m_e^2 c^3} B \approx \frac{B}{4.4\times 10^{13}\ \mathrm{G}}, \tag{10.1}$$

$$\tau = \frac{kT}{m_e c^2} \approx \frac{T}{5.9\times 10^{9}\ \mathrm{K}}, \tag{10.2}$$

$$\gamma = \frac{E}{m_e c^2} \text{ and } \zeta = \frac{\mu}{m_e c^2} \tag{10.3}$$

where the E is the energy of an electron and μ is the chemical potential of the electron gas. It is also convenient to define $\eta = (\zeta - 1)/\tau$.

10.2.1 The Thermal Structure Equation

If we assume that the pressure is supplied by the electrons alone, the general relativistic equations of thermal structure in the plane-parallel approximation assume the simple form (Hernquist 1985)

$$\frac{\mathrm{d}\tau}{\mathrm{d}\rho} = \left[\left.\frac{\partial \rho}{\partial \tau}\right|_\zeta + \left(\frac{m_u}{Y_e} \frac{\kappa}{F/g_s} - \frac{S_e}{n_e} \right) \frac{1}{k} \left.\frac{\partial \rho}{\partial \zeta}\right|_\tau \right]^{-1} \tag{10.4}$$

$$\frac{\mathrm{d}\zeta}{\mathrm{d}\rho} = \left(\left.\frac{\partial \rho}{\partial \zeta}\right|_\tau \right)^{-1} \left(1 - \left.\frac{\partial \rho}{\partial \tau}\right|_\zeta \frac{\mathrm{d}\tau}{\mathrm{d}\rho} \right) \tag{10.5}$$

$$\frac{\mathrm{d}z}{\mathrm{d}\rho} = -\frac{\mathrm{d}\zeta}{\mathrm{d}\rho} \frac{m_e c^2}{g_s} \left(1 - \frac{F}{g_s} \frac{S_e}{n_e \kappa} \right)^{-1} \tag{10.6}$$

where $Y_e = Z/A$. Z and A are the mean atomic number and mean atomic mass of the material. For partially ionized matter, Y_e is given by the product of Z/A and the ionized fraction. m_u is the atomic mass unit, F is the flux transmitted through the envelope, g_s the acceleration of gravity as measured at the surface, S_e and n_e are the entropy and number density of the electron gas. By using the plane-parallel approximation, we have assumed that the magnetic field does not vary in direction or magnitude over the scale of the thickness of the envelope (h_E), *i.e.* $|B/\nabla B| \gg h_E$. For a multipole of order n, this is equivalent to $R/n \gg h_E$, which holds for $n \ll 100$.

Since we are treating transmission at an arbitrary angle ψ with respect to the magnetic field κ, the thermal conductivity, is the sum of two contributions

$$\kappa = \kappa_{zz} \cos^2 \psi + \kappa_{yy} \sin^2 \psi \tag{10.7}$$

where the field is taken to point in the zz direction.

10.2.2 Thermodynamics and Equation of State

In an extremely strong magnetic field, the quantization of electron energies into Landau levels restricts the phase space of the otherwise free electron gas (Hernquist 1985), and its thermodynamic properties are given by

$$n_e = -\frac{\beta}{2\pi^2} \int_1^\infty d\gamma \frac{\mathrm{d}f}{\mathrm{d}\gamma} \sum_{n=0}^{n_{\max}} g_n \alpha_n \left(\frac{1}{\lambda\!\!\!^{-}_e{}^3} \right), \tag{10.8}$$

$$P_e = -\frac{\beta}{4\pi^2} \int_1^\infty d\gamma \frac{\mathrm{d}f}{\mathrm{d}\gamma} \sum_{n=0}^{n_{\max}} g_n \left[\alpha_n \gamma - \chi_n^2 \ln \left(\frac{\gamma + \alpha_n}{\chi_n} \right) \right] \times \left(\frac{m_e c^2}{\lambda\!\!\!^{-}_e{}^3} \right), \tag{10.9}$$

$$\begin{aligned}
\epsilon_e &= -\frac{\beta}{4\pi^2}\int_1^\infty d\gamma \frac{\mathrm{d}f}{\mathrm{d}\gamma}\sum_{n=0}^{n_{\rm max}} g_n \left[\alpha_n\gamma + \chi_n^2 \ln\left(\frac{\gamma+\alpha_n}{\chi_n}\right)\right] \\
&\quad \times \left(\frac{m_e c^2}{\lambdabar_e{}^3}\right), \qquad (10.10) \\
\left.\frac{\partial\rho}{\partial\zeta}\right|_{\tau,\beta} &= -\frac{\beta}{2\pi^2}\int_1^\infty d\gamma \frac{\partial f}{\partial\gamma}\gamma \sum_{n=0}^{n_{\rm max}} \frac{g_n}{\alpha_n}\left(\frac{m_u}{Y_e}\frac{1}{\lambdabar_e{}^3}\right), \qquad (10.11) \\
\left.\frac{\partial\rho}{\partial\tau}\right|_{\zeta,\beta} &= -\frac{\beta}{2\pi^2}\int_1^\infty d\gamma \frac{\partial f}{\partial\gamma}\gamma \frac{\gamma-\zeta}{\tau} \sum_{n=0}^{n_{\rm max}} \frac{g_n}{\alpha_n}\left(\frac{m_u}{Y_e}\frac{1}{\lambdabar_e{}^3}\right), \qquad (10.12) \\
S_e &= -\frac{\beta}{2\pi^2}\int_1^\infty d\gamma \frac{\partial f}{\partial\gamma}\frac{\gamma-\zeta}{\tau} \sum_{n=0}^{n_{\rm max}} g_n \alpha_n \left(\frac{k}{\lambdabar_e{}^3}\right) \qquad (10.13)
\end{aligned}$$

where

$$\begin{aligned}
n_{\rm max} &= \frac{\gamma^2-1}{2\beta} && (10.14) \\
\alpha_n^2 &= \gamma^2 - \chi_n^2 && (10.15) \\
& && (10.16) \\
g_n &= 2 - \delta_{n0} && (10.17) \\
\chi_n &= \sqrt{1+2n\beta} && (10.18) \\
f(\gamma) &= \frac{1}{1+\exp\left[(\gamma-\zeta)/\tau\right]}, && (10.19)
\end{aligned}$$

and $\lambdabar_e$ is the electron Compton wavelength.

The non-degenerate, degenerate and the unmagnetized limits of these quantities are useful in the numerical integration of the envelope.

Non-degenerate, non-relativistic limit. In the non-degenerate and non-relativistic limit, we obtain (Hernquist 1985)

$$\begin{aligned}
n_e &= \sqrt{\tau}\frac{\beta e^\eta}{(2\pi)^{3/2}}\sum_{n=0}^{\infty} g_n \exp(-n\beta/\tau)\left(\frac{1}{\lambdabar_e{}^3}\right), && (10.20) \\
P_e &= n_e \tau m_e c^2, && (10.21) \\
\epsilon_e &= n_e m_e c^2 \left[1 + \frac{\tau}{2} + \beta \,\mathrm{csch}\left(\frac{\beta}{\tau}\right)\right], && (10.22) \\
\left.\frac{\partial\rho}{\partial\zeta}\right|_{\tau,\beta} &= \frac{1}{\sqrt{\tau}}\frac{\beta e^\eta}{(2\pi)^{3/2}}\sum_{n=0}^{\infty} g_n \exp(-n\beta/\tau)\left(\frac{m_u}{Y_e}\frac{1}{\lambdabar_e{}^3}\right), && (10.23)
\end{aligned}$$

$$\begin{aligned}
\left.\frac{\partial\rho}{\partial\tau}\right|_{\zeta,\beta} &= \frac{1}{\sqrt{\tau}}\frac{\beta e^\eta}{(2\pi)^{3/2}}\sum_{n=0}^{\infty} g_n \exp(-n\beta/\tau)\left(\frac{1}{2}+\frac{n\beta}{\tau}-\eta\right) \\
&\quad \times\left(\frac{m_u}{Y_e}\frac{1}{{\lambda\!\!\!^{-}}_e{}^3}\right), \qquad (10.24)\\
S_e &= \sqrt{\tau}\frac{\beta e^\eta}{(2\pi)^{3/2}}\sum_{n=0}^{\infty} g_n \exp(-n\beta/\tau)\left(\frac{3}{2}+\frac{n\beta}{\tau}-\eta\right) \\
&\quad \times\left(\frac{k}{{\lambda\!\!\!^{-}}_e{}^3}\right). \qquad (10.25)
\end{aligned}$$

Degenerate limit. To obtain the degenerate limit of expressions 10.8 through 10.13, we compute the Sommerfeld expansions of the expressions. The first term in the expansion is obtained through the substitution

$$\frac{\mathrm{d}f}{\mathrm{d}\gamma} \to -\delta(\gamma-\zeta) - \frac{\pi^2}{6}\tau^2\delta^{(2)}(\gamma-\zeta) + \cdots. \qquad (10.26)$$

where $\delta(x)$ denotes the Dirac delta function. For expressions 10.12 and 10.13, the first term in the expansion is zero and we obtain the following results for the degenerate limit

$$\begin{aligned}
\left.\frac{\partial\rho}{\partial\tau}\right|_{\zeta,\beta} &= -\frac{\beta\tau}{6}\sum_{n=0}^{n_{\max}} g_n \frac{\chi_n^2}{\alpha_n^3}\left(\frac{m_u}{Y_e}\frac{1}{{\lambda\!\!\!^{-}}_e{}^3}\right), \qquad (10.27)\\
S_e &= \frac{\beta\tau\zeta}{6}\sum_{n=0}^{n_{\max}} \frac{g_n}{\alpha_n}\left(\frac{k}{{\lambda\!\!\!^{-}}_e{}^3}\right). \qquad (10.28)
\end{aligned}$$

All of the thermodynamic quantities above with the exception of n_e and P_e feature singularities at $\zeta = \chi_n$; therefore, these degenerate expressions are only appropriate when $|\zeta - \chi_n| \gg \tau$.

Unmagnetized Limit. If many Landau levels are filled, the unmagnetized limit of expressions 10.8 through 10.13 may provide a useful approximation. If the integrand contains singularities at $\gamma = \chi_n$, the unmagnetized limit is only useful if the distribution function is thermally broadened over many such singularities or $|\zeta - \chi_n| \gg \tau$.

In the unmagnetized limit, we obtain

$$n_e = -\frac{1}{3\pi^2}\int_1^\infty \mathrm{d}\gamma\frac{\mathrm{d}f}{\mathrm{d}\gamma}\left(\gamma^2-1\right)^{3/2}\left(\frac{1}{{\lambda\!\!\!^{-}}_e{}^3}\right), \qquad (10.29)$$

$$\begin{aligned}
P_e &= -\frac{1}{8\pi^2}\int_1^\infty \mathrm{d}\gamma \frac{\mathrm{d}f}{\mathrm{d}\gamma} \\
&\quad \times \left[\gamma\sqrt{\gamma^2-1}\left(\frac{2}{3}\gamma^2-\frac{5}{3}\right)+\ln\left(\sqrt{\gamma^2-1}+\gamma\right)\right] \\
&\quad \times \left(\frac{m_e c^2}{\lambda\!\!\!^-_e{}^3}\right), \qquad (10.30) \\
\epsilon_e &= -\frac{1}{8\pi^2}\int_1^\infty \mathrm{d}\gamma \frac{\mathrm{d}f}{\mathrm{d}\gamma} \\
&\quad \times \left[\gamma\sqrt{\gamma^2-1}\left(2\gamma^2-1\right)-\ln\left(\sqrt{\gamma^2-1}+\gamma\right)\right] \\
&\quad \times \left(\frac{m_e c^2}{\lambda\!\!\!^-_e{}^3}\right), \qquad (10.31) \\
\left.\frac{\partial\rho}{\partial\zeta}\right|_\tau &= -\frac{1}{\pi^2}\int_1^\infty \mathrm{d}\gamma \frac{\mathrm{d}f}{\mathrm{d}\gamma}\gamma\sqrt{\gamma^2-1}\left(\frac{m_u}{Y_e}\frac{1}{\lambda\!\!\!^-_e{}^3}\right), \qquad (10.32) \\
\left.\frac{\partial\rho}{\partial\tau}\right|_\zeta &= -\frac{1}{\pi^2}\int_1^\infty \mathrm{d}\gamma \frac{\mathrm{d}f}{\mathrm{d}\gamma}\gamma\sqrt{\gamma^2-1}\frac{\gamma-\zeta}{\tau}\left(\frac{m_u}{Y_e}\frac{1}{\lambda\!\!\!^-_e{}^3}\right), \qquad (10.33) \\
S_e &= -\frac{1}{3\pi^2}\int_1^\infty \mathrm{d}\gamma \frac{\mathrm{d}f}{\mathrm{d}\gamma}\left(\gamma^2-1\right)^{3/2}\frac{\gamma-\zeta}{\tau}\left(\frac{k}{\lambda\!\!\!^-_e{}^3}\right), \qquad (10.34)
\end{aligned}$$

10.2.3 Thermal Conductivities

Throughout the envelope, the heat is carried by electrons and photons. In the degenerate regime, electrons dominate the heat transfer and in the non-degenerate regime photons carry most of the heat.

Photon Conduction

As argued in the previous chapter, for the envelopes that we will examine the photon conduction is impeded mainly by free-free interactions with the electron gas rather than by electron scattering. Regardless, corrections to the free-free opacity have a negligible influence on the flux-core temperature relation (Hernquist & Applegate 1984). Here, we will use the thermal conductivities tabulated by Silant'ev & Yakovlev (1980) and the analytic expressions of Pavlov & Yakovlev (1977).

Electron conduction

For the electron conductivities, we use the calculations of Hernquist (1984). Although the analytic expressions for the parallel conductivity derived by Potekhin & Yakovlev (1996) are convenient, corresponding expressions for the transverse heat flow are lacking; therefore, for consistency, we use the parallel and perpendicular thermal conductivities of Hernquist (1984).

In the absence of an electric current, The thermal conductivity tensor ($\boldsymbol{\kappa}$) is most concisely expressed as a combination of the transport coefficients (Hernquist 1984)

$$\boldsymbol{\kappa} = \boldsymbol{\gamma} - T\boldsymbol{\lambda} \cdot (\boldsymbol{\sigma})^{-1} \cdot \boldsymbol{\lambda} \tag{10.35}$$

where $\boldsymbol{\gamma}$, $\boldsymbol{\lambda}$ and $\boldsymbol{\sigma}$ are the thermal conductivity, thermoelectric and electrical conductivity tensors respectively.

If we take the field to point along the z direction locally,

$$\begin{aligned}\begin{pmatrix}\sigma_{zz}\\ \lambda_{zz}\\ \gamma_{zz}\end{pmatrix} &= -\frac{\beta}{2\pi^2}\int_1^\infty \frac{\partial f}{\partial \gamma}\begin{pmatrix}e^2\\ -|e|k(\gamma-\zeta)/\tau\\ km_ec^2(\gamma-\zeta)^2/\tau\end{pmatrix}\phi(\nu;\beta)d\gamma\\ &\quad\times\left(\frac{1}{\hbar \lambda\!\!\!^{-}_e{}^2}\frac{1}{\sigma_0 n_i}\right) \qquad (10.36)\\ \begin{pmatrix}\sigma_{yy}\\ \lambda_{yy}\\ \gamma_{yy}\end{pmatrix} &= -\frac{1}{2\pi^2}\int_1^\infty \frac{\partial f}{\partial \gamma}\begin{pmatrix}e^2\\ -|e|k(\gamma-\zeta)/\tau\\ km_ec^2(\gamma-\zeta)^2/\tau\end{pmatrix}Q(\nu;\beta)d\gamma\\ &\quad\times\left(\frac{\hbar}{\sigma_0 n_i}\right) \qquad (10.37)\end{aligned}$$

where

$$\nu = \gamma/\beta, \tag{10.38}$$

n_i is the number density of ions (n_e/Z), σ_0 is the scattering cross section and ϕ and Q are perturbations to the distribution function and the diagonal component of the density matrix $f_{ns}(p_z, y_B)$, summed over Landau level n and spin s (Hernquist 1984).

Degenerate limit. In the fully degenerate limit, the expressions for κ_{zz} and κ_{yy} simplify,

$$\begin{aligned}\kappa_{zz} &= \frac{1}{6}\beta\tau\phi(\zeta/\beta;\beta)\left(\frac{ck}{\lambda\!\!\!^{-}_e{}^3\sigma_0 n_i}\right) \qquad (10.39)\\ \kappa_{yy} &= \frac{1}{6}\tau Q(\zeta/\beta;\beta)\left(\frac{ckn_i\sigma_0}{\lambda\!\!\!^{-}_e}\right) \qquad (10.40)\end{aligned}$$

Scattering cross sections. In the liquid state, electron-ion scattering dominates the resistance to electron conduction. Here the scattering cross section is

$$\sigma_0 = \frac{\pi Z^2\alpha^2}{\beta^2}\lambda\!\!\!^{-}_e{}^2 \tag{10.41}$$

where $\alpha \approx 1/137$ is the fine-structure constant. In the solid state, electron-phonon interactions provided the resistance and we have

$$\sigma_0 = \frac{\alpha u_{-2}}{2} \frac{\tau}{\beta} \left(\frac{1}{n_i \lambda\!\!\!^{-}_e{}^3} \right) \lambda\!\!\!^{-}_e{}^2, \tag{10.42}$$

and we take $u_{-2} \approx 13$ (Yakovlev & Urpin 1980, Potekhin & Yakovlev 1996) for a body-centered cubic lattice.

The perturbations to the distribution function. The functions Q and ϕ are laborious to calculate. Hernquist (1984) gives fitting formulae for $n < 30$ at field strengths of $B = 10^{11}$, $10^{11.5}$, 10^{12}, $10^{12.5}$, 10^{13}, $10^{13.5}$ and 10^{14} G. Additionally, to calculate the thermal structure of an envelope with an dipolar magnetic field, we have calculated the function ϕ at $B = 2 \times 10^{12}$ and 2×10^{13} G for $n < 30$ and at $B = 2 \times 10^{14}$ G for $n < 35$. Therefore, for fields $B \geq 2 \times 10^{14}$ G, the effect of the quantization of the electron phase space on the conductivity is included through the entire envelope.

When only one Landau level is filled, the functions ϕ and Q may be expressed analytically. In this limit, we use the following expressions

$$\phi_{ep}(\gamma;\beta) = \frac{1}{8} w \left[e^w E_1(w) \right]^{-1}, \tag{10.43}$$

$$Q_{ep}(\gamma;\beta) = \beta + \frac{4}{w} - 2e^w E_1(w) \tag{10.44}$$

$$\phi_{ei}(\gamma;\beta) = \frac{1}{8} w \left[\frac{1}{w + a_d} - \exp(w + a_d) E_1(w + a_d) \right]^{-1}, \tag{10.45}$$

$$\begin{aligned} Q_{ei}(\gamma;\beta) = \frac{1}{q_0^2} \Big\{ & \left[\beta(a_d + 1) + 2q_0^2 \right] \exp(w + a_d) E_1(w + a_d) \\ & + \beta(a_d + 1)(q_0^2 + 1) e^{a_d} E_1(a_d) - \beta(2 + q_0^2) \Big\} \end{aligned} \tag{10.46}$$

where

$$q_0^2 = \gamma^2 - 1, \tag{10.47}$$

$$w = \frac{2q_0^2}{\beta}, \tag{10.48}$$

$$a_d = 0.15 \left(\frac{q_0^2}{2\beta} \right)^{1/3}, \tag{10.49}$$

and $E_n(x)$ is an exponential integral which is easily calculated and is defined by

$$E_n(x) = \int_1^\infty \frac{e^{-xt}}{t^n} dt, \quad x \geq 0, \quad n = 0, 1, \ldots \tag{10.50}$$

Unquantized limit. To extend the conductivities beyond the maximum Landau level tabulated we use equations (186) through (189) of Hernquist (1984) to calculate the unmagnetized counterparts of ϕ and Q. In the liquid state we obtain,

$$\phi_{ei}(\nu;\beta) = \frac{\left(\zeta^2-1\right)^3}{6\beta^3\zeta^2\Lambda_{ei}}, \tag{10.51}$$

$$Q_{ei}(\nu;\beta) = \frac{8\Lambda_{ei}\zeta^2}{3}, \tag{10.52}$$

where the Coulomb logarithm Λ_{ei} is set to ensure continuity between the unquantized limit and the quantized calculations. It ranges from 1 at 10^{11} G to 0.55 at 10^{14} G. In the solid state we find

$$\phi_{ep}(\nu;\beta) = \frac{\left(\zeta^2-1\right)^2}{3\beta^2\left(\zeta^2+1\right)}, \tag{10.53}$$

$$Q_{ep}(\nu;\beta) = \frac{4\left(\zeta^4-1\right)}{3\beta} \tag{10.54}$$

10.2.4 Numerical Integration of the Envelope

To determine the thermal structure of the neutron star envelope, we integrate equations 10.5 through 10.6 using the photospheric boundary condition (*e.g.* Kippenhahn & Weigert 1990)

$$P_e = \frac{2}{3}\frac{g_s}{\widetilde{\kappa}} = \frac{g_s\kappa\rho}{8\sigma T^3} \tag{10.55}$$

where $\widetilde{\kappa}$ is the opacity and σ is the Stefan-Boltzmann constant. We omit Equation 10.5 from the system opting instead to solve for ζ by inverting $n_e(\zeta,\tau;\beta)$. The system is integrated with $\ln\rho$ as the independent variable using a Runge-Kutta method with adaptive step size control (Press et al. 1988). The properties of the envelope are calculated at 200 equally spaced steps in $\ln\rho$ through the envelope. A smaller stepsize results in an unacceptable accumulation of roundoff errors. The envelopes are integrated up to a density of 10^{10} g cm^{-3}.

10.3 Results

In this section we present the results of these numerical calculations. Specifically, we focus on several aspects of the envelopes: the thermal structure itself, the effect of dipolar fields on the moment of inertia of the envelope, the angular dependence of the flux for a constant field strength and the relationship between the transmitted flux and core temperature.

10.3.1 Thermal Structure

Parallel Conduction. If the quantization of the electron phase space is neglected, the magnetic field has no effect on the thermal conduction in the degenerate regime. We find that because this quantization cannot be neglected for $B > 10^{12}$ G, the magnetic field modifies the flux-core temperature relation, especially for relatively cool neutron stars. The case of parallel conduction has been treated in detail by Hernquist (1985) and Van Riper (1988), and we find similar results here.

Figure 10.1 depicts the temperature, chemical potential, entropy and thermal conductivity as a function of density through the crust at $T_{\text{eff}} = 10^6$ K. The small discontinuity in the value of S_e at low densities occurs when the integrator switches from using the nondegenerate, nonrelativistic expression for $\zeta(n, \tau; \beta)$ to numerically solving for ζ. This discontinuity does not affect the integration through the nondegenerate regime.

The run of electron entropy as a function of density or depth through the envelope is not monotonic in the presence of a strong magnetic field. When one studies the total entropy, the nuclear contribution does weaken this effect, but the total entropy still does attain a maximum as the first Landau level is being filled. This entropy inversion indicates that magnetized neutron star envelopes may be convectively unstable. However, a strong magnetic field also stabilizes a material against convection (). To determine whether convection is indeed important requires further study

Our values for the core temperatures using the Hernquist (1984) conductivities are generally slightly higher for strong fields ($\sim 3\%$) than those obtained by Hernquist (1985) because we have varied Λ_{ei} to ensure continuity between the magnetized and the unmagnetized conductivities. A more substantial difference is apparent in the value of the thermal conductivity in the nondegenerate regime. Because the thermal conductivity is nearly a power law in this region, we expect the conductivity to be nearly constant here. According to Hernquist & Applegate (1984) for a unmagnetized atmosphere, the conductivity in the nondegenerate regime is

$$\kappa = \frac{\alpha + \delta}{\alpha} \frac{F}{g_s} \frac{Y_e k}{m_u} \tag{10.56}$$

where $\alpha = 2$ and $\delta = 6.5$ for free-free scattering. However, in the magnetized case we obtain Equation 9.63,

$$\kappa = \frac{\alpha + \delta - 2}{\alpha} \frac{F}{g_s} \frac{Y_e k}{m_u}. \tag{10.57}$$

The thermal conductivity along a solution in the nondegenerate regime should be about 45 % larger for an unmagnetized envelope than for a magnetized envelope. This effect is apparent in Figures 10.1 and 10.2, but not

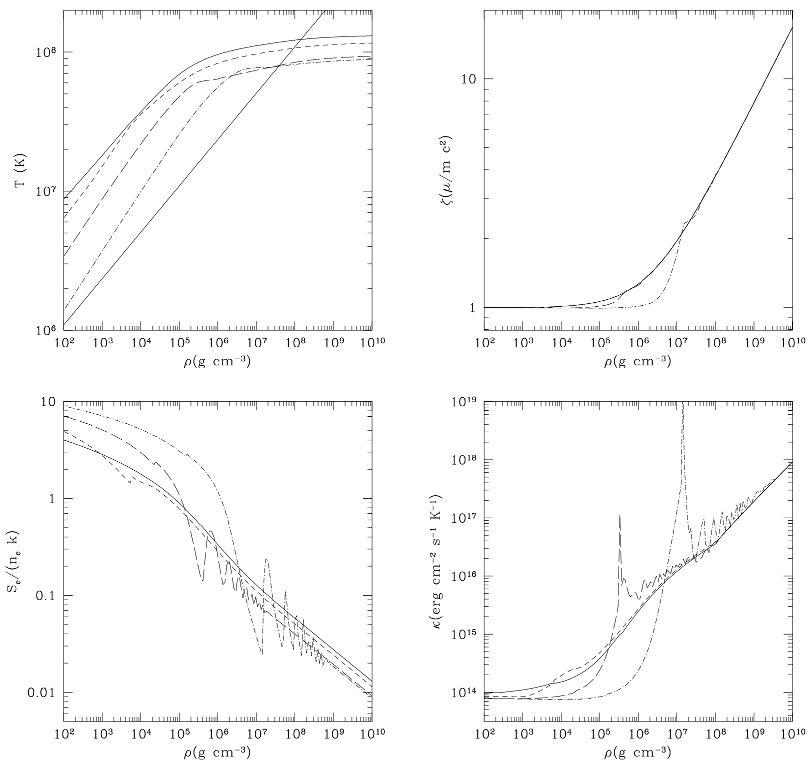

Figure 10.1: The thermal structure for a radial field at an effective temperature of 10^6 K. The solid curve traces the solutions for $B = 0$, the short dashed curve gives $B = 10^{12}$ G, the long dashed curve is 10^{13} G and the dot-dashed curve follows the $B = 10^{14}$ G solution. The solid line traces the solid-liquid phase transition in the $\rho - T$ plane.

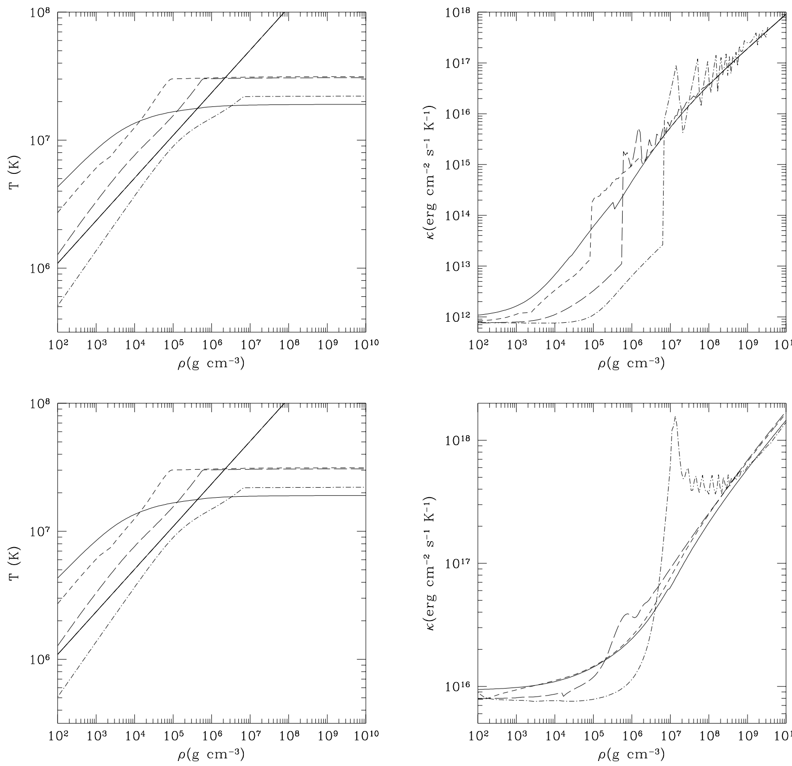

Figure 10.2: The thermal structure for a radial field at an effective temperature of $10^{5.5}$ K (upper panels) and $10^{6.5}$ K (lower panels). The lines follow the solutions for the same field strengths as in Figure 10.1.

in Figures 7 through 9 of Hernquist (1985). We find that the thermal conductivity in the nondegenerate region is given precisely by Equation 10.56 for the unmagnetized envelopes and by Equation 10.57 for the magnetized ones. The results of Hernquist (1985) both of magnetized and unmagnetized envelopes follow Equation 10.56. We are not certain of the origin of this discrepancy, but we suspect that it is due to an error in evaluating the conductivities in the nondegenerate limit. We expect that the results for cool envelopes which depend sensitively on conductivity in the region to differ between the work presented here and that of Hernquist (1985). Otherwise, the results for $T_{\text{eff}} = 10^6$ K agree well with those of Hernquist (1985).

Figure 10.2 depicts the physical conditions of the envelope as a function

Table 10.1: Values of the core temperature in units of 10^7 K

B (G)	$\log T_{\rm eff}$ 5.5	5.6	5.7	5.8	5.9	6.0
0	1.68	2.76	4.01	5.91	8.76	13.1
10^{12}	3.14	3.34	3.91	5.14	7.55	11.6
10^{13}	3.07	3.13	3.49	4.45	6.30	9.33
10^{14}	2.21	3.06	3.43	4.37	6.07	8.86

B (G)	$\log T_{\rm eff}$ 6.1	6.2	6.3	6.4	6.5
0	19.8	30.0	45.4	67.9	101.
10^{12}	17.9	27.3	41.4	61.7	91.9
10^{13}	14.3	22.1	34.4	52.8	80.9
10^{14}	13.0	19.3	28.9	43.1	62.9

of density for effective temperatures of $10^{5.5}$ K (upper panels) and $10^{6.5}$ K (lower panels). In the colder envelope, the oscillations of the thermodynamic quantities because of the quantization of the electron phase space is apparent. At higher and lower effective temperatures, the differences compared to the results of Hernquist (1985) are substantially larger. We obtain the solutions with higher core temperatures at $T_{\rm eff} = 10^{5.5}$ K than Hernquist (1985) did because of the differences in the thermal conductivities in the nondegenerate region. Additionally, the relationship between the core temperature and magnetic field strength is complicated at such low effective temperatures. Specifically we find that for $T_{\rm eff} \leq 10^{5.6}$ K the core temperature for an unmagnetized envelope is lower than in the magnetized case.

At $T_{\rm eff} = 10^{6.5}$ K the situation is reversed. The envelopes studied here tend to yield cooler core temperatures than those studied by Hernquist (1985). For the hot envelopes with $B \lesssim 10^{13}$ G, the core temperature depends sensitively on the thermal conductivity in the liquefied region where more than thirty Landau levels are filled. In this region, unlike in Hernquist (1985) we have adjusted the value of Λ_{ei} to ensure continuity between the magnetize results and the unmagnetized limit. This yields slightly higher parallel conductivities for the liquid state, and consequently lower core temperatures.

Table 10.1 summarizes the results for several effective temperatures and magnetic field strengths.

In Figure 10.3, we compare the 10^{14} G models with the analytic models

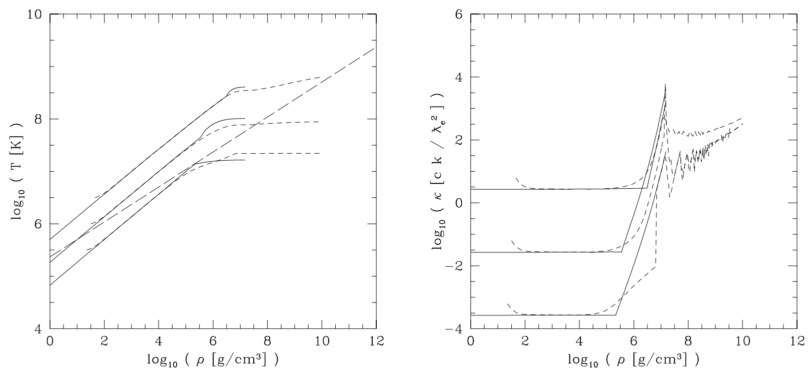

Figure 10.3: Comparison of analytic and numerical envelope solutions. From top to bottom, the curves follow the solutions for $T_{\rm eff} = 10^{5.5}$ K, 10^6 K and $10^{6.5}$ K. The left panel depicts the dependence of temperature on density through the envelope of the neutron star. The right panel gives the run of conductivity with density. The solid lines trace the analytic solutions and the dashed follows the numerical results.

discussed in Chapter 9 at $T_{\rm eff} = 10^{5.5}, 10^6$ and $10^{6.5}$ K. At $T_{\rm eff} = 10^6$ K, the numerical model has a core temperature 11 % cooler than the analytic treatment. The two approximations in the analytic model contribute errors that partially cancel. Since the analytic treatment assumes that either photon or electron conduction operates, it underestimates the conductivity in the semidegenerate region; consequently, in the degenerate regime, the analytic envelope is slightly hotter, and the resulting conductivity is larger than that of the numerical envelope at the same density. Above the density at which the first Landau level fills, the analytic treatment effectively assumes that the conductivity is infinite. Because the core temperature depends most sensitively on the conductivities in the semidegnerate region (*e.g.* Gudmundsson, Pethick & Epstein 1982), the net effect is that the numerical envelope at 10^6 K yields slightly higher core temperatures than the analytic treatment.

For hotter and cooler effective temperatures, the cancellation among the errors introduced by the approximations is far less exact. At $T_{\rm eff} = 10^{5.5}$ K the numerical treatment yields a core temperature 30 % hotter than the analytic model. At the $T_{6.5}$ K the contribution to the insulation of the core from material with more than one Landau level filled is substantial and the core temperature estimate is 50 % hotter for the numerical models than the analytic treatment.

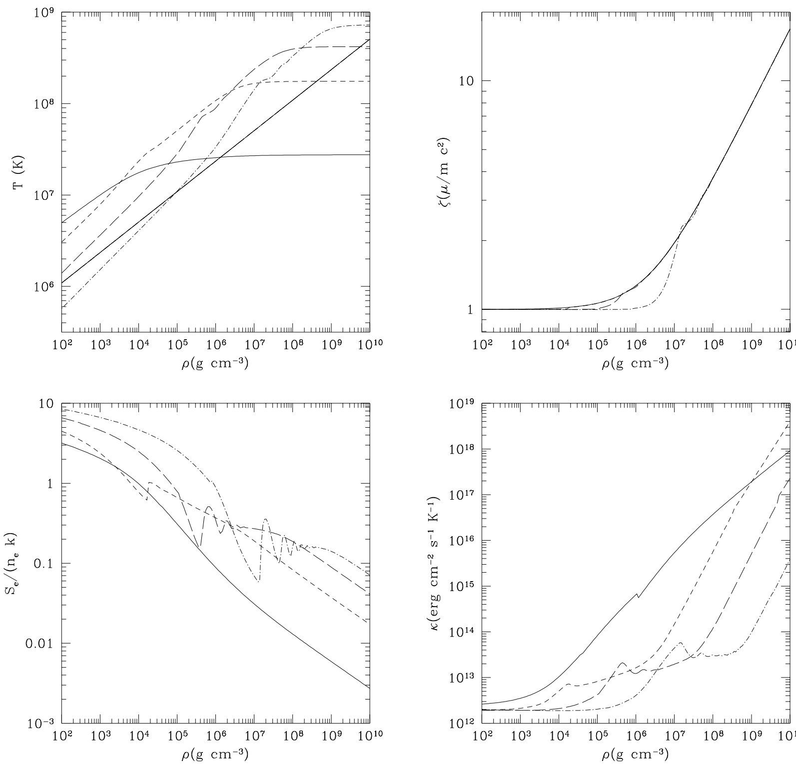

Figure 10.4: The thermal structure for a tangential field at an effective temperature of $10^{5.6}$ K. The lines follow the solutions for the same field strengths as in Figure 10.1.

Perpendicular Conduction. Even classically, conduction perpendicular to the magnetic field is affected dramatically by a strong magnetic field. We again examine several magnetic field strengths. Figure 10.4 depicts the results for an effective temperature of $10^{5.6}$ K for perpendicular conduction. The core temperature for a fixed effective temperature varies dramatically with the magnetic field strength. The bulk of the effect is classical in nature, the magnetic field deflects the electrons from carrying heat away from the surface.

The quantization of the electron phase space is also manifest for the perpendicular case. Because the function $Q(\nu, \beta)$ diverges as a Landau level begins to fill, the conductivity increases dramatically near the start of each Landau level, and the run of temperature exhibits plateaux at these densities. As we shall find in the next subsections, perpendicular transport cannot be neglected an important range of effective temperatures and magnetic field strengths.

10.3.2 Angular Dependence

To examine the angular dependence of the flux transmitted through an uniformly magnetized envelope, we will take two routes. First, we use the method demonstrated in Figure 9.7 and vary the effective temperature as a function of angle to shoot toward a fixed core temperature.

Figure 10.5 gives the results of this comparison. Both the $\cos^2\psi$ rule and the best fit $a\cos^2\psi + b\sin^2\psi$ fit the results to within 10 % of the total flux. Schaaf (1990b) presents the results of a set of two-dimensional calculations with a fitting function

$$\frac{T_{\rm eff}(\psi)}{T_{\rm eff}(0)} = \chi(\psi) = \chi\,(90^\circ) + [1 - \chi\,(90^\circ)]\cos^\alpha\psi. \qquad (10.58)$$

Schaaf (1990b) studies field strengths up to 10^{12} G, so we assume that the parameters α and $\chi\,(90^\circ)$ for $T_{\rm eff} = 10^6$ K follow a power law in the field strength for stronger fields. For $B = 10^{13}$ G, we obtain $\alpha = 0.48$ and $\chi\,(90^\circ) = 0.10$. This model is traced by the dashed line in Figure 10.5 and agrees to within 6.5 % of our results.

Bolstered by the success of the $\cos^2\psi$ rule, we perform a second test in which the flux along the surface varies at $\cos^2 psi$ and determine by how much the core temperature varies for several models. Figure 10.6 depicts the results of these calculations. A horizontal line for a given set of calculations would indicate adherence to the $\cos^2\psi$ rule. Generally, the largest departure from the $\cos^2\psi$ rule is where the heat is transmitted at large angles to the magnetic field direction.

We define a figure of merit for each value of the flux at $\psi = 0$ and magnetic field strength,

$$\Upsilon_u = \frac{1}{N}\sum_{i=1}^{N}\left|\frac{T_c(\psi_i) - T_c(0)}{T_c(0)}\right| \qquad (10.59)$$

where u signifies an unweighted summation.

A large value of Υ_u signals that conductivity perpendicular to the field lines is significant in determining the core temperature given the transmitted flux. Table 10.2 depicts the results for several field strengths and

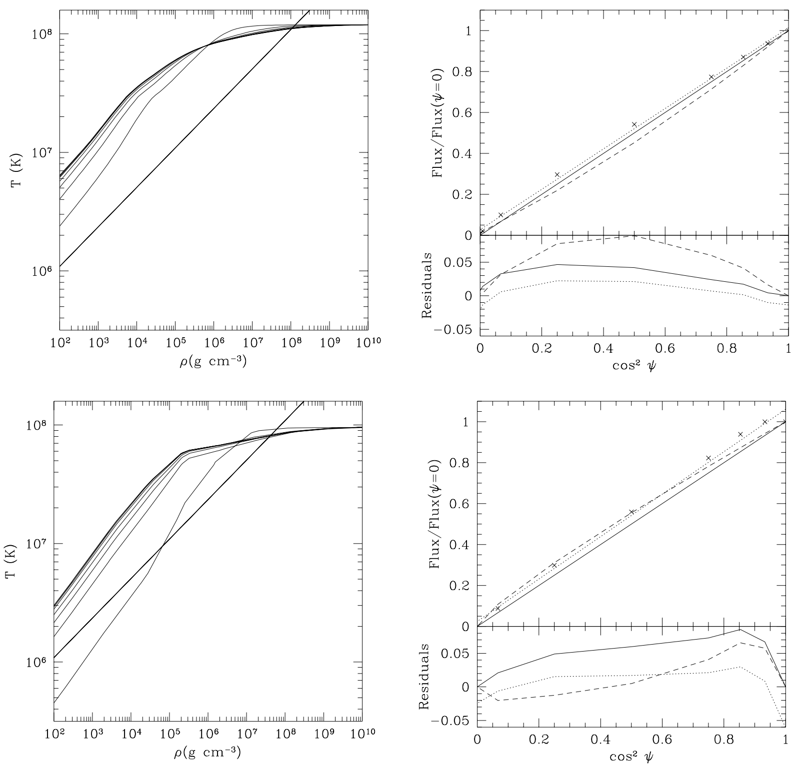

Figure 10.5: Results of a numerical two-dimensional calculation for $B = 10^{12}, 10^{13}$ G at $T_{\rm eff} = 10^6$ K for $\psi = 0$. The upper panels present the results for the weaker field strength. The left panels give $T(\rho)$ for the various models. The right panels compare the flux distribution (crosses) with the $\cos^2\psi$ rule. The lower solid line gives the $\cos^2\psi$ rule and the upper dotted line traces the best fit model of the form $a\cos^2\psi + b\sin^2\psi$. Here, $a = 1.02$ and $b = 0.0264$ for 10^{12} G, $a = 1.06$ and $b = 0.0245$ for 10^{13} G. The upper dashed line traces the results of Schaaf (1990b) (extrapolated using a power law to $B = 10^{13}$ G.)

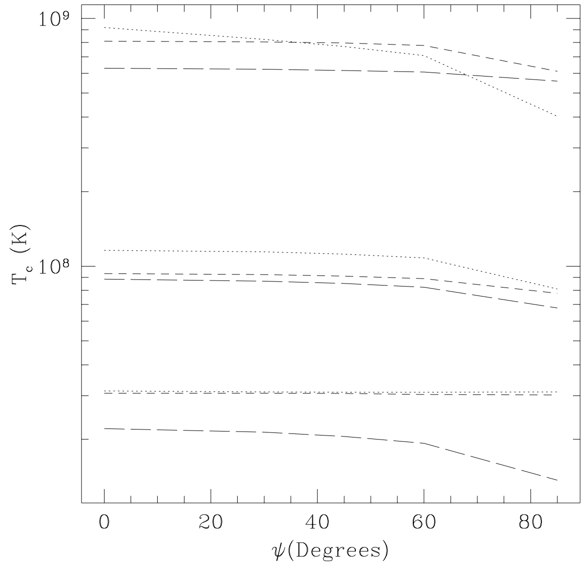

Figure 10.6: The core temperature as a function of angle for fluxes that follow the $\cos^2\psi$ rule. The lower lines are for $T_{\rm eff}(\psi = 0) = 10^{5.5}$ K, and middle lines follow the 10^6 K solutions, and the upper lines trace the $10^{6.5}$ K results. The lines follow the solutions for the same field strengths as in Figure 10.1.

Table 10.2: Values of Υ in percent as a function of magnetic field and effective temperature

	Υ_u			Υ_L		
	$\log T_{\rm eff}$			$\log T_{\rm eff}$		
B (G)	5.5	6.0	6.5	5.5	6.0	6.5
10^{12}	0.86	8.4	21.	1.1	3.7	16.
10^{13}	0.74	4.9	6.1	0.54	2.4	1.9
10^{14}	12.	7.2	3.5	7.0	4.0	2.0

effective temperatures. We find two trends. For weak fields, the low effective temperature solutions follow the $\cos^2\psi$ rule more closely than hotter envelopes. For strong fields, the trend is reversed.

From an observational point of view, the error in the total predicted luminosity of the object is more important. We weight the residuals by $\cos^2\psi\sin\psi$. This neglects gravitational lensing and assumes the field distribution is uniform. We define

$$\Upsilon_L = \sum_{i=1}^{N} \cos^2\psi\sin\psi \left|\frac{T_c(\psi_i) - T_c(0)}{T_c(0)}\right| \Bigg/ \sum_{i=1}^{N} \cos^2\psi\sin\psi \qquad (10.60)$$

where L signifies a luminosity-weighted summation. The values of Υ_L tend to be smaller than those of Υ_u because the weighting function is peaked at $\cos^2\psi = 2/3$, approximately 35°, where the departure from the $\cos^2\psi$ rule is small. We find that for effective temperatures near 10^6 K the $\cos^2\psi$ is followed. However, one must be wary in applying this rule for cool strongly magnetized envelopes where the quantization of the electron phase space increases the perpendicular conductivity dramatically or hot weakly magnetized ones where the classical relaxation time is no longer long compared to the relativistic cyclotron frequency.

10.3.3 Flux-Core-Temperature Relation

We revisit the flux-core-temperature relation presented in Table 10.1. Figure 10.7 displays these results graphically. We see that for very cool magnetized envelopes, the relationship departs from a power law. However, for $T_{\rm eff} \geq 10^{5.7}$ K, the relationship is well fit by a power law with root-mean-square residuals of less than 3%.

We also have calculated for the envelopes with conduction perpendicular to the field for $T_{\rm eff} = 10^{5.3}$ K and $10^{5.6}$ K, sufficient to determine the power-law flux-core-temperature relation for the perpendicular case. For higher effective temperatures, the core temperature exceeds 10^9 K. For such high core temperatures our assumption that the core is thermally relaxed breaks down (Nomoto & Tsuruta 1981). For lower effective temperatures, the details of the equation of state at low densities become important, *i.e.* Coulomb corrections (*e.g.* Van Riper 1988).

We fit the flux-core-temperature relation with a power law of the form,

$$T_{c,7} = T_{0,7} T_{\rm eff,6}^{\alpha}. \qquad (10.61)$$

Table 10.3 presents the results of the fitting. The slope of flux-core-temperature relation for the parallel case is approximately that found in the analytic

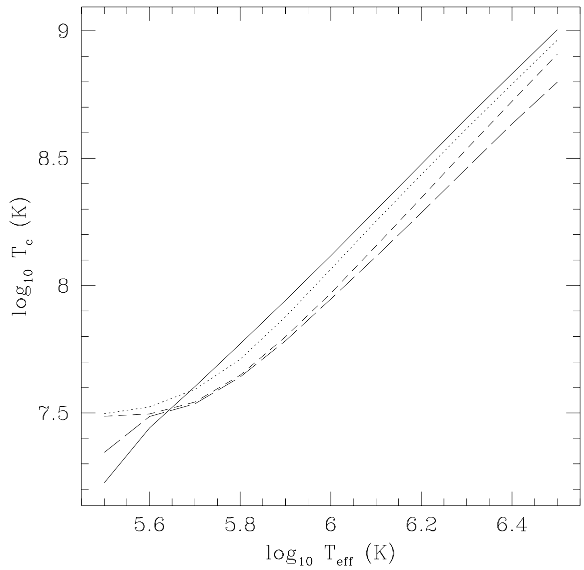

Figure 10.7: The flux-core-temperature relation as a function of magnetic field strength. The lines follow the solutions for the same field strengths as in Figure 10.1.

Table 10.3: Power-law parameters for the flux-core-temperature relation.

B (G)	$T_{\parallel,0,7}$	$\alpha_{\parallel}$	RMS Residual	$T_{\perp,0,7}$	$\alpha_{\perp}$
0	13.3	1.76	0.004		
10^{12}	12.0	1.76	0.018	53.5	1.21
10^{13}	10.1	1.76	0.030	123.	1.16
10^{14}	9.35	1.62	0.023	214.	1.17

treatment of Chapter 9 (Equations 9.71 and 9.72). However, the relationship with magnetic field strength is a much shallower power law than found earlier.

10.3.4 Dipole Fields

It is straightforward to construct the effective temperature distribution for a dipole by interpolating the flux-core-temperature relation as function of field strength and field inclination. However, determining the thermal structure in this manner is less trivial. The goal is to determine if an intense magnetic field can cause the envelope to become oblate through its effect on heat transport, so we will examine perpendicular and parallel transport for a field strength at the pole of 2×10^{14} G by recalculating an envelope solution and matching the core temperature at the pole and the equator. For illustration we choose $T_{\rm eff}(\psi = 0) = 10^{6.4}$ K which yields a core temperature of 4×10^8 K. Along the magnetic equator, substantially less heat flows through the envelope. Here, $T_{\rm eff} \approx 10^{5.38}$ K.

Figure 10.8 depicts the two solutions. The run of temperature with density is substantially different for the two solutions, so we would expect that the moment of inertia of the envelope at the pole would differ from that at the equator. To first order, the moment of inertia of the envelope depends on the total mass of the envelope and the mass weighted mean radius of the envelope. The envelope is about 0.7 % thinner and less massive at the equator than at the poles. For a neutron star with $R = 10^6$ km and $I = 1.4 \times 10^{45}$ g cm^2, the moment of inertia of the envelope at the pole differs by a factor of 1.2×10^{-3} relative to the equatorial value. This difference results in a relative difference in the moment of inertia along and perpendicular to the magnetic field of 10^{-11}.

10.4 Discussion

The calculations here are patterned after those of Hernquist (1985), and for the case of parallel conduction we reproduce his results with a few exceptions. Because we use the formulae of Pavlov & Yakovlev (1977) to extrapolate the free-free opacity in the non-degenerate regime beyond the tabulations of Silant'ev & Yakovlev (1980), we find different thermal structure in the nondegenerate region than Hernquist (1985) who extrapolated the calculations of Silant'ev & Yakovlev (1980) directly, did; consequently, for those especially cool envelopes whose core temperatures depend critically on these opacities, we find that our envelopes transmit less flux for a given core temperature. To calculate the thermal conductivity due to elec-

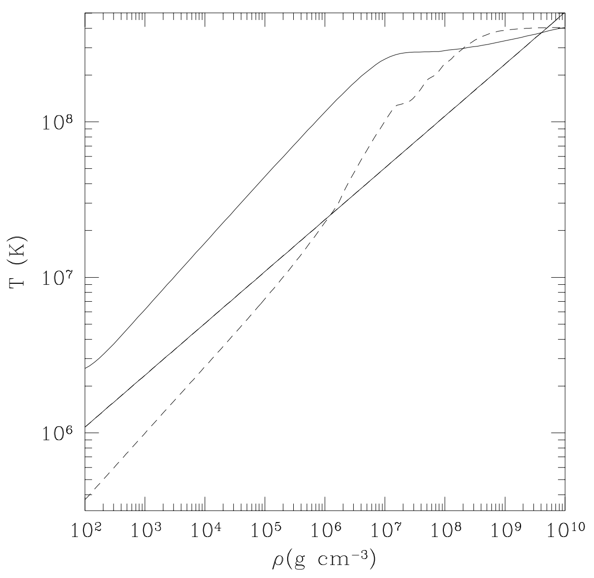

Figure 10.8: The thermal structure for a dipole field configuration. The solid curve traces the solution at the pole, and the dashed curve gives the results at the equator.

tron transport, we have extrapolated the tabulations of Hernquist (1984) for $n \geq 30$ in manner which maintains continuity between the magnetized and unmagnetized limits. Specifically, this results in a slightly higher electron conductivity for $n \geq 30$ than Hernquist (1985) used. We find that for high effective temperatures, more flux is transmitted for a given core temperature than Hernquist (1985) found.

By examining transport oblique and perpendicular to the field direction, we have extended the earlier work of Hernquist (1985) and Van Riper (1988) into two-dimensions, and the work of Schaaf (1990b) to more intense magnetic fields and more complicated field geometries. Schaaf (1990b) solves the thermal structure equation in two dimensions using the conductivities of Schaaf (1988) for $B \leq 10^{11}$ G. Using the same set of conductivities, Schaaf (1990a) treats the cases of parallel and perpendicular transport using a plane-parallel approximation for $B \leq 10^{13}$ G.

Rather than solve the two-dimensional thermal structure equations directly, We have argued in Chapter 9 that the plane-parallel approximation holds for the relatively thin envelopes of neutron stars. The slope of the flux-core-temperature relation for the longitudinal case agrees with the fit of Schaaf (1990a) to within 15 %, and the normalization agrees to within 8 %. Furthermore, Schaaf (1990a) also found an upturn in the flux-core-temperature relation for magnetized envelopes with low effective temperatures. For the transverse case, we find that the flux-core-temperature relation has a similar slope as Schaaf (1990a) but our models tend to have higher core temperatures.

Our results do not extend beyond an effective temperature of $10^{6.5}$ K (longitudinal case) and $10^{5.6}$ K (transverse case). For higher effective temperatures the core temperature exceeds 10^9 K, and it is unlikely that the core has relaxed thermally yet (Nomoto & Tsuruta 1981).

Schaaf (1990b) summarizes the results of the two-dimensional calculations in terms of fitting functions (Equation 10.58). In this notation we have examined the applicability of two models. Both models have $\alpha = 0.5$. The first fixes $\chi(90^\circ) = 0$, the $\cos^2\psi$ rule, and the second allows $\chi(90^\circ)$ to vary, the $a\cos^2\psi + b\sin^2\psi$ rule.

The two works have only the $T_{\rm eff} = 10^6$ K with $B = 10^{12}$ G model in common, but our results assume a given flux rule and determine the change in core temperature. However, we found that the model $T_{\rm eff} = 10^{5.5}$ K and $B = 10^{12}$ G is well fit by the $\cos^2\psi$ rule. Using Schaaf (1990b) interpolation formulae, we obtain $\alpha = 0.44$ and $\chi(90^\circ) = 0.32$ which yields more flux at large values of ψ than we found. We also extrapolated the interpolation formulae of Schaaf (1990b) to 10^{13} G for $T_{\rm eff} = 10^6$ K and find agreement within 7%.

Several directions for further work stand out. The equation of state at low densities may be affected by Coulomb corrections. Van Riper (1988) found that Coulomb corrections play an important role for effective temperatures less than 6×10^5 K at 10^{14} G. Their contribution sets in at lower effective temperatures for more weakly magnetized envelopes. Van Riper (1988) prescription for including Coulomb corrections resulted in negative pressures at low densities. Thorolfsson et al. (1997) have developed a Thomas-Fermi technique which accounts for the quantization of the electron phase space which may be applied to envelope calculations without encountering the difficulties that Van Riper (1988) found.

In the degenerate regime where electron conduction dominates, the conductivities are still uncertain. Potekhin & Yakovlev (1996) have derived convenient analytic formulae to calculate the longitudinal transport coefficients. Potekhin & Yakovlev (1996) make slightly different approximations. They include the Debye and electron screening in the fluid phase and the Debye-Waller factor in solid state. This factor tends to increase the conductivity over a wide range of temperatures and densities (Itoh et al. 1984, Potekhin & Yakovlev 1996). With an equally complete treatment of the transverse conductivities, this work could be extended reliably into a wider range of effective temperatures and magnetic field strengths.

To connect these results with recent observations of isolate neutron stars (*e.g.* Greiveldinger et al. 1996, Possenti, Mereghetti & Colpi 1996, and see Table 9.1), we must calculate how a magnetized atmosphere determines the emergent spectra from various locations on the neutron star (Pavlov et al. 1994, Pavlov et al. 1996; Rajagopal, Romani & Miller 1997), and convolve these spectra with the effects of gravitational self-lensing to determine the portion of the neutron star visible as a function of rotational phase (Page 1995, Chapter 9).

10.5 Conclusion

We have presented a series of numerical models of neutron star envelopes calculated in the plane-parallel approximation for $B = 10^{12}$ to 10^{14} G, $T_{\rm eff} = 10^{5.3}$ to $10^{6.5}$ K, for several inclination angles of the magnetic field. We find agreement with earlier one and two-dimensional calculations, and verify that the flux along the surface is approximately proportional to the square of the cosine of the inclination angle for neutron stars with $T_{\rm eff} \sim 10^6$ K. For hotter and cooler envelopes, this rule provides a poorer approximation.

Part IV

Magnetic Fields and Observations

Chapter 11

The Thermal Evolution of Ultramagnetized Neutron Stars

SUMMARY

Using recently calculated analytic and numerical models for the thermal structure of ultramagnetized neutron stars, we estimate the effects that ultrastrong magnetic fields $B \geq 10^{14}$ G have on the thermal evolution of a neutron star. Understanding this evolution is necessary to interpret models that invoke "magnetars" to account for soft γ-ray emission from some repeating sources.

11.1 Introduction

Neutron stars with extremely strong magnetic dipole fields ($B \gtrsim 10^{14}$ G) may form if a helical dynamo mechanism operates efficiently during the first few seconds after gravitational collapse (Thompson & Duncan 1993) or through the conventional process of flux freezing if the progenitor star has a sufficiently intense core field. These "magnetars" initially rotate with periods $P \sim 1$ ms, but would quickly slow down due to magnetic dipole radiation and cross the pulsar death line after about $10^5 - 10^6$ yr. With their strong magnetic fields, magnetars have been used to explain several phenomena including gamma-ray bursts (Usov 1992, Duncan & Thompson 1992) and soft gamma repeaters (Thompson & Duncan 1995).

Shibanov & Yakovlev (1996) have recently discussed how magnetic fields $B < 10^{13.5}$ G affect neutron star cooling. (Throughout, we will use the symbol B to denote the field strength at the magnetic pole.) They find that below $B \sim 10^{12}$ G, the magnetic field suppresses the total heat flux radiated by a neutron star. However, for $B \gtrsim 10^{12}$ G, the quantization of the electron energies enhances the conductivity along the field lines, resulting in a net increase in the heat flux. Here, we extend these results into the ultramagnetized regime with $B = 10^{14} - 10^{16}$ G.

In this *Letter*, we will discuss the cooling evolution of neutron stars which have not accreted significant material from their surroundings, *i.e.* neutron stars with iron envelopes.

11.2 Model Envelopes

Heyl & Hernquist (1997a) have developed analytic models for ultramagnetized neutron star envelopes and find that the transmitted flux through the envelope is simply related to the direction and strength of the magnetic field and to the core temperature (T_c). Using these results as a guide, we numerically integrate several envelopes with $B = 10^{14} - 10^{16}$ G for the case of parallel transport. We will present the detailed results of these calculations in a future article.

At the outer boundary, we apply the photospheric condition (*e.g.* Kippenhahn & Weigert 1990). In the non-degenerate regime, photon conduction dominates. For the range of effective temperatures considered free-free absorption is the most important source of opacity, and we estimate the anisotropy factor due to the magnetic field using the results of Pavlov & Panov (1976) and Silant'ev & Yakovlev (1980). In the degenerate regime, electrons dominate the conduction; we use the conductivities of Hernquist (1984) or Potekhin & Yakovlev (1996) and present results using both these values. In the semi-degenerate regime, both processes are important, so we sum the two conductivities.

Potekhin & Yakovlev (1996) give formulae to calculate electron conductivities in the liquid and solid regimes for arbitrary magnetic field strengths. The results of Hernquist (1984) are given for specific values of the field strength. We calculate the conductivities using the formalism and assumptions outlined in Hernquist (1984) and extend his calculations to stronger fields.

The conductivities of Hernquist (1984) and Potekhin & Yakovlev (1996) do not differ in the physical processes considered in their calculation but in the approximations employed. In the liquid state the conductivities of Hernquist (1984) tend to be approximately 15% larger for the ground Landau level and up to 40% larger for the excited levels than those of Potekhin & Yakovlev (1996). In the solid state, the conductivities of Potekhin & Yakovlev (1996) exceed those of Hernquist (1984) by a factor of several; therefore, these two models span much of the uncertainty in these quantities.

In the liquid state, the differences arise from two sources. First, both the fits of Hernquist (1984) and Potekhin & Yakovlev (1996) for the function $\phi(E)$ are inaccurate to $\sim 10\%$. Second, Hernquist (1984) assumes that electron-ion scattering is screened by the ion sphere; this process dominates in the liquid regime. Potekhin & Yakovlev (1996) include Debye and electron screening as well which dominate in the gaseous regime. Their results are appropriate for both the gaseous and liquid regimes. In the solid regime, Hernquist (1984) does not take the Debye-Waller factor into account. This factor tends to increase the conductivity over a wide range of temperatures and densities (Itoh et al. 1984, Potekhin & Yakovlev 1996).

Our iron envelope models are calculated by adopting a plane-parallel, Newtonian approximation. Hernquist (1985) found that using $Z = 26$ and $A = 56$ throughout is sufficient to accurately model the envelope. For simplicity we fix Z and A to these values, rather than use the equilibrium composition of Baym, Pethick & Sutherland (1971). In our approach, the core temperature is a function of F/g_s, B and ψ (the angle between the radial and field directions). Here, F is the transmitted heat flux, g_s is the surface gravity, and all of these values are taken to be in the frame of the neutron star surface – we have not applied the gravitational redshift to transform from the surface to the observer's frame.

For such strong fields, the models have a simple dependence on the angle ψ; *i.e.* $F/g_s \propto \cos^2 \psi$ (Greenstein & Hartke 1983, Page 1995, Shibanov et al. 1995, Shibanov & Yakovlev 1996, Heyl & Hernquist 1997a) and furthermore the flux for a fixed core temperature is approximately proportional to $B^{0.4}$. With these two facts, we find that the average flux over the surface of a neutron star with a dipole field configuration is 0.4765 times its peak value at the magnetic poles. We neglect the effects of general relativity on the field configuration, which tend to make the field more radial (Ginzburg & Ozernoy 1964), increasing the effects discussed here.

Using these models, we have calculated a grid of theoretical envelopes with average effective temperatures ranging from $10^{5.4}$ K to $10^{6.6}$ K, corresponding to a factor of $\sim 10^5$ in transmitted flux. We take $g_s = g_{s,14} 10^{14}$ cm/s^2. In the left panel, Figure 11.1 depicts the ratio of the core temperature to the zero-field case (Hernquist & Applegate 1984) as a function of the magnetic field and the mean effective temperature $\bar{T}_{\rm eff}$ over the neutron star. In the zero-field case, to determine the core temperature for a given flux we combine equations (4.7) and (4.8) of Hernquist & Applegate (1984),

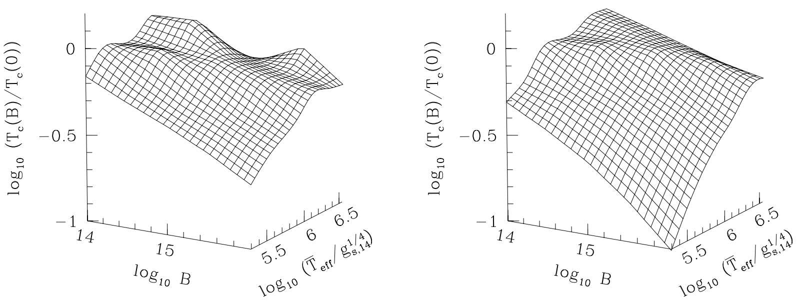

Figure 11.1: The left panel depicts the ratio of the core temperature with $B \neq 0$ to the zero-field case (Hernquist & Applegate 1984) using the conductivities of Hernquist (1984). The right panel shows the results for the Potekhin & Yakovlev (1996) conductivities.

switching from the first relation to the second when the surface effective temperature drops below 4.25×10^5 K. The results do not depend qualitatively on whether equation (4.7) or (4.8) of Hernquist & Applegate (1984) is used. The right panel shows the ratio of the core temperature with a magnetic field to the zero-field case for the conductivities of Potekhin & Yakovlev (1996).

For a given core temperature, the magnetized envelopes transmit more heat than the unmagnetized envelopes. For example, an effective temperature of 3.5×10^6 K corresponds to a core temperature of 1.1×10^9 K for an unmagnetized envelope. With $B = 10^{16}$ G, the core temperature is 5.3×10^8 K for the Hernquist (1984) conductivities and 5.8×10^8 K for the Potekhin & Yakovlev (1996) ones. Because the Hernquist (1984) conductivities in the liquid phase are ~ 20 % larger than those of Potekhin & Yakovlev (1996), we find that the effective temperature is slightly higher during the early cooling ($t \lesssim 10^5$ yr) of the neutron star if one uses the values of Hernquist (1984).

For lower core temperatures, the insulating envelope is thinner and the magnetic field has a stronger effect (Van Riper 1988); the difference in core temperatures may be even more extreme, by up to a factor of four or ten (for Hernquist 1984 and Potekhin & Yakovlev 1996 conductivities, respectively) in the coolest envelopes considered here. For the cooler envelopes the relationship between the effective temperature and the core temperature is strongly sensitive to the conductivities in the solid phase; consequently, the Debye-Waller factor is most important during the later cooling of the neutron star ($t \gtrsim 10^5$ yr). Furthermore, during this late phase, the partial ionization of iron may affect the equation of state as well as the electron and photon conductivities. This area has not been thoroughly explored, especially at high B.

For $T_c > 10^8$ K, the dominant heat loss mechanism is through neutrino emission (*e.g.* Shapiro & Teukolsky 1983) which has a cooling time proportional to T_c^{-6} for the modified URCA process. Because of this steep power law, a factor of 1.9–2.1 difference in the core temperature (the first example) would lead one to infer a cooling time of an ultramagnetized neutron star 50–80 times greater than if one did not consider the effects of the magnetic field on heat transport. And since neutrino cooling models generically have a cooling time proportional to $T_c^{-\alpha}$ with $\alpha = 4-6$ (*e.g.* Shapiro & Teukolsky 1983), one would generally underestimate the cooling ages of ultramagnetized neutron stars by a large factor.

11.3 Thermal Evolution

For $t \gtrsim 10^3$ yr, the neutron star interior has relaxed thermally (Nomoto & Tsuruta 1981), we can use the flux-to-core-temperature relation for several values of B including $B = 0$ to derive the relationship between $T_{\rm eff}$ and the cooling time. The technique is straightforward during the epoch of neutrino cooling. However, since photon emission is enhanced, the epoch of photon cooling will begin slightly earlier, and the time dependence of the temperature will have a slightly different slope. For the neutrino cooling model, we use the modified URCA process (*e.g.* Shapiro & Teukolsky 1983)

$$L_\nu = (5.3 \times 10^{39} \text{erg/s}) \frac{M}{M_\odot} \left(\frac{\rho_{\rm nuc}}{\rho} \right)^{1/3} T_{c,9}^8 \tag{11.1}$$

where $T_x = T/10^x$ K.

To understand the evolution during the photon-cooling epoch, we take into account the surface thermal emission of photons,

$$L_\gamma = 4\pi R^2 \bar{T}_{\rm eff}^4 \approx 9.5 \times 10^{32} \text{erg s}^{-1} \frac{\bar{T}_{\rm eff,6}^4}{g_{s,14}} \frac{M}{M_\odot} \tag{11.2}$$

and we take the total thermal energy of the neutron star to be (Shapiro & Teukolsky 1983)

$$U_n \simeq 6 \times 10^{47} \text{erg} \frac{M}{M_\odot} \left(\frac{\rho}{\rho_{\rm nuc}} \right)^{-2/3} T_{c,9}^2 . \tag{11.3}$$

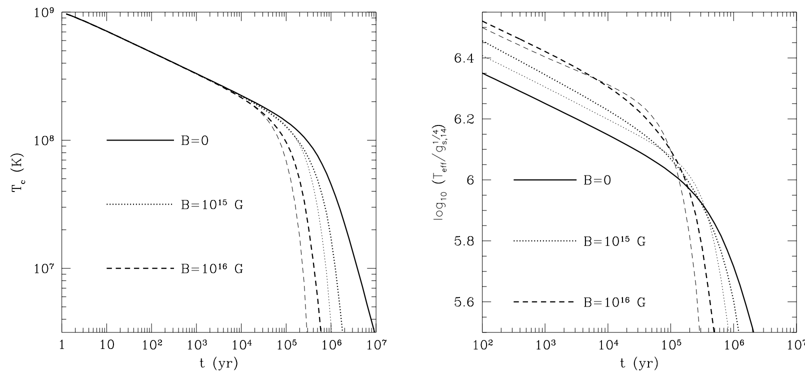

Figure 11.2: The left panel depicts the evolution of the core temperature with time for neutrino-dominated cooling (independent of B) and photon-dominated cooling for several field strengths using the conductivities of Hernquist (1984) (bold curves) and Potekhin & Yakovlev (1996) (light curves). The right panel shows the evolution of the mean effective temperature of the cooling neutron star for the neutrino and photon cooling epochs. The bold and light curves designate the same models as in the left panel.

Combining these equations yields

$$\frac{\mathrm{d}U_n}{\mathrm{d}t} = -\left(L_\nu + L_\gamma\right) \tag{11.4}$$

$$\frac{\mathrm{d}T_{c,9}}{\mathrm{d}t} = -\frac{1}{T_{c,9}}\left[\frac{1}{4\times10^7\mathrm{yr}}\frac{\bar{T}^4_{\mathrm{eff},6}}{g_{s,14}}\left(\frac{\rho}{\rho_{\mathrm{nuc}}}\right)^{2/3} + \frac{1}{8\mathrm{yr}}\left(\frac{\rho_{\mathrm{nuc}}}{\rho}\right)^{1/3}T^8_{c,9}\right] \tag{11.5}$$

where ρ is the mean density of the neutron star, and $\rho_{\mathrm{nuc}} = 2.8\times10^{14}$ g cm^{-3}.

Figure 11.2 shows the evolution of the core temperature and mean effective temperature at the surface. The evolution of the core temperature is unaffected by the magnetic field during the neutrino-cooling epoch. For fields approaching 10^{18} G, the magnetic field may begin to affect neutrino emission (*e.g.* Bander & Rubinstein 1993). However, after approximately $10^6 w$ yr, photon emission from the surface begins to dominate the evolution.

Here,

$$w = \left(\frac{\rho}{\rho_{\rm nuc}}\right)^{2/3} g_{s,14}^{-1}. \tag{11.6}$$

The cooling is accelerated by the magnetic field. In the presence of a 10^{16} G field, the core reaches a temperature of 10^7 K in only $3-6 \times 10^5 w$ yr compared to $6 \times 10^6 w$ yr for an unmagnetized neutron star. The bold curves trace the cooling of the core using the Hernquist (1984) conductivities, and the light curves follow the results for the Potekhin & Yakovlev (1996) conductivities.

The effect is more dramatic when one compares the effective surface temperatures of the models as a function of time. Again we present two sets of models. The right panel compares the cooling evolution using the conductivities of Hernquist (1984) (bold curves) and using those of Potekhin & Yakovlev (1996) (light curves) in the degenerate regime.

During the neutrino-cooling epoch the ultramagnetized neutron stars ($B = 10^{16}$ G) have 45% higher effective temperatures and emit over four times more radiation. Because during neutrino cooling the effective temperature falls relatively slowly with time, one can make a large error in estimating the age of the neutron star from its luminosity. For example, an envelope with 10^{16} G field remains above a given effective temperature 40 times longer than an unmagnetized envelope. For 10^{15} G, the timescale is increased by up to a factor of ten.

During the photon-dominated cooling era, the enhanced flux in a strong magnetic field reverses this effect. Photon cooling begins to dominate after about $10^5 w$ yr for 10^{16} G compared to $10^6 w$ yr in the zero-field case. Once photon cooling begins to dominate, the stars with stronger magnetic fields cool more quickly. A star with a 10^{16} G field reaches a given effective temperature 3–5 times faster than an unmagnetized star.

11.4 Discussion

Magnetic fields, especially those associated with magnetars, have a strong effect on the observed thermal evolution of neutron stars. In agreement with Shibanov & Yakovlev (1996), we find that during the neutrino cooling epoch, neutron stars with strong magnetic fields are brighter than their unmagnetized coevals. During the photon cooling epoch, the situation is reversed. A strongly magnetized neutron star cools more quickly during this era and emits less radiation at a given age.

It is difficult to compare our results more quantitatively with those of Shibanov & Yakovlev (1996), because besides studying more weakly magnetized neutron stars, they make slightly different assumptions regarding the properties of the envelope, include general relativistic effects on the magnetic field geometry, and use the models of Van Riper (1988) which include Coulomb corrections to the equation of state. For the larger fields investigated here we do find a stronger effect than Shibanov & Yakovlev (1996); however, the effect is not as strong as a naive power-law extrapolation from $10^{13.5}$ G (the largest field studied by Shibanov & Yakovlev 1996) to the ultramagnetized regime would indicate. Usov (1997) also extrapolates results at right field strengths and finds substantially larger photon luminosities during the neutrino-cooling epoch than we do. Again, a straightforward extrapolation from weaker fields overestimates the flux transmitted through a magnetized envelope.

We do not find the net insulating effect that Tsuruta & Qin (1995) find for weaker fields of 10^{12} G. Shibanov & Yakovlev (1996) find a similar, albeit much weaker effect, for fields $\sim 10^{10} - 10^{12}$ G. At these field strengths, the classical decrement in the thermal conductivity transverse to the field direction decreases the transmitted flux for a given core temperature. At the much stronger fields examined here, the increase in conductivity along the field lines (due to the quantization of the electron energies) dominates the decrease for perpendicular transport (in using the $\cos^2\psi$ rule we have neglected all heat transport perpendicular to the field lines).

Thompson & Duncan (1995) argue that soft gamma repeaters (SGRs) are powered by magnetic reconnection events near the surfaces of ultramagnetized neutron stars. Furthermore, Ulmer (1994) finds that a strong magnetic field can explain the super-Eddington radiation transfer in SGRs. Rothschild, Kulkarni & Lingenfelter (1994) estimate the luminosity of SGR 0526-66 in the quiescent state to be approximately 7×10^{35} erg/s. Since SGR 0526-66 is located in a supernova remnant, they can also estimate the age of the source to be approximately 5,000 years. For an isolated neutron star cooling by the modified URCA process, after 5,000 years, one would expect $L_\gamma = 6 \times 10^{33}$ erg/s for $B = 0$ and $L_\gamma = 3 \times 10^{34}$ erg/s for $B = 10^{16}$ G (we assume that the mass of the neutron star is $1.4 M_\odot$). Both these estimates fall short of the observed value. Even if SGR 0526-66 is powered by an ultramagnetized neutron star, its quiescent X-ray luminosity does not originate entirely from the thermal emission from the surface of the neutron star, unless either the age or luminosity estimates are in error by an order of magnitude, or possibly it has an accreted envelope.

11.5 Conclusions

We extend the previous studies of neutron star cooling into the ultramagnetized or magnetar regime ($B \sim 10^{15} - 10^{16}$ G) for iron envelopes.

We find that such an intense magnetic field dramatically affects the thermal evolution of a neutron star. In the neutrino-cooling epoch, effective temperatures of ultramagnetized neutron stars are up to 40% larger than their unmagnetized coevals. If the nucleons in the neutron star core are superfluid, neutrino cooling is inhibited. This will also increase the surface temperature at a given epoch.

Furthermore, if one assumes an unmagnetized evolutionary track for an ultramagnetized neutron star, one would overestimate its age by up to a factor of twenty five. During the photon-cooling epoch, the effect is reversed. Ultramagnetized neutron stars cool to a given effective temperature three times faster than their unmagnetized counterparts.

Chapter 12

Powering Anomalous Xray Pulsars by Neutron Star Cooling

SUMMARY

Using recently calculated analytic models for the thermal structure of ultramagnetized neutron stars, we estimate the thermal fluxes from young ($t \sim 1000$ yr) ultramagnetized ($B \sim 10^{15}$ G) cooling neutron stars. We find that the pulsed X-ray emission from objects such as 1E 1841-045 and 1E 2259+586 as well as many soft-gamma repeaters can be explained by photon cooling if the neutron star possesses a thin insulating envelope of matter of low atomic weight at densities $\rho < 10^7 - 10^8$ g/cm^3. The total mass of this insulating layer is $M \sim 10^{-11} - 10^{-8} M_\odot$.

12.1 Introduction

In recent years, several "breaking" (Mereghetti & Stella 1995) or "anomalous" (Van Paradijs, Taam & van den Heuvel 1995) x-ray pulsars have been discovered (Vasisht & Gotthelf 1997, Corbet et al. 1995). These objects typically have pulsed X-ray emission with steadily increasing periods ~ 10 s, X-ray luminosities $\sim 10^{35} - 10^{36}$ erg/s, soft spectra, and no detected companions or accretion disks. Furthermore, they are typically observed through hydrogen column densities $\sim 10^{22}$ cm^{-2} indicating that they are not common. Vasisht & Gotthelf (1997) describe several of these sources and present observations of 1E 1841-045, whose properties are characteristic of this class of objects.

Specifically, Vasisht & Gotthelf (1997) use archival observations of the supernova remnant Kes 73 obtained with the ASCA and ROSAT satellites. They find that the x-ray source in the center of the SNR, 1E 1841-045, had a period of 11.766684 s from the ASCA data taken in 1993 October. The ROSAT data of 1992 March is best fitted with a period of 11.7645 s, yielding a period derivative of $\dot{P} \simeq 4.73 \times 10^{-11}$s s^{-1} and a characteristic spin-down age of 4,000 yr – close to the estimated age for Kes 73 of 2,000 yr. Using these values and assuming that magnetic dipole radiation dominates the spin-down, they estimate the dipolar field strength of the neutron star to be $\sim 10^{15}$ G, well above the quantum critical field, $B_{cr} \approx 4.4 \times 10^{13}$ G. Other anomalous x-ray pulsars (AXPs) generally have small ages and long periods, leading one to derive similar field strengths.

With x-ray luminosities $L_X \sim 10^{35} - 10^{36}$ erg/s, AXPs are underluminous relative to accretion powered X-ray pulsars and are generally isolated. For 1E 1841-045, Vasisht & Gotthelf (1997) estimate a spin-down power of 10^{33} erg/s which falls short of the observed luminosity. They also argue that although 1E 1841-045 has a period near the equilibrium spin period for a young pulsar with $B \sim 10^{12}$ G and $L_X \sim 10^{35}$ erg/s, only an unlikely evolutionary process could spin down the neutron star to this rate within the 2,000 year age of Kes 73. They suggest that 1E 1841-045 may be powered by magnetic field decay in a dipolar field of strength $B \sim 10^{15}$ G (Thompson & Duncan 1996, Goldreich & Reisenegger 1992).

In this *Letter*, we propose a natural explanation for the observed X-ray emission from AXPs. Neutron stars with ages $\sim$ 1,000 yr and magnetic fields $B \gtrsim 10^{15}$ G have thermal emission in the X-ray-band with total luminosities $\sim 10^{35}$ erg/s, if their surface layers consist of light-weight material, such as hydrogen and helium. In previous papers, we have developed an analytic model for ultramagnetized neutron star envelopes (Heyl & Hernquist 1997a) and calculated the emission through iron envelopes and showed how a strong magnetic field affects neutron-star cooling (Heyl & Hernquist 1997e). Here, we will examine the properties of ultramagnetized hydrogen and helium envelopes and draw parallels with the observed properties of AXPs.

12.2 Model Envelopes

Heyl & Hernquist (1997a) have developed analytic models for ultramagnetized neutron star envelopes and find that the flux transmitted through the envelope is simply related to the direction and strength of the magnetic field and to the core temperature (T_c). Specifically, these models apply only below densities $\rho_{\rm max}$ at which the ground Landau level becomes filled; *i.e.* $2.2 \times 10^8 - 7.1 \times 10^9$ g/cm^3 for polar fields, $B = 10^{15} - 10^{16}$ G.

Here we consider hydrogen and helium envelopes with $B \sim 10^{15}$ G and core temperatures expected for cooling by the modified URCA process after $\sim$ 1,000 yr. Although our models do not extend to the high densities traditionally associated with the isothermal core of a neutron star ($\rho \gtrsim 10^{10}$ g/cm^3), for $B \sim 10^{15}$ G and $T_c \sim 10^8 - 10^{8.5}$ K, the envelope is nearly isothermal at $\rho_{\rm max}$. We denote the temperature at this density by $T_{\rm max}$ and for this analysis take it to be equal to the core temperature.

The envelope models are calculated using a plane-parallel, Newtonian approximation. In this approach, the core temperature is a function of F/g_s, B and ψ (the angle between the radial and field directions). F is the transmitted heat flux, g_s is the surface gravity, and all of these values are taken to be in the frame of the neutron star surface. For such strong fields, the models have a simple dependence on the angle ψ, *i.e.* $F/g_s \propto \cos^2 \psi$ (Heyl & Hernquist 1997a, Shibanov et al. 1995, Shibanov & Yakovlev 1996) and furthermore the flux for a fixed core temperature is approximately proportional to $B^{0.4}$. With these two facts, we find that the average flux over the surface of a neutron star with a dipole field configuration is 0.4765 times its peak value at the magnetic poles.

For a given core temperature, magnetized envelopes transmit more heat than unmagnetized ones (*e.g.* Hernquist 1985). Furthermore, as Hernquist & Applegate (1984) found, the relationship between the core temperature and the transmitted flux is strongly sensitive to the composition of the degenerate portion of the envelope, specifically iron insulates the core much more effectively that hydrogen or helium. Because of the intense magnetic field, the luminosities for a given core temperature are even larger than those found by Potekhin, Chabrier & Yakovlev (1997).

12.3 Luminosity Evolution

We have calculated the expected luminosity of an ultramagnetized neutron star as a function of time. We assume that the core of the neutron star cools by only the modified URCA process (*e.g.* Shapiro & Teukolsky 1983),

$$\Delta t(\mathrm{URCA}) \simeq 1 \left(\frac{\rho}{\rho_{\rm nuc}} \right)^{-1/3} T_{c,9}^{-6}(f) \left\{ 1 - \left[\frac{T_{c,9}(f)}{T_{c,9}(i)} \right]^6 \right\} \mathrm{yr}, \qquad (12.1)$$

where $T_x = T/10^x$ K and Δt is an estimate of the age of the neutron star. For simplicity, we will assume that the initial temperature is much larger than the current temperature $T_c(f)$.

If one ignores gravitational redshift effects which depend on the radius of the neutron star, the photon luminosity is given by

$$L_\gamma = 4\pi GM\frac{F}{g_s} \approx 9.5 \times 10^{32}\frac{\bar{T}^4_{\rm eff,6}}{g_{s,14}}\frac{M}{M_\odot}\text{erg s}^{-1} \qquad (12.2)$$

We will take $M = 1.4M_\odot$.

Figure 12.1 depicts the photon luminosity and mean effective temperature as a function of time for several field strengths with iron, helium, and hydrogen envelopes. We see that the photon luminosity increases with increasing magnetic field, but the composition of the envelope is a more important effect. The luminosity through a hydrogen envelope is ten times larger than through iron and 1.6 times larger than through helium. The relationship between core temperature and flux is most sensitive to the thermal conductivity in the liquid portion of the degenerate envelope (Gudmundsson, Pethick & Epstein 1982). In this zone, the conductivity is proportional to Z^{-1}; consequently, low Z envelopes conduct heat more readily.

To lowest order, for a given magnetic field strength and core temperature, the transmitted flux is proportional to $Z^{-2/3}$. The dependence on Z/A is weaker. The flux dips sharply for hydrogen and helium with $B = 10^{16}$ G, when the material near the degenerate-non-degenerate interface begins to solidify. At a given density the conductivity due to degenerate electrons is smaller in the solid state than in the liquid phase.

We note that our assumption that the magnetic field has no explicit influence on the phase of the matter is problematic for these intense fields. For example, the magnetic field may well alter the state of the material in the solid portion of the crust, particularly when the magnetic stress exceeds the yield stress of the lattice. The shear modulus of the lattice is $\mu \sim (Ze)^2 n_Z^{4/3}$, where n_Z is the ion number density (Ruderman 1972). Assuming that the lattice breaks when the strain angle $\chi_{\rm strain} \sim 10^{-2}$, magnetic stresses dominate when (*e.g.* Blandford & Hernquist 1982; Blandford, Applegate & Hernquist 1983)

$$B \gtrsim 1.2 \times 10^6 Z A^{-2/3}\left(\frac{\rho}{1\text{ g cm}^{-3}}\right)^{2/3}\text{G}, \qquad (12.3)$$

which is satisfied throughout the crust for fields $B \gtrsim 10^{14}$ G.

Even for the weakest field considered, $B = 10^{15}$ G, the photon luminosity through a hydrogen envelope is 1.5×10^{35} erg/s for an age of 2,000 yr. This is comparable to both the pulsed X-ray pulsed luminosity of 1E 1841-045 of $L_X \approx 5 \times 10^{34} d_7^2$ erg/s (d_7 is the distance to the source divided by

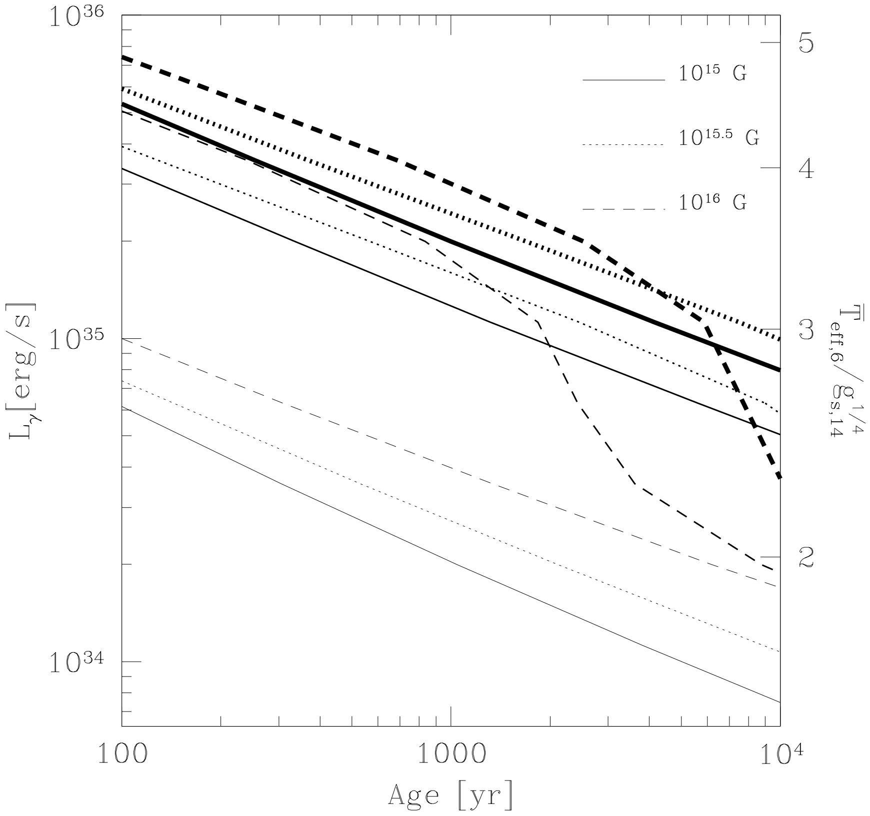

Figure 12.1: Photon luminosity and mean effective temperature as a function of the age of the neutron star. The upper bold curves trace the evolution for hydrogen envelopes, the intermediate curves give the evolution for helium envelopes and the lowest light curves follow the cooling through iron envelopes. The values of $\rho_{\rm max}$ for hydrogen envelopes are given in the legend.

7 kpc) and the total X-ray luminosity of $3.5 \times 10^{35} d_7^2$ erg/s, given observational uncertainty.

The photon luminosity is nearly large enough to account for the luminosity in the quiescent state of the soft gamma repeater (SGR 0526-66). Several authors have advanced the view that strongly magnetized neutron star power SGRs. For example, Thompson & Duncan (1995) propose that soft gamma repeaters (SGRs) are powered by magnetic reconnection events near the surfaces of ultramagnetized neutron stars. Ulmer (1994) finds that a strong magnetic field can explain the super-Eddington radiation transfer in SGRs. Rothschild, Kulkarni & Lingenfelter (1994) estimate the luminosity of SGR 0526-66 in the quiescent state to be approximately 7×10^{35} erg/s. Since SGR 0526-66 is located in a supernova remnant, they can also estimate the age of the source to be approximately 5,000 years. For this age and a magnetic field of $B = 10^{15.5} G$, we find a photon luminosity of 1.5×10^{35} erg/s, not far short of the SGR's quiescent luminosity.

12.4 Discussion

To determine the viability of our model for AXP emission, we must ascertain whether or not neutron stars with $B \sim 10^{15}$ G are likely to have an insulating envelope of the required mass in low atomic weight matter. From numerical experimentation, we have found that the relationship between the core temperature and the effective temperature is most sensitive to the composition in the degenerate, liquid portion of the envelope; *i.e.* the "sensitivity" region found by Gudmundsson, Pethick & Epstein (1982). The density in this zone is approximately in the range $10^6 - 10^7$ g/cm^3.

We can appeal to the equation of hydrostatic equilibrium to calculate the total mass up to a certain density. If we assume that the envelope is thin, we have

$$\Delta M = \frac{4\pi R^2}{g_s} P, \tag{12.4}$$

where R is the radius of the neutron star and P is the pressure at the given depth. In the region of interest, the pressure is supplied by degenerate electrons occupying the ground Landau level. In a strong magnetic field, electrons become relativistic at

$$\rho \approx 3.3 \times 10^7 B_{15} \mu_e \mathrm{g/cm}^3, \tag{12.5}$$

where $B_{15} = B/10^{15}$ G and $\mu_e = A/Z$ is the mean atomic weight per electron (*e.g.* Heyl & Hernquist 1997a).

For nonrelativistic electrons the equation of state is

$$P_e = 1.5 \times 10^{20} B_{15}^{-2} \mu_e^{-3} \rho_6^3 \text{dynes/cm}^2 \text{ for } \rho_6 \ll 33 B_{15} \mu_e, \tag{12.6}$$

where $\rho_6 = \rho/10^6$ g/cm^3.

For densities $\rho_6 \gg 33 B_{15} \mu_e$, the electrons are relativistic, and we obtain the equation of state,

$$P_e = 7.5 \times 10^{21} B_{15}^{-1} \mu_e^{-2} \rho_6^2 \text{dynes/cm}^2. \tag{12.7}$$

Therefore, depending on the maximum density of the insulating layer, we obtain for its total mass,

$$\Delta M = 7.1 \times 10^{-15} R_6^4 \left(\frac{M}{M_\odot}\right)^{-1} B_{15}^{-2} \mu_e^{-3} \rho_6^3 M_\odot \tag{12.8}$$

in the non-relativistic limit where M is the mass of the neutron star and $R_6 = R/10^6$ cm. In the relativistic limit, we obtain

$$\Delta M = 3.5 \times 10^{-13} R_6^4 \left(\frac{M}{M_\odot}\right)^{-1} B_{15}^{-1} \mu_e^{-2} \rho_6^2 M_\odot. \tag{12.9}$$

At a minimum, the low-Z insulating layer must extend into the degenerate portion of the envelope where $\rho_6 \sim 10$. The non-relativistic estimate for the mass of this layer yields $\sim 10^{-11} M_\odot$ for $B = 10^{15}$ G. If the layer extends to the density at which the first Landau level fills ($\rho_6 \sim 200$) well into the relativistic regime, $\Delta M \sim 10^{-8} M_\odot$ for $B = 10^{15}$ G.

The high temperatures accompanying core collapse are generally thought to process the material that will comprise the neutron star envelope to nuclear statistical equilibrium; therefore, the envelope is expected to consist of ^{56}Fe and heavier nuclei at higher densities (*e.g.* Shapiro & Teukolsky 1983). A hydrogen or helium envelope must contain material accreted by the neutron star from the interstellar medium or from the "detritus" of the supernova. Even with an intense magnetic field to dramatically increase the Alfven radius, a neutron star would require $\sim 10^6$ yr to accrete $\sim 10^{-11} M_\odot$ from the ISM, unless the neutron star were traveling through an unusually dense region. For example,

$$\dot{M} \sim 10^{-14} n_4^{7/9} R_6^{4/3} B_{15}^{4/9} v_7^{7/9} \left(\frac{M}{M_\odot}\right)^{2/3} M_\odot/\text{yr}, \tag{12.10}$$

where n_4 is the number density of the ISM in units of 10^4cm^{-3}, $v_7 = v/10^7$ cm/s, and v is the velocity of the neutron star. In such a dense medium, the neutron star could accrete the minimum required $10^{-11} M_\odot$ within $\approx$ 1,000 years. If the nascent neutron star received a kick during the supernova explosion, it could accrete material from the high density remnant of the progenitor star. Duncan & Thompson (1992) argue that a strong magnetic field $B \sim 10^{15}$ G can cause the neutrino emission from the nascent neutron star to be anisotropic; consequently, the neutron star would recoil at $v \sim 100$ km/s relative to center of the explosion.

Chevalier (1989) modeled the accretion by a nascent neutron star or black hole from the exploded envelope of SN 1987A. He found that $\sim 0.1 M_\odot$ will fall back within several days of the explosion. For a typical type II supernova which has an extended envelope, the total accreted mass may be a factor of 100 smaller, yielding a total of $10^{-3} M_\odot$ of material to comprise the insulating layer. Although much of this material will have been processed during the evolution of the star, the X-ray and gamma-ray light curves of SN 1987A as well as numerical simulations indicate that heavy and light elements mix during the explosion (McCray 1993 and references therein); any unprocessed remnants of the progenitor star's hydrogen envelope would quickly float to the surface (Lai & Salpeter 1997) and form a hydrogen envelope on the neutron star. Even in an intense magnetic field, pycnonuclear fusion reactions do not proceed quickly enough to substantially process the accreted material within 1,000 yr (Heyl & Hernquist 1996; Lai & Salpeter 1996). If insufficient hydrogen fell back, the photon luminosity for a helium envelope is only one third lower than that of a hydrogen envelope; consequently, even a Type Ib supernova could result in a cooling-powered neutron star with sufficient luminosity to be observed as an AXP.

Zavlin, Pavlov & Shibanov (1996) calculate several model atmospheres for cooling neutron stars including hydrogen and helium for weak magnetic fields ($B \sim 10^8 - 10^{10}$ G), and compare the emergent spectra with a blackbody distribution. Because the opacity of a hydrogen or helium atmosphere drops quickly with photon energy, high energy photons originate from deeper and hotter layers of the atmosphere; consequently, hydrogen and helium atmospheres have spectra which peak at a higher frequency and have stronger Wien tails than a blackbody spectrum with the same effective temperature (Romani 1987). Pavlov et al. (1996) convolve the spectra from neutron star atmospheres consisting of hydrogen with the ROSAT response function and find that the fitted values of $T_{\rm eff}$ are 4.17 times higher than the model value. The observed best-fit blackbody temperature for the spectrum of 1E 2259+586 is 0.45 keV. This is about twice the effective temperature of our model envelopes. The processing of the radiation by the hydrogen atmosphere may account for this shift.

Furthermore, in the energy range of 1–10 keV, hydrogen spectra tend to be less steep ($S_\nu \propto \nu^{-5}$) than the equivalent blackbody spectra. Although they are not as shallow as the non-thermal tail observed in 1E 2259+586, $S_\nu \propto \nu^{-3}$, mechanisms in the magnetosphere probably contribute to the high-energy emission.

An intense magnetic field induces a temperature variation across the surface of the neutron star (Heyl & Hernquist 1997a). This gradient combined with the limb darkening manifest in models of magnetized neutron star atmospheres (Romani 1987, Zavlin, Pavlov & Shibanov 1996) can naturally explain the observed pulsed fraction of Kes 73 of 35% (Vasisht & Gotthelf 1997).

12.5 Conclusions

We find that young ($t \sim 1,000$ yr) neutron stars with strong magnetic fields ($B \sim 10^{15}$ G) and hydrogen or possibly helium envelopes have photon luminosities similar to those observed from anomalous X-ray pulsars and soft-gamma repeaters in their quiescent state. The total mass of the insulating layer is $10^{-11} - 10^{-8} M_\odot$. A strongly magnetized neutron star could accrete enough material from the ISM within 1,000 years only if the ISM is sufficiently dense, $n \gtrsim 10^4 \mathrm{cm}^{-3}$. However, sufficient material is expected to fall back onto the neutron star surface following the explosion of massive stars.

Chapter 13

What is the nature of RX J

SUMMARY

RX J0720.4-3125 has recently been identified as a pulsating soft X-ray source in the ROSAT all-sky survey with a period of 8.391 s. Its spectrum is well characterized by a black-body with a temperature of 8×10^5 *K. We propose that the radiation from this object is thermal emission from a cooling neutron star. For this black-body temperature we can obtain a robust estimate of the object's age of* $\sim 3 \times 10^5$ *yr, yielding a polar field* $\sim 10^{14}$ *G for magnetic-dipole spin down and a value of* $\dot{P}$ *compatible with current observations.*

13.1 Introduction

"Breaking" (Mereghetti & Stella 1995) or "anomalous" (Van Paradijs, Taam & van den Heuvel 1995) x-ray pulsars (AXPs) typically have pulsed X-ray emission with steadily increasing periods ~ 10 s, X-ray luminosities $\sim 10^{35} - 10^{36}$ erg/s, soft spectra, and no detected companions or accretion disks. Haberl et al. (1997) have recently identified RX J0720.4-3125 as a pulsating, soft X-ray source with a period of 8.391 s. They estimate its bolometric luminosity to be $2.6 \times 10^{31} d_{100}^2$ erg/s, where d_{100} is the object's distance in units of 100 pc.

Wang (1997) has proposed that accretion onto a weakly magnetized neutron star powers RX J0720.4-3125, and that for the neutron star to spin down to 8.391 s within a Hubble time, it either must have been born with a period ~ 0.5 s or have experienced magnetic field decay. Our proposal begins with the second footnote of Wang (1997) which suggests the possibility that RX J0720.4-3125 is powered by an internal heat source. We propose that the neutron-star cooling powers RX J0720.4-3125. This would give it an age $\sim 3 \times 10^5$ yr, much younger than the Wang's (1997) estimated age $\gtrsim 10^9$ yr.

13.2 Calculations

In a previous paper (Heyl & Hernquist 1997d), we have argued that AXPs may be powered by neutron star cooling through an accreted envelope. Here we examine the cooling evolution of neutron stars with polar field strengths ranging from 0 to 10^{16} G. The zero field calculation is based on the envelope model of Hernquist & Applegate (1984). The results of Hernquist (1985) describe the model envelope for 10^{13} G, and the ultramagnetized cases ($10^{14} - 10^{16}$ G) are calculated from the models of Heyl & Hernquist (1997a).

We choose a simple cooling model with the modified URCA process (Shapiro & Teukolsky 1983) and photon cooling competing (Heyl & Hernquist 1997e). Both the envelope calculations and the cooling calculations are performed in the frame of the surface; consequently, the observed effective temperature for a given core temperature is proportional to $g_s^{1/4}$ (g_s is the gravitation acceleration at the surface) and $(1+z_g)^{-1}$ where

$$(1+z_g)^{-1} = \sqrt{1 - \frac{2GM}{Rc^2}}. \tag{13.1}$$

To obtain the effective temperature as observed at infinity for a given equation of state (*i.e.* M and R), these two corrections must be performed. Additionally, since for a magnetized neutron star, the thermal emission is not isotropic along the surface, we present the flux-weighted mean $\bar{T}_{\rm eff}$ over the entire surface.

Figure 13.1 depicts the thermal evolution for several values of the magnetic field at the pole. We have assumed that $g_s = 10^{14}$ cm/s^2. The horizontal line gives the value of $T_{\rm bb} = 8 \times 10^5$ K found by Haberl et al. (1997). Depending on the size and mass of the neutron star, this line may move up or down slightly; however, this will not strongly affect the age estimate because temperature drops quickly with age for $t \gtrsim 3 \times 10^5$ yr. Additionally, we see that near this temperature, neutrino cooling and photon cooling both contribute; consequently, the temperature at this age does not depend strongly on field strength or composition.

From these evolutionary tracks, we find that the age of RX J0720.4-3125 may range from 1.2×10^5 yr for a 10^{14} G field with a hydrogen envelope

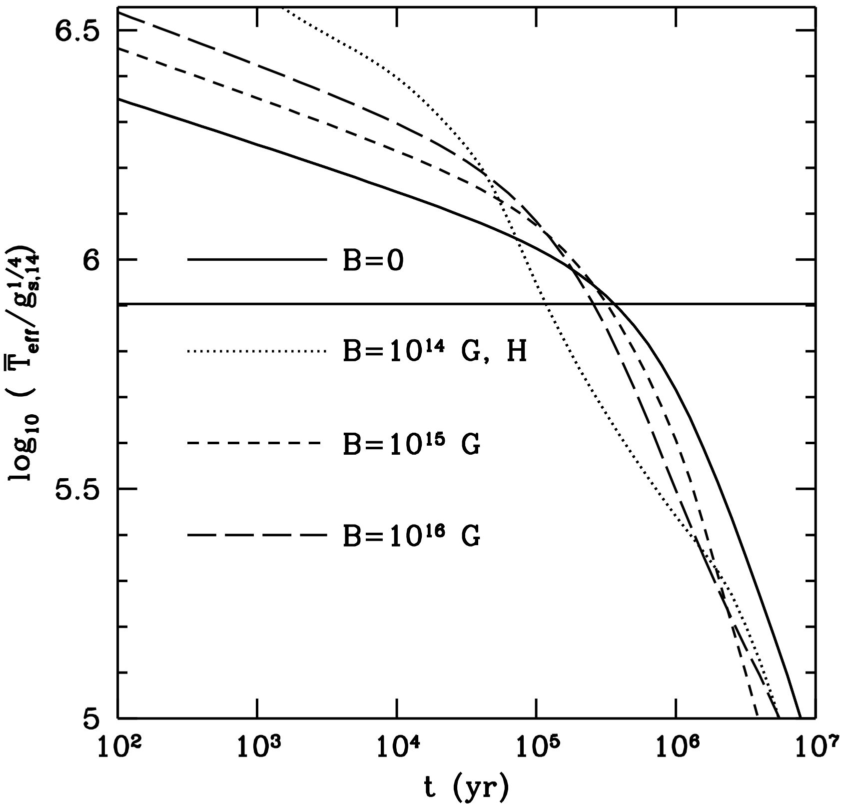

Figure 13.1: The curves trace the cooling evolution of isolated neutron stars by the modified URCA process and the radiation of photons from the surface for several field strengths with iron and hydrogen envelopes. The horizontal line traces the observed surface temperature of RX J0720.4-3125 of $8 \times 10^5 K$.

to 3.6×10^5 yr for an unmagnetized neutron star. The intense fields yield ages intermediate to these. We will assume a polar field of 10^{14} G and an iron envelope yielding an age estimate of 3.3×10^5 yr. With this age, we can obtain an estimate of the magnetic field of the neutron star, if we assume that its has spun down by magnetic dipole radiation (Shapiro & Teukolsky 1983),

$$t = \frac{3Ic^3}{B_p^2 R^6 \sin^2 \alpha \Omega_0^2}. \tag{13.2}$$

Solving for the magnetic field strength yields,

$$\begin{aligned} B_p \sin\alpha &= \sqrt{\frac{3Ic^3}{t}} \frac{P}{2\pi R^3} = 9.3 \times 10^{13} \mathrm{G} \left(\frac{M}{M_\odot}\right)^{1/2} \times \\ & \left(\frac{R}{10^6 \mathrm{cm}}\right)^{-2} \left(\frac{t}{3.3 \times 10^5 \mathrm{yr}}\right)^{-1/2} \end{aligned} \tag{13.3}$$

This age estimate also yields a value for $\dot{P}$. For spin down by magnetic dipole radiation,

$$T = \frac{P}{\dot{P}} = 2t \tag{13.4}$$

which yields $\dot{P} = 4.3 \times 10^{-13}$. This is consistent with the observed $\dot{P} = -6.0 - 0.8 \times 10^{-12}$.

13.3 Discussion

We present a simple model for RX J0720.4-3125. Its emission originates from neutron-star cooling through a magnetized envelope. We derive a magnetic field $\sim 10^{14} G$, an age $\sim 3 \times 10^5$ yr and a period derivative of 4×10^{-13}. The primary contrast between the predictions of this model and those of Wang (1997) is the value of $\dot{P}$.

Wang (1997) argues that RX 0720.4-3125 is an old object, $t \gtrsim 10^9$ yr. It initially had a much stronger field ($\sim 10^{12}$ G) than at present. Before decaying to $\sim 10^{10}$ G, the magnetic field spun down the neutron star to its present rate. Wang argues that accretion powers the present emission and that a value of $\dot{P} \lesssim 10^{-16}$ is consistent with this field-decay model.

Our prediction of $\dot{P}$ lies just within the current limits which Haberl et al. (1997) obtained over a three-year baseline. An further round of observations within the next several years could determine whether RX J0720.4-3125 is a middle-aged, isolated cooling neutron star or an ancient neutron star accreting from the interstellar medium.

Acknowledgements

I would first like to express my appreciation for my supervisor, Lars Hernquist, with whom I have had the pleasure of working over the last six years. Thank you for suggesting that I focus on the really small scale after spending several years among the galaxies. I would also like to thank Lars Bildsten, Jon Arons, Roger Romani and Mike Bolte for enlightening discussions about neutron stars and other things.

I thank the National Science Foundation which provided financial support during the first three years of my Ph.D. study and the California Space Initiative which filled the gap at the end of my study.

I would like to thank all my officemates while at Santa Cruz: Mike Keane with whom I shared a closet for a year in Nat Sci II, the solar system for whom I was a reluctant and unexpected sun, and Jennifer, Amy and Katherine. You and everyone else at Santa Cruz made it fun.

My mother and father gave me an early appreciation for science, for the ground below and the sky above. Thank you for introducing me to a grand adventure.

I thank Jenny for making sure I keep things in perspective and for supporting me all along the way.

Bibliography

Abramovici, A. *et al.* 1992, *Science,* **256**, 325.

Abramovici, A. *et al.* 1996, *Phys. Lett. A,* **218**, 157.

Abramowitz, M. & Stegun, I. A. 1970, *Handbook of Mathematical Functions*, Dover, New York

Adler, S. L. 1971, *Ann. Phys.,* **67**, 599.

Anderson, S. B., Córdova, F. A., Robinson, G. G. P. C. R. & Thompson, Jr., R. J. 1993, *ApJ,* **414**, 867.

Arons, J. 1993, *ApJ,* **408**, 160.

Baade, W. & Zwicky, F. 1934, *Phys. Rev.,* **45**, 138.

Bahcall, J. N. *et al.* 1982, *Rev. Mod. Phys.,* **54**, 767.

Baĭer, V. N., Katkov, V. M. & Strakhovenko, V. M. 1975a, *Soviet Physics - JETP,* **40**, 225.

Baĭer, V. N., Katkov, V. M. & Strakhovenko, V. M. 1975b, *Soviet Physics - JETP,* **41**, 198.

Baĭer, V. N., Milstein, A. I. & Shaisultanov, R. Z. 1996, *Photon Splitting in a Very Strong Magnetic Field*, hep-th/9604028 Preprint

Balkemore, R. P. & Frankel, R. B. 1981, *Sci. Am.,* **245**, 42.

Bander, M. & Rubinstein, H. 1993, *Phys Lett B,* **311**, 187.

Baring, M. G. 1995, *ApJL,* **440**, 69.

Barnes, E. W. 1900, *The Quarterly Journal of Pure and Applied Mathematics,* **31**, 264.

Baym, G., Pethick, C. J. & Sutherland, P. G. 1971, *ApJ,* **170**, 299.

Becker, W. & Trümper, J. 1993, *Nature,* **365**, 528.

Berestetskii, V. B., Lifshitz, E. M. & Pitaevskii, L. P. 1982, *Quantum Electrodynamics*, Pergamon, Oxford, second edition

Bialynicka-Birula, Z. 1981, *Physica D,* **2**, 513.

Binney, J. & Tremaine, S. 1987, *Galactic Dynamics*, Princeton Univ. Press, Princeton

Bjorken, J. D. & Drell, S. D. 1964, *Relativistic Quantum Mechanics*, McGraw-Hill, New York

Blandford, R. D., Applegate, J. H. & Hernquist, L. 1983, *MNRAS,* **204**, 1025.

Blandford, R. D. & Hernquist, L. 1982, *J. Phys. C: Solid State Phys.,* **15**, 6233.

Boillat, G. 1972, *Phys. Lett.,* **40A**, 9.

Bransden, B. H. & Joachain, C. J. 1989, *Introduction to Quantum Mechanics*, Longman, Harlow, England

Canuto, V. & Kelly, D. C. 1972, *Astr. Sp. Sci.,* **17**, 277.

Chen, H.-H., Ruderman, M. A. & Sutherland, P. G. 1974, *ApJ,* **191**, 473.

Chevalier, R. A. 1989, *ApJ,* **847**, 847.

Clayton, D. D. 1983, *Principle of Stellar Evolution and Nucleosynthesis*, The University of Chicago Press, Chicago

Corbet, R. H. D., Smale, A. P., Ozaki, M., Koyama, K. & Iwasawa, K. 1995, *ApJ,* **443**, 786.

Cox, J. P. & Giuli, R. T. 1968, *Principles of Stellar Structure*, Gordon and Breach, New York

Dittrich, W. & Reuter, M. 1985, *Effective Lagrangians in quantum electrodynamics*, Springer-Verlag, Berlin

Dittrich, W., Tsai, W. & Zimmermann, K.-H. 1979, *Phys. Rev D.,* **19**, 2929.

Duncan, R. C. & Thompson, C. 1992, *ApJL,* **392**, 9.

Erber, T. 1966, *Rev. Mod. Phys.,* **38**, 626.

Euler, H. & Kockel, B. 1934, *Naturwissenschaften,* **23**, 246.

Finley, J., Ögelman, H. & Kiziloglu, Y. 1992, *ApJL,* **394**, 21.

Flowers, E. G., Lee, J. F., Ruderman, M. A., Sutherland, P. G., Hillebrandt, W. & Müller, E. 1977, *ApJ,* **215**, 291.

Ginzburg, V. L. & Ozernoy, L. M. 1964, *Zh. Exp. Teor. Fiz.,* **47**, 1030.

Glen, G. & Sutherland, P. 1980, *ApJ,* **239**, 671.

Goldreich, P. & Reisenegger, A. 1992, *ApJ,* **395**, 250.

Greenstein, G. & Hartke, G. J. 1983, *ApJ,* **271**, 283.

Greiveldinger, C. *et al.* 1996, *ApJL,* **465**, 35.

Gudmundsson, E. H., Pethick, C. J. & Epstein, R. I. 1982, *ApJL,* **259**, 19.

Haberl, F., Motch, C., Buckley, D. A. H., Zickgraf, F.-J. & Pietsch, W. 1997, *A&A,*, in press

Haines, L. K. & Roberts, D. H. 1969, *Am. Journ. Phys.,* **37**, 1145.

Halpern, J. P. & Holt, S. S. 1992, *Nature,* **357**, 222.

Halpern, J. P. & Ruderman, M. 1993, *ApJ,* **415**, 286.

Halpern, J. P. & Wang, F. Y. H. 1997, *ApJ,* **477**, 905.

Heisenberg, W. & Euler, H. 1936, *Z. Physik,* **98**, 714.

Hernquist, L. 1984, *ApJS,* **56**, 325.

Hernquist, L. 1985, *MNRAS,* **213**, 313.

Hernquist, L. & Applegate, J. H. 1984, *ApJ,* **287**, 244.

Hewish, A., Bell, S. J., Pilkington, J. D. H., Scott, P. F. & Collins, R. A. 1968, *Nature,* **217**, 709.

Heyl, J. S. & Hernquist, L. 1996, *Phys Rev C,* **54**, 2751.

Heyl, J. S. & Hernquist, L. 1997a, *Almost Analtyic Models of Ultramagnetized Neutron Star Envelopes*, submitted to *MNRAS*

Heyl, J. S. & Hernquist, L. 1997b, *Phys. Rev. D,* **55**, 2449.

Heyl, J. S. & Hernquist, L. 1997c, *Jour. Phys. A,* **30**, 6485.

Heyl, J. S. & Hernquist, L. 1997d, *ApJL,* **489**, 67.

Heyl, J. S. & Hernquist, L. 1997e, *ApJL,* **491**, 95.

Itoh, N., Yasuharu, Kohyama, Matsumoto, N. & Seki, M. 1984, *ApJ,* **285**, 758.

Itzykson, C. & Zuber, J.-B. 1980, *Quantum Field Theory*, McGraw-Hill, New York

Ivanov, B. V. 1992, *Phys. Let. B,* **282**, 228.

Jackson, J. D. 1975, *Classical Electrodynamics*, John Wiley, New York, second edition

Kippenhahn, R. & Weigert, A. 1990, *Stellar Structure and Evolution*, Springer, Berlin

Klein, J. J. & Nigam, B. P. 1964a, *Phys. Rev.,* **135**, B 1279.

Klein, J. J. & Nigam, B. P. 1964b, *Phys. Rev.,* **136**, B 1540.

Lai, D. & Salpeter, E. E. 1995, *Phys. Rev. A.,* **52**, 2611.

Lai, D. & Salpeter, E. E. 1996, *Phys. Rev. A.,* **53**, 152.

Lai, D. & Salpeter, E. E. 1997, *Hydrogen Phases on the Surface of a Strongly Magnetized Neutron Star*, astro-ph/9704130

Lai, D., Salpeter, E. E. & Shapiro, S. L. 1992, *Phys. Rev. A.,* **45**, 4832.

Landau, L. D. & Lifshitz, E. M. 1977, *Quantum Mechanics*, Pergamon, Oxford, third edition

Landau, L. D. & Lifshitz, E. M. 1987a, *The Classical Theory of Fields*, Pergamon, Oxford, fourth edition

Landau, L. D. & Lifshitz, E. M. 1987b, *Fluid Mechanics*, Pergamon, Oxford, second edition

Landau, L. D. & Lifshitz, E. M. 1989, *Quantum Mechanics : Non-Relativistic Theory*, Pergamon, Oxford, third edition

Le Guillou, J. C. & Zinn-Justin, J. 1984, *Ann. Phys.,* **154**, 440.

Lopez, J. C., Hess, P. & Turbiner, A. 1997, H_2^+ *ion in strong magnetic field: an accurate calculation*, astro-ph/9707050

Loudon, R. 1959, *Am. J. Phys.,* **27**, 649.

Lutzky, M. & Toll, J. S. 1959, *Phys. Rev.,* **113**, 1649.

McCray, R. 1993, *ARA&A,* **31**, 175.

Mereghetti, S. & Stella, L. 1995, *ApJL,* **442**, 17.

Mészáros, P. 1992, *High-Energy Radiation from Magnetized Neutron Stars*, University of Chicago Press, Chicago

Mielniczuk, W. J. 1982, *J. Phys. A: Math. Gen.,* **15**, 2905.

Mielnieczuk, W. J., Lamm, D. R. & Valluri, S. R. 1988, *Can. J. Phys.,* **66**, 692.

Mietner, L. & Kösters, H. 1933, *Z. Phys.,* **84**, 144.

Milstein, A. I. & Schumacher, M. 1994, *Phys. Rep.,* **243**, 183.

Morrison, R. & McCammon, D. 1983, *ApJ,* **270**, 119.

Müller, E. 1984, *A&A,* **130**, 415.

Neuhauser, D., Koonin, S. E. & Langanke, K. 1987, *Phys. Rev. A,* **36**, 4163.

Nomoto, K. & Tsuruta, S. 1981, *ApJL,* **250**, 19.

Ögelman, H. 1995, in M. A. Alpar, U. Kiziloglu & J. V. Paradijs (eds.), *The Lives of Neutron Stars*, p. 101, Kluwer, Dordrecht

Ögelman, H. & Finley, J. P. 1993, *ApJL,* **413**, 31.

Ögelman, H., Finley, J. P. & Zuckerman, H. U. 1993, *Nature,* **361**, 136.

Page, D. 1995, *ApJ,* **442**, 273.

Page, D. & Sarmiento, A. 1996, *ApJ,* **473**, 1067.

Pandharipande, V. R. 1971, *Nucl Phys A,* **178**, 178.

Pavlov, G. G. & Panov, A. N. 1976, *Sov. Phys. JETP,* **44**, 300.

Pavlov, G. G., Shibanov, Y. A., Ventura, J. & Zavlin, V. E. 1994, *A&A,* **289**, 837.

Pavlov, G. G. & Yakovlev, D. G. 1977, *Astrophysics,* **13**, 89.

Pavlov, G. G., Zavlin, V. E., Trümper, J. & Neuhäuser, R. 1996, *Multi-wavelength observations of isolated neutron stars as a tool to probe the properties of their surfaces*, astro-ph/9609097

Possenti, A., Mereghetti, S. & Colpi, M. 1996, *A&A,* **313**, 565.

Potekhin, A. Y., Chabrier, G. & Yakovlev, D. G. 1997, *A&A,* **323**, 415.

Potekhin, A. Y. & Yakovlev, D. G. 1996, *A & A,* **314**, 341.

Press, W. H., Flannery, B. P., Teukolsky, S. A. & Vettering, W. T. 1988, *Numerical Recipes in C,* Cambridge Univ. Press, Cambridge, first edition

Rajagopal, M., Romani, R. W. & Miller, M. C. 1997, *ApJ,* **479**, 347.

Romani, R. W. 1987, *ApJ,* **313**, 718.

Rothschild, R. E., Kulkarni, S. R. & Lingenfelter, R. E. 1994, *Nature,* **368**, 432.

Ruder, H. *et al.* 1994, *Atoms in Strong Magnetic Fields : Quantum Mechanical Treatment and Applications in Astrophysics and Quantum Chaos*, Springer-Verlag, New York

Ruderman, M. 1972, *ARA&A,* **10**, 427.

Ruderman, M. A. 1974, in C. J. Hansen (ed.), *Physics of Dense Matter*, Reidel, Dordrecht, Holland

Schaaf, M. E. 1988, *A&A,* **205**, 335.

Schaaf, M. E. 1990a, *A&A,* **227**, 61.

Schaaf, M. E. 1990b, *A&A,* **235**, 499.

Schwarzschild, M. 1965, *Structure and Evolution of the Stars*, Dover, New York

Schwinger, J. 1951, *Physical Review,* **82**, 664.

Shapiro, S. L. & Teukolsky, S. A. 1983, *Black Holes, White Dwarfs, and Neutron Stars*, Wiley-Interscience, New York

Shibanov, Y. A., Pavlov, G. G., Zavlin, V. E. & Tsuruta, S. 1995, in H. Böhringer, G. E. Morfill & J. E. Trümper (eds.), *Seventeenth Texas Symposium on Relativistic Astrophysics and Cosmology,* Vol. 759 of *Annals of the New York Academy of Sciences*, p. 291, The New York Academy of Sciences, New York

Shibanov, Y. A. & Yakovlev, D. G. 1996, *A&A,* **309**, 171.

Silant'ev, N. A. & Yakovlev, D. G. 1980, *Astrophys. Sp. Sci.,* **71**, 45.

Slattery, W. L., Doolen, G. D. & DeWitt, H. E. 1980, *Phys. Rev. A,* **21**, 2087.

Taylor, J. H., Manchester, R. N. & Lyne, A. G. 1993, *ApJS,* **88**, 529.

Thompson, C. & Duncan, R. C. 1993, *ApJ,* **408**, 194.

Thompson, C. & Duncan, R. C. 1995, *MNRAS,* **275**, 255.

Thompson, C. & Duncan, R. C. 1996, *ApJ,* **473**, 322.

Thorolfsson, A., Rögnvaldsson, O. E., Yngvason, J. & Gudmundsson, E. H. 1997, *Thomas-Fermi Calculations of Atoms and Matter in Magnetic Neutron Stars II: Finite Temperature Effects*, astro-ph/9711091

Thorsson, V., Prakash, M. & Lattimer, J. M. 1994, *Nucl Phys A,* **572**, 693.

Tooker, J. 1994, *Segment Specification (Level 3A) for the Collider System of the Superconducting Super Collider Laboratory*, Technical report, Superconducting Super Collider Laboratory, NO:E10-000007

Tsai, W. Y. & Erber, T. 1975, *Phys. Rev. D,* **12**, 1132.

Tsuruta, S. 1979, *Phys. Rep.,* **56**, 237.

Tsuruta, S., Canuto, V., Lodenquai, J. & Ruderman, M. 1972, *ApJ,* **176**, 739.

Tsuruta, S. & Qin, L. 1995, in H. Böhringer, G. E. Morfill & J. E. Trümper (eds.), *Seventeenth Texas Symposium on Relativistic Astrophysics and Cosmology*, Vol. 759 of *Annals of the New York Academy of Sciences*, p. 299, The New York Academy of Sciences, New York

Ulmer, A. 1994, *ApJL,* **437**, 111.

Urpin, V. A. & Yakovlev, D. G. 1980, *Astrophysics,* **15**, 429.

Usov, V. V. 1992, *Nature,* **357**, 472.

Usov, V. V. 1997, *A&A,* **317**, 87.

Van Paradijs, J., Taam, R. E. & van den Heuvel, E. P. J. 1995, *A&A,* **299**, 41.

Van Riper, K. A. 1988, *ApJ,* **329**, 339.

Van Riper, K. A. & Lamb, D. Q. 1981, *ApJL,* **244**, 13.

Vasisht, G. & Gotthelf, E. V. 1997, *The Discovery of an Anomalous X-ray Pulsar in the Supernova Remnant Kes 73*, astro-ph/9706058

Wang, J. C. L. 1997, *Evidence for magnetic field decay in RX J0720.4-3125*, astro-ph/9706288, submitted to ApJL

Weisskopf, V. S. 1936, *Kongelige Danske Videnskaberns Selskab, Mathematisk-Fysiske Meddelelser,* **14(6)**, 1.

Wilson, R. R. 1953, *Phys. Rev.,* **90**, 720.

Wiringa, R. B., Fiks, V. & Fabrocini, A. 1988, *Phys Rev C,* **38**, 100.

Yakovlev, D. G. 1984, *Astrophys. Sp. Sci.,* **98**, 37.

Yakovlev, D. G. & Urpin, V. A. 1980, *Soviet. Astr.,* **24**, 303.

Yancopoulos, S., Hamilton, T. T. & Helfand, D. J. 1994, *ApJ,* **429**, 832.

Zavlin, V. E., Pavlov, G. G. & Shibanov, Y. A. 1996, *A& A,* **315**, 141.

Zavlin, V. E., Pavlov, G. G., Shibanov, Y. A. & Ventura, J. 1995, *A&A,* **297**, 441.

Zheleznyakov, V. V. & Fabrikant, A. L. 1982, *Sov. Phys. JETP,* **55**, 794.